Structure-Composition-Property Relationships of Stoichiometric and Non-stoichiometric "$Bi_{12}MO_{20}$" Sillenites

Department of Materials Science and Engineering

The University of Sheffield

Thesis

Yu Hu

Submitted in partial fulfilment of the requirements for the

degree of Doctor of Philosophy

Supervisors:

Professor Derek C. Sinclair

and Professor Anthony R. West

October 2008 – May 2013

Declaration

This thesis is submitted for consideration of the award of Doctor of Philosophy. It is believed to be completely original, except where due references has been made. Part of the work from this thesis has been published as a paper in a scientific journal:

Y. Hu and D. C. Sinclair, *Relaxor-like dielectric behavior in stoichiometric sillenite $Bi_{12}SiO_{20}$.* Chemistry of Materials, 2013, 25(1), pp 48-54.

Acknowledgements

First and foremost, I would like to acknowledge my deep sense of gratitude to my primary supervisor Professor Derek C. Sinclair for his open mind, patience, encouragement, thoughtfulness and dedication throughout my years of study in Sheffield. I shall be forever indebted to him for his continued support and guidance. I am also grateful to my secondary supervisor Professor Anthony R. West for his kind guidance and support, especially valuable suggestions about Rietveld refinement work at the final stage of my study.

Secondly, my special thanks go to Dr. Nik Reeves-McLaren, Dr. Jan Pokorny, Dr. Yang Liu, Dr. Matthew Ferrarelli, Dr. Cathy Shields, Dr. Peng Zeng and Dr. Le Ma for providing me with useful training over my time in Sheffield. My gratitude goes to Dr. Andy Donovan, Dr. Andrew Mcqueen, Dr. Ming Li and Mr. Linhao Li (Leo) for their help with collection of neutron diffraction data. The same gratitude goes to Dr. Kevin Knight at ISIS, Rutherford Appleton Laboratory, Oxford for guidance with the neutron diffraction experiments and Dr. John Hanna at University of Warwick for nuclear magnetic resonance spectroscopy measurements. I would also like to thank Dr. Andy Donovan for passing on valuable knowledge and getting me started on the sillenite project; Mr. Andrew Mould for always been there to provide useful help when I needed him. Big thanks to all the MSE clerical and technical staff: Karen Burton, Ann Newbould, Frances Kirk, Wendy Dutton, Beverley Lane, Ben Palmer, Gordon Brown, Steve Mason, Ian Watts, Dean Haylock, Mel Carter, Frank Fletcher, Helen Fletcher and Phil Station. Big love to all the electroceramics members past and present: Abtsam, Andy, Alexis, Andrew Mcqueen, Ashu, Ben, Beata, Chaou, Chen Zhang, Cherry, Denis, Emma, Fayas, Greg, Hidayat, Ian Chen, Iasmi, Lina, Leo, Jing, Jack, John, Jordi, Kambiz, Matt, Ming Li, Mouldy, Nahum, Nik, Nouf, Pengrong, Phei Yi, Rozana, Sarah, Shine, Shu Miao, Sobri, Tina, Tutu, Winson, Yang Liu, and Yan Lei. With all the interesting discussions, motivation and friendship, my time in Sheffield became memorable and enjoyable. I also thank the EPSRC and the CCL for financial support of this project.

Finally, I would like to thank my parents and my husband, Hong. Without your unending support and love I would not have made this far. This thesis is dedicated to you.

Abstract

The structure-composition-property relationships of sillenite-type compounds $Bi_{12}M_xO_{20\pm\delta}$, where M = Zn^{2+}, Mg^{2+}, Fe^{3+}, Al^{3+}, In^{3+}, Ga^{3+}, B^{3+}, Si^{4+}, V^{5+} and P^{5+} have been investigated. This has enabled improved understanding associated with the following aspects: (i) approval of the structural model of Radaev and co-workers' (R model); (ii) validity of the general formula for sillenites suggested by Valant and Suvorov (VS); (iii) rationalisation of the linear trend(s) between dopant ion (M) size and unit cell length as reported by Poleti *et al.*; (iv) the origins of the low (LT) and high temperature (HT) bulk dielectric relaxation effects in sillenites; (v) the variation in bulk conductivity of stoichiometric and non-stoichiometric sillenites; (vi) potential physical applications of sillenites as Low Temperature Co-fired Ceramics (LTCC) dielectrics and/or mixed ionic-electronic conductors.

Rietveld analysis on Neutron Powder Diffraction, NPD, data of $Bi_{12}(Bi_{0.5}Zn_{0.5})O_{19.25}$, $Bi_{12}(Bi_{0.3}Al_{0.7})O_{19.5}$ and $Bi_{12}(Bi_{0.7}In_{0.3})O_{19.5}$ showed the R model to be the most appropriate structural model and confirmed the space group to be *I*23.

Not all of the studied sillenites obeyed the simple VS general formula of: $Bi_{12}(Bi^{3+}_{4/5-nx}M^{n+}_{5x})O_{19.2+nx}$. The formation and composition(s) of sillenites requires consideration of both the dopant (M) charge and ion size. Poleti's linear trends between dopant ion size and sillenite unit cell parameter were found to be only partially correct. Sillenites can be treated as a composite structure consisting of two parts: 'rigid' MO_4 tetrahedral units and a 'flexible' Bi-O framework. The size of the overall M-site ion, r, has a significant influence on the sillenite lattice parameter when $r > 0.31$ Å; however, the Bi-O framework effect has a strong influence on the sillenite unit cell parameter when $r < 0.31$ Å. A value of 0.31 Å represents the ideal ionic radius of an interstitial ion packed perfectly in a regular MO_4 tetrahedron in the sillenite structure. Various linear trends exist between the overall M-site ionic radius and the sillenite unit cell parameter. Each linear trend has its own slope that is influenced by the degree of structural distortion within the Bi-O framework unit.

Two, non-ferroelectric, bulk dielectric relaxations with one at high temperature (> 400 K) and one at low temperature (< 400 K) were observed via *rf* fixed frequency and

Impedance Spectroscopy (IS) measurements. The low temperature (LT) relaxation behaviour is only present when $r < 0.25$ Å (i.e. boron and phosphate/vacancy containing sillenites); whereas the high temperature (HT) relaxation behaviour is universal and exists in all sillenites. This study is the first report of the universal high temperature (HT) dielectric relaxation behaviour in sillenites. IS data associated with the LT and HT relaxation effects were successfully modelled by equivalent circuit analysis. Raman spectroscopy (RS) showed significant temperature dependence associated with Bi-O1 vibrations (~ 538 cm^{-1}) whereas there is negligible change in Bi-O2/O3 vibrations (~ 85 cm^{-1}). The downshifting and broadening of the ~ 538 cm^{-1} peak with increasing temperature indicates increasing distortion of the framework and increasing interatomic distances between Bi and O1 atoms. The connectivity of adjacent Bi atoms via O1 atoms (site $1b$ and $1c$) and the presence of the $6s^2$ electron lone pair on the Bi atoms permits considerable structural flexibility associated with the BiO$_5$LP bipyramids. Combined RS and IS results suggest the HT relaxation originates from non-correlated local dipole moments associated with the movement of Bi^{3+} in the BiO$_5$LP framework units. Additional NMR results further revealed the LT relaxation behaviour might be induced by a random, disordered distribution of small M-dopants over the tetrahedral sites.

Finally, the bulk conductivity, quality factor (Q.f) and onset temperature of the γ-δ phase transition of sillenites was compared. In general, an increase in activation energy of the bulk conductivity causes an increase in Q.f. Higher Q.f values indicate a more robust and ordered structure. A higher onset temperature of the γ-δ phase transition indicates a more stable sillenite compound. Generally stoichiometric sillenites show excellent microwave dielectric properties and have the most promise as potential LTCC dielectric materials. Many sillenites exhibit dielectric relaxation effects near ambient temperature and this results in low Q.f and high dielectric loss, thus eliminating them as potential LTCC materials. IS results for superstoichiometric sillenites with an excess oxygen sublattice such as $Bi_{12}(Bi^{3+}_{0.03}P^{5+}_{0.89}\square_{0.08})O_{20.27}$, $Bi_{12}(P^{5+}_{0.86}\square_{0.14})O_{20.15}$ and even $Bi_{12}(Bi_{0.7}In_{0.3})O_{19.5}LP_{0.7}$ and $Bi_{12}(Bi_{0.6}In_{0.4})O_{19.5}LP_{0.6}$ exhibit oxide ionic conductivity at T > 773 K. Electrical conductivity results show these superstoichiometric sillenites to be mixed electronic and ionic conductors.

Annex

It is noteworthy to mention that all the sillenites in this thesis are written in the format of using Valant and Suvorov's general formula (VS general formula) [1] for stoichiometric sillenites: $Bi_{12}(Bi^{3+}_{4/5-nx}M^{n+}_{5x}\square_{1/5-(5-n)x})O_{19.2+nx}$, where M represents ion(s) on a tetrahedral site, n is the charge on the dopant ion, M; x is the upper substitution limit and $\square$ is the remaining vacant M-site cations. This general formula can be simplified as $Bi_{12}(Bi^{3+}_{4/5-nx}M^{n+}_{5x})O_{19.2+nx}$. Variable formulae are derived depend on different oxidation states of M-dopants, n (i.e. n is usually from 2+ to 5+). For instance,

$$M^{2+} \text{ ions: } Bi_{12}(Bi^{3+}_{0.67}M^{2+}_{0.33})O_{19.33} \ (x_{max} = 1/15) \tag{1.1}$$

$$M^{3+} \text{ ions: } Bi_{12}(Bi^{3+}_{0.5}M^{3+}_{0.5})O_{19.5} \ (x_{max} = 1/10) \tag{1.2}$$

$$M^{4+} \text{ ions: } Bi_{12}(M^{4+})O_{20} \ (x_{max} = 1/5) \tag{1.3}$$

$$M^{5+} \text{ ions: } Bi_{12}(M^{5+}_{4/5}\square_{1/5})O_{20} \ (x_{max} = 4/5) \tag{1.4}$$
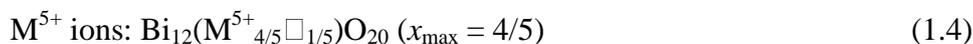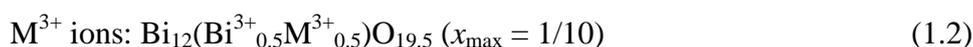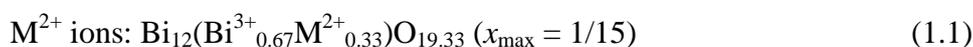
The Valant and Suvorov's general formula is consistent with the Radaev and coworker's structural model (R model) [2,3] based on the concept that 80 % of the M-sites consist of Bi^{3+} ions for $x = 0$ to reflect the connection with the parent structure of γ-Bi_2O_3 and the need to accommodate lone pairs of any M-site Bi^{3+} ions to complete the anion sublattice to a stoichiometric value of 20, i.e. $Bi_{12}(Bi_{0.8})O_{19.2}LP_{0.8}$.

References:

[1]   M. Valant and D. Suvorov, A stoichiometric model for sillenites, Chemistry of Materials, 2002. **14**: p. 3471-3476.

[2]   S. F. Radaev, L. A. Muradyan and V. I. Simonov, Atomic structure and crystal chemistry of sillenites $Bi_{12}(Bi^{3+}_{0.50}Fe^{3+}_{0.50})O_{19.50}$ and $Bi_{12}(Bi^{3+}_{0.67}Zn^{2+}_{0.33})O_{19.33}$, Acta Crystallographica Section B-Structural Science, 1991. **47**: p. 1-6.

[3]   S. F. Radaev, V. I. Simonov and Y. F. Kargin, Structural features of g-phase Bi_2O_3 and its place in the sillenite family, Acta Crystallographica Section B-Structural Science, 1992. **48**: p. 604-609.

Table of Contents

1 Introduction and Literature Review

1.1 Introduction

Sillenites or doped bismuth oxides (isomorphous to γ-Bi_2O_3) are versatile materials with dopants ranging from the *s*-, *p*- and *d*- blocks in the periodic table. Nowadays sillenites with a general formula of $Bi_{12}MO_{20\pm\delta}$ comprise a family with over 60 members. Their complex structures give rise to various properties that depend on the dopant concentration, temperature, frequency and pressure. The compositional and structural variation originates from the flexibility of the sillenite framework structure, where various cationic substitutions incorporated with Bi-O polyhedra can accommodate and tolerate structural and compositional deviation from the ideal sillenite structure and composition of $Bi_{12}M^{4+}O_{20}$.

Sillenites adopt a pseudo-body-centred cubic and non-centrosymmetric cell with space group *I*23. A cubic system of this type can be piezoelectric but not ferroelectric. The sillenite framework (described in section 1.3.1) is highly distorted even in 'ideal' sillenites due to the ionic radius mismatch of the M-site cation in the tetrahedral site and also the Bi^{3+} lone pair effects in the Bi-O framework polyhedra. Such lone pairs occupy a volume in space similar in size to an O^{2-} ion. The stereochemical activity of the electron lone pairs has a significant role in the bonding between the Bi and O atoms and therefore influences the electronic structure, vibrational modes and dielectric properties. It is not surprising, therefore, that sillenites exhibit a variety of electro-optical and electrical properties including piezoelectricity[1], Second Harmonic Generation (SHG)[2] and high relative permittivity[3] and, in the case of some non-stoichiometric compositions, mixed oxide ionic-electronic conduction[4, 5].

This chapter can be separated into two parts. The first part of this chapter reviews the structural details of different types of sillenites, the formation and subgroups of sillenites and their physical properties. The second part of the chapter summaries the intrinsic and extrinsic mechanisms for high permittivity in electroceramics.

1.2 Bismuth Oxide (Bi$_2$O$_3$)

1.2.1 Polymorphism of Bismuth Oxide (Bi$_2$O$_3$)

Bismuth oxide has four well-known polymorphs: α-, β-, γ- and δ-Bi$_2$O$_3$. During heating, the stable low temperature monoclinic α-phase (space group $P2_1/c$) transforms to the stable, high temperature, faced-centred cubic δ-phase (space group Fm-3m) at 729 ℃. This fcc δ-phase melts at 824 ℃. During cooling, two metastable phases (either tetragonal β-phase or body-centred cubic γ-phase) can form depending on temperature, thermal treatment, chemical doping etc.[6, 7] The tetragonal β-phase (space group P-4b2) forms at ~ 650 ℃ and transforms to a stable α-phase at ~ 330 ℃, whereas the bcc γ-phase (space group I23) forms at ~ 639 ℃ and can be retained at room temperature during slow cooling. The phase transformation and thermostability range has been summarized by Harwig and Gerards[8], Figure 1.1.
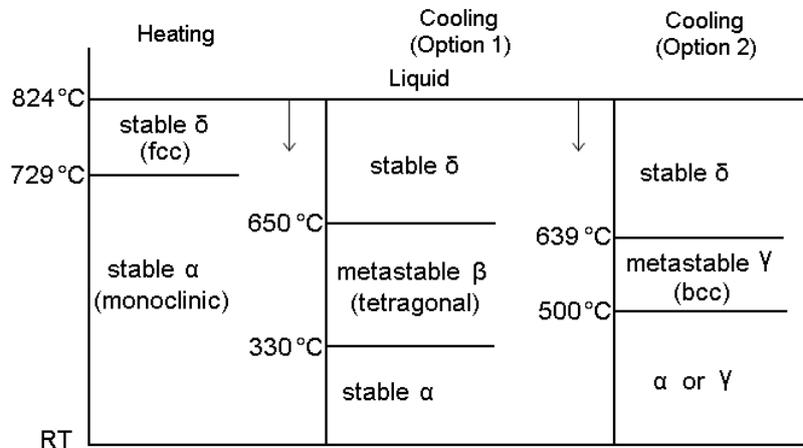
Figure 1.1[8] Transformation of Bi$_2$O$_3$ polymorphs, of which α-Bi$_2$O$_3$ is monoclinic with space group $P2_1/c$[9]; β-Bi$_2$O$_3$ is tetragonal with space group P-4b2[10]; δ- and γ-Bi$_2$O$_3$ is cubic with space group Fm-3m [11] and I23[9], respectively.

Recently, two new Bi$_2$O$_3$ polymorphs were reported by particular synthesis routes: a metastable triclinic ω-Bi$_2$O$_3$ polymorph existing on BeO substrate thin films at 800 ℃[12] and a metastable orthorhombic ε-Bi$_2$O$_3$ phase under hydrothermal synthesis at 400 ℃ during cooling from a β- to α-phase transformation.[13]

1.2.2 The Conductivity of Bi$_2$O$_3$

The conductivity of α-, β-, γ- and δ-Bi$_2$O$_3$ during repeated heating and cooling cycles was plotted by Harwig and Gerards, Figure 1.2.[8] The conductivity of α-Bi$_2$O$_3$ is *p*-type at room temperature and transforms to *n*-type at ~ 550 ℃, whereas the conductivity in β-, γ- and δ-Bi$_2$O$_3$ is mainly ionic, with oxide ions being the charge carrier.[8, 14] The conductivity of δ-Bi$_2$O$_3$ is ~ 1-2 orders of magnitude greater than YSZ ($Zr_{1-x}Y_xO_{2-x/2}$). The high conductivity in δ-Bi$_2$O$_3$ is accounted for by the highly disordered fluorite-type structure, where 1/4 of the oxygen sites are vacant; in addition, the accommodated Bi^{3+} ions enable a highly disordered and polarisable network to aid oxide ion mobility.[15] As a consequence, extensive studies have been performed on Bi$_2$O$_3$-based materials to explore good oxygen ion conductors for applications as solid oxide fuel cells and oxygen sensors, particularly for doped δ-Bi$_2$O$_3$ materials containing lanthanides and transition metal cations, such as Y, V, Nb, P, Ta[16-19]; BIMEVOX[20] and Aurivillius phases[21].
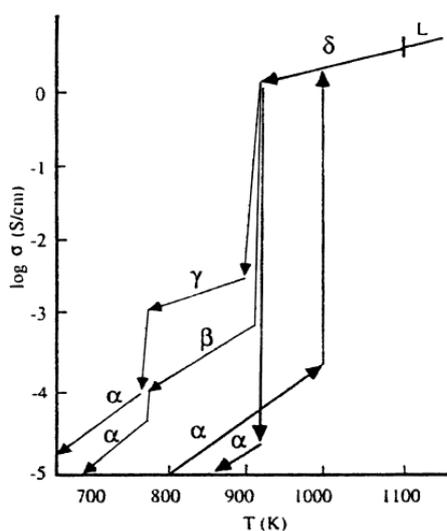
Figure 1.2[8] Electrical conductivity of Bi$_2$O$_3$ polymorphs as a function of temperature during heating (▶) and cooling (◀) cycles.

1.3   Sillenites

Sillenite (i.e. stabilised γ-Bi$_2$O$_3$) was discovered in 1937 and named after L. G. Sillén[22], who accidently obtained a body-centred cubic phase by firing Bi$_2$O$_3$ with Al$_2$O$_3$ at 900 °C for 5 minutes. This phase was also obtained by Schumb and Rittner[23] in 1943 by "fusing" Bi$_2$O$_3$ with SiO$_2$ at 875 °C for 20 minutes. Aurivillius and Sillén[24] then noticed it was possible to stabilize γ-Bi$_2$O$_3$ at room temperature by using a small amount of various cations with ionic radii from 0.4 – 0.6 Å. Since then more than 60 sillenite members have been reported.

1.3.1 Sillenite Structures

Sillenite has a general formula of Bi$_{12}$M^{4+}O$_{20}$, where M represents ion(s) on a tetrahedral site with an average oxidation state from 2+ to 5+ and ionic radius from 0.1 Å (B^{3+}) to 0.98 Å (Pb^{2+}) [25]. The ideal stoichiometric sillenite contains a tetravalent M-cation of ionic radius, r = 0.31 Å, forming geometrically regular MO(3)$_4$ tetrahedra[26] and a fully occupied oxygen sublattice (i.e. 20) [25], Figure 1.3 (a). The closest known examples are Bi$_{12}$M^{4+}O$_{20}$ with M = Si^{4+} (r = 0.26 Å), Ge^{4+} (r = 0.39 Å), and Ti^{4+} (r = 0.42 Å) [7, 22] with the most 'perfect' crystal lattice being Bi$_{12}$GeO$_{20}$ based on structural refinement [27] and Raman spectroscopy data [28].

(a)   (b)
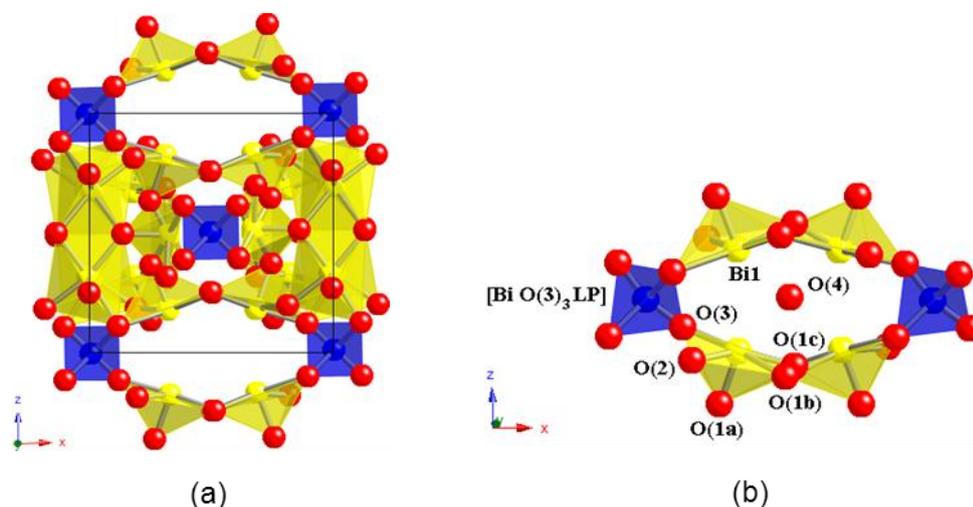
Figure 1.3 Structure of (a) ideal (Bi$_{12}$M^{4+}O$_{20}$) sillenite[22] viewed along the (001) plane,

where yellow, blue and red spheres represent Bi^{3+}, M^{4+}, and O^{2-} ions, respectively; black lines indicate the body-centred cubic unit cell of the structure. (b) A fragment of the sillenite [29] structure to show the various crystallographic sites of sillenites.

In general, sillenites have a pseudo-body-centred cubic unit cell ($a \sim 10.25$ Å [9]) and the average structure belongs to the non-centrosymmetric space group $I23$ (no. 197), Figure 1.3 (a). The complex three-dimensional (3D) framework structure is formed by Bi-O distorted polyhedra, BiO_5LP, where Bi^{3+} ions are coordinated with five oxygen ions as well as its stereochemically active $6s^2$ lone electron pairs (denoted as LP), Figure 1.3 (b). Pairs of these distorted Bi octahedra edge-share through two oxygen ions (i.e. O(1b) and O(1c)) and corner-share with O(3) ions from the adjacent $MO(3)_4$ tetrahedra, these chains form a 3D network by corner-sharing through the other two oxygen ions, O(1a) and O(2). The O(4) site is empty in ideal $Bi_{12}MO_{20}$ but is reported to be partially occupied for oxygen excess sillenites, e.g. $Bi_{12}(Bi_{0.03}V_{0.89})O_{20.27}$.[25]

The sillenite framework structure can also be considered as the connectivity of many condensed units, as shown in Figures 1.4 (a)-(e). [30] A condensed unit, Figure 1.4 (b) is formed by connecting two sets of edge-sharing BiO_5LP bipyramids, Figure 1.4 (a), in an inverted position. The $Bi_{24}O_{40}$ sublattice, Figure 1.4 (c), is then constructed by orienting the condensed units along each edge of the cubic cell. The 6 condensed units sharing oxygen atoms at the corner of the unit cell create a cube that contains the M atoms, Figure 1.4 (c). This half of the structure consists of three sets of perpendicular chains of condensed units that intersect at the cubes. The other half of the structure consists of an identical set of chains which intersect at the centre of the unit cell. These two sets of chains are connected by displacement of each other at (1/2, 1/2, 1/2) to obtain a body centred unit cell, Figure 1.4 (d). One slice of the connected structure perpendicular to one of the cubic axes is shown in Figure 1.4 (e), where M represents cations in the tetrahedral sites. [30]
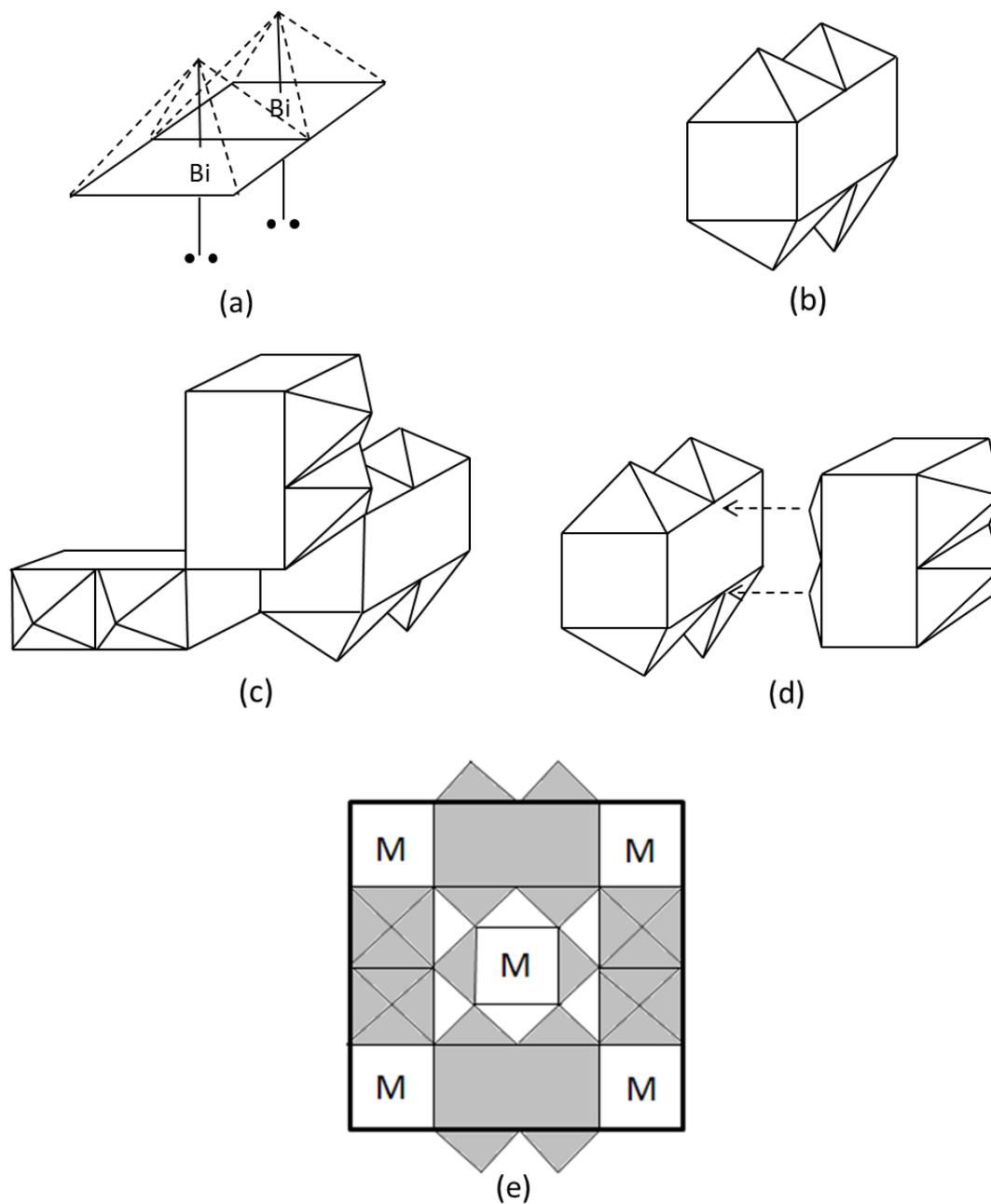
Figure 1.4[30] Construction of the sillenite framework structure by condensed units.

1.3.2 Polyhedra in Sillenite

According to the structural model proposed by Radaev *et al.* [25] (Section 1.3.3), several different types of Bi-O polyhedra (or condensed units[30]) are summarized here to describe the structural distortion in sillenites.

1.3.2.1 Configuration of Bi-O polyhedra: BiO_5LP and BiO_4LP in the framework of sillenite

BiO_5LP, Figure 1.5 (a), is a distorted octahedron with O(3)-O(1c)-O(1b)-O(2) in the equatorial plane and axial vertices O(1a) and Bi^{3+} $6s^2$ unshared electron pair (LP).

BiO_4LP, Figure 1.5 (b), is a distorted trigonal bipyramid with the equatorial plane containing LP-O(1a)-O(1b) and the axial vertices along O(2) and O(1c). This configuration exists in the structure where there is a missing oxygen atom at the O(3) position from the adjacent tetrahedron. Orientation of the unshared electron pair varies so as to make the new polyhedron stable.
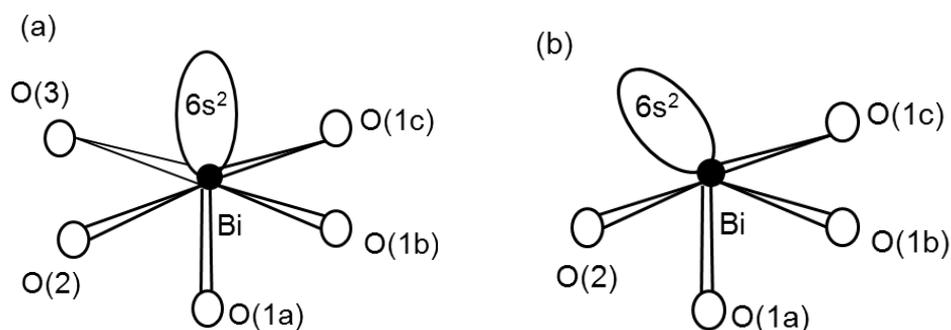
Figure 1.5 [25] The structure of (a) a distorted octahedron - BiO_5LP in the ideal sillenite structure and (b) a distorted trigonal bipyramid - BiO_4LP in a distorted sillenite structure with partial O(3) atoms missing (e.g. $Bi_{12}(Bi_{0.5}Fe_{0.5})O_{19.5}$).

1.3.2.2 Configuration of Bi-O polyhedra: MO_4, BiO_3LP and $\square_MO_4$ in the tetrahedra of sillenites

MO_4, Figure 1.6 (a), is a typical tetrahedron with the oxidation states of M-dopants from 2+ to 5+.

BiO_3LP, Figure 1.6 (b), 'Umbrella-like' distorted tetrahedra, where a large and asymmetric Bi^{3+} ion occupies the tetrahedral site with its $6s^2$ lone electron pair hosted in the vacant O(3) site. The Bi^{3+} ion displaced towards its lone electron pair, increasing the distances between the Bi atom and the other three O(3) atoms.

$\square_MO_4$ is a void tetrahedron with cationic deficiency in the M tetrahedral interstitial, which gives rise to charge balance to compensate for the significant electron deficiency associated with vacant O(3) atoms. For instance, there are 20% such tetrahedra in the γ-Bi_2O_3 structure, i.e. $Bi^{3+}_{12}(Bi^{3+}_{0.8}\square_{0.2})O_{19.2}LP_{0.8}$, where $\square$ represents the void tetrahedral site.
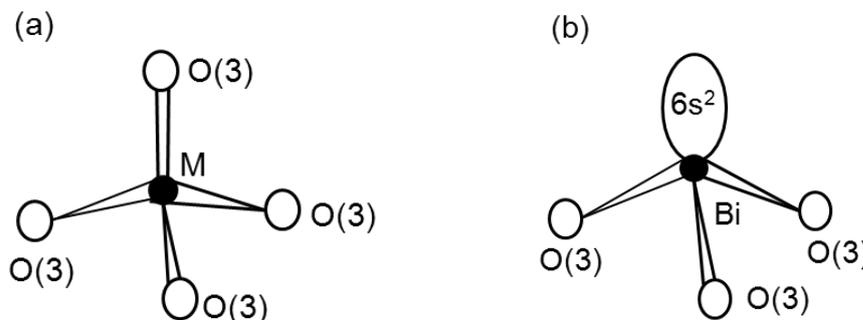
Figure 1.6 The structure of (a) a regular tetrahedron – MO_4 and (b) an 'umbrella-like' distorted tetrahedron – BiO_3LP in a distorted sillenite structure with partial O(3) atoms missing (e.g. $Bi_{12}Bi_{0.5}Fe_{0.5}O_{19.5}$).

1.3.2.3 Off-centred Ion Displacement

The off-centred ion displacement refers to the movement of a cation from the centre of its coordinated polyhedron. Off-centred ion displacements usually result in symmetry changes of the structure, however, some of them do occur in untilted perovskites.[31] Ions prone to have off-centred displacements are the lone pair cations and d^0 cations. Lone pair effects

are a characteristic of elements with a ns^2 valence shell containing a pair of electrons, e.g. Tl^+, Pb^{2+} and Bi^{3+}, which can be stabilised by surrounding oxygen atoms.

1.3.3 Radaev and Coworkers' Structural Model (R Model)[29, 32]

There have been disputes for years regarding the composition-structure relationships of sillenites, particularly due to the uncertainty of the oxidation states of Bi ions and the associated atomic arrangements. Many different structural models have been suggested. Among them there are two general structural approaches: Craig & Stephenson (CS model)[33] and Radaev & coworkers (R model)[29, 32]. The fundamental difference between them is whether Bi^{5+} ions exist in sillenites.

Since the initial X-ray diffraction studies by Abrahams *et al.*[27], early investigation of sillenite single crystals was from the oxygen stoichiometry approach, such as Levin and Roth [7], Craig and Stephenson (CS) [33], Abrahams *et al.* [34, 35], Efendiev *et al.*[36], Swindell & Gonzalez[37] *etc.* The most representative model is the CS model, where alternating occupancy of the tetrahedral sites by Bi^{3+} and Bi^{5+} ions maintains the charge neutrality for a fully occupied oxygen sublattice, e.g. $Bi_{12}(Bi^{5+}_{0.5}Bi^{3+}_{0.5})O_{20}$ for γ-Bi_2O_3; $Bi_{12}(Bi^{5+}_{0.67}Zn^{2+}_{0.33})O_{20}$ and $Bi_{12}(Bi^{5+}_{0.5}Fe^{3+}_{0.5})O_{20}$. The average charge of the M-site dopants should be 4+ when the oxygen sublattice is fully occupied (=20). Until recently, some research groups such as Grabmaier[38], Watanabe[39], Neov[40] etc. still support the CS model. However, the CS model gave unconvincing experimental evidence for the presence of Bi^{5+} ions in γ-Bi_2O_3 or in other sillenites. Aurivillius and Sillén[24] did not find any evidence of Bi^{5+} ions in $Bi_{26}O_{40}$ within the limits of errors.

Radaev and coworkers[29, 32] developed a structural model (R model) that established the atomic mechanisms of broad sillenite analogues based on refinements of neutron diffraction data. The R model has been confirmed by many researchers and it is able to explain many experimental observations.[41, 42] In this model all the Bi atoms are Bi^{3+} ions and charge compensation is achieved by variations in the oxygen sublattice, i.e. variable

occupation of the O(3) sites. Depending on the valence and electronic configuration of the M-dopants, noticeable deviations from the ideal formula of $Bi_{12}MO_{20}$ have been found. For instance, in $Bi_{12}(Bi^{3+}_{0.5}Fe^{3+}_{0.5})O_{19.5}$ and/or $Bi_{12}(Bi^{3+}_{0.67}Zn^{2+}_{0.33})O_{19.33}$, $FeO(3)_4$ and/or $ZnO(3)_4$ units were replaced statistically by different amounts of distorted Bi tetrahedra, i.e. umbrella-like $BiO(3)_3LP$ groups, Figure 1.6 (b). The presence of the extraordinarily large and asymmetric Bi^{3+} cation with a lone electron pair in the tetrahedral voids was confirmed by the R model, where one oxygen vertex in the tetrahedra was missing and replaced by the Bi^{3+} $6s^2$ lone electron pairs.

Since sillenites are stabilized forms of metastable γ-Bi_2O_3, Radaev *et al*.[32] structurally linked γ-Bi_2O_3 with sillenite: γ-Bi_2O_3 is actually a distorted version of the ideal sillenite structure. γ-Bi_2O_3 can therefore be expressed in a form of sillenite: $6.4 \times Bi_2O_3 = Bi_{12}Bi_{0.8}O_{19.2} = Bi_{12}[BiO_3]_{0.8}[\square O_4]_{0.2}O_{16} = Bi^{3+}_{12}[Bi^{3+}_{0.8}\square_{0.2}]O_{19.2}LP_{0.8}$, i.e. with 80 % occupancy of the tetrahedral site by distorted $Bi(O3)_3LP$ tetrahedra and 20 % occupancy by void tetrahedra.

In conclusion, Radaev *et al*.[25] suggested the crystal chemistry of sillenite-based phases to be complex, versatile and adaptive: there is more than one sillenite structural model and each particular model depends on the size and nature of the M cation(s).

1.3.4 Valant and Suvorov's General Formula (VS Formula)[43]

Valant and Suvorov[43] divided sillenites into two main groups: <u>stoichiometric</u> and <u>non-stoichiometric</u>, depending on whether the oxygen sublattice is fully occupied (i.e. = 20) or not.

Stoichiometric sillenites can be subdivided into two groups based on the oxygen content: either the oxygen sublattice is fully occupied by oxygen ions, e.g. $Bi_{12}Si^{4+}O_{20}$ and $Bi_{12}(B^{3+}_{0.5}P^{5+}_{0.5})O_{20}$ or by a combination of oxygen ions and lone electron pairs of Bi^{3+} ions, e.g. $Bi_{12}(Bi^{3+}_{2/3}Zn^{2+}_{1/3})O_{19.33}LP_{0.67}$ and $Bi_{12}(Bi^{3+}_{0.5}Fe^{3+}_{0.5})O_{19.5}LP_{0.5}$. The overall M-cation valence in the latter group of sillenites may not be 4+.

Non-stoichiometric sillenites are defined where the oxygen sublattice is not fully occupied and aliovalent substitutions of the M-site cations make the non-stoichiometric sillenites possible. They can be subdivided into two groups: <u>sub-stoichiometric</u> with a deficient oxygen sublattice (< 20), e.g. $Bi_{12}B^{3+}O_{19.5}$ and <u>super-stoichiometric</u> with an excess oxygen sublattice (> 20), e.g. $Bi_{12}(Bi^{3+}_{0.03}V_{0.89}\square_{0.08})O_{20.27}LP_{0.03}$.

Valant and Suvorov[43] developed a general formula for stoichiometric sillenites: $Bi_{12}(Bi^{3+}_{4/5-nx}M^{n+}_{5x}\square_{1/5-(5-n)x})O_{19.2+nx}$, where n is the charge on the dopant ion; x is the upper substitution limit and $\square$ is the remaining vacant M-site cations. This general formula (simplified as $Bi_{12}(Bi^{3+}_{4/5-nx}M^{n+}_{5x})O_{19.2+nx}$) is consistent with the R model based on the concept that 80 % of the M-sites consist of Bi^{3+} ions for $x = 0$ to reflect the connection with the parent structure of γ-Bi_2O_3 and the need to accommodate lone pairs of any M-site Bi^{3+} ions to complete the anion sublattice to a stoichiometric value of 20, i.e. $Bi_{12}(Bi_{0.8})O_{19.2}LP_{0.8}$. It is used for stoichiometric sillenites with an oxidation state of M-dopants (n) from 2+ to 5+. For instance,

$$M^{2+} \text{ ions: } Bi_{12}(Bi^{3+}_{0.67}M^{2+}_{0.33})O_{19.33} \; (x_{max} = 1/15) \tag{1.1}$$

$$M^{3+} \text{ ions: } Bi_{12}(Bi^{3+}_{0.5}M^{3+}_{0.5})O_{19.5} \; (x_{max} = 1/10) \tag{1.2}$$

$$M^{4+} \text{ ions: } Bi_{12}(M^{4+})O_{20} \; (x_{max} = 1/5) \tag{1.3}$$

$$M^{5+} \text{ ions: } Bi_{12}(M^{5+}_{4/5}\square_{1/5})O_{20} \; (x_{max} = 4/5) \tag{1.4}$$
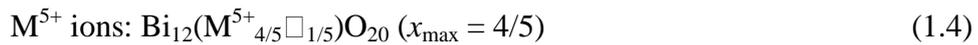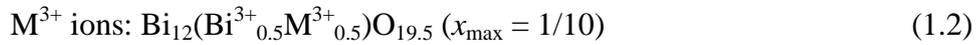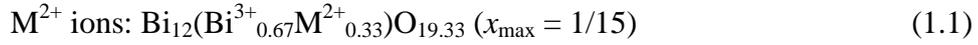
These formulae indicate the substitution mechanism must have an upper limit for M-dopants (x_{max}). For $n = 2 - 4$, the upper substitution limit is similar with all the vacant tetrahedral sites occupied, i.e. $\square_{1/5-(5-n)x} = 0$. However, for $n = 5$, the upper limit for this series is not only limited by the vacancy concentration but also by the Bi^{3+} concentration in the tetrahedral site. In this analogue, the vacancies ($\square$) usually exist in the tetrahedral site to compensate charge neutrality for 5+ M-dopants. The upper limit is reached when all the Bi^{3+} ions are removed from the tetrahedral sites.

1.3.5 Relationship between Lattice Parameter and M^{n+} Ionic Radius

An empirical linear relation between lattice parameter of sillenite and ionic radius of M^{n+} dopants was first proposed by Levin and Roth [7]: the bigger the M-site ion, the larger the unit cell. Recently, Poleti *et al.*[44] collated lattice parameter (*a*) values of 23 sillenites from literature and plotted *a* versus ionic radius of the M^{n+} dopants (*r*) over the range $0.1 \leq r \leq 0.98$ Å. They postulated the data could be divided into two linear trends which might indicate two different phase formation mechanisms, Figure 1.7 [44].
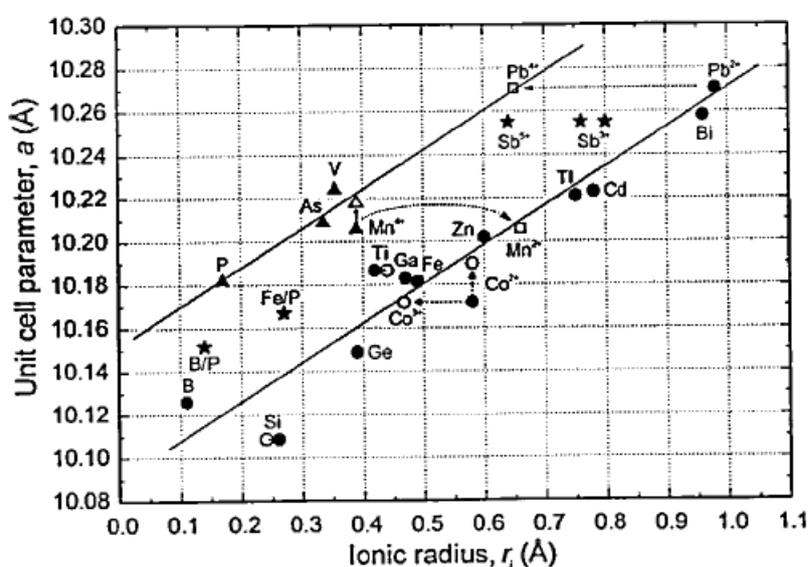
Figure 1.7[44] Relationships between unit cell parameter (*a*) and ionic radius (*r*) of various M-ion doped sillenites, after Poleti *et al.*

For M^{n+} ions with $n = 2$-4 a linear fit equation of $a = 0.18(2)\ r + 10.09$ with a correlation coefficient of R = 0.96 was obtained whereas data for M^{5+} ions also gave a linear fit with the same slope but a larger intercept on the *a* axis: $a = 0.18(4)\ r + 10.15$ with a correlation coefficient of R = 0.95. They pointed out that some samples were intermediate between these two linear lines and attributed this to samples with mixed valent M-dopants, e.g. M^{3+}/M^{5+} dopants: $Bi_{12}(B^{3+}_{1/2}P^{5+}_{1/2})O_{20}$ with $a = 10.1515(5)$ Å for $x = 0.14$ Å. [44]

However, the accuracy of the plot is debatable for the following reasons:

1. The ionic radius data of M^{n+} dopants were extracted only from dopants with regular tetrahedral coordination i.e. MO_4 tetrahedra, whereas those from Bi^{3+} ions

form with 'umbrella-like' distorted tetrahedra-BiO_3LP was not taken into account. They reported the unit cell size of sillenites to be significantly influenced by the size of regular MO_4 tetrahedra, especially by the size of M^{n+} dopants; whereas distorted BiO_3LP tetrahedra had little influence on the overall unit cell. They explained that introducing Bi^{3+} ions in the tetrahedral site would create oxygen vacancies and reduce the size of the unit cell. However, this statement is controversial with the R model, where the created oxygen vacancies are occupied by the unshared $6s^2$ lone electron pair of Bi^{3+} ions by forming 'umbrella-like' BiO_3LP tetrahedra. Hence, the ionic radius data of M^{n+} dopants should consider all dopants located in the M-site, by means of regular MO_4 tetrahedra, distorted BiO_3LP tetrahedra or other polyhedra, e.g. BO_3 trigonal units that fit into the tetrahedral M-O skeleton.

2. The lattice parameter data in the plot were selected based on an 'averaged' experimental value from different literature with different stoichiometries. For instance, for the Zn sillenite shown in Figure 1.7, the lattice parameter ($a = 10.202$ Å) was an averaged value from three sets of literature data: $Bi_{12}(Bi^{5+}_{0.67}Zn^{2+}_{0.33})O_{20}$ with $a = 10.194(3)$ Å[33]; $Bi_{12}ZnO_{20}$ with $a = 10.205$ Å[45] and $Bi_{12}(Bi^{3+}_{0.67}Zn^{2+}_{0.33})O_{19.33}$ with $a = 10.207(3)$ Å.[29] Some of the data sets are inconsistent with the R model and therefore make the overall reliability suspicious.

Therefore, it is necessary to revise the relationship between unit cell parameter and M^{n+} ionic radius based on one's own lab results with the guidance of only one structural model, the R model, and to testify the existence (if any) of the linear trend(s) in the plot(s), as shown in Figure 1.7.

1.3.6   Physical Properties of Sillenites

Investigations of sillenites have long been motivated by their excellent electro-optic and piezoelectric properties in stoichiometric sillenite analogues: $Bi_{12}SiO_{20}$, $Bi_{12}TiO_{20}$ and $Bi_{12}GeO_{20}$. Their physical properties such as photoconductivity, photo-refractivity, piezo-modulus etc. are widely used in industry for optical switching, information processing and holographic data storage applications, where single-crystals free from grain-boundary effects are a necessity.[36, 46-49] Recently, however, polycrystalline sillenites have attracted attention as being suitable dielectric materials in low temperature co-fired ceramic (LTCC) technology due to their low sintering temperatures (commonly $\leq$ 850 ℃), chemical compatibility with silver electrodes, low dielectric loss and temperature-stable permittivity, ε_r, of ~ 35-40 near room temperature.[3, 50, 51] Sillenite phases have also been reported to exhibit high ionic and mixed conductivity, which draws special research attention to their applicability in electrochemical cells.

1.3.6.1 Low Temperature Co-fired Ceramic (LTCC)

LTCC technology combines a series of thin layers of glass ceramics or ceramic tapes forming multilayer LTCC modules, which enables a versatile mix of passive electrical components (such as micro-strips, antennas, filters, resonators, capacitors, resistors, inductors etc.) interconnecting each other with 3D stripline circuitry. [52-54] LTCC technology realises cost-effective development of complex miniaturised circuits by using highly conductive and inexpensive metal electrodes such as silver or copper. Metal electrodes are embedded between layers of green ceramic tapes before co-firing together to densify. This requires the applied materials to possess low sintering temperatures of $\leq$ 850 ℃ and low thermal expansion of ~3 MK^{-1} to match with silicon-based substrates mounted on the exterior of the LTCC module.[55]
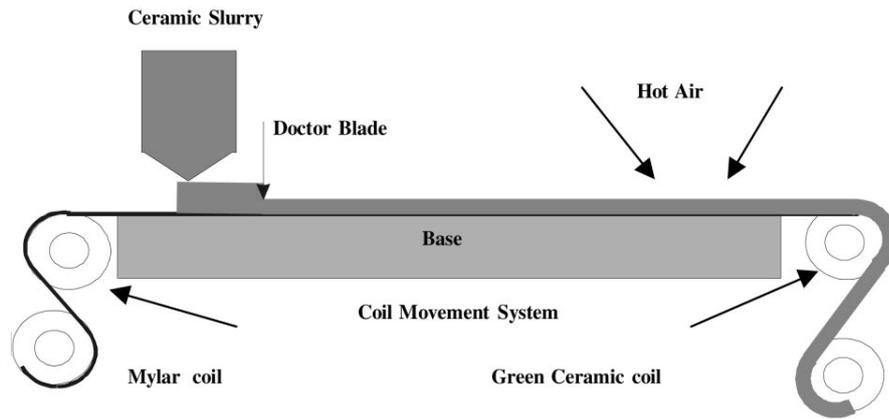
Figure 1.8[56] A doctor blade set-up for casting LTCC tape.

In LTCC technology, a doctor blade is usually used to control the thickness of the green LTCC tape, Figure 1.8.[56] Doctor blade processing requires careful control to avoid warping, out of tolerance thickness and other defects. Casting is completed by spreading the ceramic slurry formulation on a moving carrier substrate (usually a film of cellulose acetate, Teflon, Mylar, or cellophane) to form a paste. Hot air is blown on the other side of the machine to remove some of the volatiles in the paste and a thin, flexible green tape is obtained that is ready to be cut and laminated into the required configuration. Multiple layers of green tapes are fabricated in a similar method and stacked together as a 3D "composite" structure prior to firing. Each layer may have cavities, channels, and internal passive elements such as capacitors, resistors etc.

● *Relative Permittivity (ε_r)*

The resonant frequency of a standing wave in microwave dielectric material is given by Equation 1.5[55]:

$$f_0 = \frac{c}{D\,\varepsilon_r^{1/2}} \tag{1.5}$$

where f_0 is the resonant frequency; c is the speed of light in vacuum; D is the diameter of the dielectric material; ε_r is the relative permittivity, which should be large to minimise D under the same f_0.

The relative permittivity or dielectric constant, ε_r, of a dielectric material can be calculated from the Clausius-Mossotti Equation, Equation 1.6, [57] which relates ε_r to its total ionic and electronic polarisability, α_D^T, per molar volume of the material, V_m.

$$\alpha_D^T = \frac{3}{4\pi}\left[\frac{(V_m)(\varepsilon_r - 1)}{(\varepsilon_r + 2)}\right] \qquad (1.6)$$

Therefore,

$$\varepsilon_r = \frac{3V_m + 8\pi\,\alpha_D^T}{3V_m - 4\pi\,\alpha_D^T} \qquad (1.7)\;[58]$$

where α_D^T is determined by the additivity rule, i.e. the sum of the polarisabilities of individual ions. Ion polarisabilities of the constituent ions used in this thesis were based on the scale produced by Shannon[58], which has been reported to be accurate for many microwave dielectric materials.[59, 60] As the Clausius-Mossotti equation only takes into account the ionic and electronic polarisability of the material, it can be used to estimate whether other polarisation mechanisms exist, as the measured and calculated ε_r will differ significantly.

● *Quality Factor (Q.f)*

The quality factor Q.f (= 1/tan δ) measures the shape/selectivity of a resonance peak at 3dB of the peak maximum, Δf, under the microwave resonant frequency, f_o, Figure 1.9[55] and Equation 1.8.[55] A high value of Q.f is desired as it gives better selectivity and therefore increases the density of channels in a given frequency range. From Equations 1.5 and 1.8, there should be a 'fundamental compromise' between Q.f and ε_r: materials with higher ε_r should have lower Q.f due to their inverse proportional correlations.
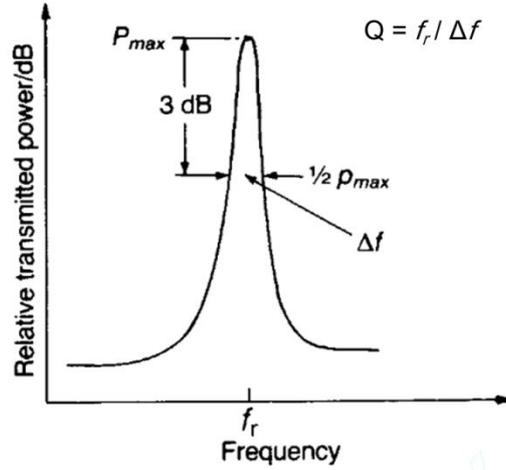
Figure 1.9[55] Schematic representation of resonant peak showing the definition of Q.f.

$$Q.f = \frac{f_0}{\Delta f} \tag{1.8}$$

Besides intrinsic losses such as anharmonic lattice vibrations between the phonons of the crystal and crystal lattice defects due to dopant atoms, vacancies *etc.*, Q is very sensitive to sample processing conditions.[61-63] In many cases, Q is dominated by extrinsic losses such as grain boundaries, inclusions and secondary phases.[64]

● *Temperature Coefficient of Resonant Frequency (τ_f)*

The temperature coefficient of the resonant frequency (τ_f) measures the thermal stability of dielectric materials. It is desirable that τ_f is close to zero so that the resonant frequency is independent of temperature fluctuations. τ_f is compensated by the temperature coefficient of linear expansion of the ceramic (α_L) and the temperature coefficient of the permittivity (τ_ε), Equation 1.9. [55]

$$\tau_f = - \alpha_L - \frac{\tau_\varepsilon}{2} \tag{1.9}$$

Harrop[65] correlated the temperature coefficient of permittivity τ_ε with relative permittivity ε_r, Figure 1.10. Generally, as ε_r increases τ_f becomes increasingly positive. In many complex perovskites, τ_f has also been related to structural parameters such as phase transition(s) involving octahedral tilting[66, 67], tolerance factor[68] and bond valence sums[69]

etc. In practice, a near zero τ_f can be tuned by forming a composite or solid solution of two materials with opposite signs of τ_f.
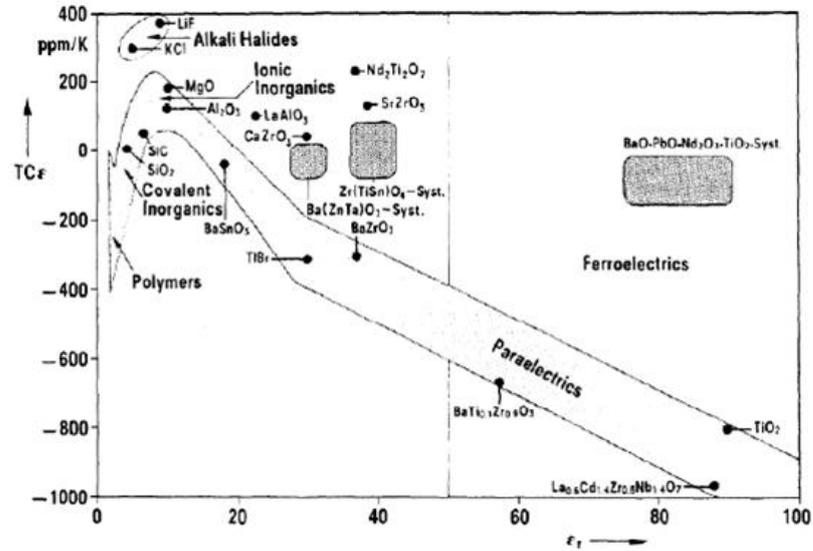
Figure 1.10 [65] Temperature coefficient of permittivity τ_ε versus relative permittivity ε_r for various materials after Harrop.

1.3.6.2 Solid Oxide Fuel Cell (SOFC)

A solid oxide fuel cell (SOFC) is an electrochemical cell that produces electricity from oxidizing a gaseous fuel. A SOFC consists of three parts: anode, cathode and electrolyte. Air or O_2 gas is filled from the cathode and separated from a fuel gas, e.g. H_2, CO from the anode by a solid oxide or ceramic electrolyte. Oxygen ions conduct through the electrolyte from the cathode to the anode and then react with gaseous fuel on the anode side. The electrochemical reactions within a SOFC are listed in Equations 1.10[70]:

Cathode (air side): $\quad \frac{1}{2}O_2 + 2e^- \rightarrow O^{2-}$

Anode (fuel side): $\quad$ (H_2 fuel) $H_2 + O^{2-} \rightarrow H_2O + 2e^-$

$\qquad\qquad\qquad$ (or CO fuel) $CO + O^{2-} \rightarrow CO_2 + 2e^-$

Overall: $\qquad\qquad$ (H_2 fuel) $O_2 + 2H_2 \rightarrow 2H_2O$

$\qquad\qquad\qquad$ (or CO fuel) $O_2 + 2CO \rightarrow 2CO_2$ $\qquad\qquad\qquad$ (1.10)
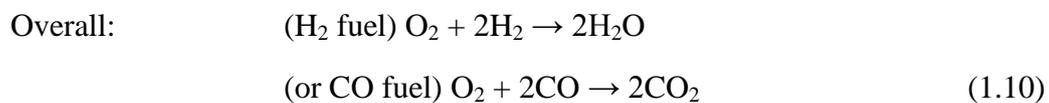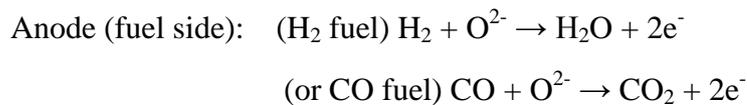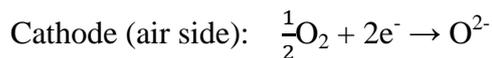
The structural design of a planar SOFC is illustrated in Figure 1.11[70]. The components are assembled in flat stacks, with air and fuel flowing though interconnects built into the cathode and anode. The electrolyte material has to be a dense ceramic with high ionic conductivity and negligible electronic conductivity. Usually, stabilized zirconia (ZrO_2 doped with Y, Ca or Mg) is used, which is a good ionic conductor from 600-1000 ℃. For a cathode material, a porous mixed conductor, e.g $LaMnO_3$ is required to allow a large surface area for O^{2-} transportation to the electrolyte. For an anode material, apart from the requirements of being porous and mixed conducting, the ability to be stable in a highly reducing environment and matching the thermal expansion coefficient of the electrolyte and interconnect is also crucial. A composite material mixed with metal and ceramic, e.g. cermet, Ni/ZrO_2 is used. The interconnect is placed on the outside of the cell electrodes to increase the electron mobility and the channels created in the interconnect are used to supply the air and fuel to the cell. Hence the interconnect material should be an excellent electronic conductor with a thermal expansion coefficient compatible with the other cell components, e.g. $LaCrO_3$.
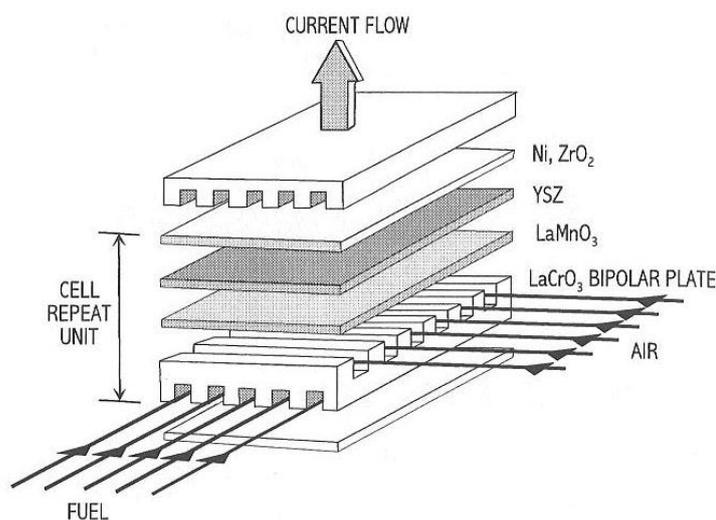
Figure 1.11 [70] Structure of a planar SOFC.

Research on Bi_2O_3-based ceramics is also focused on high ionic and mixed conductivity for applications as intermediate and low temperature SOFC materials, particularly stabilized fluorite-type δ-Bi_2O_3, sillenite, γ-$Bi_4V_2O_{11}$ and other Aurivillius phases. Although bismuth oxide based compounds are much better solid electrolytes than stabilized zirconia, they have several disadvantages including high thermal expansion

coefficients, thermodynamically instability in reducing atmospheres, volatilization of bismuth oxide at moderate temperatures, a high corrosion activity and low mechanical strength. These have prevented them from applications in commercial, high temperature SOFCs. The current major difficulty is to restrict their instability in reducing atmospheres and therefore to operate at lower temperatures where reduction is less problematic. Research to overcome this disadvantage is vital to enable commercialisation of Bi_2O_3-based compounds in low and intermediate temperature fuel cells and gas sensors. [4, 71, 72] Recently Wacshman and Lee reported a Bi_2O_3-based compound, $Dy_{0.08}W_{0.04}Bi_{0.86}O_{1.56}$, to be a suitable SOFC material with an intermediate operating temperature at 500 °C.[73]

1.4   Polarisation Mechanisms

In dielectric materials, the total polarisation within a material, α_T, is the summation of the four possible polarisation components, Equation 1.11[74],

$$\alpha_T = \alpha_e + \alpha_i + \alpha_d + \alpha_s \tag{1.11}$$

where electronic polarisability, α_e, originates from the slight displacement of the electron cloud of an atom or ion relative to the positive nucleus; ionic polarisability, α_i, is caused by the relative displacement of anions and cations in an ionic crystal; dipolar polarisability, α_d, arises in materials that contain permanent electric dipoles which exist even in the absence of an electric field. These dipoles are very temperature dependent and may be "frozen in" at low temperatures; space charge polarisability, α_s, occurs in defect ionic materials where mobile charges are trapped at an interface and blocked by the electrodes. Although it is not a bulk material polarisation mechanism, a space charge induced electrical double layer (electrode-sample interface) can contribute to the polarisability of a material. Space charge polarisability usually has a larger magnitude with a dielectric constant of $\sim 10^6$-10^7 with a corresponding double-layer capacitance of $\sim 10^{-6}$ F and commonly occurs at low frequencies ($f < 10^3$ Hz). [74]

1.5   The Origin of High Permittivity

Ferroelectric materials usually exhibit high permittivity, where permanent dipoles occur to disrupt the centric symmetry of the crystal structure. However, many high permittivity oxides originate from extrinsic mechanisms, such as a Surface Barrier Layer Capacitor (SBLC) effect, Internal Barrier Layer Capacitor (IBLC) effect and/or non-ohmic contacts from the electrode-sample interface.

1.5.1 Ferroelectricity, Incipient Ferroelectricity and Relaxor Ferroelectricity

● Ferroelectricity:

Ferroelectric materials have non-centrosymmetric structures and exhibit spontaneous polarisation from a net dipole moment, which can be reversed under an applied electric field, Figure 1.12.[55] In the ferroelectric hysteresis loop, as the electric field increases a saturation polarisation, Ps, is reached, which corresponds to the maximum displacement of dipoles from the central positions. On removal of the electric field, a remanent polarisation, Pr, is observed due to the presence of the dipoles. At a reverse electric field (or coercive field Ec), the polarisation can be set to zero as the corresponding dipoles are randomized.
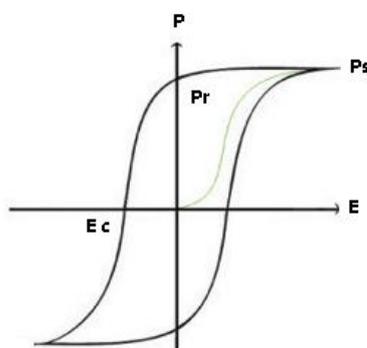
Figure 1.12[55] Hysteresis (P-E) loop of a ferroelectric material.

Ferroelectric materials generally have a phase transition to a centrosymmetric cell with

increasing temperature, where ferroelectricity can be transformed to paraelectricity above the phase transition temperature or so-called the Curie temperature, Tc. The ferroelectric phase transition can be determined by the temperature dependent peak in ε_r, Figure 1.13[55]. Above Tc, ε_r usually obeys the Curie-Weiss law, Equation 1.12[55].

$$\varepsilon_r = \frac{C}{T-\theta}$$ (1.12)

where C is the Curie constant, T is the temperature and θ is the Curie-Weiss temperature.
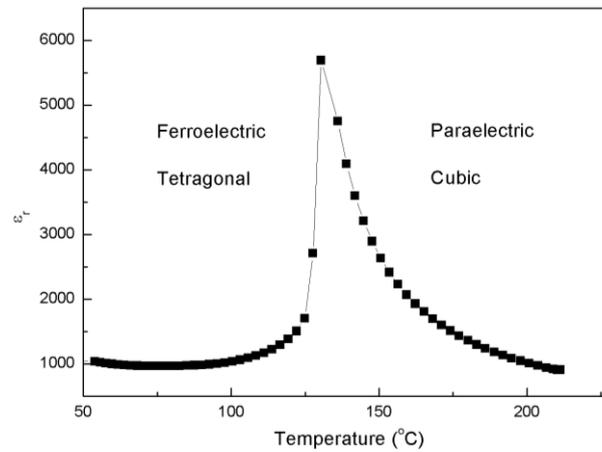
Figure 1.13[55] Temperature dependence of ε_r showing the Ferroelectric-Paraelectric phase transition of undoped $BaTiO_3$ ceramic.

● Incipient Ferroelectricity:

Incipient ferroelectricity is also known as quantum paraelectricity, where ε_r increases with decreasing temperature and saturates at low temperatures, Figure 1.14. Well-known classical incipient ferroelectric materials are $SrTiO_3$, $KTaO_3$ and $CaTiO_3$ and TiO_2. Some incipient ferroelectrics exhibit phase transitions e.g. $SrTiO_3$ at ~ 105 K, whereas some do not, e.g. $CaTiO_3$ and $KTaO_3$.[75, 76] The origin of incipient ferroelectricity can be explained by the effects of quantum fluctuations by using the Barrett Equation.[77]
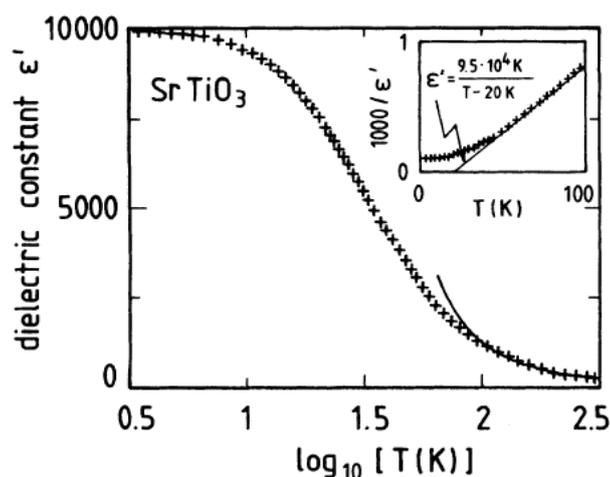
Figure 1.14[78] The dielectric constant ε' as a function of temperature measured along the [110] direction of a $SrTiO_3$ single crystal. The curved line is a fit with the Curie-Weiss law and the inset shows the relation of the inverse ε' versus temperature, after Viana *et al.*

● Relaxor Ferroelectricity:

Relaxor ferroelectrics exhibit broad permittivity maxima, where both the real and imaginary parts of permittivity are temperature- and frequency- dependent. The magnitude of the real permittivity peak maxima decreases as temperature and frequency increase, whereas the magnitude of the imaginary permittivity peak maxima increases as temperature and frequency increase, Figure 1.15. Relaxor ferroelectrics usually appear in mixed compounds, e.g. $Pb(B'B'')O_3$ and some tungsten bronze structures.[55, 79]
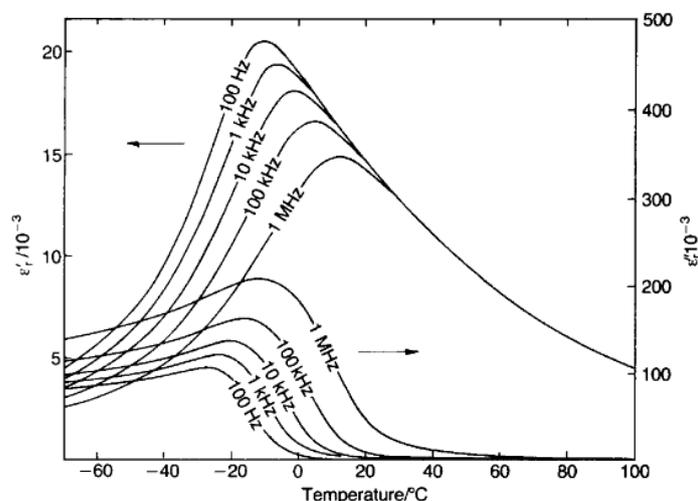
Figure 1.15[55] Temperature dependence of ε' and ε'' of $Pb(Mg_{1/3}Nb_{2/3})O_3$ (PMN).

In relaxor ferroelectrics a gradual transition from a ferroelectric to paraelectric phase is observed above the Curie temperature, where the Vogel-Fulcher law is obeyed, Equation 1.13.

$$\tau = (\omega_o)^{-1} \; exp \; [\frac{E_a}{k(T-T_f)}] \qquad\qquad (1.13) \; [80]$$

where τ is the relaxation time for a gradual phase transition, E_a is the activation energy, T_f is the temperature of the dynamic freezing of the polar clusters and ω_o, k are constants. Satisfaction of the V-F equation is considered as a sign of freezing of the dipole system at T_f.[80] Upon cooling the thermal motion of the dipoles decreases and the size of the polar micro regions and the potential barriers increase. The interaction of dipole moments in relaxor ferroelectrics is analogous to that in spin glasses, where a glassy state with frozen random orientation of dipole moments is transformed from the paraelectric state at the freezing temperature.

● Dielectric Relaxation:

Dielectric relaxation is the momentary delay of polarization response with respect to an alternating electric field. It usually occurs in randomized local structures such as glass, where a considerable time is taken for the thermally-activated ion migration and re-orientation of dipoles under an the applied electric field. The time lag between the electric field and the polarization infers an irreversible loss of free energy (G).[79] The impedance equivalent circuit to describe the dielectric relaxation process is shown in Figure 1.16. The series combination of R_1C_1 represents polarisation associated with lattice relaxation process(es) in the electric field and C_2 represents the bulk capacitance. [81]
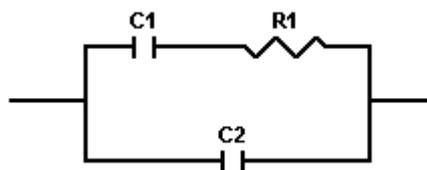
Figure 1.16 A common equivalent circuit to model dielectric relaxation, where the series

combination of R_1C_1 represents lattice relaxation process(es) under the electric field and C_2 represents the bulk capacitance.

Dielectric relaxations are usually represented by plotting data in the form of complex permittivity, ε^*,

$$\varepsilon^* = \varepsilon' - j\,\varepsilon'' \qquad\qquad (1.14)^{[81]}$$

where ε' and ε'' represent the measured permittivity and the dielectric losses in the material, respectively. The corresponding variation of ε' and ε'' as a function of frequency and the complex permittivity plane plots are shown in Figures 1.17 and 1.18, respectively. In the combined ε' and ε'' spectroscopic plot, ε'' exhibits a peak maximum at the frequency where ε' is intermediate between its maximum and minimum values. The ε'' peak is called a Debye peak, which indicates an ideal single relaxation process with an ε'' peak maximum occurring at $\omega\tau = 1$ (i.e. $2\pi f_{max}\tau = 1$).
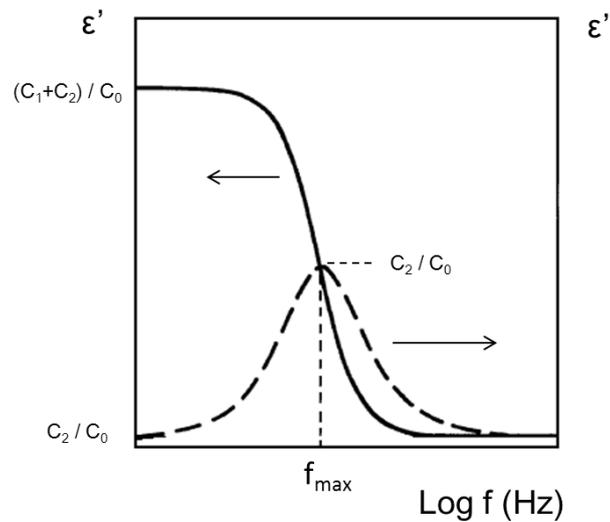
Figure 1.17[81] ε' and ε'' as a function of frequency.

The corresponding complex permittivity plane diagram (ε'' is plotted against ε') is also known as a Cole-Cole plot, Figure 1.18, which is an ideal semi-circular arc with a non-zero intercept on the real ε' axis.
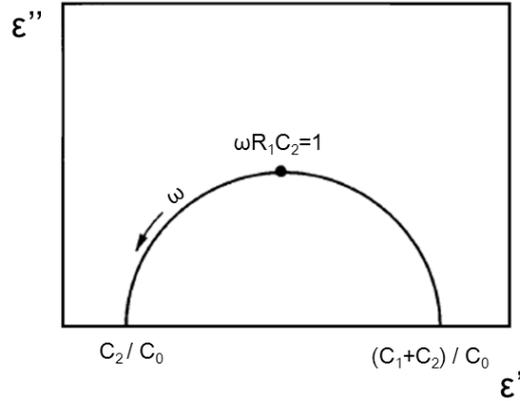
Figure 1.18[81] Cole-Cole plot for a dielectric relaxation.

However, in practice, such Cole-Cole plots are often not an ideal semicircle but are depressed for a wide variety of polar liquids and solids. Similarly, the ε'' Debye peak is broadened and can become asymmetric.[82] A distributed impedance element such as a constant phase element (CPE) is usually used to describe the non-ideal electrical response. The impedance of a CPE, Z^*_{CPE}, is defined as,

$$Z^*_{CPE} = [A(j\omega^n)]^{-1} = [A\omega^n (cos(n\pi/2) + j\ sin(n\pi/2))]^{-1} \qquad (1.15)\ ^{[81]}$$

where A and n are constant and can be determined from the real admittance Y' spectroscopic plot, Figure 1.19. The expression for Y' for the circuit shown in the inset of Figure 1.19 is,

$$Y' = R^{-1} + A\omega^n\ cos(n\pi/2) \qquad\qquad\qquad (1.16)\ ^{[81]}$$

where the frequency-independent Y' plateau at low frequencies has a value of R^{-1}; the gradient of the linear dispersion region at high frequency gives the value of n and log[Acos(nπ/2)] is the intercept of the log Y' axis at ω = 1 Hz, where the value of A can be determined. A CPE describes an ideal capacitor for n = 1 and an ideal resistor for n = 0. If 0 < n < 1, the magnitude of both capacitive and resistive components are frequency-dependent. The physical origin of a CPE is often unclear and many workers use it only as a circuit fitting parameter. However, it seems inherently linked with polarization fluctuations in relaxors and can be used to represent time-dependent relaxation phenomena.[83]
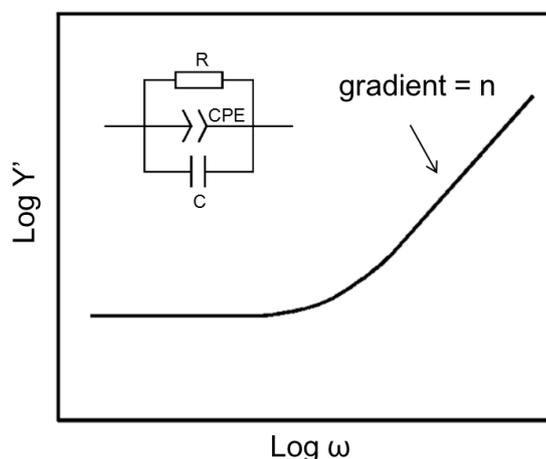
Figure 1.19[81] Log Y' versus log ω plot. Inset shows a possible equivalent circuit to model the impedance response.

1.5.2 Extrinsic Mechanisms

● Surface and Internal Barrier Layer Capacitor (SBLC and IBLC):

Barrier-Layer (BL) capacitors are also known as two types: Surface Barrier Layer Capacitors (SBLC) and Internal Barrier Layer Capacitors (IBLC), where an insulating surface or grain boundary layer is formed outside a semiconducting ceramic or grain cores, respectively. Schematic representation of a SBLC and IBLC ceramic are shown in Figure 1.20. In each case, conductive grain cores can be formed in titanate-based ceramics by donor doping or reduction firing of the ceramic.[84, 85] The surface or grain boundaries are then oxidised to produce thin resistive layers. High permittivity is therefore achieved due to a trapped electron layer, i.e. a Schottky barrier layer is developed between the insulating and semiconducting sample interfaces.
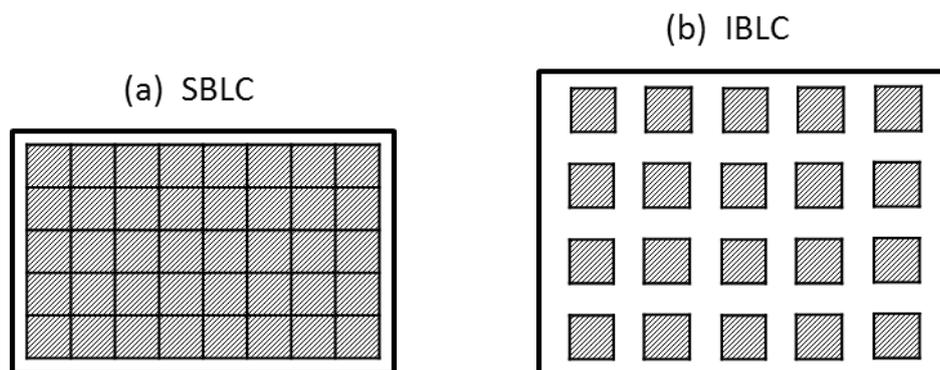
Figure 1.20 Cross-section of (a) SBLC and (b) IBLC ceramic.

● Non-Ohmic Contacts:

Non-ohmic contacts are also known as a blocking or Schottky barrier contacts at the metal-semiconductor interface, where the I-V (current-voltage) characteristics are non-linear and asymmetric. A Schottky barrier is created due to a mismatch of the Fermi level of the metal electrode and the semiconductor material, which essentially blocks the mobile charge carriers and results in high effective permittivity.

1.6 Thesis Aims and Outlines

Sillenites or doped γ-Bi$_2$O$_3$ has an adaptable structure, where a wide range of dopants are found to form single-phase sillenites with variable compositions. Their electrical properties are strongly dependent on the structural and compositional variations. In this project, a variety of new and existing sillenites are prepared, and their crystal structure and electrical properties are investigated. The aim of the project is to establish their composition-structure-property relationships and to clarify some debatable issues in the literature, such as: the formation of sillenites with various compositions[7, 86]; the thermal stability of sillenites; the structural models for sillenites; the existence of any Bi^{5+} ions in sillenites[33]; the occurrence of any sub-ambient phase transitions[87] and dielectric dispersion phenomena below and above room temperature[88, 89]; and to establish their dielectric and conduction properties.

Chapter 1 reviews the structural, thermal stability, formation and different groups of sillenites and their physical properties from current literature. The second part summarise the general intrinsic and extrinsic mechanisms for high permittivity in ceramics.

Chapter 2 briefly presents the experimental procedures and basic theory of the corresponding techniques.

Chapter 3 describes tetravalent cation ($M = Si^{4+}$) doping in "ideal" sillenite, $Bi_{12}SiO_{20}$. The preparation, microstructure and dielectric properties are studied. A frequency-dependent dielectric dispersion phenomenon above room temperature (HT relaxation behaviour) is observed for the first time and is analyzed by a combined study of Raman and Impedance spectroscopy. The origin of this HT relaxation behaviour is attributed to dielectric lattice relaxation of the distorted BiO_5LP units in the sillenite framework structure.

Chapter 4 reports divalent/trivalent cation ($M = Zn^{2+}$, Fe^{3+}, Al^{3+} and In^{3+}) doped sillenites. The validity of Radaev's (R) structural model and Valant and Suvorov's (VS) general formula for M^{2+}/M^{3+} sillenites are investigated. Similar to $Bi_{12}SiO_{20}$ from Chapter 3, the HT relaxation phenomenon was observed in all M^{2+}/M^{3+} sillenites, which also originated from the Bi^{3+} polarization effect in BiO_5LP framework units. The influences of M-dopants and phase stability on the microwave dielectric properties are also discussed. $Bi_{12}(Bi_{0.5}Fe_{0.5})O_{19.5}$ is the most stable sillenite and exhibits excellent microwave dielectric properties ($\varepsilon_r \sim 36.6$; Q.f ~ 2500 GHz and $\tau_f \sim -15$ ppm/K), which makes it a suitable candidate for commercial LTCC applications. In addition, detectable levels of oxide ion conductivity are observed in superstoichiometric indium (In^{3+}) sillenites when T > 653 K.

Chapter 5 describes B^{3+} containing sillenites, where several new and existing B^{3+} containing sillenites are synthesised and characterised according to the general formula $(1-x)Bi_{12}BO_{19.5}–xBi_{12}MO_{20+\delta}$, where $M = Fe^{3+}$, Al^{3+}, Ga^{3+}, Si^{4+}, P^{5+} and V^{5+}. The relationships between the lattice parameter and the M-cation radius, and hence the influence of the ionic radius on the stability of the sillenite phase are investigated. The

bi-phasic nature with two coexisting sillenites is detected in $Bi_{12}(B_{0.5}P_{0.5})O_{20}$ and $Bi_{12}(B_{0.5}V_{0.5})O_{20}$ by XRPD. The bi-phasic phenomenon can be eliminated by using air quenching, which reveals the metastability of both compounds. Structural features for boron containing sillenites reveal the co-existence of boron three- and four- fold coordination in the tetrahedral units from Rietveld refinement of NPD data, Nuclear Magnetic Resonance (NMR) and Raman spectroscopy results. The dielectric properties as a function of frequency and temperature show characteristic, low temperature (LT) relaxation behaviour for B^{3+} containing sillenites. This unique LT relaxation behaviour is different from the HT relaxation behaviour. It is believed to originate from the randomness and switching between BO_4 to BO_3 units on the tetrahedral site, leading to a Bi^{3+} ion from adjacent BiO_5LP moving towards BO_3 units to achieve electroneutrality. In addition, the microwave dielectric properties of B^{3+} containing sillenites are strongly influenced by the LT relaxation behaviour which is present near room temperature. Low values of Q.f and high dielectric losses exclude the possibility of B^{3+} containing sillenites to be used as LTCC materials.

Chapter 6 describes P^{5+} containing sillenites. The aim of this chapter is to continue investigating whether other P^{5+} containing sillenites also exhibit the characteristic LT relaxation behaviour (~ 200-400 K) as studied in $Bi_{12}(B_{0.5}P_{0.5})O_{20}$ from Chapter 5. Four P^{5+} containing sillenites are prepared: $Bi_{12}(Bi^{3+}_{0.03}P^{5+}_{0.89}\square_{0.08})O_{20.27}$, $Bi_{12}(P^{5+}_{0.86}\square_{0.14})O_{20.15}$, $Bi_{12}(Fe^{3+}_{0.5}P^{5+}_{0.5})O_{20}$ and $Bi_{12}(Mg^{2+}_{0.33}P^{5+}_{0.67})O_{20}$ and all show the universal HT relaxation behaviour, however, only two sillenites with $P^{5+}/\square$ on the tetrahedral site exhibit LT relaxation phenomena. The LT relaxation in P^{5+} containing sillenites seems to arise from the local Bi^{3+} polarization effect of the BiO_5LP framework polyhedra, which is induced by the random distribution of $P/\square$ over the same tetrahedral site.

Chapter 7 discusses all the compounds investigated in Chapter 3-6 to allow an overall picture of the composition-structure-property relationships of sillenites to be established.

Finally, Chapter 8 contains general conclusions and suggestions for future work.

1.7 References

[1]   S. C. Abrahams, P. B. Jamieson and J. L. Bernstei, Crystal structure of piezoelectric bismuth germanium oxide $Bi_{12}GeO_{20}$, Journal of Chemical Physics, 1967. **47**: p. 4034-4041.

[2]   V. Tassev, G. Diankov and M. Gospodinov, Optical activity of doped and codoped $Bi_{12}SiO_{20}$ crystal, Journal of the Optical Society of America B-Optical Physics, 1997. **14**: p. 1761-1764.

[3]   M. Valant and D. Suvorov, Processing and dielectric properties of sillenite compounds $Bi_{12}MO_{20-d}$ (M = Si, Ge, Ti, Pb, Mn, $B_{1/2}P_{1/2}$), Journal of the American Ceramic Society, 2001. **84**: p. 2900-2904.

[4]   V. V. Kharton, E. N. Naumovich, A. A. Yaremchenko and F. M. B. Marques, Research on the electrochemistry of oxygen ion conductors in the former Soviet Union - IV. Bismuth oxide-based ceramics, Journal of Solid State Electrochemistry, 2001. **5**: p. 160-187.

[5]   S. L. Lee, C. K. Lee and D. C. Sinclair, Synthesis and characterisation of bismuth phosphate-based sillenites, Solid State Ionics, 2005. **176**: p. 393-400.

[6]   E. M. Levin and R. S. Roth, Polymorphism of bismuth sesquioxide I. Pure Bi_2O_3, Journal of Research of the National Bureau of Standards Section a-Physics and Chemistry, 1964. **A 68**: p. 189-196.

[7]   E. M. Levin and R. S. Roth, Polymorphism of bismuth sesquioxide 2. Effect of oxide additions on polymorphism of Bi_2O_3, Journal of Research of the National Bureau of Standards Section a-Physics and Chemistry, 1964. **A 68**: p. 197-206.

[8]   H. A. Harwig and A. G. Gerards, Polymorphism of bismuth sesquioxide, Thermochimica Acta, 1979. **28**: p. 121-131.

[9]   H. A. Harwig, Structure of bismuthsesquioxide - alpha,beta,gamma and delta-phase, Zeitschrift Fur Anorganische Und Allgemeine Chemie, 1978. **444**: p. 151-166.

[10]   G. Gattow and D. Schutze, Uber wismutoxide.6. Uber ein wismut(Iii)-oxid mit hoherem sauerstoffgehalt (beta-modifikation), Zeitschrift Fur Anorganische Und Allgemeine Chemie, 1964. **328**: p. 44-68.

[11]   G. Gattow and H. Schroder, Uber wismutoxide. 3. Die kristallstruktur der hochtemperaturmodifikation von wismut(Iii)-oxid (delta-Bi_2O_3), Zeitschrift Fur Anorganische Und Allgemeine Chemie, 1962. **318**: p. 176-189.

[12]   A. F. Gualtieri, S. Immovilli and M. Prudenziati, Powder X-ray diffraction data for the new polymorphic compound omega-Bi_2O_3, Powder Diffraction, 1997. **12**: p. 90-92.

[13]   N. Cornei, N. Tancret, F. Abraham and O. Mentre, New epsilon-Bi_2O_3 metastable polymorph, Inorganic Chemistry, 2006. **45**: p. 4886-4888.

[14]   P. Shuk and H. H. Mobius, Oxide ion conducting solid electrolytes. Transport numbers and electric-conductivity from modifications of Bi_2O_3, Zeitschrift Fur Physikalische Chemie-Leipzig, 1985. **266**: p. 9-16.

[15]   G. Mairesse, Bismuth-based oxide conductors novel structural and electrical features, Fast Ion Transport in Solids, 1993. **250**: p. 271-290.

[16]   H. Iwahara, T. Esaka, T. Sato and T. Takahashi, Formation of high oxide ion conductive phases in the sintered oxides of the system Bi_2O_3-Ln_2O_3 (Ln = La-Yb), Journal of Solid State Chemistry, 1981. **39**: p. 173-180.

[17]   R. K. Datta and J. P. Meehan, System Bi_2O_3-R_2O_3 (R=Y, Gd), Zeitschrift Fur Anorganische Und Allgemeine Chemie, 1971. **383**: p. 328-337.

[18]   T. Takahashi, H. Iwahara and T. Esaka, High oxide ion conduction in sintered oxide of system Bi_2O_3-M_2O_5, Journal of the Electrochemical Society, 1977. **124**: p. 1563-1569.

[19]   A. Watanabe, $Bi_{23}M_4O_{44.5}$ (M=P and V): New oxide-ion conductors with triclinic structure based on a pseudo-fcc subcell, Solid State Ionics, 1997. **96**: p. 75-81.

[20]   F. Abraham, J. C. Boivin, G. Mairesse and G. Nowogrocki, The BIMEVOX series - a new family of high performances oxide ion conductors, Solid State Ionics, 1990. **40-1**: p. 934-937.

[21]   B. Aurivillius, Mixed bismuth oxides with layer lattices 1. The structure type of $CaNb_2Bi_2O_9$, Arkiv for Kemi, 1950. **1**: p. 463-480.

[22]   L. G. Sillen, Ark. Kemi Mineral. Geol., 1937. **12A**: p. 1-13.

[23]   W. C. Schumb and E. S. Rittner, Polymorphism of bismuth trioxide, Journal of the American Chemical Society, 1943. **65**: p. 1055-1060.

[24]   B. Aurivillius and L. G. Sillen, Polymorphy of bismuth trioxide, Nature, 1945. **155**: p. 305-306.

[25]   S. F. Radaev and V. I. Simonov, Structure of sillenites and atomic mechanisms of isomorphous substitutions, Kristallografiya, 1992. **37**: p. 914-941.

[26]   R. D. Shannon, Revised effective ionic-radii and systematic studies of interatomic distances in halides and chalcogenides, Acta Crystallographica Section A, 1976. **32**: p. 751-767.

[27]   S. C. Abrahams, P. B. Jamieson and Bernstei.Jl, Crystal structure of piezoelectric bismuth germanium oxide $Bi_{12}GeO_{20}$, Journal of Chemical Physics, 1967. **47**: p. 4034-4041.

[28]   V. I. Burkov, V. S. Gorelik, A. V. Egorysheva and Y. F. Kargin, Laser Raman spectroscopy of crystals with the structure of sillenite, Journal of Russian Laser Research, 2001. **22**: p. 243-267.

[29]   S. F. Radaev, L. A. Muradyan and V. I. Simonov, Atomic structure and crystal chemistry of sillenites $Bi_{12}(Bi^{3+}_{0.50}Fe^{3+}_{0.50})O_{19.50}$ and $Bi_{12}(Bi^{3+}_{0.67}Zn^{2+}_{0.33})O_{19.33}$, Acta Crystallographica Section B-Structural Science, 1991. **47**: p. 1-6.

[30]   H. S. Horowitz, A. J. Jacobson, J. M. Newsam, J. T. Lewandowski and M. E. Leonowicz, Solution synthesis and characterization of sillenite phases, $Bi_{24}M_2O_{40}$ (M = Si, Ge, V, As, P), Solid State Ionics, 1989. **32-3**: p. 678-690.

[31]   R. H. Mitchell, *Perovskites: modern and ancient*. Thunder Bay: Almaz Press, 2002.

[32]   S. F. Radaev, V. I. Simonov and Y. F. Kargin, Structural features of g-phase Bi_2O_3 and its place in the sillenite family, Acta Crystallographica Section B-Structural Science, 1992. **48**: p. 604-609.

[33]   D. C. Craig and N. C. Stephenson, Structural studies of some body-centered cubic phases of mixed oxides involving Bi_2O_3 : the structures of $Bi_{25}FeO_{40}$ and $Bi_{38}ZnO_{60}$, Journal of Solid State Chemistry, 1975. **15**: p. 1-8.

[34]   S. C. Abrahams, J. L. Bernstein and C. Svensson, Crystal structure and absolute piezoelectric d14 coefficient in levorotatory $Bi_{12}SiO_{20}$, Journal of Chemical Physics, 1979. **71**: p. 788-792.

[35]   C. Svensson, S. C. Abrahams and J. L. Bernstein, Levorotatory $Bi_{12}GeO_{20}$ - remeasurement of the structure, Acta Crystallographica Section B-Structural Science, 1979. **35**: p. 2687-2690.

[36]   S. M. Efendiev, V. E. Bagiev, A. C. Zeinally, V. A. Balashov, V. A. Lomonov and A. A. Majer, Optical properties of $Bi_{12}TiO_{20}$ single crystals, Physica Status Solidi a-Applied Research, 1981. **63**: p. K19-K22.

[37]   D. C. N. Swindells and J. L. Gonzalez, Absolute configuration and optical activity of laevorotatory $Bi_{12}TiO_{20}$ Acta Crystallographica Section B-Structural Science,

1988. **44**: p. 12-15.

[38]   B. C. Grabmaier and R. Oberschmid, Properties of pure and doped $Bi_{12}GeO_{20}$ and $Bi_{12}SiO_{20}$ crystals, Physica Status Solidi a-Applied Research, 1986. **96**: p. 199-210.

[39]   A. Watanabe, H. Kodama and S. Takenouchi, Nonstoichiometric phase with sillenite-type structure in the system Bi_2O_3-P_2O_5, Journal of Solid State Chemistry, 1990. **85**: p. 76-82.

[40]   S. Neov, V. Marinova, M. Reehuis and R. Sonntag, Neutron-diffraction study of $Bi_{12}MO_{20}$ single crystals with sillenite structure (M = Si, $Si_{0.995}Mn_{0.005}$, $Bi_{0.53}Mn_{0.47}$), Applied Physics A-Materials Science & Processing, 2002. **74**: p. S1016-S1018.

[41]   R. N. Vannier, F. Abraham, G. Nowogrocki and G. Mairesse, New structural and electrical data on Bi-Mo mixed oxides with a structure based on $[Bi_{(12)}O_{(14)}](\infty)$ columns, Journal of Solid State Chemistry, 1999. **142**: p. 294-304.

[42]   J. C. Champarnaud-Mesjard and B. Frit, A structural model for the $Bi_{1-x}Cd_xO_{1.5-x/2}$ (0 <= x <= 0.0256) sillenite-type solid solution, Comptes Rendus De L Academie Des Sciences Serie Ii Fascicule C-Chimie, 1999. **2**: p. 369-374.

[43]   M. Valant and D. Suvorov, A stoichiometric model for sillenites, Chemistry of Materials, 2002. **14**: p. 3471-3476.

[44]   D. Poleti, L. Karanovic and A. Hadzi-Tonic, Doped gamma-Bi_2O_3: synthesis of microcrystalline samples and crystal chemical analysis of structural data, Zeitschrift Fur Kristallographie, 2007. **222**: p. 59-72.

[45]   S. D. Kirik, V. A. Kutvitskii and T. I. Koryagina, Nature of isomorphism in crystals of bismuth zinc and bismuth cadmium double oxides with the sillenite structure, Journal of Structural Chemistry, 1985. **26**: p. 569-574.

[46]   S. L. Hou and D. S. Oliver, Pockels readout optical memory using $Bi_{12}SiO_{20}$, Applied Physics Letters, 1971. **18**: p. 325-328.

[47]   R. E. Aldrich, S. L. Hou and M. L. Harvill, Electrical and optical properties of $Bi_{12}SiO_{20}$, Journal of Applied Physics, 1971. **42**: p. 493-494.

[48]   P. V. Lenzo, E. G. Spencer and A. A. Ballman, Optical activity and electrooptic effect in bismuth germanium oxide $Bi_{12}GeO_{20}$, Applied Optics, 1966. **5**: p. 1688-1689.

[49]   J. P. Huignard and F. Micheron, High sensitivity read-write volume holographic storage in $Bi_{12}SiO_{20}$ and $Bi_{12}GeO_{20}$ crystals, Applied Physics Letters, 1976. **29**: p.

591-593.

[50]   J. Link, J. Fontanella and C. G. Andeen, Temperature-variation of the dielectric properties of bismuth germanate and bismuth germanium oxide, Journal of Applied Physics, 1980. **51**: p. 4352-4355.

[51]   M. Valant and D. Suvorov, New generation of LTCC materials, Boletin De La Sociedad Espanola De Ceramica Y Vidrio, 2004. **43**: p. 634-639.

[52]   R. R. Tummala, Ceramic and glass-ceramic packaging in the 1990s, Journal of the American Ceramic Society, 1991. **74**: p. 895-908.

[53]   M. A. Rodriguez, P. Yang, P. Kotula and D. Dimos, Microstructure and phase development of buried resistors in low temperature co-fired ceramic, Journal of Electroceramics, 2000. **5**: p. 217-223.

[54]   M. T. Sebastian and H. Jantunen, Low loss dielectric materials for LTCC applications: a review, International Materials Reviews, 2008. **53**: p. 57-90.

[55]   A. J. Moulson and J. M. Herbert, *Electroceramics: materials, properties, applications. (Second Edition)*. Chichester, England: John Wiley & Sons Ltd., 2003.

[56]   M. R. Gongora-Rubio, P. Espinoza-Vallejos, L. Sola-Laguna and J. J. Santiago-Aviles, Overview of low temperature co-fired ceramics tape technology for meso-system technology (MsST), Sensors and Actuators a-Physical, 2001. **89**: p. 222-241.

[57]   D. A. A. S. Narayana Rao, "Ionic polatisation in crystals: additivity in double salts," in *Proceedings of the Indian Academy of Sciences, Section A* vol. 30, ed, 1949, pp. 317-319.

[58]   R. D. Shannon, Dielectric polarizabilities of ions in oxides and fluorides, Journal of Applied Physics, 1993. **73**: p. 348-366.

[59]   I. N. Jawahar, N. I. Santha and M. T. Sebastian, Microwave dielectric properties of $MO-La_2O_3-TiO_2$ (M = Ca, Sr, Ba) ceramics, Journal of Materials Research, 2002. **17**: p. 3084-3089.

[60]   G. K. Choi, J. R. Kim, S. H. Yoon and K. S. Hong, Microwave dielectric properties of scheelite (A = Ca, Sr, Ba) and wolframite (A = Mg, Zn, Mn) $AMoO_4$ compounds, Journal of the European Ceramic Society, 2007. **27**: p. 3063-3067.

[61]   I. M. Reaney and D. Iddles, Microwave dielectric ceramics for resonators and filters in mobile phone networks, Journal of the American Ceramic Society, 2006.

89: p. 2063-2072.

[62]   T. Negas, G. Yeager, S. Bell, N. Coats and I. Minis, $BaTi_4O_9/Ba_2Ti_9O_{20}$-based ceramics. Resurrected for modern microwave applications, American Ceramic Society Bulletin, 1993. **72**: p. 80-89.

[63]   A. Templeton, X. R. Wang, S. J. Penn, S. J. Webb, L. F. Cohen and N. M. Alford, Microwave dielectric loss of titanium oxide, Journal of the American Ceramic Society, 2000. **83**: p. 95-100.

[64]   W. Wersing, Microwave ceramics for resonators and filters, Current Opinion in Solid State & Materials Science, 1996. **1**: p. 715-731.

[65]   P. J. Harrop, Temperature coefficients of capacitance of solids, Journal of Materials Science, 1969. **4**: p. 370-374.

[66]   E. L. Colla, I. M. Reaney and N. Setter, Effect of structural changes in complex perovskites on the temperature coefficient of the relative permittivity, Journal of Applied Physics, 1993. **74**: p. 3414-3425.

[67]   R. Rawal, A. J. McQueen, L. J. Gillie, N. C. Hyatt, E. E. McCabe, K. Samara, N. M. Alford, A. Feteira, I. M. Reaney and D. C. Sinclair, Influence of octahedral tilting on the microwave dielectric properties of $A_3LaNb_3O_{12}$ hexagonal perovskites (A=Ba, Sr), Applied Physics Letters, 2009. **94**: 192904.

[68]   I. M. Reaney, E. L. Colla and N. Setter, Dielectric and structural characteristics of Ba-based and Sr-based complex perovskites as a function of tolerance factor, Japanese Journal of Applied Physics Part 1-Regular Papers Short Notes & Review Papers, 1994. **33**: p. 3984-3990.

[69]   M. W. Lufaso, Crystal structures, modeling, and dielectric property relationships of 2 :1 ordered $Ba_3MM'_2O_9$ (M = Mg, Ni, Zn; M ' = Nb, Ta) perovskites, Chemistry of Materials, 2004. **16**: p. 2148-2156.

[70]   A. R. West, *Basic Solid State Chemistry*, 2nd ed. Chichester: J. Wiley & Sons, 1999.

[71]   P. Shuk, H. D. Wiemhofer, U. Guth, W. Gopel and M. Greenblatt, Oxide ion conducting solid electrolytes based on Bi_2O_3, Solid State Ionics, 1996. **89**: p. 179-196.

[72]   N. M. Sammes, G. A. Tompsett, H. Nafe and F. Aldinger, Bismuth based oxide electrolytes - Structure and ionic conductivity, Journal of the European Ceramic Society, 1999. **19**: p. 1801-1826.

[73]   E. D. Wachsman and K. T. Lee, Lowering the temperature of solid oxide fuel cells, Science, 2011. **334**: p. 935-939.

[74]   A. R. West, *Solid state chemistry and its applications*. Aberdeen: John Wiley & Sons, 1989.

[75]   K. A. Muller and H. Burkard, $SrTiO_3$: an intrinsic quantum paraelectric below 4 K, Physical Review B, 1979. **19**: p. 3593-3602.

[76]   V. V. Lemanov, A. V. Sotnikov, E. P. Smirnova, M. Weihnacht and R. Kunze, Perovskite $CaTiO_3$ as an incipient ferroelectric, Solid State Communications, 1999. **110**: p. 611-614.

[77]   J. H. Barrett, Dielectric constant in perovskite type crystals, Physical Review, 1952. **86**: p. 118-120.

[78]   R. Viana, P. Lunkenheimer, J. Hemberger, R. Bohmer and A. Loidl, Dielectric spectroscopy in $SrTiO_3$, Physical Review B, 1994. **50**: p. 601-604.

[79]   Z. G. Ye, Relaxor ferroelectric complex perovskites: Structure, properties and phase transitions, Key Engineering Materials, 1998. **155-156**: p. 81-122.

[80]   D. Viehland, M. Wuttig and L. E. Cross, The glassy behavior of relaxor ferroelectrics, Ferroelectrics, 1991. **120**: p. 71-77.

[81]   J. R. Macdonald and E. Barsoukov, *Impedance spectroscopy:theory, experiment, and applications, 2nd edition*: John Wiley & Sons, 1987.

[82]   K. S. Cole and R. H. Cole, Dispersion and absorption in dielectrics I. Alternating current characteristics, Journal of Chemical Physics, 1941. **9**: p. 341-351.

[83]   R. A. M. Osman and A. R. West, Electrical characterization and equivalent circuit analysis of $(Bi_{1.5}Zn_{0.5})(Nb_{0.5}Ti_{1.5})O_7$ pyrochlore, a relaxor ceramic, Journal of Applied Physics, 2011. **109**: 074106.

[84]   D. C. Sinclair, T. B. Adams, F. D. Morrison and A. R. West, $CaCu_3Ti_4O_{12}$: One-step internal barrier layer capacitor, Applied Physics Letters, 2002. **80**: p. 2153-2155.

[85]   L. Wu, C. F. Yang and T. S. Wu, Influence of sintering and annealing temperature on grain-boundary barrier layer capacitors in a modified reduction reoxidation method, Journal of Materials Science-Materials in Electronics, 1992. **3**: p. 272-277.

[86]   S. Chehab, P. Conflant, M. Drache and Boivin, Solid-state reaction pathways of sillenite-phase formation studied by high-temperature X-ray diffractometry and differential thermal analysis, Materials Research Bulletin, 2003. **38**: p. 875-897.

[87] T. I. Mel'nikova, G. M. Kuz'micheva, V. B. Rybakov, N. B. Bolotina and A. B. Dubovsky, On symmetry of sillenites, Crystallography Reports, 2010. **55**: p. 229-232.

[88] M. Valant and D. Suvorov, Dielectric characteristics of bismuth oxide solid solutions with a fluorite-like crystal structure, Journal of the American Ceramic Society, 2004. **87**: p. 1056-1061.

[89] M. Valant and D. Suvorov, Synthesis and characterization of a new sillenite compound $Bi_{12}(B_{0.5}P_{0.5})O_{20}$, Journal of the American Ceramic Society, 2002. **85**: p. 355-358.

2 Experimental Procedure

2.1 Solid State Synthesis

Samples were prepared by using the conventional solid state reaction method. Reagents were dried at the indicated temperatures in Table 2.1, weighed (~ 10 g total), mixed with acetone in an agate mortar, ground manually by pestle for 30 minutes, and then heated in a gold foil boat at 700 – 850 °C with intermittent grinding every 12 h to aid the reaction. Samples with reagents that have low melting temperatures were heated initially to 400 °C for 2 hours with a heating rate of 1 °C/min to evaporate any H_2O, CO_2 and NH_3 *etc.* in the reagents and then heated to reaction temperature with a heating and cooling rate of 10 °C/min. The process of grinding and reacting was repeated until the sample was examined as phase-pure by X-ray powder diffraction.

Table 2.1 Drying temperature and purity for precursors of reagents.

Reagent	Drying Temperature (°C)	Manufacturer and Purity
Bi_2O_3	180	Sigma-Aldrich, 99.9 %
SiO_2	600	Alfa Aesar, 99.5 %
ZnO	600	Sigma-Aldrich, 99.99 %
Fe_2O_3	400	Sigma-Aldrich, 99.999%
Al_2O_3	900	Sigma-Aldrich, 99 %
In_2O_3	900	Aldrich, 99.9 %
$B(OH)_3$	Not Applicable	Sigma-Aldrich, 99.5 %
$(NH_4)H_2PO_4$	Not Applicable	Sigma-Aldrich, 99.5%
Ga_2O_3	600	Aldrich, 99.99+%
V_2O_5	180	Aldrich, 99.6 %
$Mg(CO_3)_4 Mg(OH)_2 5H_2O$	Not Applicable	Aldrich, 99 %

Pellets were pressed uniaxially under 0.6 tonnes in an 8-10 mm diameter, stainless steel die. Green pellets were then placed on a gold foil and fired between 715-880 °C. The obtained pellet density was calculated from the measured dimensions compared with the theoretical crystallographic density and the errors were ~ 10 %.

2.2 X-ray Powder Diffraction (XRPD)

X-ray powder diffraction (XRPD) is a widely used technique to characterise crystalline materials, to monitor phase purity and to determine their structure details, such as lattice parameters, unit cell types, space group, crystallite sizes etc. It is extremely useful for phase identifications, as each solid crystalline material has a unique 'fingerprint' XRPD pattern and therefore, the presence of any phases can be identified by comparing with the reference source of International Centre for Diffraction Data (ICDD) database.

Phase identification in this work used a Philips D500 diffractometer with Cu $K\alpha$ radiation ($\lambda_{K\alpha1}$ = 1.54059 Å; $\lambda_{K\alpha2}$ = 1.54433 Å) using a Hägg-Guinier focusing method in reflection mode and a Stoë STADI P diffractometer with Cu $K\alpha_1$ radiation in transmission mode. Data were collected over a scanning angle, 2θ, ranging of 15 °< 2θ < 65 °with a step size of 0.1 °.

Lattice parameters determination for Rietveld refinement analysis were collected by operating a Stoë STADI P diffractometer with Cu $K\alpha_1$ radiation ($\lambda_{K\alpha1}$ = 1.54059 Å) with a small, linear position sensitive detector (PSD) in transmission mode, step size 0.01 °and 2θ range 10-90 °, Figure 2.1. The instrument was calibrated using Si external standard.
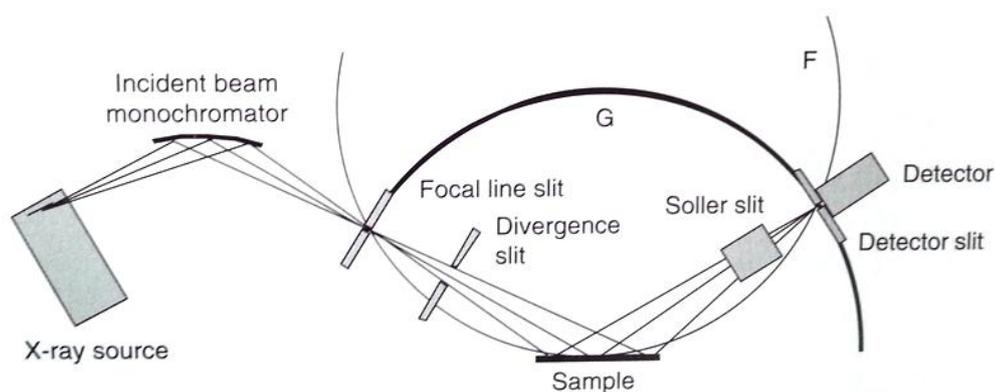
Figure 2.1[1] Schematic representation of an X-ray diffractometer with an incident beam monochromator, after Clearfield *et al*.

2.3 Neutron Powder Diffraction (NPD)

Neutron powder diffraction (NPD) is a useful diffraction technique to characterise the atomic and/or magnetic structure of a material. It is very expensive and usually only available in national facilities. NPD is usually used to complement XRPD due to their different scattering properties. Unlike X-rays that are scattered by electron clouds of an atom, neutrons interact with both the nucleus of an atom and magnetic moments of unpaired electrons around an atom. As a result, the scattering power of an atom to NPD is not simply dependent on the atomic number/weight, Figure 2.2. This is particularly useful to distinguish and locate atomic positions and occupancies for light elements, e.g. O and H and/or elements with similar atomic numbers e.g. Mn/Fe in structural analysis where XRPD is inadequate.
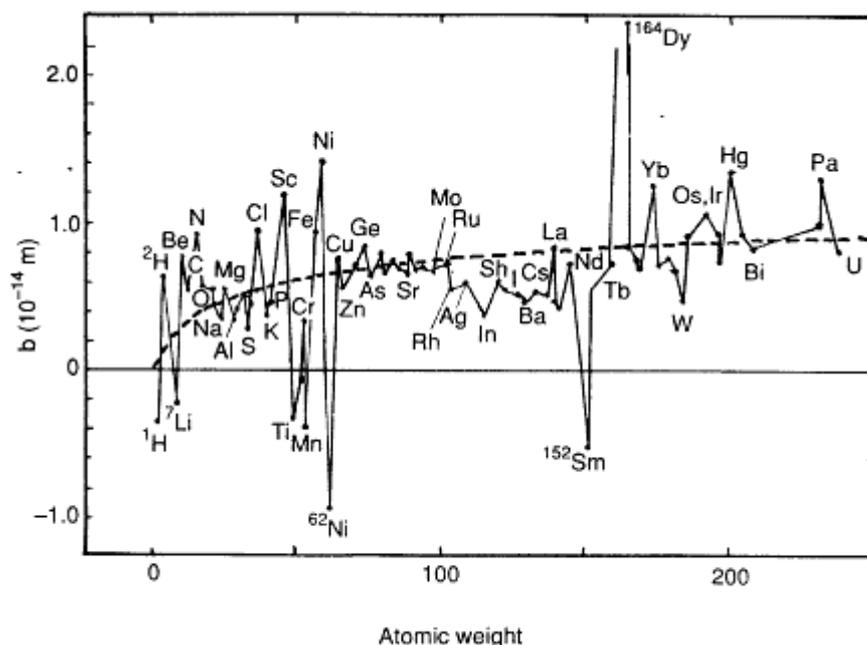
Figure 2.2[2] Nuclear scattering lengths for thermal neutrons shown as a function of atomic weight, after Young.

The differences between two types of NPD data i.e. neutron constant wavelength and neutron time-of-flight are listed in Table 2.2. The neutron constant wavelength data is usually generated continuously from a nuclear reactor, where the diffraction angle, θ, and d-spacing, d, are variable and the wavelength, λ, is fixed. Composition $Bi_{12}(Bi_{0.3}Al_{0.7})O_{19.5}$

and $Bi_{12}(Bi_{0.7}In_{0.3})O_{19.5}$ in this study were collected in the neutron constant wavelength format on the D2B powder diffractometer at the Institut Laue-Langevin (ILL) in Grenoble, France, Figure 2.3. The sample was placed in a vanadium can prior to operate under a neutron beam diffracted by a Ge monochromator over a range of $5° < 2\theta < 160°$ with a step size of $0.05°$.
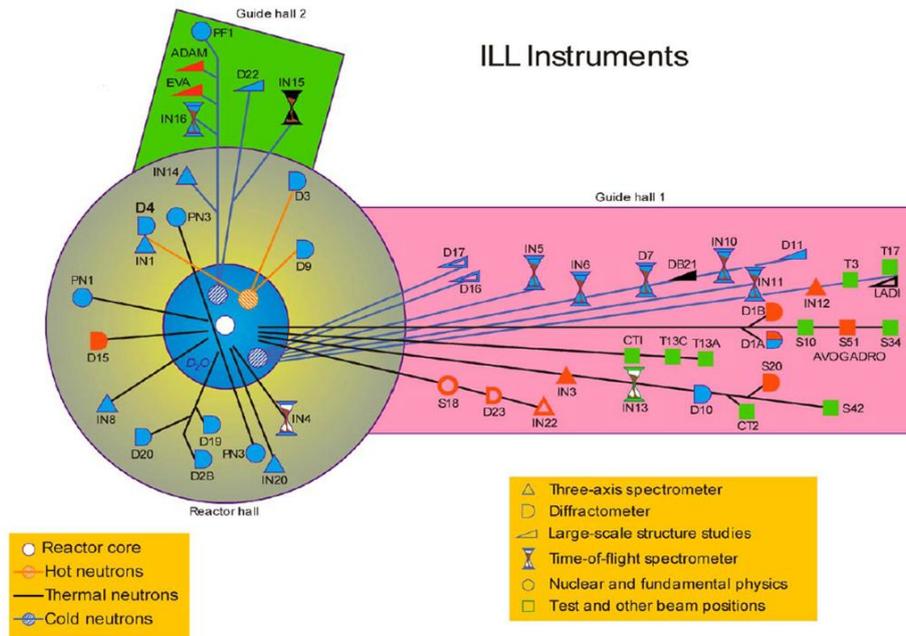
Figure 2.3[3] The instrument layout at the ILL.

The neutron time-of-flight data is generated from a pulsed source, where the initial position and the velocity of the neutron is known and the time for pulse of neutrons detected by the detector are measured. Therefore, λ and d are variables at fixed θ. NPD data of $Bi_{12}(Bi_{0.5}Zn_{0.5})O_{19.25}$ in this work were collected in time-of-flight (ToF) format at room temperature on the Polaris diffractometer at ISIS at the STFC Rutherford Appleton Laboratory (RAL) in Oxfordshire, UK, Figure 2.4. Powder ~ 10 g was placed in a vanadium can. The time taken for the neutrons to travel from the initial position to the final position back to the detector is measured and the interatomic distance (i.e. d-spacing) of the sample is measured and plotted against intensity.
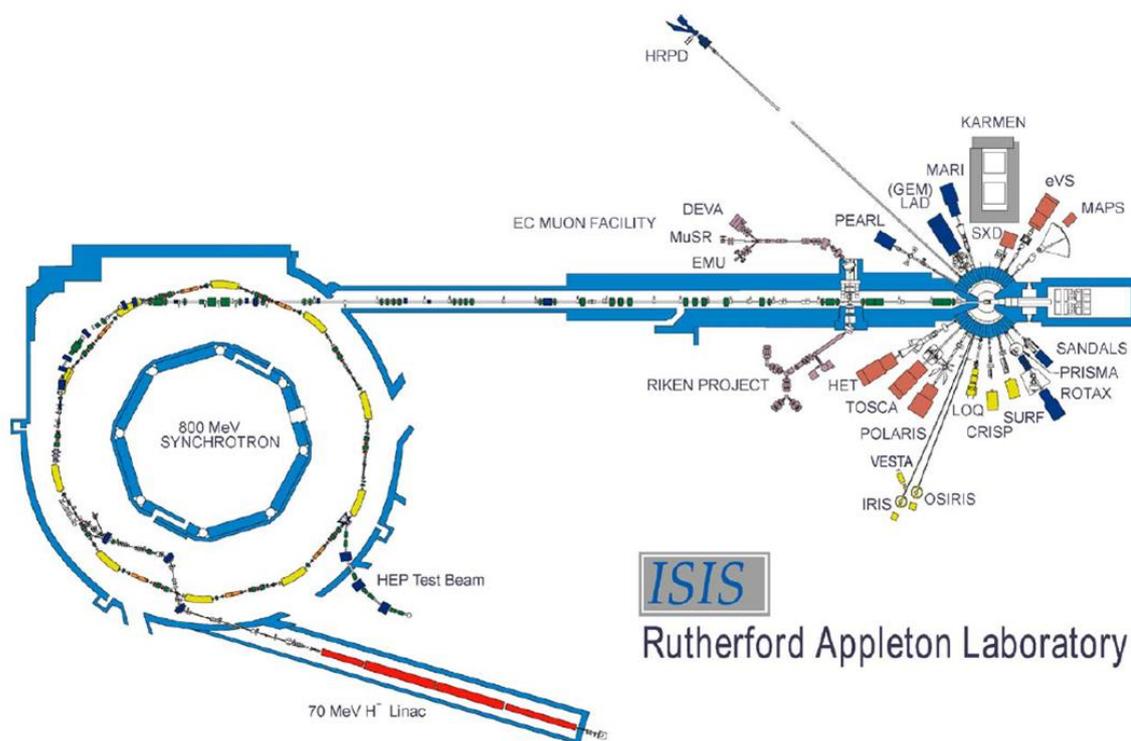
Figure 2.4[4] The instrument layout at ISIS.

Table 2.2 Comparisons between steady-state neutron sources with neutron constant wavelength format and pulsed neutron sources with neutron time-of-flight format.

Neutron constant wavelength	Neutron time-of-flight
Steady-state neutron source (usually reactor)	Pulsed neutron source (usually spallation)
Monochromatic beam	Polychromatic beam
λ fixed; θ and d dispersive	θ fixed; λ and d dispersive
	Use time of flight, t, of detected neutron to calculate λ (i.e. $\lambda = 2\ d\ \sin\theta = ht/m_nL$; $d = ht/2m_nL\ \sin\theta$, where L = length of flight path; m_n = neutron mass, 1.675×10^{-27} kg; h = Planck constant, 6.626×10^{-34} J.s) [2]

2.4 Rietveld Refinements

Rietveld refinement, named after its inventor H. R. Rietveld[5], is a least-squares method that is widely used to characterise the structure of materials by minimising the differences between the theoretical diffraction pattern and the observed one. Structural details such as atomic positions, site occupancies, atomic thermal parameters, lattice parameters, bond lengths/angles, elemental analysis and material composition *etc.* are determinable with

Rietveld refinements on the powder diffraction patterns (both XRPD and NPD). To carry out Rietveld refinement, a starting structural model is required and it should have a structure (with known space group, lattice parameters, atomic information and instrumental profile parameters) close enough to the observed structure. A calculated structural model is generated automatically after each least-squares refinement cycle. The purpose of Rietveld refinement is to obtain the minimised residual, S_y, between the calculated and the observed profile with improving and sensible structural information, Equation 2.1[6].

$$S_y = \sum_i w_i [y_i(obs) - y_i(calc)]^2 \qquad (2.1)$$

Where w_i is the weighted difference ($= \frac{1}{y_i}$)

  $y_i(obs)$ is the observed intensity at the i th step

  $y_i(calc)$ is the calculated intensity at the i th step

The basic Rietveld refinement procedures are listed in Figure 2.5. The quality of fit between the observed and calculated profile is evaluated by three numerical values, R_{wp}, R_{exp} and χ^2, Equation 2.2 – 2.4.[6] R_{wp} is the weighted-profile R value, which takes additional background contribution into account; R_{exp} is the statistically expected data showing the quality of the fit; χ^2 is the overall goodness-of-fit value and is the ratio between R_{wp} and R_{exp}. χ^2 should be approach to the value of 1, as R_{wp} should be close to R_{exp}.

Weighted-profile R value: $R_{wp} = \left[\dfrac{\sum_i w_i[y_i(obs)-y_i(calc)]^2}{\sum_i w_i[y_i(obs)]^2}\right]^{1/2}$ (2.2)

Expected R value: $R_{exp} = \left[\dfrac{N-P}{\sum_i^N w_i y_i(obs)^2}\right]^{1/2}$ (2.3)

Goodness-of-fit: $\chi^2 = \dfrac{R_{wp}}{R_{exp}}$ (2.4)

Where N is the number of observation and P is the number of refined parameters.
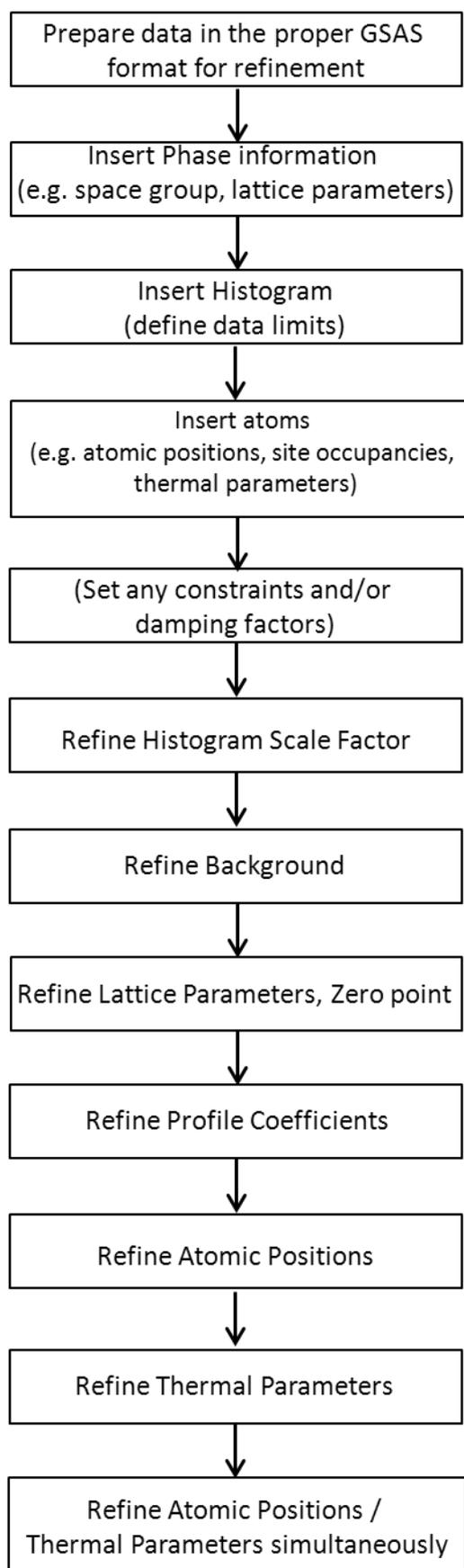
Figure 2.5 Basic Rietveld refinement procedures.[7]

These three numerical parameters (R_{wp}, R_{exp} and χ^2) should be considered together to assess the quality of the fit, since a low R_{wp} can be produced misleadingly by data with a high background. Le Bail algorithm with a structure-free refinement would be useful to distinguish the false minimum of R_{wp} values. Usually R_{wp} with eliminated background contribution should be used to assess the quality of the whole structural information. Other important factors to evaluate the quality of a Rietveld refinement are graphical plot observations, atomic bond length/angles and sometimes bond valence sums.

In this study Rietveld refinements were carried out on the collected NPD data (constant wavelength and time-of-flight) by using the EXPGUI (Experimental Graphical User Interface)[8] from GSAS (General Structural Analysis System)[7] package.

2.5 Electron Microscopy

Microstructure characterisation, e.g. sample density, grain distribution and elemental analysis was carried out by Scanning Electron Microscope (SEM) and Energy Dispersive X-ray Spectroscopy (EDX) using a Joel JSM 6400 operated with an accelerating voltage of 20 kV. Pellets were cut into pieces for measurements. Fractured samples were then placed on the aluminium stubs with silver paint and carbon-coated to prevent surface charging from the electron beam.

2.6 Differential Scanning Calorimetry (DSC)

Differential Scanning Calorimetry (DSC) measures the energy changes of a sample during controlled heating and cooling cycles. Two identical crucibles, one containing the sample and the other one containing an inert reference are put next to each other in the same furnace. Two thermocouples attached are used to measure the energy changes between the sample and the inert reference to keep the temperatures the same. In this work a Netzsch DSC 404C was used. ~ 40 mg of the powdered sample was put in an aluminium crucible with repeated heating and cooling cycles until the DSC pattern was unchanged. The heating and cooling rate was 10 ℃/minute.

2.7 Dilatometry (DIL)

Dilatometry (DIL) measures the linear thermal expansion of a sample as a function of temperature. It only gives an averaged thermal expansion coefficient for a polycrystalline sample. In this work the DIL measurements were carried out on a Netzsch DIL 402C. Pelletised samples were placed horizontally on a tube-typed aluminium sample support with a thermocouple next to it. Two horizontal pushrods were pressed on the parallel faces of the pellet and the thermal expansion coefficients were recorded while each thermal cycle with a heating and cooling rate of 10 ℃/minute. Prior to each measurement, the instrument was calibrated using a rod-shaped Si single crystal as a standard.

2.8 Nuclear Magnetic Resonance (NMR) Spectroscopy

Nuclear Magnetic Resonance (NMR) Spectroscopy, firstly measured by I. I. Rabi[9], describes the magnetic spin energy absorbed and re-emitted in the form of electromagnetic radiation by the atomic nuclei under the applied magnetic field. NMR was widely used in molecular substances for the determination of the local molecular structure. From the NMR peak positions and relative intensities, much structural information such as atom coordination numbers, next nearest neighbours, elemental analysis etc. can be obtained. For solid state studies, NMR absorption spectra can be enhanced and sharpened by the MAS (Magic Angle Spinning) technique, where the sample is rotated at a specific angle of 54.74 °towards the applied magnetic field.[10]

NMR spectroscopy in this work was performed by Dr J. V. Hanna from University of Warwick. To determine the chemical environments of the MO_4 tetrahedra, ^{11}B and ^{31}P one pulse spectra from sample $Bi_{12}(B_{0.5}P_{0.5})O_{20}$ and $Bi_{12}(Bi_{0.03}P_{0.89}\square_{0.08})O_{20.27}$ were measured in a Bruker 850 kHz Solid Static NMR spectrometer at magnetic field of 14.1 T and 7.05 T with induced frequency of 12.5 kHz MAS, respectively.

2.9   Raman Spectroscopy (RS)

Raman Spectroscopy (RS), named after Sir C. V. Raman, is used to observe the rotational and vibrational states of an atom in a sample. A monochromatic light (i.e. laser) interacts with the atomic vibrations and/or rotations by exciting the atom from the ground state to a virtual energy state, resulting in the energy of the emitted laser light being shifted in terms of a frequency-related unit, wavenumber, $\tilde{v}$. The emitted photon shifts to a lower frequency indicates the final vibrational state of the atom has more energy than its initial state, represented as Stokes Raman scattering; in contrast, the emitted photon shifts to a higher frequency indicates the final atomic vibration has less energy than its initial state, represented as Anti-Stokes Raman scattering.

RS measurement was performed using a Renishaw inVia micro-Raman spectrometer with an Ar-laser (514.5 nm) and recorded in backscattering geometry. A laser power of 10 mW was focused on a ~ 2 μm spot on the sample. A Linkam THMS600 cell was used for obtaining data below and above room temperature. All RS data were corrected for the Bose-Einstein thermal factor.

2.10 Microwave Dielectric Resonance Measurement

The microwave dielectric properties of samples were measured by the cylindrical cavity method, where the pellet (with diameter ~ 10 mm and thickness ~ 5 mm) was placed on a 4.77 mm high quartz spacer in a 20 mm copper cavity. Connected with a resonant system, a coupling loop with two probes formed an open circuit to measure the frequencies induced in the volume of the dielectric pellets. The bandwidth of the resonant signal was observed by a vector network analyser Advantest R3767CH with an analysis range of 40 MHz – 8 GHz. The ε_r and the unloaded Q can be calculated from the measured resonant frequency (f_0), the loaded Q factor (i.e. $f_0/\Delta f_0$) and the insertion loss (S_{21}).

The temperature coefficient of resonant frequency (τ_f) is used to measure the temperature stability of the sample (i.e. the degree of temperature dependency of the

resonant frequency peak position). The more independent of f_0 peak with temperature, the closer the τ_f towards zero. In this work, the sample was placed in the same copper cavity and heated from 25 to 80 ℃ with 5 intermittent measurements. At each temperature, the sample was left for 30 minutes to equilibrate. The heating and cooling system was controlled by Peltier UPS. The measurement of τ_f can be expressed by Equation 2.5[11].

$$\tau_{f\,=} \frac{1}{f_0}\frac{\partial f_0}{\partial T} \qquad\qquad (2.5)$$

where f_0 is the resonant frequency measured at room temperature, $\frac{\partial f_0}{\partial T}$ is the change of resonant frequency with respect to change of temperature. τ_f is the gradient of $\frac{\partial f_0}{f_0}$ with respect to change of temperature ∂T. τ_f is usually expressed as parts per million per Kelvin (ppm/K), which is obtained by multiplying the results by 10^6.

2.11 Fixed Frequency Capacitance Measurement

Radio frequency (rf) fixed frequency capacitance measurements were used to measure the capacitance and dielectric loss (tan δ) of the sample at 1, 10, 100 k and 1 M Hz ranging from 10 – 800 K. Low temperature measurements (~ 10-320 K) used an Agilent E4980A LCR meter with an Oxford Instrument cryocooler for cooling and high temperature measurements (~ 320-800 K) used a Hewlett-Packard 4284 A precision LCR meter with a tube furnace for heating. All data were corrected for sample geometry prior to analysis.

2.12 Impedance Spectroscopy (IS)

2.12.1 Background

Impedance spectroscopy is an extremely useful technique to analysis the electrical properties of electroceramics. It can be used to characterise the microstructure of the materials associated with different regions e.g. grain, grain boundary and interfacial

phenomena; to determine the charge carrier and to assess the electrical homogeneity of the sample with variable frequency, temperature, oxygen partial pressure and dc bias.[12] IS measurements are usually carried out over the frequency range from 10^{-2} to 10^7 Hz. In general, different electro-active regions of the material are represented by a parallel RC element (resistor R and capacitor C), which can be identified by IS according to each characteristic electrical relaxation time or time constant, τ, Equation 2.6.

$$\tau = RC \tag{2.6}$$

To describe each electro-active region in terms of Debye-type response, Equation 2.6 can be expressed with frequency domains, Equation 2.7,

$$\omega_{max}RC = 1 \tag{2.7}$$

where ω_{max} is the angular frequency with $\omega_{max} = 2\pi f_{max}$ (f_{max} is the applied frequency at Debye peak maximum).[13] The separation of different responses depends on the resolution of their associated time constants. Generally, two well-resolved Debye peaks are given by two time constants with their difference greater than two orders of magnitude.[14]

2.12.2 Four Interrelated Complex Formalisms

The advantage of IS is the four interrelated complex formalisms: impedance (Z*) admittance (Y*), permittivity (ε*) and electric modulus (M*). All of them can be represented in terms of real and imaginary parts, where the notation single prime (') represents the real components and the double prime notation (") represents the imaginary components, for instance, Z*, Equation 2.8.

$$Z^* = Z' - jZ'' \tag{2.8}$$

The same set of data can be readily presented in one or more of the four complex formalisms by simple mathematically transformations, Equation 2.9 - 2.12.

$$Y^* = 1/Z^* \tag{2.9}$$

$$\varepsilon^* = 1/M^* \tag{2.10}$$

$$M^* = j\omega C_0 Z^* \tag{2.11}$$

$$\varepsilon^* = Y^*/j\omega C_0 \tag{2.12}$$

where C_0 is the vacuum capacitance of the cell.[15] It can be easily shown that M' is related to Z'' (i.e. M' = $\omega C_0 Z''$) and M'' is related to Z' (i.e. M'' = $\omega C_0 Z'$). Likewise, ε' is related to Y'' and ε'' is related to Y'. In addition, ε' is also related to C', Equation 2.13.

$$\varepsilon' = \frac{C'}{\varepsilon_0} \frac{l}{A} \tag{2.13}$$

where C' is the capacitance of the sample; ε_0 is the permittivity of the free space, 8.854×10^{-14} F cm^{-1}; l is the sample thickness and A is the measured sample surface area covered by the electrodes.

These four IS complex formalisms highlight different weighing factors. In brief, Z* is dominated by elements with high resistance, R value, and it is usually useful to analyse the grain boundary response. M* is dominated by elements with low capacitance, C; therefore, it can be used to analyse low capacitance, i.e. the bulk response of the sample. In addition, ε* and Y* are useful to examine the permittivity and conductivity of the sample. The correct equivalent circuit should give good fit for all of the four formalisms with extracted parameters showing physical significance.

2.12.3 Brick Layer Model

In many polycrystalline electroceramics, an equivalent circuit with two parallel RC elements connected in series, known as the Brick Layer Model, are usually used to model bulk and grain boundary response in the sample, Figure 2.6. In this model, ceramics are assumed to have conductive grains surrounded by thin resistive grain boundary layers.[16] Other components, such as R, C, CPE etc. in equivalent circuit can be connected in parallel or series to represent different IS responses.

Investigation of different IS electro-active regions can be achieved through their associated capacitance, C values. The general capacitance values and the interpretations are listed in Table 2.3. Based on this table, it is easy to assign the responsible phenomena to a particular electrical response. Other methods, such as measuring the temperature dependence of sample resistance and capacitance over a wide temperature range, polishing

sample surfaces, can also be useful to distinguish between similar electrical responses with overlapping C values, e.g. grain boundary, surface layer etc.

Table 2.3 Capacitance values and their interpretations. [13][15]

Capacitance [F]	Phenomenon Responsible
$10^{-12} = 1$ pF	Bulk
10^{-11}	Minor, second phase
$10^{-11} – 10^{-8} \sim 1$nF	Grain boundary
$10^{-10} – 10^{-9}$	Bulk ferroelectric near T_c
$10^{-9} – 10^{-7} \sim 1$ μF	Surface layer
$10^{-7} – 10^{-5}$	Sample-electrode interface
10^{-4}	Electrochemical reactions
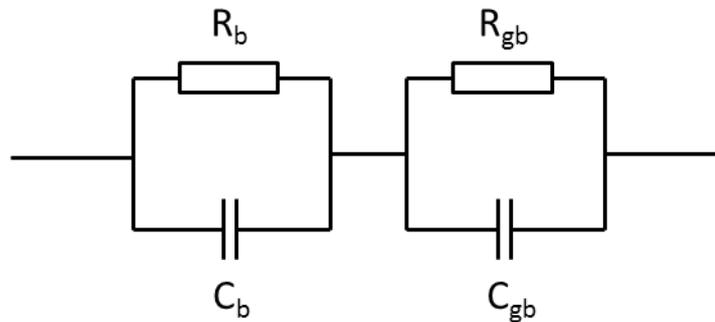
Figure 2.6 An equivalent circuit consisting of two parallel *RC* elements in series.

IS data are usually presented in different plots, for instance complex impedance plane Z* plot, combined Z" and M" spectroscopic plots, real capacitance C' spectroscopic plots etc. Figure 2.7 is used as an example to show the IS data of the equivalent circuit with two parallel RC elements in series in Figure 2.6, where R_b, R_{gb}, C_b and C_{gb} are assumed as typical values of 1 MΩ cm, 100 MΩ cm, 10 pF cm^{-1} and 1 nF cm^{-1}, respectively. In the complex impedance Z* plot, Figure 2.7 (a), a perfect semicircular arc associated with a highly resistive grain boundary component dominates the plot, where the conductive bulk component is shown in the inset. Each R values can be determined from the intercept of each semicircular arc on the Z' axis; Each C value can be calculated from the maximum of each semicircle according to the relation $\omega_{max}RC = 1$. In the Z" and M" spectroscopic plot, Figure 2.7 (b), two Debye peaks associated with the two parallel RC elements are shown with the bulk response at higher frequency and the grain boundary response at lower

frequency. Based on Equation 2.14 and 2.15, Z" spectra is dominated by components with higher R values, normally the grain boundary; and M" spectra is dominated by components with lower C values.

$$Z" = R_b \left[\frac{\omega R_b C_b}{1+(\omega R_b C_b)^2} \right] + R_{gb} \left[\frac{\omega R_{gb} C_{gb}}{1+(\omega R_{gb} C_{gb})^2} \right] \qquad (2.14)$$

$$M" = \frac{C_0}{C_b} \left[\frac{\omega R_b C_b}{1+(\omega R_b C_b)^2} \right] + \frac{C_0}{C_{gb}} \left[\frac{\omega R_{gb} C_{gb}}{1+(\omega R_{gb} C_{gb})^2} \right] \qquad (2.15)$$

The R and C values of each component can also be determined from the maximum of the Debye peaks in Z" and M" spectroscopic plot as $R = 2Z"_{max}$ and $C = M"_{max} / 2$. In the real capacitance C' spectroscopic plot, two typical capacitance plateaux are shown in Figure 2.7 (c). Similar to complex impedance Z* plot and Z"/M" spectroscopic plot, the bulk component is present at higher frequency and the grain boundary component is shown at lower frequency. Different regions of the sample can be assigned from the magnitude of each capacitance plateau.
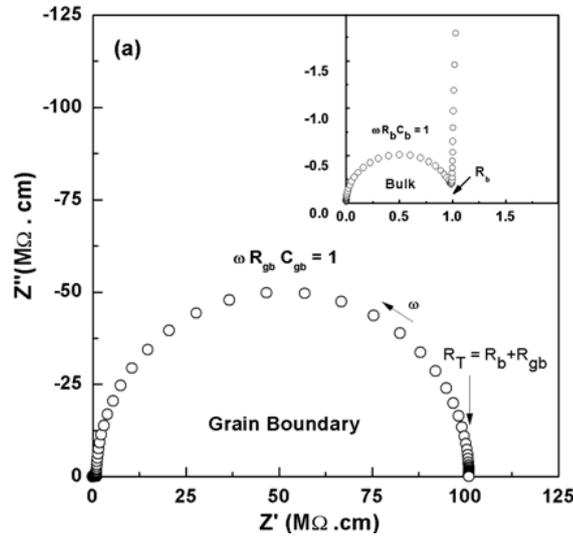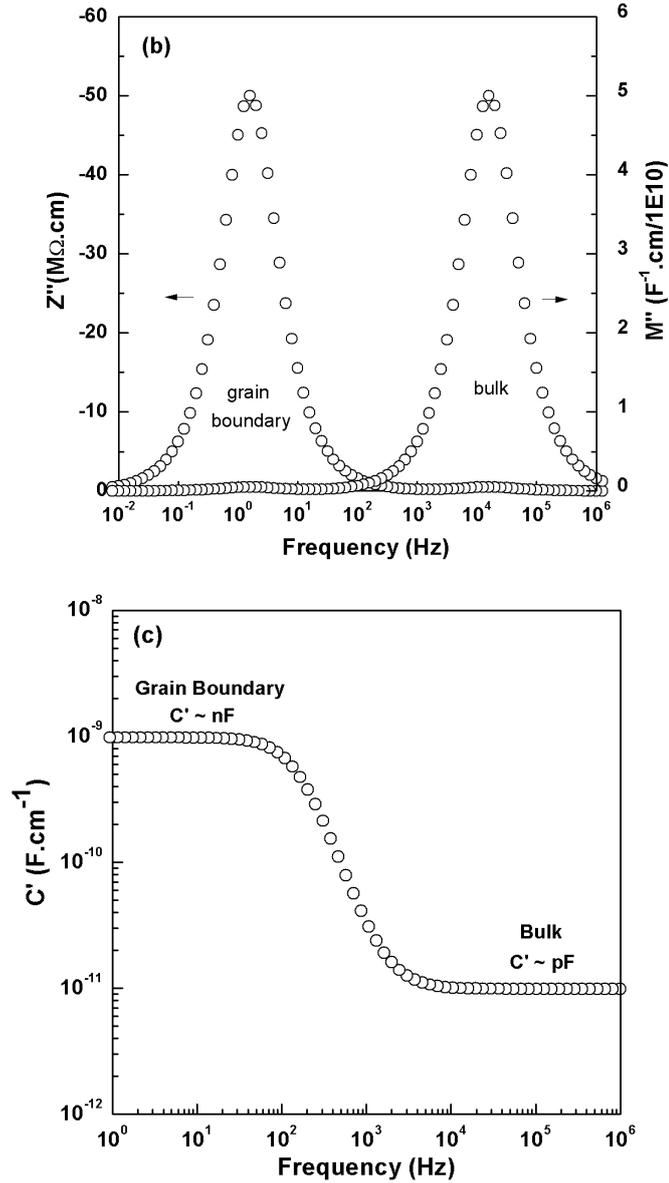
Figure 2.7 (a) complex impedance plane Z* plot (b) combined Z" and M" spectroscopic plot (c) real capacitance C' spectroscopic plot of stimulated IS data for Brick Layer Model.

2.12.4 Arrhenius Equation

The Arrhenius equation, Equation 2.16, is used to determine the activation energy of conductivity, Ea, of the sample. Ea is calculated from the slope of the Arrhenius plot, i.e. log σ_b vs. 1000/T (K).

$$\sigma = \sigma_0 \exp\left(\frac{-Ea}{kT}\right) \qquad\qquad (2.16)$$

where σ is the conductivity of the sample, i.e. $\sigma = 1/R$; σ_0 is a pre-exponential factor, k is the Boltzmann constant and T is the temperature.

In this work, AC impedance spectroscopy measurements were carried out by using two sets of equipment. For low temperature IS measurements (10 – 320 K), an Agilent E4980A LCR meter with an operating frequency range of 20 Hz to 2 MHz was used. For high temperature IS measurements (25 – 500 °C), an HP4192A impedance analyser with an operating frequency range of 5 Hz – 10 MHz was used. The geometric factor of the sample was measured. Gold-sputtered or organo-gold paste was used as electrodes covering the parallel faces of the pellet. Two insulating blocks were attached to each parallel face of the ceramics, sandwiched between each of them were two platinum stripes which were used to connect the sample and the conductivity jig. High temperature IS measurements were taken by controlled temperature steps within ± 3 °C and the laboratory setup is shown in Figure 2.8.
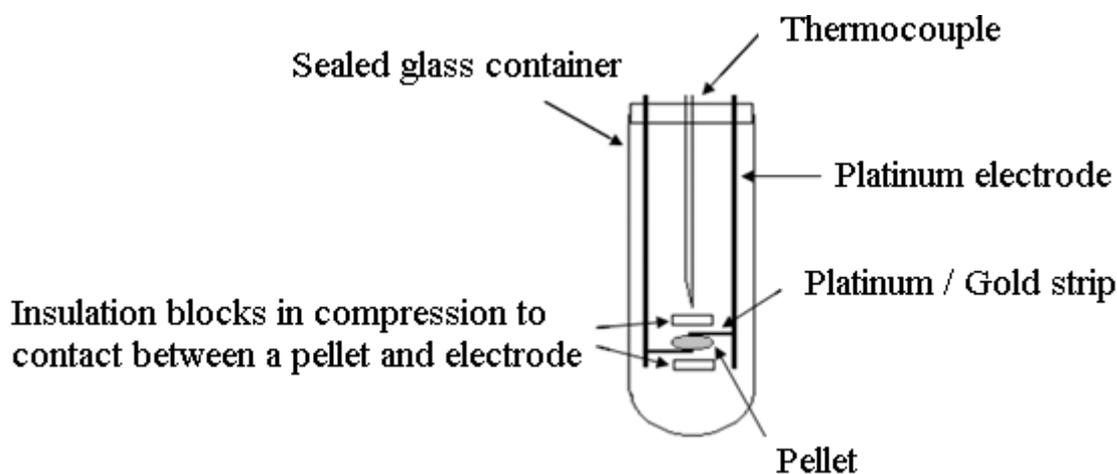
Figure 2.8 Schematic diagram of high temperature IS equipment setup, where pellet connected with platinum electrodes in a compression jig.

2.13 References

[1]   A. Clearfield, Reibenspies, J. and Bhuvanesh N., *Principles and applications of powder diffraction*, 1st ed. Chichester: John Wiley & Sons Ltd., 2008.

[2]   R. A. Young, *The Rietveld Method*, I.U.o.Crystallography ed. New York: Oxford University Press, 1993.

[3]   http://www.ill.fr.

[4]   http://isis.rl.ac.uk.

[5]   H. M. Rietveld, A profile refinement method for nuclear and magnetic structures, Journal of Applied Crystallography*,* 1969. **2**: p. 65-71.

[6]   L. B. McCusker, R. B. Von Dreele, D. E. Cox, D. Louer and P. Scardi, Rietveld refinement guidelines, Journal of Applied Crystallography*,* 1999. **32**: p. 36-50.

[7]   A. C. Larson and R. B. Von Dreele, "General Structure Analysis System (GSAS)," ed: Los Alamos National Laboratory LAUR 86-748, 1994.

[8]   B. H. Toby, EXPGUI, a graphical user interface for GSAS, Journal of Applied Crystallography*,* 2001. **34**: p. 210-213.

[9]   I. I. Rabi, J. R. Zacharias, S. Millman and P. Kusch, A new method of measuring nuclear magnetic moment, Physical Review*,* 1938. **53**: p. 318-318.

[10]   A. R. West, *Solid state chemistry and its applications*. Aberdeen: John Wiley & Sons, 1989.

[11]   A. J. Moulson and J. M. Herbert, *Electroceramics: materials, properties, applications. (Second Edition)*. Chichester, England: John Wiley & Sons Ltd., 2003.

[12]   J. R. Macdonald and E. Barsoukov, *Impedance spectroscopy:theory, experiment, and applications, 2nd edition*: John Wiley & Sons, 1987.

[13]   J. T. S. Irvine, D. C. Sinclair and A. R. West, Electroceramics: Characterization by impedance spectroscopy, Advanced Materials*,* 1990. **2**: p. 132-138.

[14]   E. J. Abram, D. C. Sinclair and A. R. West, A strategy for analysis and modelling of impedance spectroscopy data of electroceramics: Doped lanthanum gallate, Journal of Electroceramics*,* 2003. **10**: p. 165-177.

[15]   D. C. Sinclair and A. R. West, Impedance and modulus spectroscopy of semiconducting BaTiO$_3$ showing positive temperature-coefficient of resistance, Journal of Applied Physics, 1989. **66**: p. 3850-3856.

[16]   J. Fleig and J. Maier, The impedance of ceramics with highly resistive grain boundaries: Validity and limits of the brick layer model, Journal of the European Ceramic Society, 1999. **19**: p. 693-696.

3   A Study of Tetravalent Cation Doping in "Ideal" Sillenites: $Bi_{12}M^{4+}O_{20}$, where M = Si.

3.1   Introduction

Sillenites have a pseudo body-centred cubic unit cell and the average structure belongs to the non-centrosymmetric space group $I23$ (no. 197). Their unit cell contains two formula units with tetrahedrally coordinated M atoms located in the centre and four vertices of the cubic structure, i.e. (2a) site. These tetrahedra corner-share with two, distorted Bi-octahedral, BiO_5LP units that form dimers (LP is denoted as the Bi^{3+} stereochemically $6s^2$ electron lone pairs). Altogether they form a complex three-dimensional framework structure, Figure 3.1[1].

The ideal sillenite has a general formula $Bi_{12}M^{4+}O_{20}$ with a M^{4+} cation of ionic radius, r = 0.31 Å forming geometrically regular $MO(3)_4$ tetrahedra[2] and a fully occupied oxygen sublattice (i.e. 20). The closest known examples are $Bi_{12}MO_{20}$ with M = Si^{4+} (r = 0.26 Å), Ge^{4+} (r = 0.39 Å) and Ti^{4+} (r = 0.42 Å)[3], with the most "perfect" crystal lattice being $Bi_{12}GeO_{20}$ based on structural refinement of neutron diffraction[4] and Raman spectroscopy data[5].
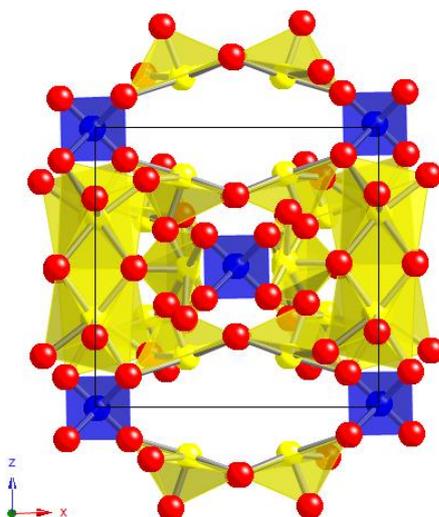
Figure 3.1[1] The structure of an ideal $Bi_{12}M^{4+}O_{20}$ sillenite viewed along the (001) plane, where yellow, blue and red spheres represent Bi^{3+}, M^{4+} and O^{2-} ions, respectively; black lines indicate the body-centred cubic unit cell of the structure.

Among the ~ 60 known sillenite members, ideal sillenites are scarce. The majority of sillenites have a more disordered structure, where the MO_4 tetrahedra and basic framework polyhedra, BiO_5LP, are highly distorted. Classification of sillenites in the literature [1, 6, 7] has been based on ion size, valence and electronic structure of the M cations and on the oxygen sublattice. For instance, Radaev *et al.* [1] classified sillenites into three groups depending on the M-dopants as: ideal stoichiometric sillenites, e.g. $Bi_{12}GeO_{20}$; defect sillenites, e.g. $Bi_{12}Ti_{0.9}O_{19.8}$ and sillenites with "composite" M cations, e.g. $Bi_{12}(Fe^{3+}_{0.35}P^{5+}_{0.59}\square_{0.06})O_{20}$, $Bi_{12}(Bi^{3+}_{0.5}Ga^{3+}_{0.5})O_{19.5}$ and $Bi_{12}(Bi^{3+}_{0.03}V^{5+}_{0.89}\square_{0.08})O_{20.27}$. Subsequently, based on the concentration of the sillenite oxygen sublattice, Valant and Suvorov developed a model (the VS model) [6] that divided sillenites into: (1) stoichiometric, where the oxygen sublattice is fully occupied (=20) by oxygen ions or/and lone electron pairs of Bi^{3+} ions located on the M-site, e.g. $Bi_{12}SiO_{20}$, $Bi_{12}(Bi_{0.5}Fe_{0.5})O_{19.5}LP_{0.5}$; and (2) non-stoichiometric, where an oxygen deficiency (< 20) or an oxygen excess (> 20) sublattice named as sub-stoichiometric or super-stoichiometric sillenites, e.g. $Bi_{12}B^{3+}O_{19.5}$ [8] and $Bi_{12}(Bi^{3+}_{0.03}V^{5+}_{0.89})O_{20.27}$ [1], respectively.

Neither classification is wrong, as every sillenite exhibits its unique character and there is no general model to fit the structural-composition-property relationships of all sillenites. Recently, Avdeev *et al.* [7] listed existing M-dopants for all reported families of sillenites. Table 3.1 is a modified version of their work [7] and new formulae from this work are included. Here, we characterise sillenites into three groups:

(i)   Ideal sillenites, e.g. $Bi_{12}M^{4+}O_{20}$;

(ii)   Sillenites obeying the VS formula [6], with umbrella-like distorted tetrahedra, BiO_3LP and/or void tetrahedra, $\square_MO_4$, e.g. $Bi_{12}(Bi_{0.67}Zn_{0.33})O_{19.33}LP_{0.67}$, $Bi_{12}(M^{5+}_{0.8}\square_{0.2})O_{20}$; these sillenites are basically derived from the Radaev & coworkers (R) structural model [9, 10] and generalised as the VS formula [6];

(iii)   "Composite" M-cation sillenites, with either 2 or 3 M-site dopants; compounds in this group have a variety of possible formulae to form stoichiometric or nonstoichiometric sillenites that obey or disobey the VS formula [6], e.g. $Bi_{12}(Mg^{2+}_{0.33}P^{5+}_{0.67})O_{20}$ [7] and $Bi_{12}(Ge^{4+}_{0.96}Bi^{5+}_{0.02}Al^{3+}_{0.02})O_{20}$ [11].

Non-stoichiometric

Stoichiometric

(i) (ii) (iii)

(iii)
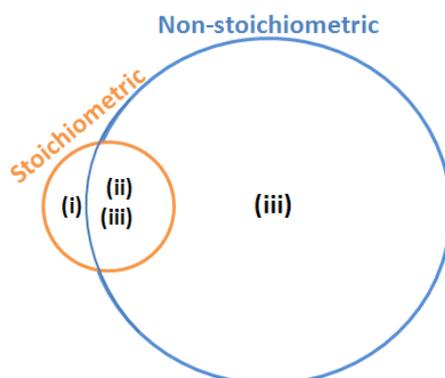
Figure 3.2 Interrelationship of three sillenites groups, where orange- and blue-coloured circles represent stoichiometric and non-stoichiometric sillenites by Valant & Suvorov[6], respectively.

Table 3.1 Classification of existing sillenites.

Type	General Formula	\multicolumn{2}{c}{VS Formula: $Bi_{12}(Bi^{3+}_{4/5-nx}M^{n+}_{5x})O_{19.2+nx}$ [6]}	Dopants[7]
(ii) Parent	γ-Bi_2O_3	$n = 0$, $x = 0$:	$Bi_{12}(Bi^{3+}_{0.8}\square_{0.2})O_{19.2}LP_{0.8}$	-
(i) Ideal	$Bi_{24}M^{4+}_2O_{40}$	$n = 4$, $x = 1/5$:	$Bi_{12}M^{4+}O_{20}$	M = Si, Ge, Ti
(ii)	$Bi_{25}M^{3+}O_{39}$	$n = 3$, $x = 1/10$:	$Bi_{12}(Bi_{0.5}M^{3+}_{0.5})O_{19.5}LP_{0.5}$	M = Al, Ga, Tl, Fe
(ii)	$Bi_{38}M^{2+}O_{58}$	$n = 2$, $x = 1/15$:	$Bi_{12}(Bi_{0.67}M^{2+}_{0.33})O_{19.33}LP_{0.67}$	M = Zn, Co
(ii)	$Bi_{24}M^{5+}_2O_{41}$	$n = 5$, $x = 4/5$:	$Bi_{12}(M^{5+}_{0.8}\square_{0.2})O_{20}$	M = P, As, V, Cr,
			$Bi_{12}(M^{5+})O_{20.5}$	Mn
(iii)	$Bi_{24}A^{3+}B^{5+}O_{40}$		$Bi_{12}(A^{3+}_{0.5}B^{5+}_{0.5})O_{20}$	A^{3+} =B, Al, Ga, In,
				Fe, Co
				B^{5+} = P, V, As
(iii)	$Bi_{36}A^{2+}B^{5+}_2O_{60}$		$Bi_{12}(A^{2+}_{1/3}B^{5+}_{2/3})O_{20}$	A^{2+} = Zn, Mg, Mn,
				Co
				B^{5+} = P, V, A
(iii)	$Bi_{36}A^{3+}_2B^{6+}O_{60}$		$Bi_{12}(A^{3+}_{2/3}B^{6+}_{1/3})O_{20}$	A^{3+} = Ga, Fe
				B^{6+} = Mo, W
(iii) (*)	$Bi_{36}A^{3+}_2B^{2+}O_{58}$		$Bi_{12}(A^{3+}_{0.67}B^{2+}_{0.33})O_{19.33}$	A^{3+} = B
				B^{2+} = Zn
(iii) (*)	$Bi_{24}A^{3+}B^{3+}O_{39}$		$Bi_{12}(A^{3+}_{0.5}B^{3+}_{0.5})O_{19.5}$	A^{3+} = B
				B^{3+} = Al, Fe

Three groups of sillenites: (i) ideal sillenite (ii) sillenites obeying the VS general formula[6] with BiO_3LP and/or $\square_MO_4$ distorted tetrahedra (iii) "composite" sillenites with 2 or more M-dopants. Notation (*) indicates new sillenite phases found in this work.

Type (i) and (ii) compounds are the most well investigated sillenites, however, there has been little research performed on type (iii) sillenites. Exploration of new sillenite phases in the future should focus on type (iii), where variable formulae might be attained by

"mix-and-match" of two or more M-dopants, such as a combination of two M-dopants with valence states of 3+/2+, 3+/3+ and 3+/5+. Possible M-dopants could predominantly be from the d- , p- and s-blocks. Some compounds from type (iii) were reported as more distorted sillenites by lowing the symmetry from space group $I23$ to $P23$, such as $Bi_{24}[Bi^{3+}_{0.215(3)}(V^{4+}, V^{5+})_{0.205}Si^{4+}_{0.58}]_2(O_{39.97(2)}\square_{0.03})$ [12]. The interrelationship of these three groups of sillenites is shown in Figure 3.2, which is a graphical representation of Table 3.1.

Single-crystals of ideal sillenites $Bi_{12}SiO_{20}$, $Bi_{12}GeO_{20}$ and $Bi_{12}TiO_{20}$ have been used in the fields of electro-optics, acoustics, piezotechnics and ultrasonic devices for their properties such as photoconductivity, photorefractivity, elastic and piezoelectric constants.[13-16] Lately, sillenites have been reported as suitable microwave dielectric materials in LTCC technology.[17, 18]

In this chapter, the stoichiometric sillenite $Bi_{12}SiO_{20}$ is studied. Other compounds with tetravalent M-dopants, where M = Ti^{4+} and Ge^{4+} were prepared (i.e. $Bi_{12}TiO_{20}$, $Bi_{12}Ti_{0.95}O_{19.9}$, $Bi_{12}Ti_{0.9}O_{19.8}$, $Bi_{12}Ti_{0.8}O_{19.6}$ and $Bi_{12}GeO_{20}$), but single-phase samples could not be formed by the solid state reaction method, as shown by XRPD results in Appendix I. However, single-phase stoichiometric sillenites $Bi_{12}MO_{20}$, where M = Si^{4+}, Ti^{4+} and Ge^{4+} prepared from the growth of single-crystal methods are frequently reported based on their outstanding electro-optics properties. In the case of Ti^{4+}-doped sillenite, the exact stoichiometry is debatable. Radaev *et al.* [19] reported phase-pure $Bi_{12}Ti_{0.9}O_{19.8}$ single-crystals that belong to "defect" sillenites, with 10 % cation vacancies on the tetrahedral sites. Recently, Singla *et al.*[20] studied the Ti^{4+} substituted Bi_2O_3 solid system using a solid state reaction route: $(1-x)Bi_2O_3(x)TiO_2$ where x = 0.05, 0.10, 0.15 and 0.2, which is equivalent to four different Ti-sillenites: $Bi_{12}(Bi_{2/3}Ti_{1/3})O_{19.67}$, $Bi_{12}Ti_{2/3}O_{19.33}$, $Bi_{12}Ti_{1.06}O_{20.12}$ and $Bi_{12}Ti_{1.5}O_{21}$, respectively. Opposed to Radaev *et al.*[19], they reported a Ti-rich compound $Bi_{12}Ti_{1.06}O_{20.12}$ (x = 0.15) to be phase pure by XRPD using the solid state reaction route.

As an ideal sillenite, the preparation, microstructure and dielectric properties of $Bi_{12}SiO_{20}$ are presented and discussed. X-ray Powder Diffraction (XRPD), Differential Scanning Calorimetry (DSC), Scanning Electron Microscopy (SEM) and Energy Dispersive X-ray

Spectroscopy (EDS) measurements were performed to investigate the structural and compositional properties of the ceramic. Microwave dielectric properties were established using Microwave (MW) dielectric resonance measurements and compared with that reported by Valant and Suvorov [17]. Impedance Spectroscopy (IS) was used to characterise the electrical properties of $Bi_{12}SiO_{20}$ ceramics. Modelling of IS data was completed by using equivalent circuit analysis. The strategy of choosing the correct equivalent circuit involved combined analysis of the four IS complex formalisms: impedance, electric modulus, admittance and permittivity by consideration of the frequency- and temperature- dependence of the data.

Other techniques such as Raman Spectroscopy (RS) and Dilatometry (DIL) measurements were undertaken to evaluate the structural and thermal expansion characteristics as a function of Temperature, respectively. In the end, Nuclear Magnetic Resonance (NMR) spectroscopy was performed and verified the existence of geometrically regular SiO_4 tetrahedra in $Bi_{12}SiO_{20}$ by measuring isotope ^{29}Si one pulse spectra under a magnetic field of 7.05 T (5 kHz MAS). In addition, the MW dielectric properties and Raman spectra of this material are used as a "benchmark" to be compared with other structurally more distorted/complex sillenites reported in Chapters 4, 5 and 6.

3.2 Results

3.2.1 Initial Investigation of $Bi_{12}SiO_{20}$ Ceramic

$Bi_{12}SiO_{20}$ obeys the VS formula, i.e. $Bi_{12}(Bi^{3+}_{4/5-nx}M^{n+}_{5x})O_{19.2+nx}$[6], where $M^{n+} = Si^{4+}$ and $x = 1/5$. A stoichiometric powder batch was mixed by mortar and pestle and heated in a muffle furnace at 840 ℃ for 48 hours with intermediate grinding. XRPD results showed composition $Bi_{12}SiO_{20}$ to be single-phase with all reflections indexed using space group $I23$ [3] and a refined lattice parameter of $a = 10.10345(7)$ Å, Figure 3.3. Green pellets were pressed and sintered at 870, 880 and 890 ℃ in air to find the optimised sintering temperature. A relative pellet density maximum of 90% was obtained for sintering at 880 ℃. The highest density pellets were used for electrical property characterisation.
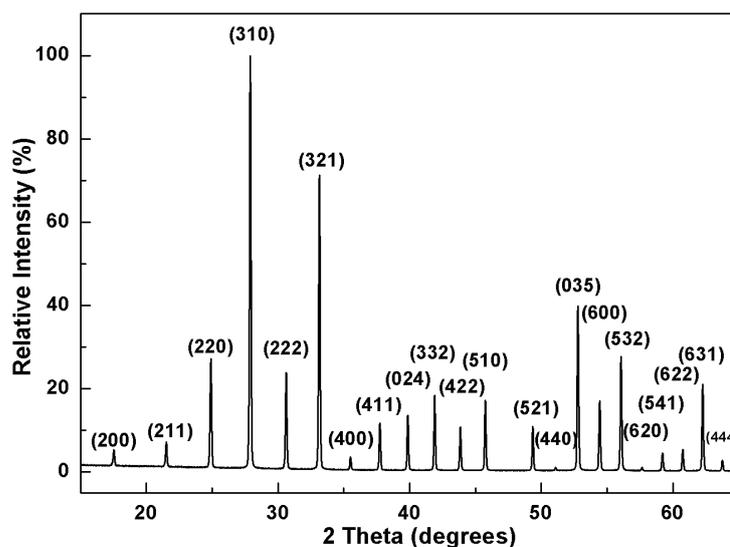
Figure 3.3 XRPD results of single-phase sillenite $Bi_{12}SiO_{20}$ after sintering at 850 ℃ for 48 hours indexed with ICDD card [80-627] after Horowitz *et al.* [3].

To investigate the thermal stability of $Bi_{12}SiO_{20}$, DSC was performed from ~400-1123 K for three heating and cooling cycles. The enthalpy changes between the sample and reference during heating and cooling from the second heating/cooling cycle are shown in Figure 3.4. Two pairs of reversible peaks with endothermic processes during heating and corresponding exothermic processes during cooling were observed at ~920 and 1103 K, respectively, which indicates a plausible reversible $\gamma \rightarrow \beta \rightarrow \delta \rightarrow \beta \rightarrow \gamma$ [21] phase transition sequence occurring in

this sample. XRPD data confirmed the sample retained the same (γ) sillenite phase on post-DSC measurements, suggesting $Bi_{12}SiO_{20}$ is a thermally-stable compound.
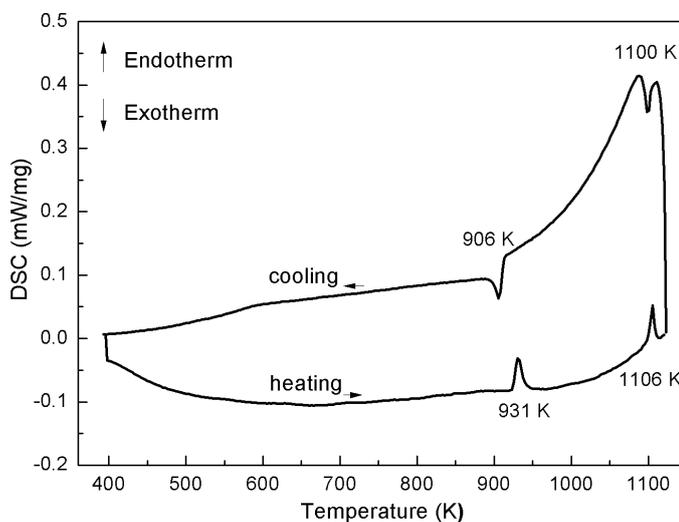
Figure 3.4 DSC trace of $Bi_{12}SiO_{20}$ powder.

To investigate the purity and composition of $Bi_{12}SiO_{20}$ ceramics on a micrometer (μm) scale, EDS combined with Scanning Electron Microscopy (SEM) was performed on a pellet sintered at 860 °C with a relative density of 85%. The pellet was polished and thermally etched at 774 °C (i.e. ~ 90% of the sintering temperature) for 30 minutes, then carbon-coated on the sample surface to prevent surface charging from the electron beam. The microstructure of a $Bi_{12}SiO_{20}$ pellet from the SEM image, Figure 3.5, showed the grain size varied from ~ 3 to 15 μm indicating grain growth was occurring. The grain morphology was uniform and well-packed with some open porosity located along the grain boundaries.

Composition measurements were carried out by EDS on ten randomly selected points on a carbon-coated $Bi_{12}SiO_{20}$ pellet. An EDS spectrum is shown in Figure 3.6. The measured percentage of atomic ratio between Bi and Si are listed in Table 3.2. The EDS derived composition, $Bi_{12.01(7)}Si_{0.99(7)}O_{20.01(3)}$ is in agreement with the nominal starting composition, $Bi_{12}SiO_{20}$.
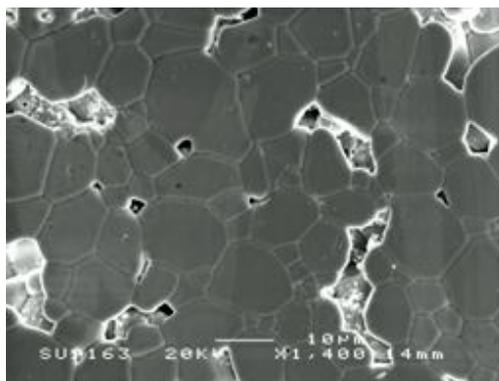
Figure 3.5 SEM image of $Bi_{12}SiO_{20}$ ceramic.
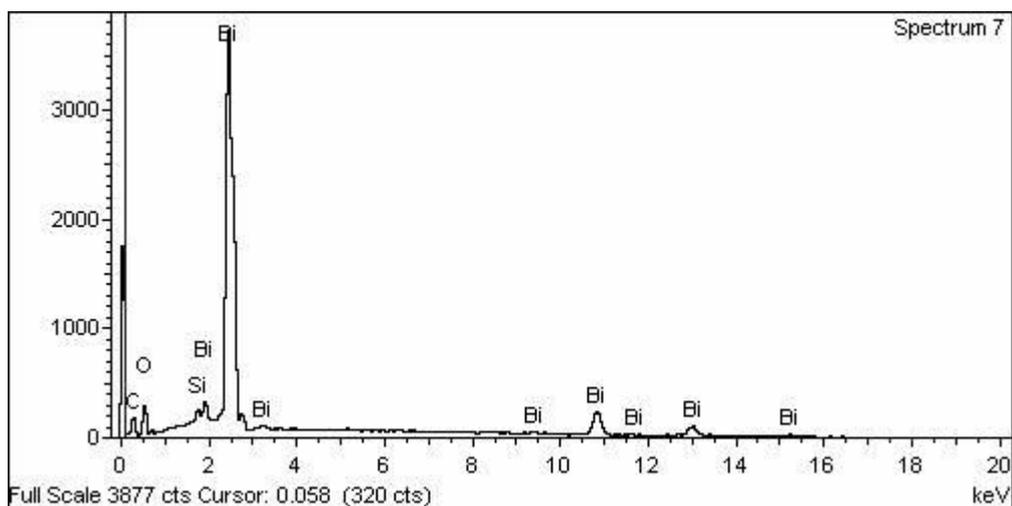
Figure 3.6 EDS spectrum of $Bi_{12}SiO_{20}$.

Table 3.2 Atomic ratios of Bi and Si obtained via EDS of $Bi_{12}SiO_{20}$. It is noteworthy that oxygen contents are calculated from Bi and Si contents.

$Bi_{12}SiO_{20}$	Bi (atomic %)	Si (atomic %)
No.1	92.52	7.48
No.2	91.49	8.51
No.3	93.12	6.88
No.4	92.03	7.97
No.5	93.00	7.00
No.6	92.61	7.39
No.7	92.59	7.41
No.8	92.16	7.84
No.9	92.23	7.77
No.10	91.76	8.24
EDS Averaged Values	**92.4(5)**	**7.6(5)**
Theoretical Values	**92.31**	**7.69**
EDS Derived Composition	$Bi_{12.01(7)}Si_{0.99(7)}O_{20.01(3)}$	

The microwave dielectric properties of $Bi_{12}SiO_{20}$ ceramics were first reported by Valant and Suvorov[17] and it was suggested as a suitable candidate for LTCC applications. Our measured dielectric properties on a 90% dense $Bi_{12}SiO_{20}$ ceramic (i.e. $\varepsilon_r \sim 36$; Q.f ~ 7037 GHz at a resonant frequency of 6.83 GHz; $\tau_f \sim -30$ ppm/K) were in good agreement with the reported data (i.e. $\varepsilon_r \sim 37.6$; Q.f ~ 8100 GHz; $\tau_f \sim -20$ ppm/K) [17] on a 97% dense $Bi_{12}SiO_{20}$ ceramic. Both the measured and reported ε_r is close to that calculated from the Clausius-Mossotti equation ($\varepsilon_{r\_CM} \sim 41$). The Clausius-Mossotti equation seems to be a good estimate of ε_r values for this silicate sillenite indicating only electronic and ionic polarisability phenomena are contributing to ε_r in this phase.

3.2.2 Frequency- and Temperature- dependent Electrical Properties and Impedance Analysis

The variation of capacitance (hence, ε_r) and dielectric loss (tan δ) with temperature were obtained from fixed frequency measurements at 1, 10, 100 k and 1 MHz over the range 10 – 800 K for $Bi_{12}SiO_{20}$ ceramic (pellet relative density $\sim 90\%$). Prior to measurements, the two parallel surfaces of the pellet were polished to remove any surface layers and then sputtered with Au electrodes. A frequency dispersive region of ε_r and tan δ was observed above room temperature, Figure 3.7 (a) and (b). The dispersion region of ε_r and tan δ was frequency- and temperature-dependent, with the peak maximum shifting to higher temperature with increasing frequency. The relaxation peaks are broad and asymmetric. In the permittivity plot, the magnitude of the peak height decreases with increasing frequency, which is similar to typical relaxor characteristics.[22] However, $Bi_{12}SiO_{20}$ is non-ferroelectric with dipolar glass-like relaxor behaviour. In the ε_r plot, the 1, 10 and 100 kHz data exhibit a peak with an ε_r maximum of ~ 335, 136 and 66 at ~ 597, 661 and 739 K, respectively. The corresponding capacitance maximum of the 1, 10 and 100 kHz data is 2.97×10^{-11}, 1.20×10^{-11} and 5.84×10^{-12} $F.cm^{-1}$, respectively. The data at 1 MHz do not show the presence of a peak maxima within the

measured temperature range but it exhibits an increase in ε_r from ~ 37 at 200 K to ~ 45 at 800 K, corresponding to an increase in capacitance values to ~ 3.28×10^{-12} and ~ 3.98×10^{-12} F.cm^{-1}, respectively. In the tan δ plot, the 1, 10 and 100 kHz data exhibit corresponding peaks with maximum values of ~3.4, 3.6, and 4.1 at ~ 543, 619 and 746 K, respectively.
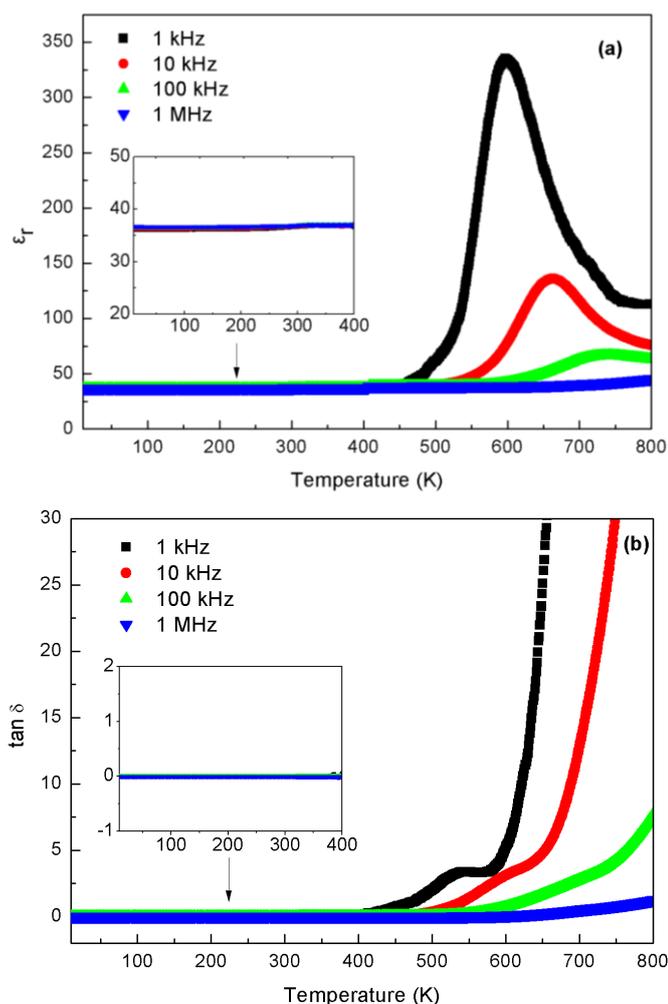
Figure 3.7 Temperature dependence of (a) permittivity, ε_r, and (b) dielectric loss, tan δ, of $Bi_{12}SiO_{20}$. Insets are an expanded view of lower temperature data between 10 and 400 K.

The relaxation behaviour associated with a dispersion region of ε_r and tan δ peak maxima above RT is not unique to the stoichiometric sillenite $Bi_{12}SiO_{20}$, but is a common phenomenon in all sillenites and some Bi_2O_3 containing compounds, such as fluorite δ-Bi_2O_3 as reported by Valant *et al*.[23]. Its origin in fluorite δ-Bi_2O_3 solid solutions was attributed to a high level of ion disorder in the cation and oxygen sublattice[23]. This dielectric relaxation behaviour was usually enhanced at lower frequencies. In addition, superimposed on this relaxation behaviour,

there was a frequency- and temperature-dependent increase of ε_r and tan δ (e.g. in the ε_r plot, a rising tail began to show at 1 kHz within the measured temperature range), which was due to a space-charge polarization that originates from the increasing concentration of mobile charge carriers with increasing temperature.[23-26]

For sillenites (γ-Bi$_2$O$_3$), however, Valant and Suvorov[27] mentioned the dielectric properties were different from the above case and showed "relaxor ferroelectric" behaviour below room temperature for the stoichiometric compound Bi$_{12}$(B$_{0.5}$P$_{0.5}$)O$_{20}$, where Si is replaced by 50% B^{3+} and 50% P^{5+} on the M-site. Their statement is at odds with our experimental results. We found sillenites also exhibit the same relaxation behaviour above room temperature similar to fluorite δ-Bi$_2$O$_3$ compounds. The aforementioned "relaxor-like" dielectric anomaly in Bi$_{12}$(B$_{0.5}$P$_{0.5}$)O$_{20}$ below room temperature was a different intrinsic phenomenon occurring in many other B-doped and P-doped sillenites, which will be discussed in detail in Chapters 5 and 6, respectively.

To further understand the origin of the dielectric relaxation behaviour of Bi$_{12}$SiO$_{20}$ above room temperature, Impedance Spectroscopy (IS) was performed on a gold-sputtered coated Bi$_{12}$SiO$_{20}$ pellet (relative pellet density ~90%) from low (10 K) to high temperature (798 K).

3.2.2.1 High Temperature IS data (573 – 798 K)

The sample was resistive at room temperature and required temperatures above 573 K to obtain a bulk (grain) response. Z* plots for Bi$_{12}$SiO$_{20}$ at 573, 623, 673, 723 and 773 K are shown in Figure 3.8 (a)-(f).
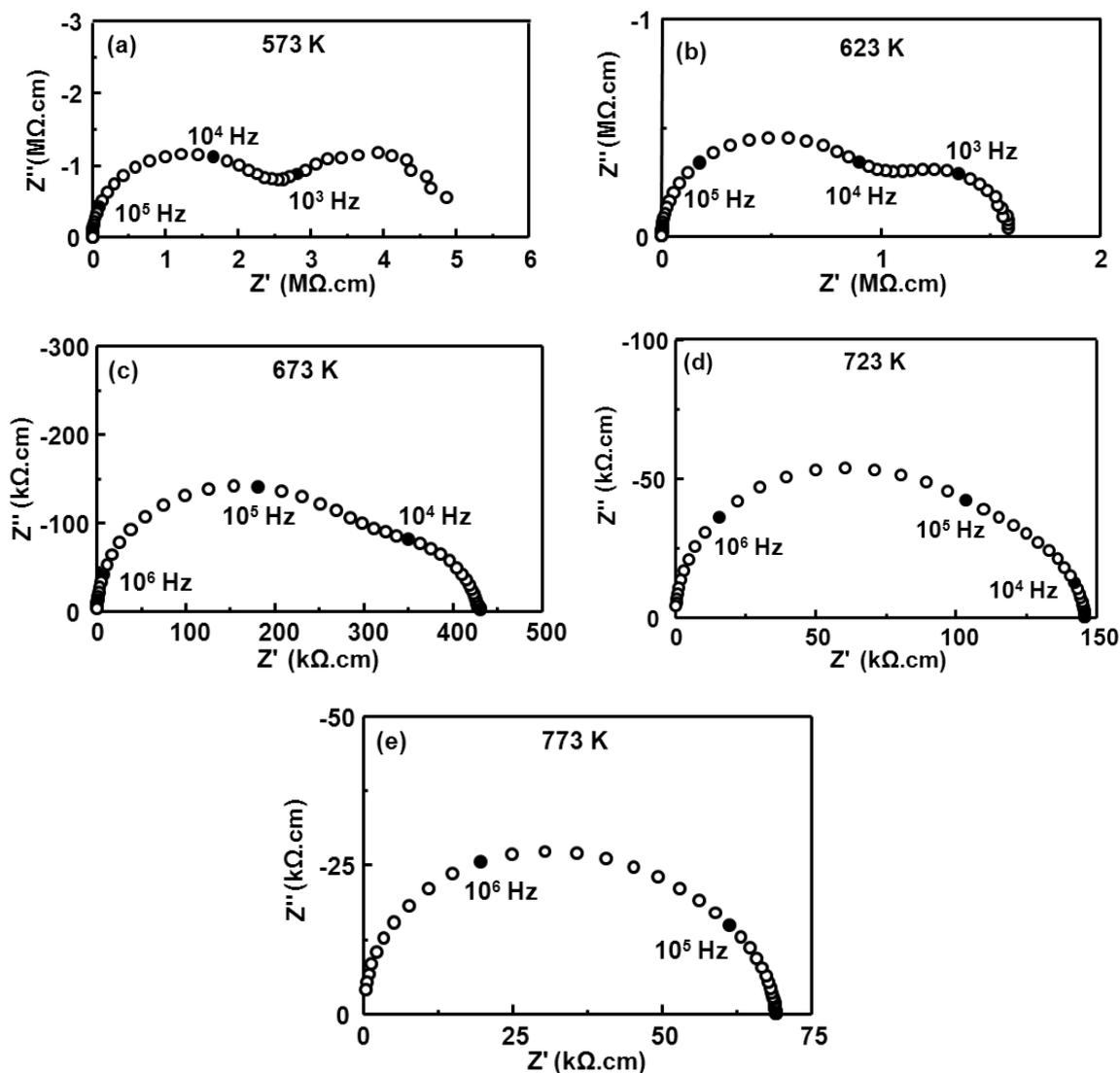
Figure 3.8 Z* plots for $Bi_{12}SiO_{20}$ ceramics at (a) 573, (b) 623, (c) 673, (d) 723 and (e) 773 K.

At 573 K, Figure 3.8 (a), two semicircles were observed. However, the lower frequency semicircular arc was not fully resolved.

At 623 K, Figure 3.8 (b), there were two semicircular arcs: one at high frequency and another at low frequency with estimated associated capacitance values, C', of 4.1 pF cm^{-1} (ε_r ~ 46) and 21.7 pF cm^{-1} (ε_r ~ 245), respectively, based on a model of 2 parallel RC elements connected in series (see Circuit A in Figure 3.11). With increasing temperature, the low frequency semicircular arc gradually shifted to higher frequency and started to merge with the high frequency semicircular arc.

At 673 K, Figure 3.8 (c), two semicircular arcs at high and low frequency can still be

resolved.

At 723 and 773 K, Figure 3.8 (d) and (f), only the high frequency semicircular arc can be observed. This arc is asymmetric and broad indicating the existence of the second component at lower frequency. This can be observed more prominently in spectroscopic plots of C' at various temperatures between 10 and 773 K, Figure 3.9, where two capacitance plateaux appeared in the measured temperature range: one at high frequency and one at low frequency. The high frequency C' plateau is frequency-independent and exists over almost the entire measured temperature range with $C'_{high} \sim 3.6$ pF.cm^{-1} ($\varepsilon'_{high} \sim 41$), whereas the low frequency C' plateau is frequency-dependent and present above 573 K with the capacitance plateau decreasing by $\sim$ two orders of magnitude with increasing temperature: $C'_{low} \sim 24$ pF.cm^{-1} ($\varepsilon'_{low} \sim 272$) at 623 K to $C'_{low} \sim 11$ pF.cm^{-1} ($\varepsilon'_{low} \sim 126$) at 773 K at 1 kHz.

The frequency-independent high frequency C' plateau corresponds to the large, high frequency semicircular arc observed in the Z* plots, Figure 3.8 (a), (b) and (c), and the high frequency Debye peak in the combined –Z"/M" spectroscopic plots, Figure 3.10 (a) and (b), which is attributed to the bulk response of the sample with $C' \sim 3.6 \times 10^{-12}$ F.cm^{-1} ($\varepsilon' \sim 41$). The frequency-dependent low frequency C' plateau corresponds to the smaller, low frequency semicircular arc in the Z* plots, Figure 3.8 (a), (b) and (c), and the low frequency peak in the –Z" spectra, Figure 3.10 (a) and (b), which is attributed to the intrinsic bulk relaxation of the sample. Evidence of the assignments will be provided from equivalent circuit fitting analysis, as outlined later in this chapter.
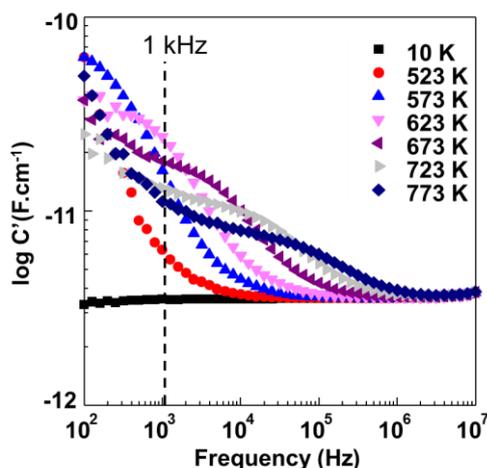
Figure 3.9 C' spectroscopic plots at various temperatures for Bi$_{12}$SiO$_{20}$ ceramic.
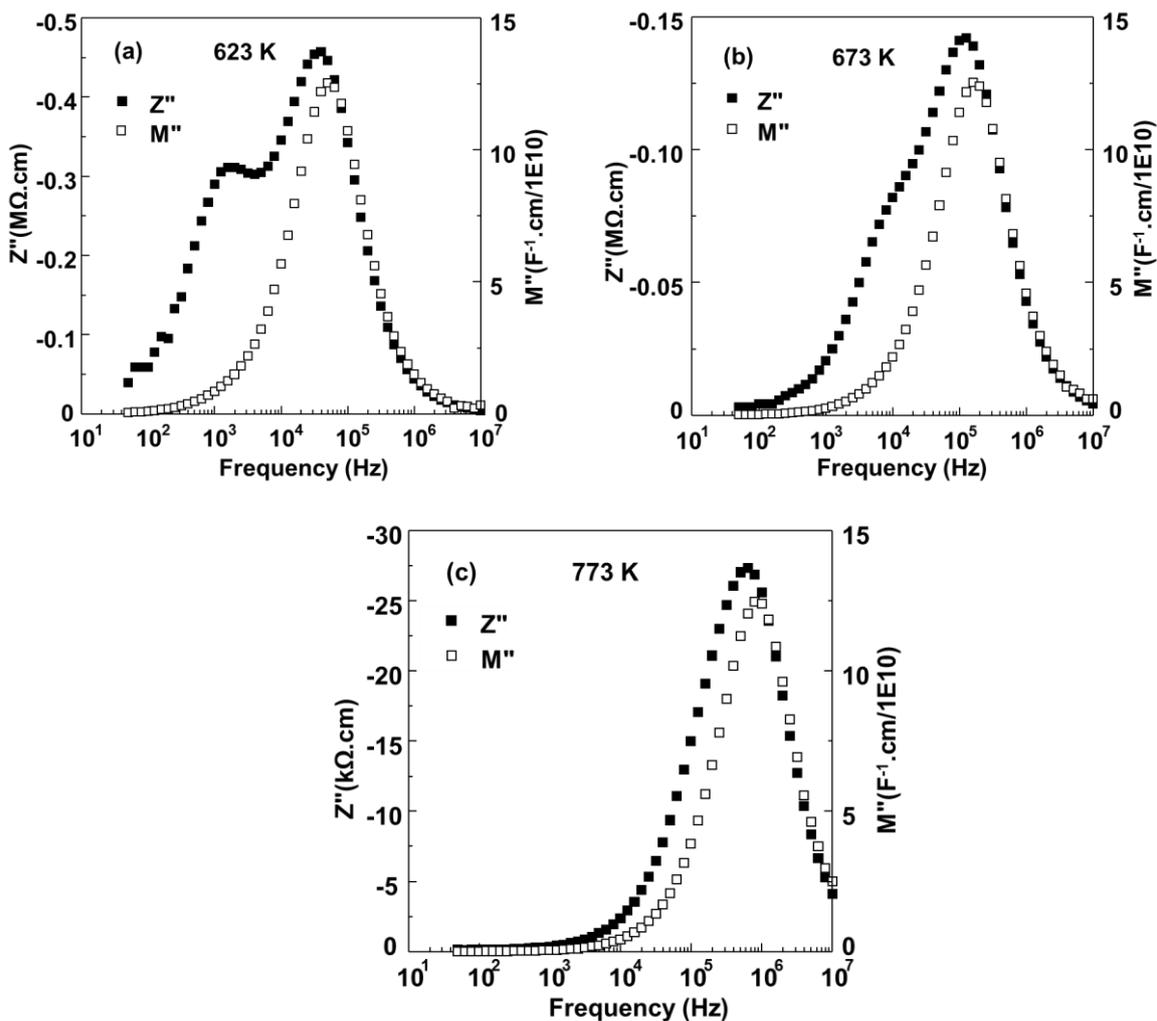
Figure 3.10 Combined of –Z" and M" spectroscopic plots of $Bi_{12}SiO_{20}$ at (a) 623 and (b) 673 and (c) 773 K.

3.2.3 Equivalent Circuit Analysis for High Temperature IS Data (573 – 798 K)

In general, for many electro-ceramic materials, IS data are analysed based on the brick layer model, which distinguishes different microstructural regions by the assumption that uniformly-sized thick grain cubes (i.e. low C'_g ~ pF cm^{-1}) are separated by thin grain boundaries (i.e. high C'_{gb} ~ nF cm^{-1}). Ideally each electrically distinct region gives rise to a semicircular arc in the Z* plot, which is modelled by a parallel RC element. The overall circuit is made up of many parallel RC elements connected in series. The assignment of each semicircular arc is based on the magnitude of the capacitance as each arc corresponds to an individual region with a different thickness. Each region has a characteristic relaxation time, τ, = RC (see Chapter 2 for more details). [28]

Five equivalent circuits (A, B, C, D and E), Figure 3.11, were used to model the IS electrical response of $Bi_{12}SiO_{20}$ ceramics by using ZView software.
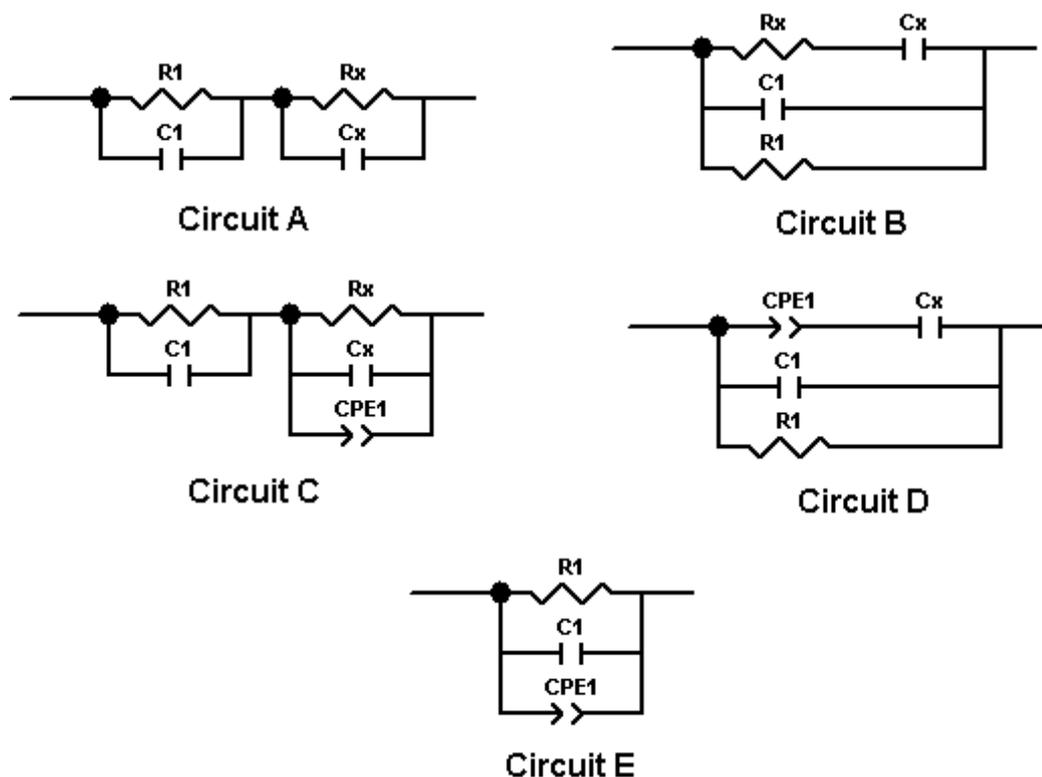
Figure 3.11 Equivalent circuits A, B, C, D and E to model high temperature IS data for $Bi_{12}SiO_{20}$ ceramic. Circuit D is the correct circuit (see Section 3.2.3.4 for details)

Two sets of equivalent circuits (Set 1: Circuit A and B; Set 2: Circuit C and D) have the same overall electrical response for all four plots: impedance, admittance, electric modulus and permittivity. All four equivalent circuits A-D can give rise to two semicircular arcs in the complex impedance plot, Figure 3.8 (a)-(c), and two capacitance plateaux in the capacitance versus frequency plot, Figure 3.9. Therefore, pure mathematical circuit fitting of the electrical response cannot distinguish between the two circuits in each set; although the intercept values of R_1, C_1, R_x and C_x obtained from Circuit A and B are very different (see Appendix II for the derivation of relevant equations).

The solution to choose the correct equivalent circuit relies on the basis that all extracted parameters have some physical significance. Among them, Circuit A generally represents an equivalent circuit for a semiconducting bulk ceramic (R_1C_1) with the resistive grain boundary component (R_xC_x). Circuit B represents an equivalent circuit for a "leaky dielectric" material, where the series combination of R_xC_x indicates the relaxation process associated with short-range ordering of dipoles in the electrical field; R_1 indicates the long-range dc conduction and C_1 indicates the crystal lattice polarisation (i.e. the bulk capacitance). Circuit C and D are modified versions with the inclusion of Constant-Phase Element (CPE) in Circuit A and B, respectively.

3.2.3.1 Circuit A
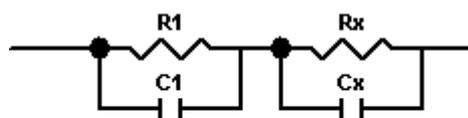
Circuit A

Assume that Circuit A is the correct equivalent circuit, with two series-connected parallel RC elements: R_1C_1 and R_xC_x representing the bulk and grain boundary components, respectively. The values of R_1, C_1, R_x and C_x were firstly estimated by hand-fitting of the data using ZView software. The values of R_1 and C_1 can be extracted from the high frequency semicircular arc in the Z* plot, as an example see the IS data at 673 K in Figure 3.12. R_1 was determined from the intercept of the arc on the Z' axis whereas C_1 was calculated using the

relation '$\omega R_1 C_1 = 1$, where $\omega = 2\pi f_{max}$' at the Z" peak maximum of the semicircle. R_x can be subtracted from the total resistance (i.e. $R_x = R_T - R_1$). C_x was then obtained by the same relation '$\omega R_x C_x = 1$, where $\omega = 2\pi f_{max}$' at the Z" peak maximum of the low frequency arc. The final estimated hand-fitting values were $R_1 = 3.07 \times 10^5$ Ω.cm, $C_1 = 4.11 \times 10^{-12}$ F.cm^{-1}, $R_x = 1.23 \times 10^5$ Ω.cm and $C_x = 1.3 \times 10^{-10}$ F.cm^{-1}. However, the C_x plateau in C' spectroscopic plot was 1.01×10^{-11} F.cm^{-1}, which differs from the hand-fitting C_x values by almost one order of magnitude. In addition, the rapid decrease in magnitude of the C_x plateaux with increasing temperature, Figure 3.9, made the assignment of the low frequency component to be problematic. The interpretation of the low frequency element as a grain boundary response with a temperature-dependent capacitance seems to be physically unreasonable. Therefore, Circuit A was not correct as it cannot explain the physical significance for the low frequency component in the Z* plots.
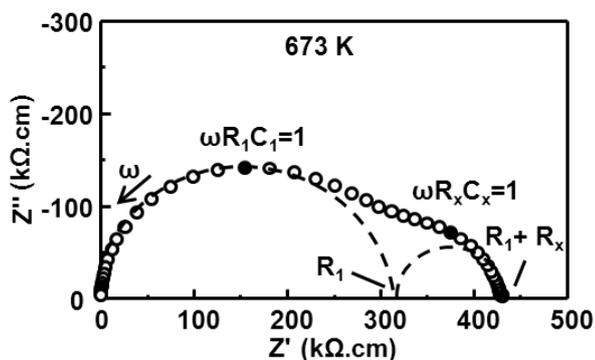
Figure 3.12 Z* plot of Bi$_{12}$SiO$_{20}$ at 673 K.

3.2.3.2 Circuit B
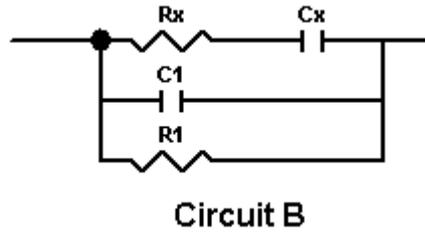
Circuit B

Circuit B is a typical equivalent circuit to model dielectric relaxation behaviour in materials. The series combination of R_x and C_x is known as a Cole-Cole branch which is used to describe interactions e.g. dipole-dipole, or lattice relaxations in the structure.[29] R_1 represents the long-range dc conduction and C_1 represents the bulk capacitance.

Circuit fitting using Circuit B is shown in Figure 3.13. Circuit B almost gave a good fit to the higher frequency semicircular arc in the Z* plots, but over-estimated the lower frequency semicircular arc, Figure 3.13 (a). The poorly fitted lower frequency semicircular arc in the Z* plot also exhibited poorly fitted results in other spectroscopic plots, such as in Figure 3.13 (b) C', (c) Y', (d) tan δ, and (e) combined -Z" and M". This indicates a distributed impedance component – "constant-phase element" (CPE) should be included to Circuit B to model this frequency-dependent region, or alternatively the non-ideal Debye response with a distribution of relaxation times. The impedance of a CPE (Z*$_{CPE}$) is, Equation 3.1[29]:

$$Z^*_{CPE} = [A(j\omega)^n]^{-1} = [A\omega^n(\cos(n\pi/2)+j\sin(n\pi/2)]^{-1} \qquad (3.1)$$

where A and n are constants and are frequency independent. A CPE describes the non-ideal relaxation behaviour of an ideal (pure) capacitor for $n = 1$ and an ideal resistor for $n = 0$.
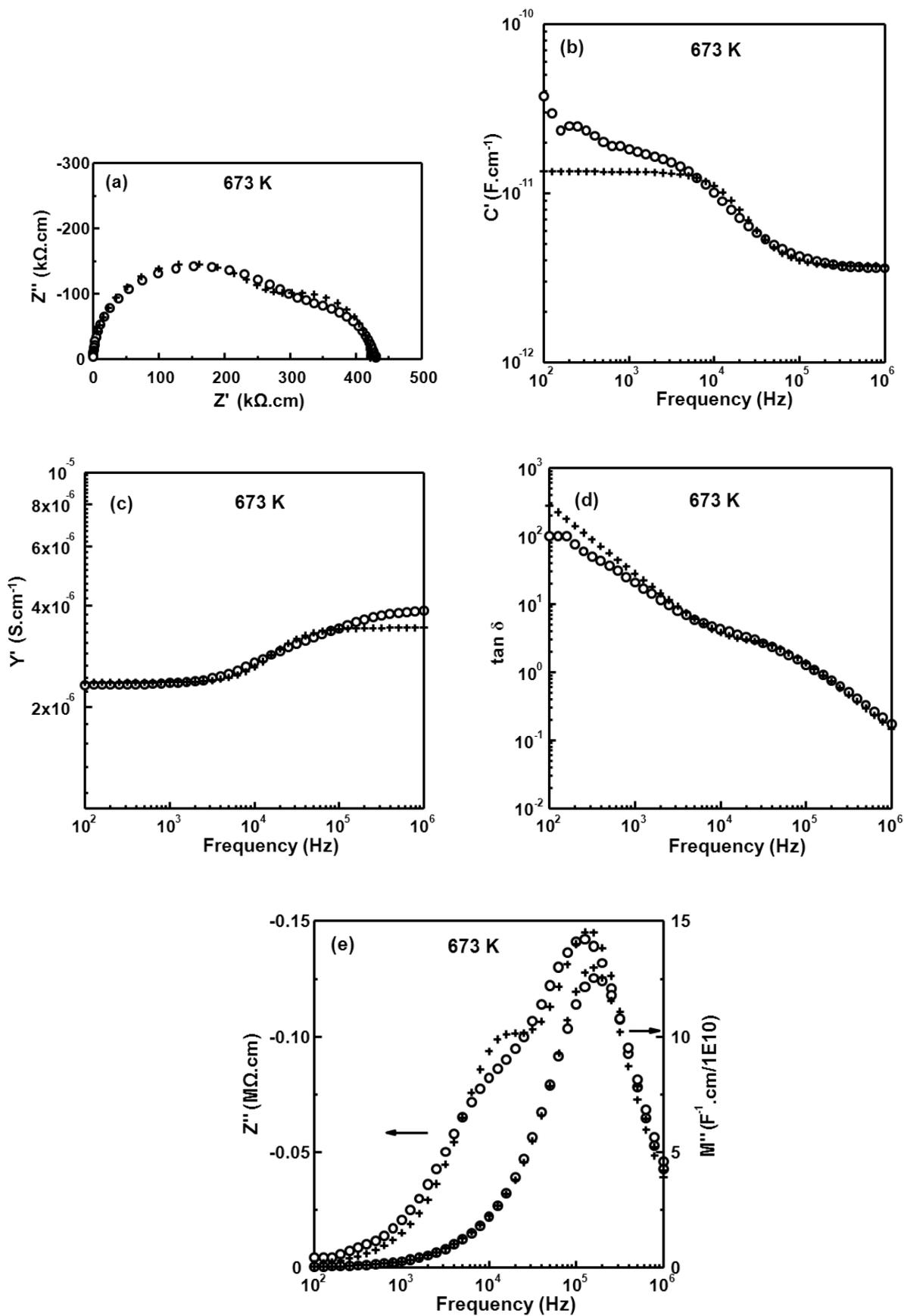
Figure 3.13 (a) Impedance Z* plot and spectroscopic plots of (b) C', (c) Y', (d) tan δ and (e) −Z" and M" of $Bi_{12}SiO_{20}$ measured at 673 K (open symbols) and the best-fit results (cross

symbols) for Circuit B.

3.2.3.3 Circuit C
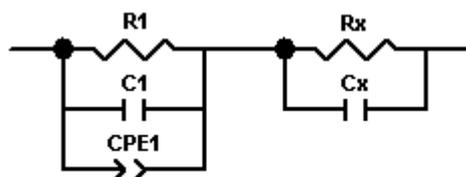
Circuit C

Circuit C is a modified version of Circuit A with the inclusion of the 'constant-phase element' (CPE) in this circuit. Both circuits C and D gave good fits to the Z* plot and –Z"/M" spectroscopic plot over the fitted frequency range from 100 to 10^6 Hz, e.g. at 673K, Figure 3.14 (a) and (e). However, circuit C is inadequate to fit the low-frequency plateau of the C' spectroscopic plot and the corresponding high-frequency plateau of the Y' spectroscopic plot, Figure 3.14 (b) and (c). The fitting parameters of using circuit C at 673 K were: $R_1 = 1.8 \times 10^7$ Ω.cm, $C_1 = 3.8$ pF.cm^{-1}, $R_x = 4.9 \times 10^6$ Ω.cm, $C_x = 3.9 \times 10^{-11}$ F.cm^{-1} and CPE1 $n = 0.35$ and $A = 4.1 \times 10^{-9}$ S.s^n. The assignment of each semicircular arc in circuit C is based on the magnitude of fitted capacitances C_1 and C_x. Therefore, C_1 and C_x correspond to the capacitance of the bulk and grain boundary regions, respectively and R_1 and R_x, the bulk and grain boundary resistance, respectively. Inclusion of the CPE1 in parallel with R_1C_1 allows accurate fitting to describe a frequency-dependent bulk response of the sample. However, the poor fitting of the low-frequency plateau in the C' spectroscopic plot, Figure 3.14 (b), indicates circuit C is not adequate to describe this highly frequency-dependent 'grain boundary' behaviour. A second CPE component in parallel with R_xC_x might be the solution to improve the fitting. This could lead to indistinguishable fits between circuit C and D, although the fitting values of R_1, C_1, R_x and C_x are different. The only possible method to distinguish between circuit C and D relies on the basis that all parameters have a physical meaning. Circuit C is a modified version of circuit A, which generally represents an equivalent circuit for a semiconducting bulk ceramic (R_1C_1) with a resistive grain boundary (R_xC_x). Circuit D is modified from circuit B, which describes the behaviour of 'leaky dielectrics' with the parallel combination of R_1 and C_1

representing the long-range dc conduction of the bulk component, and the series combination of R_x and C_x (or CPE and C_x) representing the short-range reorientation of dipoles in an electric field. CPE is used here as a substitute for R_x to model the non-ideal frequency-dependent dielectric relaxation behaviour, which is a consequence of as the local polarisation fluctuations in the framework of the sillenite structure. (See evidence in section 3.2.4, Raman spectroscopy results). Therefore, circuit C is not the best equivalent circuit to describe the electrical response of $Bi_{12}SiO_{20}$ ceramic.
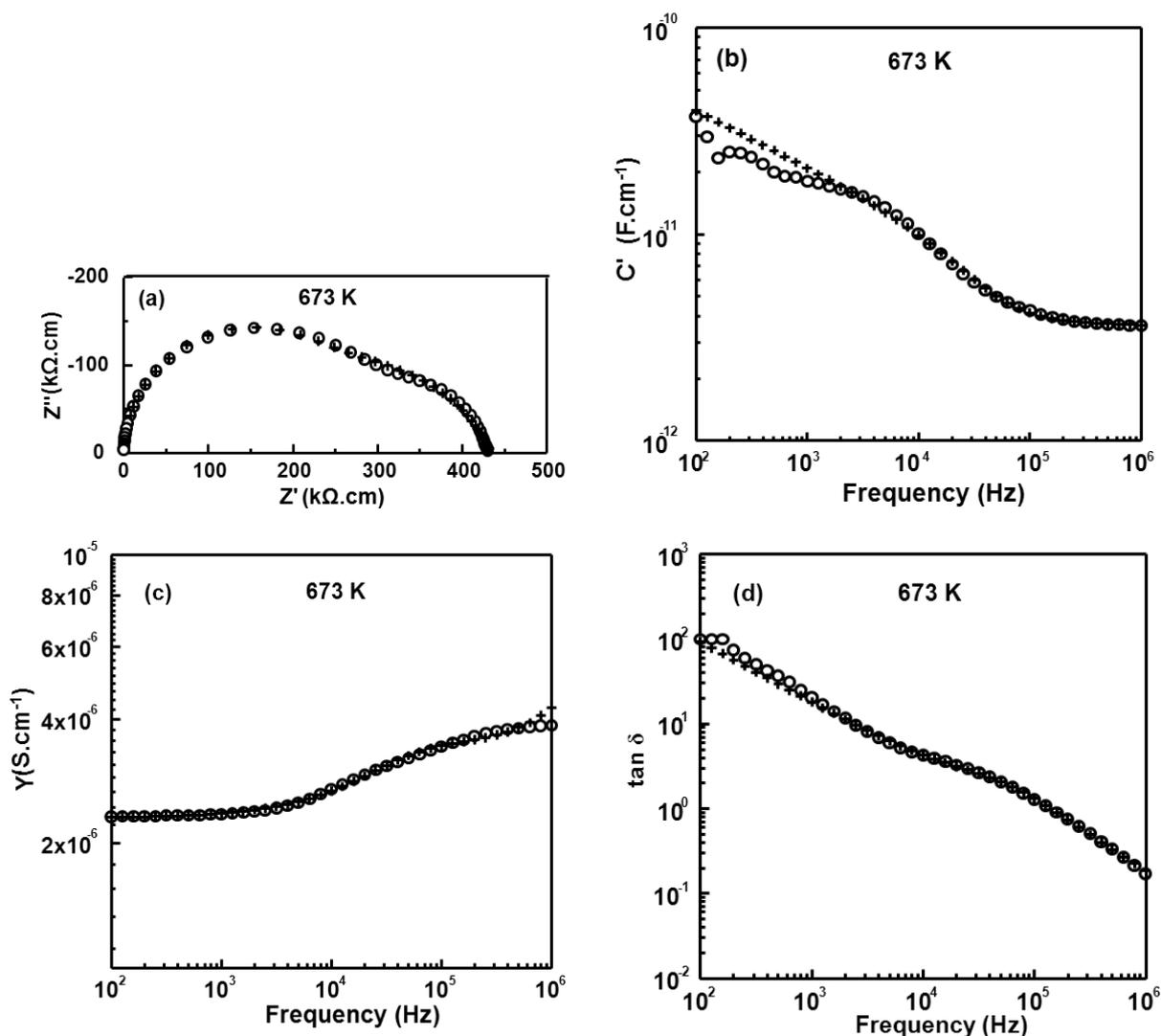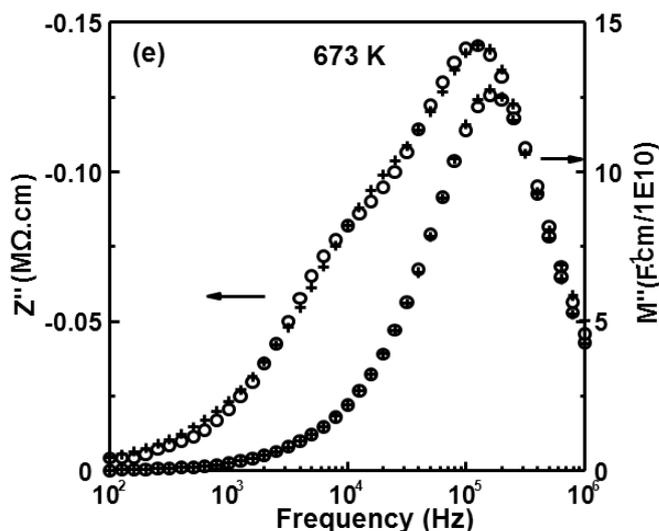
Figure 3.14 (a) Impedance Z* plot and spectroscopic plots of (b) C', (c) Y', (d) tan δ and (e) −Z" and M" of $Bi_{12}SiO_{20}$ measured at 673 K (open symbols) and the best-fit results (cross symbols) for Circuit D.

3.2.3.4 Circuit D
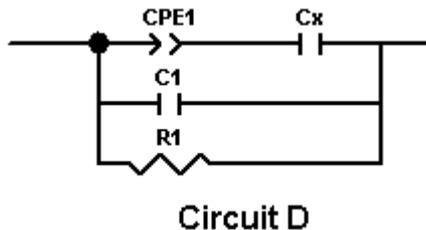
Circuit D

Circuit D is a modified version of Circuit B with the replacement of R_x with a Z_{CPE} in series with C_x, as the fitted R_x is too large to measure and eliminated from this circuit. Circuit D gave the best fit with reasonable physical significance to all the data over the fitted frequency range from 100 to 10^6 Hz, e.g. at 673 K, Figure 3.15. The final fitting values at 673 K were R_1 = 4.3×10^5 Ω.cm, C_1 = 3.6 pF.cm^{-1}, C_x = 1.5×10^{-11} F.cm^{-1} and CPE1 n = 0.15 and A = 1.6×10^{-7} S.s^n. The fitted parameters showed reasonable values: R_1 was the total resistance of the sample, indicating both the high frequency and low frequency semicircles contribute to the bulk component of the sample as assigned by a parallel $R_1 C_1$ element. C_1 has a value of pico-farads, which is a typical bulk capacitance ($\varepsilon \sim 40$). In the series combination of CPE and C_x, a CPE with n = 0.15 (in between of 0 and 1) indicates a frequency-dependent capacitor

and a mostly-influenced resistor, therefore it substitutes the R_x response in Circuit B. The final

fitting values of R_1, C_1, C_x and CPE (A and n) by using Circuit D are listed in Table 3.3.
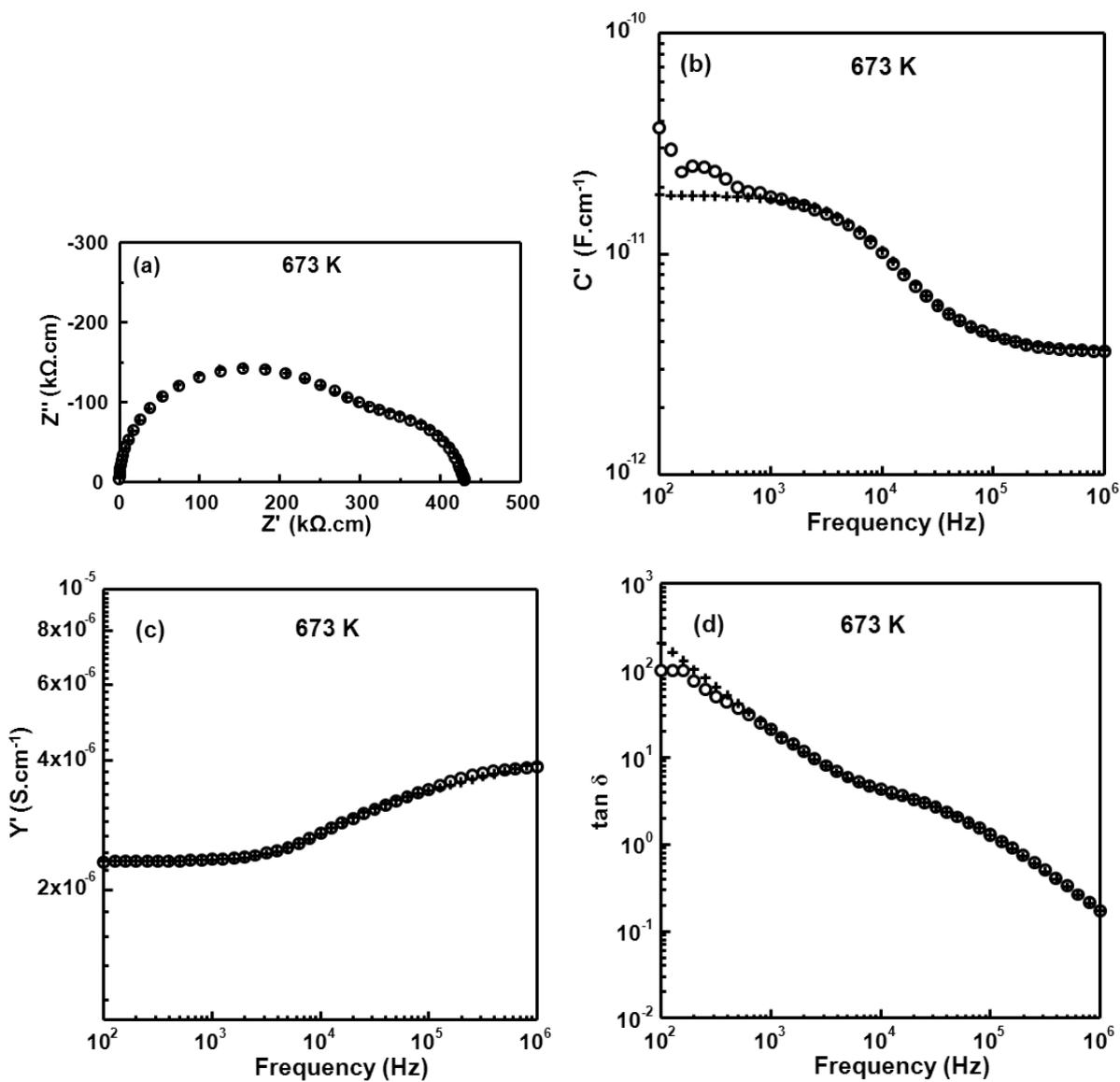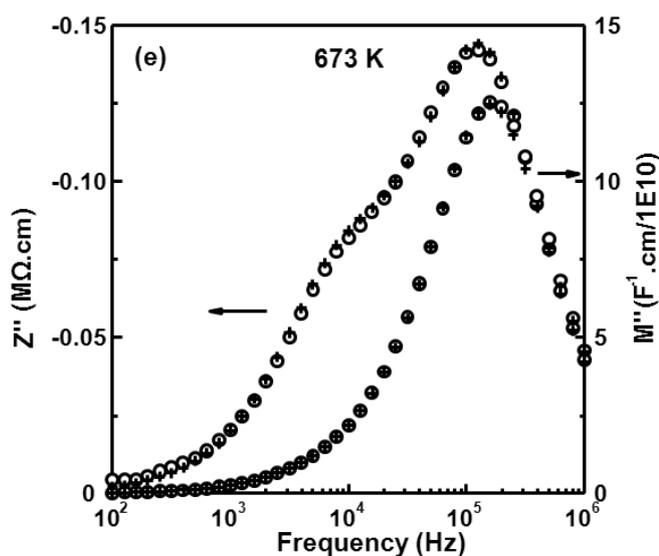
Figure 3.15 (a) Impedance Z* plot and spectroscopic plots of (b) C', (c) Y', (d) tan δ and (e) −Z" and M" of $Bi_{12}SiO_{20}$ measured at 673 K (open symbols) and the best-fit results (cross symbols) for Circuit D.

3.2.3.5 Circuit E
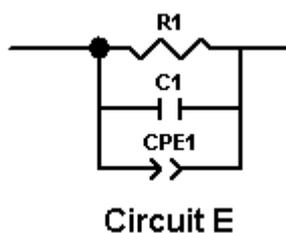
Circuit E is a common equivalent circuit to model the non-ideal Debye response of the bulk component. It is mentioned here as the impedance data of the sample showed only bulk-type electrical behaviour. However, it cannot be used to model the dielectric relaxation behaviour of this sample, as it displayed two capacitance plateaux in C' spectroscopic plots whereas Circuit E gives rise to a single plateaux in such plots.

3.2.3.6 Summary of Equivalent Circuit Analysis

Five equivalent circuits, Figure 3.11, were analysed and used to model the IS data of $Bi_{12}SiO_{20}$ ceramics. Circuit D gave the best fit and showed reasonable physical significance of all parameters.

Both of the semicircles in the Z* plots are related to the bulk response of the sample. The appearance of the lower frequency arc overlapping with the higher frequency arc can be explained on the basis of two mean time constants initially greater than two orders of magnitude apart at 573–723 K to give well-resolved arcs and then within two orders of magnitude above 773 K to show a single, distorted arc. The direct evidence of the relaxation behaviour was observed from the real capacitance spectroscopic plot by the appearance of two capacitance plateaux. It was also shown in a slightly broadened M" Debye peak with its FWHM of 1.29 decades, which exceeds the theoretical value of 1.14 decades (i.e. $\log(\frac{2+\sqrt{3}}{2-\sqrt{3}})$).

To describe the frequency-dependent non-ideal IS reponse, a CPE component must be included in the equivalent circuit. A series combination of the capacitance C_x and CPE are used to model dielectric relaxation behaviour, which is assigned as the local polarisation fluctuations in the framework of the sillenite structure. (See evidence in section 3.2.4, Raman spectroscopy results). Generally the appearance of a dielectric dispersion below the optical phonon frequency range (i.e. terahertz (THz)) is a signature of some disorder in the dielectric material (with the exception of piezoelectric resonances in piezoelectric materials).[30] IS data revealed the ideal stoichiometric sillenite $Bi_{12}SiO_{20}$ with geometrically regular tetrahedra $MO(3)_4$ to, surprisingly, exbihit dielectric relaxation behaviour, which is more usually found in disordered solids such as dipolar glasses[31] and relaxor ferroelectrics[22]. The sillenite framework is well-known to consist of highly distorted Bi^{3+} octahedra caused by the specific electronic configuration of the Bi^{3+} cation with its lone pair of electrons. The irregular octahedron has one vertex missing and is occupied by the lone electron pairs of the Bi^{3+} cation, and can lead to various random oriented electric dipole moments. Similar to dipolar glasses, the long-range crytalline periodicity is still maintained, and only local environments experience short-range structural distortion. This local disorder creates random local potential

barriers with different potential heights which influences the charge storage and dielectric losses. The assoicated activation energy of relaxation obeys the Arrhenius format only under the assumption of having a uniform potential barrier height. However, in reality the activation energy of relaxation should no longer be the same for all species. This results in a permittivity and dielectric loss dispersion region compared with a single, ideal "Debye" type behaviour.[22]

The sample conductivity can be shown in the real admittiance spectroscopic plot, Y' versus frequency, with the expression of Y', Equation 3.2[32]:

$$Y' = R^{-1} + A\omega^n(\cos n\pi/2) \qquad (3.2)$$

where generally R^{-1} indicates a frequency-independent dc conductivity at low frequency and a frequency-dependent ac conductivity region which obey power law behaviour with n signifying the gradient of the slope and A extracted from expression $\log[A\cos(n\pi/2)]$ at log Y' intercept at $\omega = 1$ Hz, Figure 3.16 (a).[32]
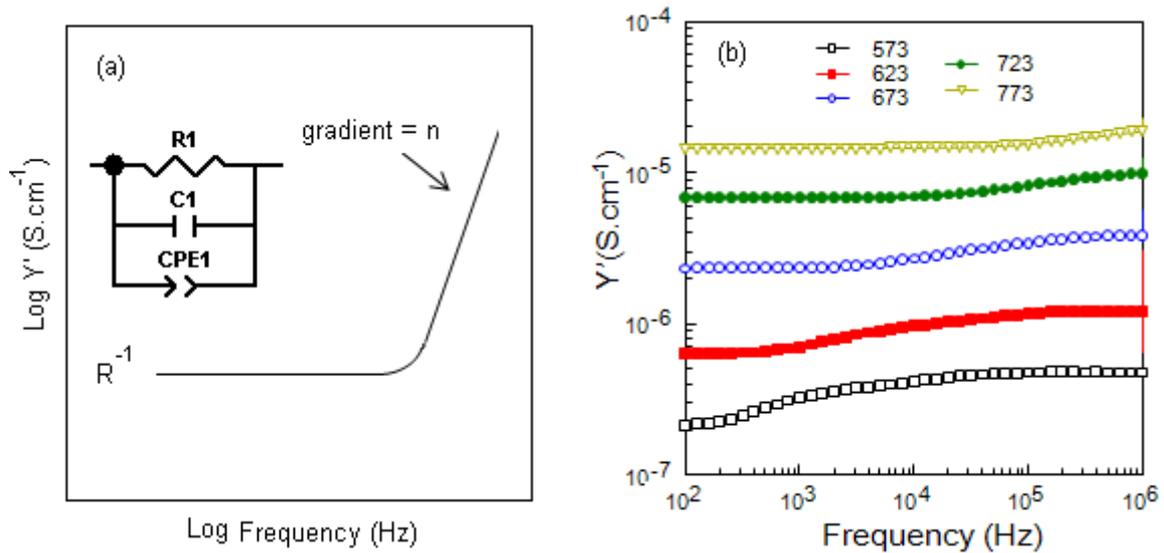
Figure 3.16 Log Y' spectroscopic plot (a) for a typical equivalent circuit of parallel R_1, C_1 and CPE components and (b) log Y' spectroscopic data for $Bi_{12}SiO_{20}$ between 573 and 773 K.

However, the Y' spectroscopic plot in our case, Figure 3.16 (b), shows 3 distinct regions: (1) a frequency-independent plateau attributed to the dc conductivity, R^{-1}, at low frequencies; (2) a frequency-dependent power law behaviour at intermediate frequencies and (3) a unknown

frequency-independent plateau at high frequency. Corresponding to the capacitance data from the same data set, Figure 3.9; (1) a frequency- independent plateau at high frequency was observed and attributed to the bulk capacitance of the sample, C_1; (2) a frequency- dependent plateau which rises towards lower frequency and assigned as the dielectric relaxation response, C_x; (3) an unknown continued rise towards low frequency, which was reported due to space-charge polarization by Valant and Suvorov [22]. In the Y' spectroscopic plot, Figure 3.16 (b), at higher temperatures (e.g. 773 K) the dc plateau and power law behaviour dominate the data, whereas at lower temperatures (e.g. 573 K) the unknown frequency-dependent plateau dominates. The unknown Y' plateau at high frequency indicates complex ac conductivity behaviour occurs and is possibly associated with different activation energies in the dielectric relaxation process. The origin, either a temperature-dependent gradual release of the freezing dipolar moments or some other new relaxation behaviour is still unknown. Further work using higher frequency measurements might be useful to investigate this anomaly.

An Arrhenius plot of the long-range dc (bulk) conductivity (σ_{b_R1}) of the $Bi_{12}SiO_{20}$ ceramic, Figure 3.17, is extracted from the fitting values of R_1 by using Circuit D and the associated activation energy (E_a) is 0.84(1) eV.
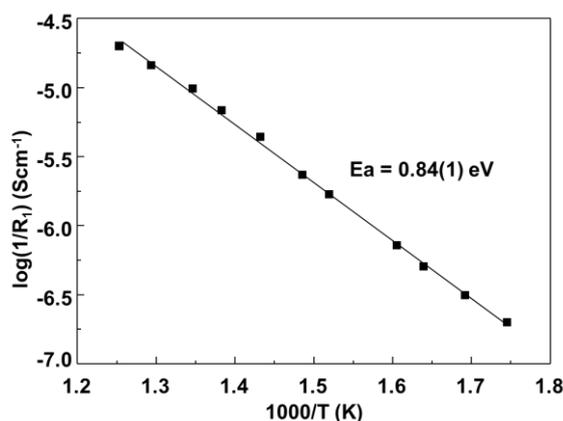
Figure 3.17 Arrhenius plot of bulk conductivity for $Bi_{12}SiO_{20}$.

Table 3.3 Fitting data of Equivalent Circuit D for $Bi_{12}SiO_{20}$ from 573 to 773 K. Errors associated with the fitted circuit parameters R_1, C_1, C_x, A and n are $< \pm 0.4\%$, $< \pm 0.3\%$, $< \pm 1.5\%$, $< \pm 8\%$ and $< \pm 2.5\%$, respectively.

Temperature (K)	R_1 (Ω cm)	C_1 (F cm^{-1})	C_x (F cm^{-1})	A (Ω^{-1} cm^{-1} rad^{-1})	n
573	5030700	3.54×10^{-12}	6.32×10^{-11}	6.01×10^{-8}	0.12
591	3192800	3.54×10^{-12}	4.73×10^{-11}	6.32×10^{-8}	0.13
610	1971700	3.53×10^{-12}	3.50×10^{-11}	7.05×10^{-8}	0.14
623	1388800	3.53×10^{-12}	3.11×10^{-11}	7.91×10^{-8}	0.15
658	596350	3.52×10^{-12}	1.75×10^{-11}	9.80×10^{-8}	0.17
673	427730	3.51×10^{-12}	1.59×10^{-11}	1.11×10^{-7}	0.18
698	226740	3.51×10^{-12}	1.07×10^{-11}	1.40×10^{-7}	0.19
723	145860	3.51×10^{-12}	7.64×10^{-12}	1.63×10^{-7}	0.20
743	101940	3.51×10^{-12}	5.54×10^{-12}	1.84×10^{-7}	0.20
773	69007	3.48×10^{-12}	4.33×10^{-12}	1.60×10^{-7}	0.23

The temperature-dependence of the bulk capacitance C_1 and the lattice relaxation capacitance C_x are shown in Figure 3.18 for a temperature range from 573 to 798 K. C_x is more temperature-dependent than C_1. The magnitude of C_1 is temperature-independent with values ~ 3.5 pF.cm^{-1} ($\varepsilon_r \sim 40$-39) from 573-798 K, whereas the magnitude of C_x decreases rapidly with increasing temperature from 6.32×10^{-11} Fcm^{-1} ($\varepsilon_r \sim 714$) at 573 K to 3.37×10^{-12} Fcm^{-1} ($\varepsilon_r \sim 38$) at 798 K.
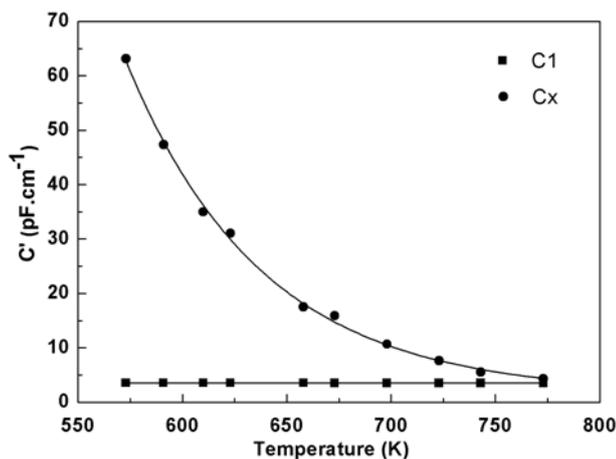
Figure 3.18 Temperature-dependence of the real capacitance C_1 (■) and C_x (●) from fitted values.

3.2.4 Raman Spectroscopy (298 – 773 K)

Raman Spectroscopy (RS) of a $Bi_{12}SiO_{20}$ pellet was performed from 298 to 773 K to investigate any local structural variation with increasing temperature. Raman spectra of $Bi_{12}SiO_{20}$ at 298 and 773 K were selected and shown in Figure 3.19 and the corresponding Raman peak assignments based on the literature[33, 34] are listed in Table 3.4. The peak intensity of the Raman spectra was normalized by the strongest peak of ~ 530 cm^{-1} (line 15) for the RT measurement. Two important features can be captured with increasing temperature: (1) the Raman peak shape at ~ 530 cm^{-1} (representing the breathing of framework O1 atoms) became broader; and (2) the Raman peak height at ~ 88 cm^{-1} (representing the elongating vibrations of framework Bi-O3, Bi-O2 vibrations) became larger. The associated peak shape and height, i.e. the Full Width Half maximum (FWHM) can be used to evaluate the degree of ordering: samples with a higher degree of ordering generally exhibit narrower peak widths and smaller values of FWHM. The FWHM of the ~530 cm^{-1} peak at 298 and 773 K are 13.2 and 33.7 cm^{-1}, respectively, whereas the FWHM of the ~ 88 cm^{-1} peak at RT and 773 K are the same with a value of 7.5 cm^{-1}. The broadening and downshifting of the ~538 cm^{-1} peak with increasing temperature indicates the interatomic distances between Bi and O1 atoms are getting larger and the framework of the structure is becoming highly disordered. This is evidence to suggest the dielectric relaxation modelled by the IS equivalent circuit is due to vibrations of a distorted sillenite framework.
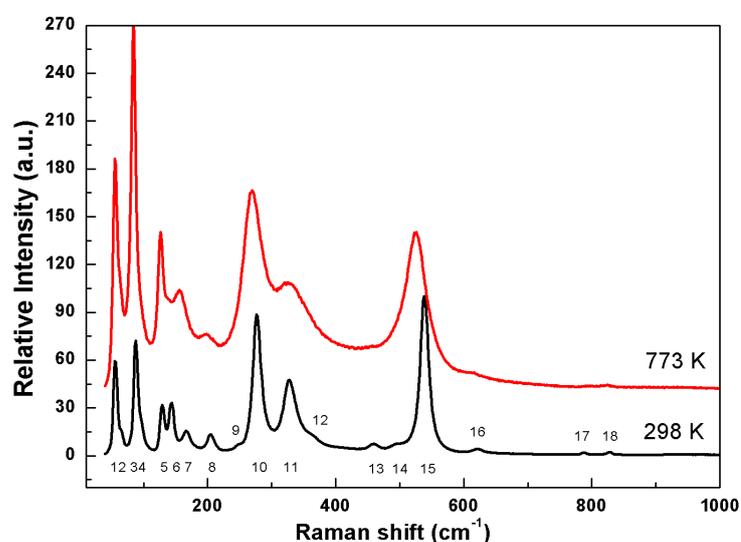
Figure 3.19 Raman Spectra from the same grain of a $Bi_{12}SiO_{20}$ pellet at 298 and 773 K. Peak

intensities are normalized by the peak at ~ 530 cm^{-1} for the RT measurement.
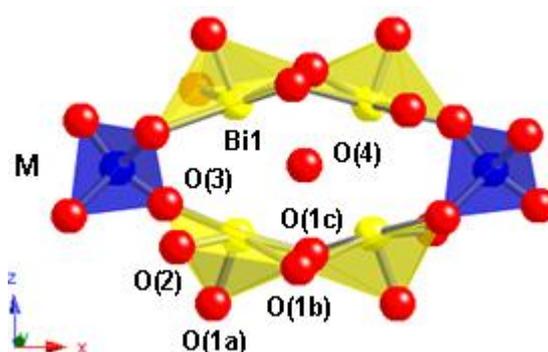
Figure 3.20 The correlated crystallographic sites in the sillenite structure.

Table 3.4 Raman peak assignments of stoichiometric sillenite $Bi_{12}SiO_{20}$.

Line No.	Raman Shift (cm^{-1})	Mode[33]	Type of Vibrations[33, 34]
1	55	F	Bi,O2,O3 and M vibration
2	63	E	Bi,O1,O2 and O3vibrations elongating the cluster along either [100] or [001]
3	88	E	Bi,O2 and O3 vibrations elongating the cluster
4	95	A	Bi-O1 bonds vibration and 'breathing' of O2 atoms
5	129	E	Bi and O2 vibrations elongating the cluster along either [100] or [010]
6	144	A	'breathing' of Bi and O2 atoms
7	166	A	'breathing' of Bi and all O atoms
8	204	F	Bi-O1 stretching & Bi-O2-Bi bending and weak Bi-O1 rocking
9	251	E	Bi-O1 rocking and weak O2 vibrations elongating the cluster along either [100] or [001]
10	276	A	O2 'breathing' and weak Bi-O1 rocking
11	328	A	Bi-O1 rocking and weak O2 'breathing'
12	358	F	O1-Bi-O2 and O1-Bi-O3 bending
13	460	E	O2 vibration elongating the cluster along either [001] or [010] and weak Bi-O1 and Bi-O3 rocking
14	488	F	Bi-O1 stretching and deformation of MO4 tetrahedra
15	538	A	'breathing' of O1 atoms
16	621	E	O3 vibrations elongating the cluster along either [010] or [100] and weak Bi-O1 and Bi-O2 rocking
17	788	A	Symmetric stretching of MO4 tetrahedra
18	829	FTO	Anti-symmetric stretching of MO4 tetrahedra

Figure 3.20 is a section of the sillenite structure to illustrate the correlated crystallographic sites mentioned in Table 3.4. To briefly summarise the peak assignments reported in the literature, lines 1, 3, 5, 6, 8, 10, 11 and 15 (i.e. Raman shifts = 55, 88, 129, 144, 204, 276, 328 and 538 cm^{-1}, respectively) were assigned as Bi-O(1), Bi-O(2) and Bi-O(3) framework vibrations; whereas lines 17 and 18 (i.e. Raman shifts = 788 and 829 cm^{-1}, respectively) were related to vibrations in the MO_4 tetrahedra. The Raman peak positions are inversely proportional to the mass of the groups of bonded atoms; therefore, the vibrational modes of framework Bi polyhedra, BiO_5LP, dominate the Raman spectra at lower frequencies (below ~ 600 cm^{-1}), whereas the vibration modes of the MO_4 tetrahedra occurred at higher frequencies (above ~ 600 cm^{-1}).

The peak intensity of various Raman spectra peaks were normalized to the strongest peak at RT, i.e. ~ 530 cm^{-1} (line 15). However, the strongest peak gradually changes to the one at ~ 88 cm^{-1} (line 3) at 773 K. The intensity of the Raman peak indicates the strength of the correlated vibrations. The intensity ratio of the peaks at ~88 and ~530 cm^{-1} (i.e. Int. 88 cm^{-1}/ Int. 530 cm^{-1}) versus temperature measured from the same grain of the sample is an indicator of the degree of local distortion associate with the framework O(1) atoms as a function of temperature. This is the main contributor for the distorted Bi polyhedra, BiO_5LP for the framework of sillenites, Figure 3.21.
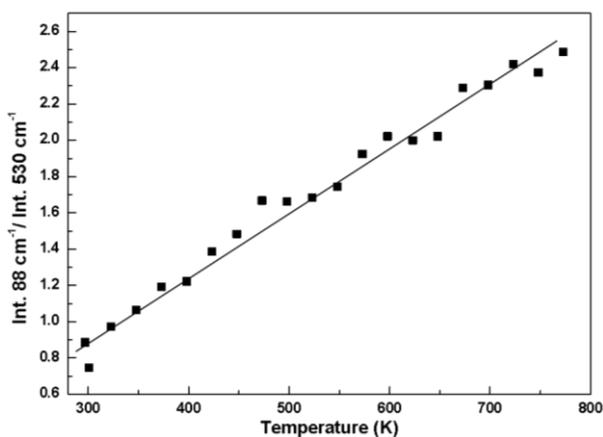
Figure 3.21 The intensity ratio of Raman peak ~ 88 cm^{-1} to peak ~ 530 cm^{-1} versus temperature from the same grain of $Bi_{12}SiO_{20}$ ceramic.

3.2.5 Dilatometry (DIL)

Dilatometry measurements were performed to monitor the change in sample volume over the measured temperature range on the heating (373 to 883 K) and cooling (883 to 373 K) cycles. There was an almost linear volume expansion with a rate of ~ 1.2(1) % with increasing temperature, Figure 3.22, which is consistent with the linear trend extracted from intensity ratio of Raman peak ~88 to 530 cm^{-1}, Figure 3.21.
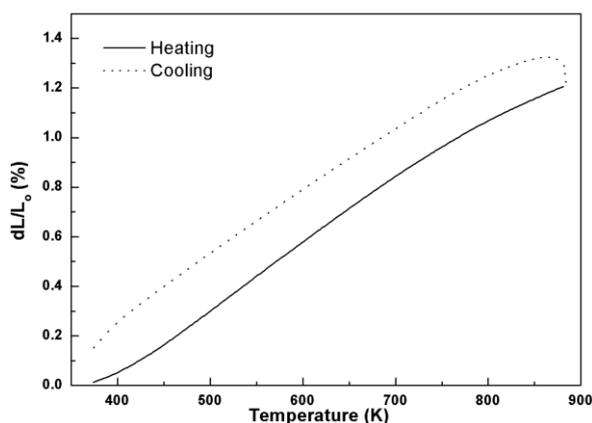
Figure 3.22 DIL trace of $Bi_{12}SiO_{20}$ pellet from 373 to 883 K.

3.2.6 Nuclear Magnetic Resonance (NMR) Spectroscopy

NMR spectroscopy was performed by Dr. John V. Hanna from University of Warwick to provide detailed information about the tetrahedral environment of $Bi_{12}SiO_{20}$. Isotope ^{29}Si one pulse spectra of $Bi_{12}SiO_{20}$ were carried out under a magnetic field of 7.05 T (5 kHz MAS). One peak with a chemical environment of SiO_4 was detected, Figure 3.23 and Table 3.5, which proves the appearance of geometrically regular MO_4 tetrahedra in $Bi_{12}SiO_{20}$. The NMR spectra with a regular, undistorted MO_4 tetrahedron indirectly suggests that the dielectric relaxation of IS data arises from the distortion in the framework of sillenite structure.

Table 3.5 Summary of NMR spectra of isotope ^{29}Si from $Bi_{12}SiO_{20}$.

Peak	Isotropic Shift (ppm)	Width (ppm)	Environment
1	-78.3	7.3	SiO_4
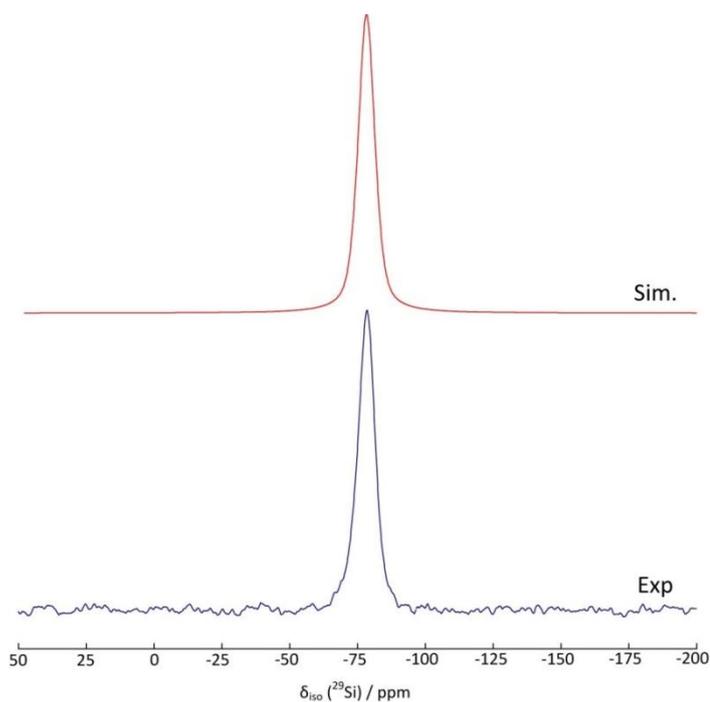
Figure 3.23 Simulated (red) and Experimental (black) NMR spectra of isotope ^{29}Si one pulse spectra of $Bi_{12}SiO_{20}$ carried out at 7.05 T (5 kHz MAS).

3.3   Discussion

Investigation of the stoichiometric sillenite $Bi_{12}SiO_{20}$ showed it to exhibit similar microwave dielectric properties as that reported by Valant and Suvorov[17], which can be used as a suitable material in LTCC applications. XRPD results, Figure 3.3, showed the synthesized $Bi_{12}SiO_{20}$ ceramic to be single-phase with all reflections indexed in the space group I23. The refined lattice parameter, a = 10.10345(7) Å was very similar to the reported lattice parameter, a = 10.109(1) Å[17]. DSC results, Figure 3.4, revealed two pairs of reversible peaks that occurred at ∼ 920 and 1103 K, respectively, which indicates a plausible reversible $\gamma \rightarrow \beta \rightarrow \delta \rightarrow \beta \rightarrow \gamma$[21] phase transition occurring in this sample. XRPD data confirmed the sample retained the same sillenite phase on post-DSC measurements.

The variation of ε_r with temperature for $Bi_{12}SiO_{20}$ ceramic (pellet relative density ∼ 90%), Figure 3.7 (a), revealed the same frequency dispersive region above room temperature as

found in M^{2+}/M^{3+} sillenites (Chapter 4). Similar relaxation behaviour is not unique in sillenites, but is a common behaviour that occurs in other disordered systems, such as fluorite δ-Bi_2O_3 solid solutions[23], dipolar glasses[30] and relaxor ferroelectrics[21].

IS data revealed the same frequency-dispersive relaxation behaviour of the sample. Direct evidence was obtained from the C' spectroscopic plots by the appearance of two capacitance plateaux: a frequency-independent high frequency plateau and a frequency-dependent low frequency plateau, Figure 3.9. These two capacitance plateaux correspond to the two overlapping semicircular arcs in the Z* plots and two peaks in the −Z" spectra from −Z"/M" spectroscopic plots. The frequency-independent high frequency capacitance plateau, C'_{high}, and the frequency-dependent low frequency capacitance plateau, C'_{low}, were associated with the bulk and the lattice relaxation responses of the sample, respectively. Both of the semicircles in the Z* plots are related to the bulk response of the sample. The appearance of the lower frequency arc overlapping with the higher frequency arc can be explained on the basis of two mean time constants that are initially greater than two orders of magnitude apart at 623–673 K to give well-resolved arcs and then within two orders of magnitude at/above 773 K to show a single, distorted arc.

Five equivalent circuits, Figure 3.11, were analysed and used to model the IS data of $Bi_{12}SiO_{20}$ ceramics. Among them, Circuit D gave the best fit and showed reasonable physical significance of all parameters. Circuit D is a modified version of a standard circuit (Circuit B) for dielectric relaxation processes, where the series combination of Z_{CPE} and C_x indicates relaxation process(es) associated with short-range orientation of dipoles in the electrical field; R_1 indicates the long-range dc conduction and C_1 indicates the bulk capacitance. The CPE in the circuit is not only used as a fitting parameter, but also represented the frequency-dispersive phenomenon by the parallel connection of a frequency-dependent capacitor and resistor. Although the physical origin of the CPE is still uncertain, it seems that it is correlated with the frequency-dependent reorientation of the short-range dipole moments in this case.

Figure 3.18 shows the temperature dependence of extracted C_1 and C_x from the fitted values in Table 3.3. The magnitude of C_1 is temperature-independent whereas that of C_x is

strongly temperature-dependent. The peculiarity of the rapid decrease in magnitude of C_x from 6.32×10^{-11} Fcm^{-1} ($\varepsilon_r \sim 714$) at 573 K to 3.37×10^{-12} Fcm^{-1} ($\varepsilon_r \sim 38$) at 798 K, indicates a decrease in the polarization from the polar nanodomains in the bulk relaxation. It is noteworthy that the fitted values of C_x are underestimated at higher temperatures, e.g. the fitted C_x ($\sim 3.37 \times 10^{-12}$ Fcm^{-1}) is even smaller than C_1 ($\sim 3.48 \times 10^{-12}$ Fcm^{-1}) at 798 K. The reason is due to the increasing influence of the capacitive nature and the decreasing influence of the resistive nature of the CPE, where n increases from $\sim$ 0.12-0.24 at 573-798 K. The trend of C_x is different in other divalent/trivalent/pentavalent cation doped sillenites (Chapters 4, 5 and 6); a detailed study of C_x may provide information on the local structural distortions in sillenites.

The origin of the relaxation behaviour is proved to arise from the distorted framework structure by Raman Spectroscopy measurements. The Raman peak at $\sim$ 530 cm^{-1} designating the framework vibration became broader with increasing temperature: the FWHM of the peak was 13.2 and 33.7 cm^{-1} at 298 and at 773 K, respectively, which indicates the sillenite framework exhibits a higher degree of disordering and elongation of the Bi-O(1) bond. The increasing of Bi-O1 bond length with temperatures might be due to the significant increasing of Bi-O1(b) and Bi-O1(c) by a plausible expansion of the O(4) site in the void of the framework as the cell expands on heating. However, the Raman peak at $\sim$ 89 cm^{-1} (associated with the elongating vibrations of the framework Bi-O3, Bi-O2 vibrations [33]) remains unchanged with increasing temperature, indicating changes in the Bi-O3 and Bi-O2 bond lengths are negligible. The intensity ratio of the two strongest peaks $\sim$88 and $\sim$530 cm^{-1} at 298 and 773 K, respectively, (i.e. Int. 88 cm^{-1}/ Int. 530 cm^{-1}) versus temperature measured from the same grain of the sample is an indicator of the degree of distortion of the local framework associated with O(1) atoms with temperature, Figure 3.21. Dilatometry, Figure 3.22, showed a linear volume expansion with a rate of $\sim$ 1.2(1) % from 298 to 883 K, showing the change in average structure to be regular as a function of temperature.

By combined consideration of the IS data (the rapid decrease in magnitude of C_x indicates a decrease in the polarisation from the bulk relaxation) and the Raman spectra, a structural suggestion can be proposed for local dipolar fluctuations. Assuming the O(4) site is expanding

with increasing temperatures as the average volume of the cell increases, the Bi-O1(b) and Bi-O1(c) bond lengths increase and the bond angles between O1(a)-Bi-O1(b) and O1(a)-Bi-O1(c) decrease, whereas Bi-O(2) and Bi-O(3) bond length are almost unchanged, then Bi atomic shifts towards O1(a) atoms can occur to maintain the equatorial plane of the distorted Bi octahedra. The atomic shifts of Bi atoms towards O1(a), i.e. apart from its electron lone pairs (LP), is energetically favoured compared with a distortion associated with O(3) atoms in the SiO_4 tetrahedra. Therefore, it is possible that the local polarisation from the Bi-LP dipole moments in the distorted octahedra, BiO_5LP, decreases with increasing temperature.

3.4 Conclusions

Stoichiometric sillenite $Bi_{12}SiO_{20}$ was successfully synthesized and obeyed Valant and Suvorov's general formula for tetravalent cation doped sillenites (n = 4). The structural symmetry, composition and electrical properties of $Bi_{12}SiO_{20}$ were investigated using XRPD, EDS, microwave dielectric measurements and IS, respectively. The microwave dielectric properties on a 90 % dense $Bi_{12}SiO_{20}$ ceramic, ε_r ~ 36; Q.f ~ 7037 GHz at resonant frequency of 6.83 GHz; τ_f ~ -30 ppm/K, its low sintering temperature (< 900 °C) and chemical compatibility with Ag electrodes confirms $Bi_{12}SiO_{20}$ to be a potential useful material in LTCC applications, which is in good agreement with previously reported data[17]. The measured ε_r was close to that calculated from the Clausius-Mossotti equation (i.e. ε_{r_CM} ~ 41).

$Bi_{12}SiO_{20}$ is catalogued as an 'ideal'-type sillenite: Si^{4+} (ionic radii r = 0.26 Å) form $MO(3)_4$ tetrahedra, which is close to a geometrically regular $MO(3)_4$ tetrahedron (r = 0.31 Å [2]). However, IS measurements revealed $Bi_{12}SiO_{20}$ to exhibit dipolar glass-like relaxation behaviour by the appearance of a frequency-dependent C' plateau at lower frequency, which was successfully modelled by equivalent circuit analysis and the origin of this plateau explained as a dielectric relaxation associated with the framework structure of the sillenite. This is directly proved by Raman Spectroscopy, which showed the vibration of the distorted sillenite framework with increasing temperature.

Equivalent circuit fitting revealed deviations at lower frequencies ($f < 10^3$ Hz) in C' spectroscopic plots, which might be due to space-charge polarisation.[23-26] Space-charge polarisation seems to be a very common electrical behaviour in many Bi-contained compounds.[23] Further work based on lower frequency measurements/high temperature may be useful to investigate the physical origin of the electrical behaviour at $f < 10^3$ Hz in sillenites.

By combined consideration of the IS and Raman spectroscopy data, the mechanism for local structural distortions is suggested: the O(4) site is expanding with temperature, which causes an increase in the bond lengths of Bi-O1(b) and Bi-O1(c) and a decrease of the bond angles between O1(a)-Bi-O1(b) and O1(a)-Bi-O1(c). This promotes Bi atomic shifts towards the O1(a) atoms to maintain the equatorial plane of the distorted Bi octahedra, which alters the Bi-LP orientation and may decrease the local dipole moments.

3.5   References

[1]   S. F. Radaev and V. I. Simonov, Structure of sillenites and atomic mechanisms of isomorphous substitutions, Kristallografiya, 1992. **37**: p. 914-941.

[2]   R. D. Shannon, Revised effective ionic radii and systematic studies of interatomic distances in halides and chalcogenides, Acta Crystallographica Section A, 1976. **32**: p. 751-767.

[3]   H. S. Horowitz, A. J. Jacobson, J. M. Newsam, J. T. Lewandowski and M. E. Leonowicz, Solution synthesis and characterization of sillenite phases, $Bi_{24}M_2O_{40}$ (M = Si, Ge, V, As, P), Solid State Ionics, 1989. **32-3**: p. 678-690.

[4]   S. C. Abrahams, P. B. Jamieson and J. L. Bernstei, Crystal structure of piezoelectric bismuth germanium oxide $Bi_{12}GeO_{20}$, Journal of Chemical Physics, 1967. **47**: p. 4034-4041.

[5]   V. I. Burkov, V. S. Gorelik, A. V. Egorysheva and Y. F. Kargin, Laser Raman spectroscopy of crystals with the structure of sillenite, Journal of Russian Laser Research, 2001. **22**: p. 243-267.

[6]   M. Valant and D. Suvorov, A stoichiometric model for sillenites, Chemistry of Materials, 2002. **14**: p. 3471-3476.

[7]   G. V. Avdeev, T. I. Milenov, A. V. Egorysheva, K. P. Petrov, V. M. Skorikov, R. K. Titorenkova and P. M. Rafailov, Crystal structure of $Bi_{36}MgP_2O_{60-d}$, Russian Journal of Inorganic Chemistry, 2011. **56**: p. 913-918.

[8]   M. Burianek, P. Held and A. Muhlberg, Improved single crystal growth of the boron sillenite "$Bi_{24}B_2O_{39}$" and investigation of the crystal structure, Crystal Research and Technology, 2002. **37**: p. 785-796.

[9]   S. F. Radaev, L. A. Muradyan and V. I. Simonov, Atomic structure and crystal chemistry of sillenites $Bi_{12}(Bi^{3+}_{0.5}Fe^{3+}_{0.5})O_{19.5}$ and $Bi_{12}(Bi^{3+}_{0.67}Zn^{2+}_{0.33})O_{19.33}$, Acta Crystallographica Section B-Structural Science, 1991. **47**: p. 1-6.

[10]   S. F. Radaev, V. I. Simonov and Y. F. Kargin, Structural features of g-phase Bi_2O_3 and its place in the sillenite family, Acta Crystallographica Section B-Structural Science, 1992. **48**: p. 604-609.

[11]   H. Marquet, M. Tapiero, J. C. Merle, J. P. Zielinger and J. C. Launay, Determination of the factors controlling the optical background absorption in nominally undoped and doped sillenites, Optical Materials, 1998. **11**: p. 53-65.

[12]   T. I. Mel'nikova, G. M. Kuz'micheva, V. B. Rybakov, N. B. Bolotina, A. B. Dubovskii and A. Cousson, Composition and structure of solid solutions in the Bi_2O_3-SiO_2-$V_2^{5+}O_5$ system with the structure sillenite, Journal of Structural Chemistry, 2011. **52**: p. 510-516.

[13]   J. P. Huignard and F. Micheron, High sensitivity read-write volume holographic storage in $Bi_{12}SiO_{20}$ and $Bi_{12}GeO_{20}$ crystals, Applied Physics Letters, 1976. **29**: p. 591-593.

[14]   J. Link, J. Fontanella and C. G. Andeen, Temperature variation of the dielectric properties of bismuth germanate and bismuth germanium oxide, Journal of Applied Physics, 1980. **51**: p. 4352-4355.

[15]   S. L. Hou and D. S. Oliver, Pockels readout optical memory using $Bi_{12}SiO_{20}$, Applied Physics Letters, 1971. **18**: p. 325-328.

[16]   V. I. Chmyrev, V. M. Skorikov and M. I. Subbotin, Piezoelectric Effect in Crystals of $Bi_{12}GeO_{20}$, $Bi_{12}SiO_{20}$, and $Bi_{12}TiO_{20}$, Inorganic Materials, 1983. **19**: p. 242-246.

[17]   M. Valant and D. Suvorov, Processing and dielectric properties of sillenite compounds $Bi_{12}MO_{20-d}$ (M = Si, Ge, Ti, Pb, Mn, $B_{1/2}P_{1/2}$), Journal of the American Ceramic

Society, 2001. **84**: p. 2900-2904.

[18]   M. T. Sebastian and H. Jantunen, Low loss dielectric materials for LTCC applications: a review, International Materials Reviews, 2008. **53**: p. 57-90.

[19]   S. F. Radaev and V. I. Simonov, Structure of sillenites and atomic mechanisms of their isomorphic substitutions, Kristallografiya, 1992. **37**: p. 484-499.

[20]   G. Singla, P. K. Jha, J. K. Gill and K. Singh, Structural, thermal and electrical properties of Ti^{4+} substituted Bi_2O_3 solid systems, Ceramics International, 2012. **38**: p. 2065-2070.

[21]   H. A. Harwig and A. G. Gerards, Polymorphism of bismuth sesquioxide, Thermochimica Acta, 1979. **28**: p. 121-131.

[22]   A. J. Moulson and J. M. Herbert, *Electroceramics: materials, properties, applications. (Second Edition)*. Chichester, England: John Wiley & Sons Ltd., 2003.

[23]   M. Valant and D. Suvorov, Dielectric characteristics of bismuth oxide solid solutions with a fluorite-like crystal structure, Journal of the American Ceramic Society, 2004. **87**: p. 1056-1061.

[24]   T. Takahashi and H. Iwahara, Oxide ion conductors based on bismuth sesquioxide, Materials Research Bulletin, 1978. **13**: p. 1447-1453.

[25]   I. de Oliveira and J. Frejlich, Dielectric relaxation time measurement in absorbing photorefractive materials, Optics Communications, 2000. **178**: p. 251-255.

[26]   E. D. Wachsman, P. Jayaweera, N. Jiang, D. M. Lowe and B. G. Pound, Stable high conductivity ceria/bismuth oxide bilayered electrolytes, Journal of the Electrochemical Society, 1997. **144**: p. 233-236.

[27]   M. Valant and D. Suvorov, Synthesis and characterization of a new sillenite compound $Bi_{12}(B_{0.5}P_{0.5})O_{20}$, Journal of the American Ceramic Society, 2002. **85**: p. 355-358.

[28]   J. T. S. Irvine, D. C. Sinclair and A. R. West, Electroceramics: Characterization by impedance spectroscopy, Advanced Materials, 1990. **2**: p. 132-138.

[29]   J. R. Macdonald and E. Barsoukov, *Impedance spectroscopy:theory, experiment, and applications, 2nd edition*: John Wiley & Sons, 1987.

[30]   S. Kamba, V. Porokhonskyy, A. Pashkin, V. Bovtun, J. Petzelt, J. C. Nino, S. Trolier-McKinstry, M. T. Lanagan and C. A. Randall, Anomalous broad dielectric relaxation in $Bi_{1.5}Zn_{1.0}Nb_{1.5}O_7$ pyrochlore, Physical Review B, 2002. **66**: p. 054106.

[31]   U. T. Hochli, K. Knorr and A. Loidl, Orientational glasses, Advances in Physics, 1990. **39**: p. 405-615.

[32]   E. J. Abram, D. C. Sinclair and A. R. West, A strategy for analysis and modelling of impedance spectroscopy data of electroceramics: Doped lanthanum gallate, Journal of Electroceramics, 2003. **10**: p. 165-177.

[33]   A. V. Egorysheva, V. I. Burkov, Y. F. Kargin, V. G. Plotnichenko, V. V. Koltashev, E. D. Obraztsova and S. V. Terekhov, Atomic structure features of sillenite crystals as probed by Raman spectroscopy, Russian Journal of Inorganic Chemistry, 2005. **50**: p. 238-245.

[34]   B. Mihailova, M. Gospodinov and L. Konstantinov, Raman spectroscopy study of sillenites. I. Comparison between $Bi_{12}(Si,Mn)O_{20}$ single crystals, Journal of Physics and Chemistry of Solids, 1999. **60**: p. 1821-1827.

4 A Study of Divalent and Trivalent Cation Doping in Sillenite Analogues: $Bi_{12}(Bi^{3+}_{0.67}M^{2+}_{0.33})O_{19.33}$ and $Bi_{12}(Bi^{3+}_{0.5}M^{3+}_{0.5})O_{19.5}$.

4.1 Introduction

The Valant and Suvorov (VS) general formula: $Bi_{12}(Bi^{3+}_{4/5-nx}M^{n+}_{5x})O_{19.2+nx}$ [1] states that divalent or trivalent cations doping sillenite analogues form single-phase compounds with composition $Bi_{12}(Bi^{3+}_{0.67}M^{2+}_{0.33})O_{19.33}[LP]_{0.67}$ or $Bi_{12}(Bi^{3+}_{0.5}M^{3+}_{0.5})O_{19.5}[LP]_{0.5}$, respectively. They are grouped as stoichiometric sillenites with a fully occupied oxygen sublattice (i.e. = 20) by oxygen ions and lone electron pairs from Bi^{3+} ions. In addition, they can also be considered as isomorphic substitutions of parent γ-Bi_2O_3 with an average M-site cation valence less than +4.[2] Hence, compared with the ideal sillenite $Bi_{12}M^{4+}O_{20}$ (e.g. $Bi_{12}SiO_{20}$ in Chapter 3), local distortions in the crystal structure of these M^{2+}/M^{3+} doped sillenites are expected due to the presence of Bi^{3+} ions forming "umbrella-like" distorted polyhedra, BiO_3LP, in the tetrahedral sites.[3]

Current investigations on these divalent and trivalent cation doping sillenite analogues mainly focused on the crystallographic features, particularly the atomic position arrangements on the tetrahedral sites. According to most researchers[4, 5], the Radaev and coworkers' structural model (R model) [2, 6] can explain all the experimental observations, where all the Bi atoms in the tetrahedral sites instead of Bi^{5+} can be expressed as Bi^{3+} only. The charge compensation is achieved by filling one vacant oxygen O(3) site with Bi^{3+} electron lone pairs, which forms distorted tetrahedra units, $BiO(3)_3LP$, Figure 4.1[3]. Radaev *et al.*[2, 6] also proposed that there is actually more than one sillenite model depending on the valence state of the M cations and each particular model can only be decided experimentally.[2, 6]
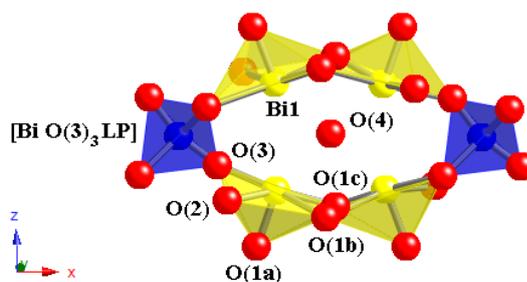
Figure 4.1[3] Fragment of distorted sillenite structure viewed along the (001) plane with Bi^{3+} cations occupying the tetrahedral site; blue, red and yellow spheres represent the M^{n+}, oxygen and bismuth ions, respectively.

The aim of this chapter is to investigate the validity of the R model and therefore the VS general formula of M^{2+}/M^{3+} sillenite analogues. Single-phase sillenites were formed from *d*- and *p*- block dopants with $M^{2+} = Zn^{2+}$ and $M^{3+} = Fe^{3+}$, Al^{3+} and In^{3+}. The intermediate values of *x* from the binary phase diagram M_xO_y-Bi_2O_3 are prepared to explore possible solid solutions. Other attempted dopants such as Mg^{2+} and Sc^{3+} did not form phase-pure sillenites successfully by the solid state reaction method, as shown in the XRPD results, Appendix I.

In this chapter, the synthesis, composition and thermal analysis of M^{2+}/M^{3+} doping sillenite analogues, where $M = Zn^{2+}$, Fe^{3+}, Al^{3+} and In^{3+} were probed using XRPD, SEM, EDS and DSC. The validity of the VS general formula is discussed. The influence of different cation-doping on the structure of M^{2+}/M^{3+} sillenite analogues was studied using Neutron Powder Diffraction (NPD) and Raman Spectroscopy (RS). To characterise the electrical properties, Impedance Spectroscopy (IS), *rf* fixed frequency capacitance measurements and microwave (MW) dielectric resonance measurements were systematically studied for the first time. Equivalent circuit analysis with a combination of a parallel R, C and Cole-Cole branch (i.e. CPE in series with a C) was used to model the IS data. As a result, the structure-composition-property relationships of M^{2+}/M^{3+} containing sillenites are established.

4.2   Results

4.2.1 Synthesis of M^{2+}/M^{3+} Sillenite Ceramics

Based on the Valant and Suvorov (VS) general formula $Bi_{12}(Bi^{3+}_{4/5-nx}M^{n+}_{5x})O_{19.2+nx}$, where $M^{2+} = Zn^{2+}$ and $M^{3+} = Fe^{3+}$, Al^{3+} and In^{3+} and intermediate values of x from the formula are explored. All compositions were synthesized by the solid state reaction method. Precursors of reagents were dried before weighing as listed in Table 2.1 from Chapter 2: Experimental Procedure. The weighed powders were ground with acetone in an agate mortar and pestle by hand for ~ 30 minutes until the acetone evaporated. The mixed powders were then heated in an Au foil boat at a firing temperature from 700 to 780 ℃ with interval grinding to assist reaction. The heating and grinding process was stopped when the equilibrium state of the sample was detected by X-ray powder diffraction. The reaction conditions and solubility limits established from XRPD and NPD of the single-phase compositions are listed in Table 4.1.

Table 4.1 Summary of single-phase compositions examined by XRPD and NPD.

VS formula	Single-phase Composition	Reaction Temperature / ℃	Reaction Time / h	Sintering Temperature / ℃
$Bi_{12}(Bi^{3+}_{0.67}M^{2+}_{0.33})O_{19.33}$	$Bi_{12}(Bi_{0.67}Zn_{0.33})O_{19.33}$	735	> 240	738
$Bi_{12}(Bi^{3+}_{0.5}M^{3+}_{0.5})O_{19.5}$	$Bi_{12}(Bi_{0.5}Fe_{0.5})O_{19.5}$	745	48	770
	$Bi_{12}(Bi_{0.3}Al_{0.7})O_{19.5}$	730	36	735
	$Bi_{12}(Bi_{0.4}Al_{0.6})O_{19.5}$	730	36	735
	$Bi_{12}(Bi_{0.6}In_{0.4})O_{19.5}$	750	36	780
	$Bi_{12}(Bi_{0.7}In_{0.3})O_{19.5}$	750	36	780

4.2.2 X-ray Power Diffraction (XRPD)

● **Zinc sillenites**

According to the VS general formula for M^{2+} dopants: $Bi_{12}(Bi^{3+}_{0.67}M^{2+}_{0.33})O_{19.33}[LP]_{0.67}$,[1] where $M^{2+} = Zn^{2+}$, variable molar ratios of Bi^{3+} and Zn^{2+} cations were prepared to explore

possible sillenite phases and solid solution ranges. Compositions $Bi_{12}(Bi_{0.8}Zn_{0.2})O_{19.4}$, $Bi_{12}(Bi_{0.75}Zn_{0.25})O_{19.375}$, $Bi_{12}(Bi_{0.7}Zn_{0.3})O_{19.35}$, $Bi_{12}(Bi_{0.67}Zn_{0.33})O_{19.33}$, $Bi_{12}(Bi_{0.5}Zn_{0.5})O_{19.25}$, $Bi_{12}(Bi_{0.33}Zn_{0.67})O_{19.167}$, $Bi_{12}(Bi_{0.25}Zn_{0.75})O_{19.125}$, $Bi_{12}(Bi_{0.2}Zn_{0.8})O_{19.1}$ and $Bi_{12}ZnO_{19}$ were synthesized by the solid state reaction method and heated between 700 to 740 °C for ~ 240 hours. XRPD results of some selected compositions are shown in Figure 4.2.
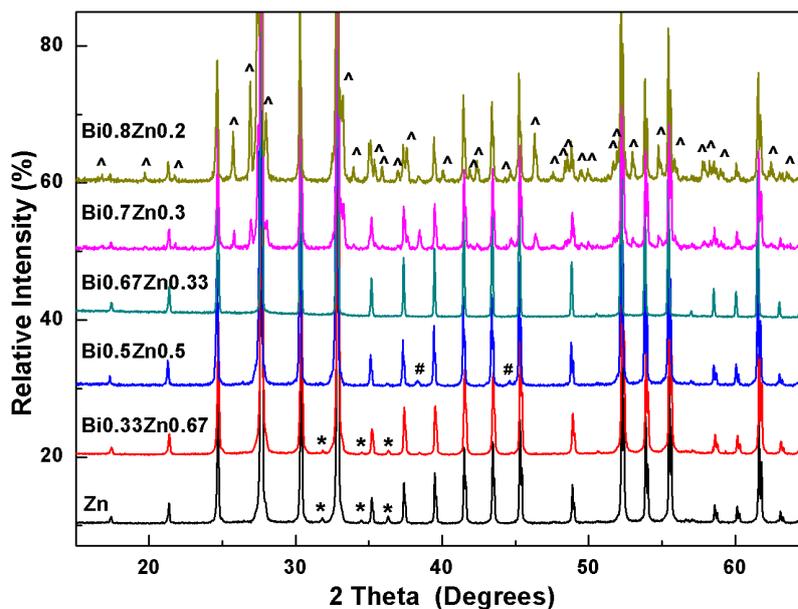
Figure 4.2 XRPD results of zinc sillenites, where single-phase compounds are $Bi_{0.67}Zn_{0.33}$ and $Bi_{0.5}Zn_{0.5}$. Notations *, # and ^ indicate impurity ZnO phase (ICCD card [36-1451]), Aluminum metal peaks (ICCD card [4-787]) from the sample holder of the Philips D500 X-ray diffractometer and impurity α-Bi_2O_3 phase (ICCD card [41-1449]), respectively.

Single-phase compounds detected by XRPD were $Bi_{12}(Bi_{0.67}Zn_{0.33})O_{19.33}$ and $Bi_{12}(Bi_{0.5}Zn_{0.5})O_{19.25}$. However, Neutron Powder Diffraction (NPD) data of $Bi_{0.5}Zn_{0.5}$ (using tetrahedral-site cations as an abbreviation) revealed the presence of a secondary phase ZnO in the sample. Rietveld refinement with fixed composition $Bi_{12}(Bi_{0.67}Zn_{0.33})O_{19.33}$ showed it is the only single-phase sillenite in the Bi_2O_3-ZnO binary system, Section 4.2.3 and Figure 4.7. Therefore, Zn^{2+} sillenite obeys the VS formula.

- **Iron sillenites**

Compositions $Bi_{12}(Bi_{0.33}Fe_{0.67})O_{19.5}$, $Bi_{12}(Bi_{0.4}Fe_{0.6})O_{19.5}$, $Bi_{12}(Bi_{0.45}Fe_{0.55})O_{19.5}$, $Bi_{12}(Bi_{0.5}Fe_{0.5})O_{19.5}$, $Bi_{12}(Bi_{0.55}Fe_{0.45})O_{19.5}$, $Bi_{12}(Bi_{0.6}Fe_{0.4})O_{19.5}$ and $Bi_{12}(Bi_{0.67}Fe_{0.33})O_{19.5}$ were prepared and heated between 730 and 750 °C for 48 hours.

Figure 4.3 shows the XRPD results of selected iron sillenites, where single-phase $Bi_{12}(Bi_{0.5}Fe_{0.5})O_{19.5}$ was observed, obeying the VS general formula: $Bi_{12}(Bi^{3+}_{0.5}M^{3+}_{0.5})O_{19.5}[LP]_{0.5}$ for M^{3+} dopants [1].
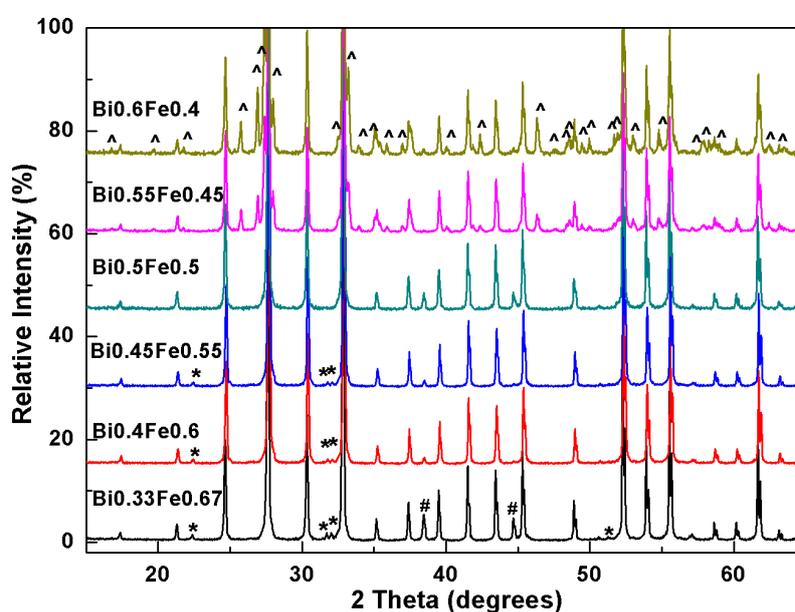
Figure 4.3 XRPD results of iron sillenites, where $Bi_{0.5}Fe_{0.5}$ is phase-pure. Notation of *, # and ^ marked as impurity phase $BiFeO_3$ (ICCD card [72-2035]); Al metal peaks from sample holder (ICCD card [4-787]) and α-Bi_2O_3 phase (ICCD card [41-1449]), respectively.

- **Aluminum sillenites**

Figure 4.4 shows the XRPD results of aluminium sillenites: $Bi_{12}(Bi_{0.6}Al_{0.4})O_{19.5}$, $Bi_{12}(Bi_{0.5}Al_{0.5})O_{19.5}$, $Bi_{12}(Bi_{0.4}Al_{0.6})O_{19.5}$, $Bi_{12}(Bi_{0.3}Al_{0.7})O_{19.5}$ and $Bi_{12}(Bi_{0.2}Al_{0.8})O_{19.5}$, which were heated between 730 and 750 °C for ~ 36 hours. Consistent with the preliminary work of Donovan[7], a limited solid solution between $Bi_{12}(Bi_{0.4}Al_{0.6})O_{19.5}$ and $Bi_{12}(Bi_{0.3}Al_{0.7})O_{19.5}$ was detected by XRPD, Figure 4.5, which disobeys the VS general formula[1].

An impurity phase of γ-Bi_2O_3 was present in $Bi_{0.5}Al_{0.5}$ and $Bi_{0.2}Al_{0.8}$, which were two adjacent compositions at each end of the solid solution. The reason for the appearance of a γ-Bi_2O_3 impurity phase in aluminium sillenites is unknown, but its formation might be due to the instability of Al sillenites.
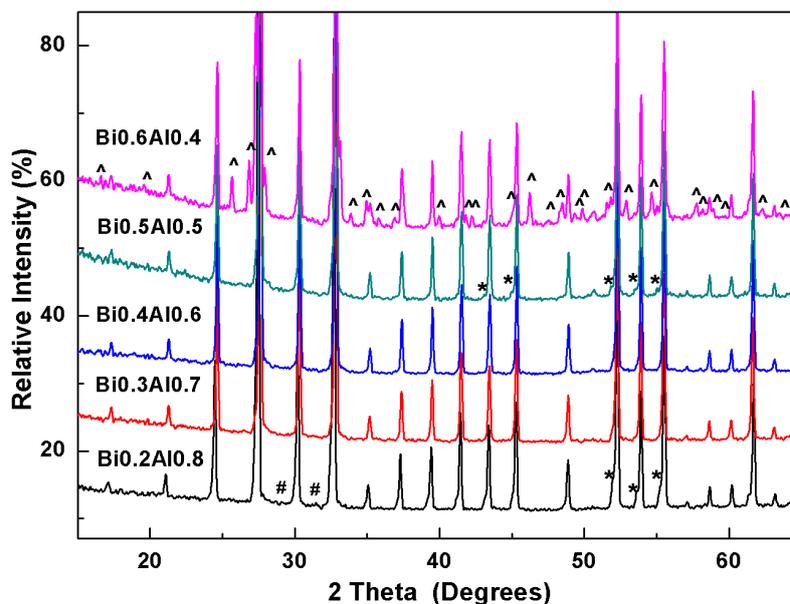
Figure 4.4 XRPD results of aluminium sillenites, where a narrow solid solution range between $Bi_{0.4}Al_{0.6}$ and $Bi_{0.3}Al_{0.7}$ was obtained. Notations *, # and ^ indicate γ-Bi_2O_3 (ICCD card [45-1344]), $Bi_2Al_4O_9$ (JCPDS card [25-1048]) and α-Bi_2O_3, respectively.
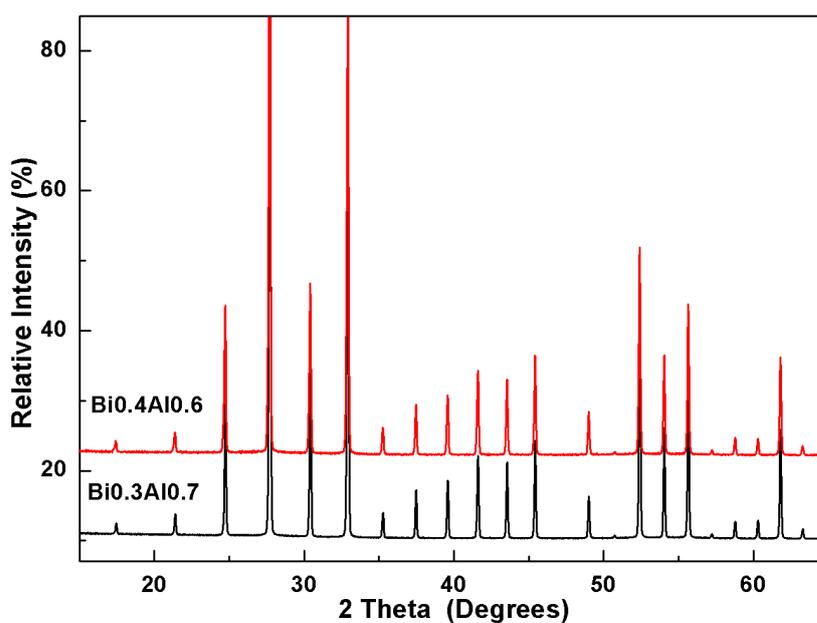
Figure 4.5 XRPD results of single-phase compounds $Bi_{0.3}Al_{0.7}$ and $Bi_{0.4}Al_{0.6}$.

- **Indium sillenites**

Consistent with the preliminary work on indium sillenites by Donovan[7], a solid solution between compositions $Bi_{12}(Bi_{0.6}In_{0.4})O_{19.5}$ and $Bi_{12}(Bi_{0.7}In_{0.3})O_{19.5}$ was confirmed by XRPD, Figure 4.6, which again disobeys the VS formula [1].
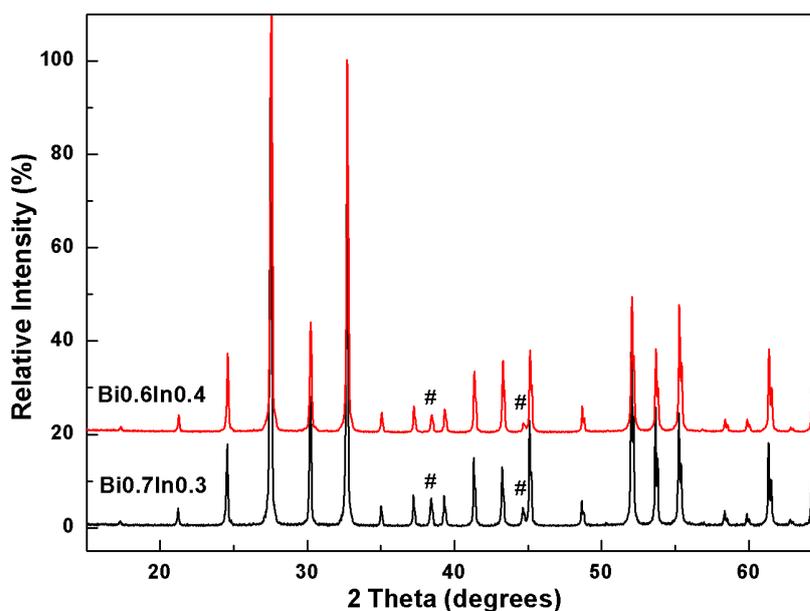
Figure 4.6 XRPD of single-phase $Bi_{12}(Bi_{0.6}In_{0.4})O_{19.5}$ and $Bi_{12}(Bi_{0.7}In_{0.3})O_{19.5}$. Al peaks caused by the sample holders are marked as #.

4.2.3 Neutron Powder Diffraction (NPD)

Compound $Bi_{12}(Bi_{0.5}Zn_{0.5})O_{19.25}$ was the only zinc sillenite available for Neutron powder diffraction (NPD). NPD data of $Bi_{12}(Bi_{0.5}Zn_{0.5})O_{19.25}$ were collected in time-of-flight (ToF) format at room temperature on the Polaris diffractometer at ISIS at the STFC Rutherford Appleton Laboratory (RAL) in Oxfordshire, UK. NPD data of compounds $Bi_{12}(Bi_{0.3}Al_{0.7})O_{19.5}$ and $Bi_{12}(Bi_{0.7}In_{0.3})O_{19.5}$ were collected at room temperature on the D2B diffractometer at the Institut Laue-Langevin (ILL) in Grenoble, France.

Rietveld refinements of the NPD data for compounds $Bi_{12}(Bi_{0.5}Zn_{0.5})O_{19.25}$, $Bi_{12}(Bi_{0.3}Al_{0.7})O_{19.5}$ and $Bi_{12}(Bi_{0.7}In_{0.3})O_{19.5}$ were carried out on space group, $I23$, based on the R structural model as a starting point.[3, 6] NPD data revealed $Bi_{12}(Bi_{0.3}Al_{0.7})O_{19.5}$ and $Bi_{12}(Bi_{0.7}In_{0.3})O_{19.5}$ were phase pure whereas $Bi_{12}(Bi_{0.5}Zn_{0.5})O_{19.25}$ was not. An impurity phase of ZnO was detected, shown as red tick marks in Figure 4.7 (a). A two-phase Rietveld refinement of the NPD data for the starting composition $Bi_{12}(Bi_{0.5}Zn_{0.5})O_{19.25}$ revealed ~ 3.48 weight% ZnO secondary phase (phase 2) based on a fixed composition of $Bi_{12}(Bi_{0.67}Zn_{0.33})O_{19.33}$ as phase 1. The chosen space group $I23$ was testified to be stable with the relatively temperature-independent permittivity for these three compounds at room temperature, as shown by rf fixed frequency capacitance measurements (see Figure 4.26). The refinement profiles are shown in Figure 4.7 and the overall refined fitting parameters (R_{wp}(%), R_p(%), χ^2) for compounds $Bi_{12}(Bi_{0.67}Zn_{0.33})O_{19.3}$, $Bi_{12}(Bi_{0.3}Al_{0.7})O_{19.5}$ and $Bi_{12}(Bi_{0.7}In_{0.3})O_{19.5}$ were (4.02, 6.04, 1.512), (7.29, 5.43, 8.952) and (6.9, 5.18, 6.91), respectively.
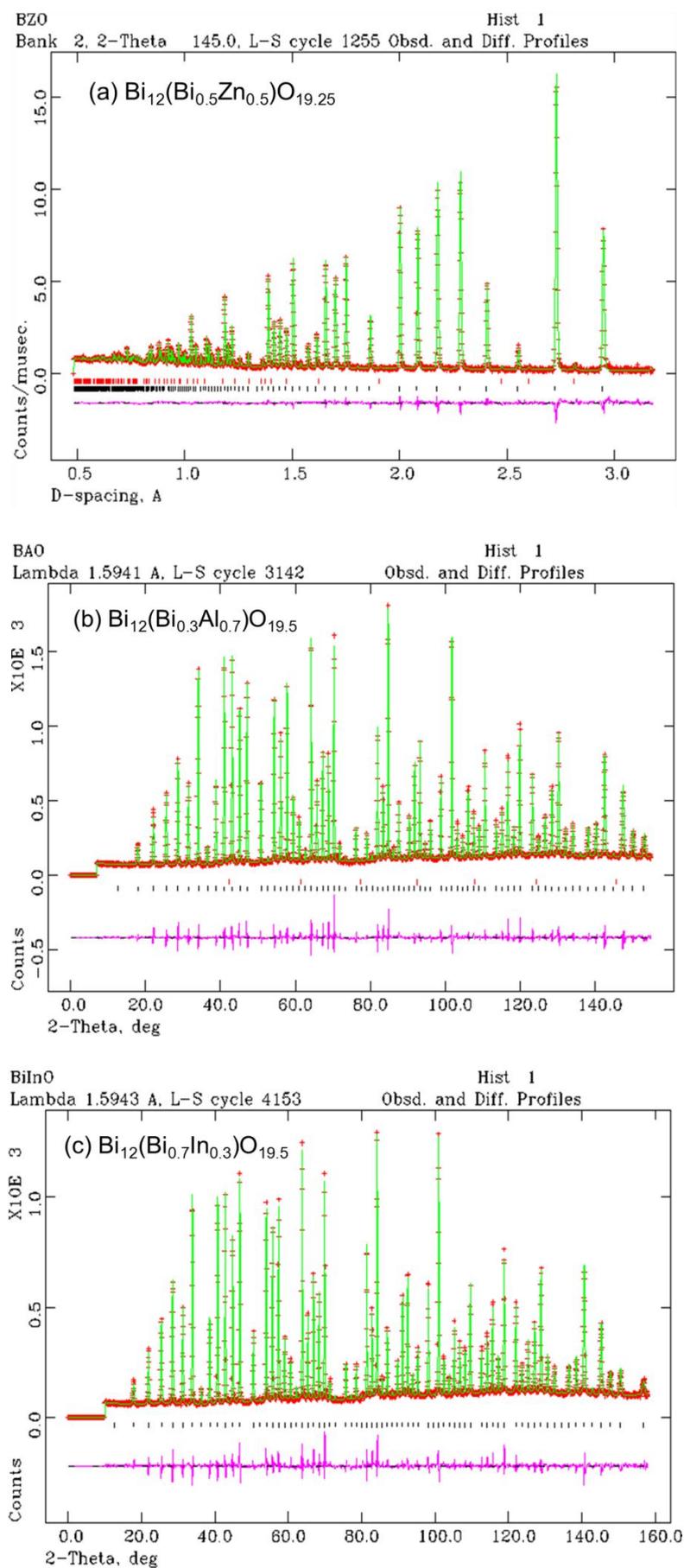
Figure 4.7 Calculated, experimental and difference profile plot from Rietveld refinement

of (a) $Bi_{12}(Bi_{0.5}Zn_{0.5})O_{19.25}$, (b) $Bi_{12}(Bi_{0.3}Al_{0.7})O_{19.5}$ and (c) $Bi_{12}(Bi_{0.7}In_{0.3})O_{19.5}$ using NPD data at room temperature to show the goodness of the fit between the R structural model (+) and the observed data (-). Black ticks (|) indicate Bragg reflections of the sillenite phase, whereas red ticks indicates reflection positions of (a) secondary phase ZnO and (b) vanadium peaks due to the vanadium can.

Table 4.2 Final atomic parameters for $Bi_{12}(Bi_{0.67}Zn_{0.33})O_{19.33}$, $Bi_{12}(Bi_{0.3}Al_{0.7})O_{19.5}$ and $Bi_{12}(Bi_{0.7}In_{0.3})O_{19.5}$ from Rietveld refinement by using NPD data with space group $I23$.

		$M = Zn^{2+}$	$M = Al^{3+}$	$M = In^{3+}$
Space group: $I23$	a / Å	10.2086(2)	10.17061(5)	10.2312(1)
Bi1	24f, x, y, z	0.1765(12)	0.1763(2)	0.1762(1)
		0.31845(13)	0.3180(2)	0.3191(1)
		0.0140(1)	0.0134(2)	0.0121(2)
	Occupancy of Bi1	1	1	1
	Bi1, Uiso ×100 / Å^2	U_{11} = 0.33(5);	U_{11} = 1.1(1);	U_{11} = 1.2(1);
		U_{22} = 2.79(7);	U_{22} = 2.3(1);	U_{22} = 1.3(1);
		U_{33} = 1.06(5);	U_{33} = 0.86(8);	U_{33} = 1.03(9);
		U_{12} = 0.37(4);	U_{12} = 0.26(7);	U_{12} = 0.10(7);
		U_{13} = 0.14(4);	U_{13} = 0.1(1);	U_{13} = 0.2(1);
		U_{23} = 0.74(4)	U_{23} = 0.64(7)	U_{23} = 0.66(8)
Bi2	8c, x, x, x	-0.0203(8)	-	-
	2a, 0, 0, 0	-		
M	2a, 0, 0, 0			
	Occupancy of Bi2	0.1667	0.3	0.7
	Occupancy of M2	0.3333	0.7	0.3
	Bi2, Uiso×100 / Å^2	0.2(2)	2.3(2)	3.6(2)
	M2, Uiso×100 / Å^2	0.7(6)	2.3(2)	3.6(2)
O1	24f, x, y, z	0.1349(2)	0.1349(2)	0.1351(2)
		0.2525(2)	0.2524(3)	0.2493(3)
		0.4858(2)	0.4853(2)	0.4884(2)
O2	8c, x, x, x	0.1879(2)	0.1905(2)	0.1860(3)
O3	8c, x, x, x	0.8895(3)	0.8958(3)	0.8878(4)
	Occupancy of O1	1	1	1
	Occupancy of O2	1	1	1
	Occupancy of O3	0.8333	0.875	0.875
	O1, Uiso×100 / Å^2	1.20(3)	1.28(4)	1.04(4)
	O2, Uiso×100 / Å^2	1.19(6)	1.2(1)	1.3(1)
	O3, Uiso×100 / Å^2	1.55(7)	2.0(1)	2.3(1)
	R_{wp} / %	4.02	7.29	6.90
	R_p / %	6.04	5.43	5.18
	χ^2	1.512	8.952	6.91

Details of the refinement results for the three sillenites including fractional atomic coordinates, multiplicity, site-occupancy and thermal parameters are listed in Table 4.2. Starting models had a statistical distribution of Bi2 and M cations over the same tetrahedral site, however, as this site was refined, the fitting improved by a site preference of the Bi2

cation to the lower symmetry 8-fold $8c$ site and the higher symmetry 2-fold $2a$ site is occupied exclusively by Zn for the $Bi_{12}(Bi_{0.67}Zn_{0.33})O_{19.33}$ phase. For both Al and In analogues, constraints on the atomic coordinates at the $2a$ site (0, 0, 0) and Uiso's must be added for both Bi2 and M atoms on the M-site to achieve a stable structural model. The fact that Bi2 and M cations in both Al and In analogues required constraints over the same $2a$ site is an indicator of showing the existence of some degree of disorder in the local cation distribution. Significant ionic radii mismatch between the Bi2 and M atoms was found in Bi^{3+} and Al^{3+}, (i.e. $\Delta_{(Bi3+/Al3+)} = 0.57$ Å[8]), whereas the ionic radii mismatch in Zn and In sillenites are similar (i.e. $\Delta_{(Bi3+/Zn2+)} = 0.36$ Å and $\Delta_{(Bi3+/In3+)} = 0.34$ Å[8]). Zn^{2+} and In^{3+} are similar in size, but differ in charge and electron configuration.

Table 4.3 Selected bond distances (Å), bond angles (°) and calculated bond valence sums ($\sum$BVS) for $Bi_{12}(Bi_{0.67}Zn_{0.33})O_{19.33}$, $Bi_{12}(Bi_{0.3}Al_{0.7})O_{19.5}$ and $Bi_{12}(Bi_{0.7}In_{0.3})O_{19.5}$ from Rietveld refinement using NPD data. Bond length values of the ideal sillenite $Bi_{12}GeO_{20}$ reported by Radaev and Simonov[9] are added for comparison.

Bond length / Å	$M = Zn^{2+}$	$M = Al^{3+}$	$M = In^{3+}$	$M=Ge^{4+}$ [9]
Bi1-O1(a)	2.0766(20)	2.0688(27)	2.0680(27)	2.072(1)
Bi1-O1(b)	2.2457(21)	2.2414(27)	2.2678(27)	2.221(1)
Bi1-O1(c)	2.6284(18)	2.6220(28)	2.5892(27)	2.622(1)
Bi1-O2	2.2225(11)	2.2247(16)	2.2428(16)	2.2146(6)
Bi1-O3	2.5639(22)	2.5878(28)	2.5551(28)	2.6241(8)
Bi2-O3	1.595(16) 2.101(8)$\times$3	1.836(6)$\times$4	1.987(7)$\times$4	
M-O3	1.954(4)$\times$4	1.836(6)$\times$4	1.987(7)$\times$4	
Bond Angles / °	**$M = Zn^{2+}$**	**$M = Al^{3+}$**	**$M = In^{3+}$**	
Bi1-O2-Bi1	117.93(4)	117.21(6)	118.24(6)	
Bi1-O3-Bi1	108.84(10)	106.33(13)	109.11(14)	
Bi1-O3-M	110.09(9)	112.45(12)	109.83(14)	
Bi1-O3-Bi2	110.09(9) 102.41(29) 118.42(35) 109.05(10)	112.45(12)	109.83(12)	
O3-M-O3	109.471(1)	109.471(0)	109.471(0)	
O3-Bi2-O3	118.6(6) 99.0(8)	109.471(0)	109.471(0)	
$\sum$BVS_calc.	**$M = Zn^{2+}$**	**$M = Al^{3+}$**	**$M = In^{3+}$**	
Bi1	2.9	2.92	2.88	
Bi2	2.91	5.96	3.96	
M	2.04	2.43	3.12	

Selected bond details including bond lengths, bond angles and calculated bond valence sum ($\sum$BVS_calc.) from Rietveld refinements for $Bi_{12}(Bi_{0.67}Zn_{0.33})O_{19.33}$, $Bi_{12}(Bi_{0.3}Al_{0.7})O_{19.5}$ and $Bi_{12}(Bi_{0.7}In_{0.3})O_{19.5}$ are listed in Table 4.3. BVS calculations for atoms can be used as a check on the reliability of the determined structure.[10] For the Zn^{2+} sillenite, $\sum$BVS_calc. of Bi1, Bi2 and Zn are similar to the theoretical values, indicating reasonable bond lengths, altogether with the refined fitting parameters, an acceptable structural refinement was obtained.

For the Al^{3+} sillenite, $\sum$BVS_calc. of Bi1 is similar to the theoretical value, indicating reasonable bond lengths were attained for the framework of the sillenite structure. However, $\sum$BVS_calc. of Bi2 is much larger than the theoretical value, indicating highly over-bonded bond lengths associated with Bi2 atoms, whereas $\sum$BVS_calc. of Al is under-bonded. The mismatch between calculated and theoretical BVS values of Bi2 and Al indicates there was significant disorder in the tetrahedral sites, which probably arises due to the large difference in the ionic radii of two atoms sharing the same crystallographic site, hence it leads to high fitting parameters: $R_p(\%), wR_p(\%), \chi^2$.

For the In^{3+} sillenite, $\sum$BVS_calc. of Bi1 is similar to the theoretical value, but slightly under-bonded. $\sum$BVS_calc. of Bi2 and In are larger than the theoretical value, indicating over-bonded bond lengths. This indicates there was some degree of disorder in the tetrahedral sites as well as on the framework of the structure, leading to slightly higher fitting parameters: $R_p(\%), wR_p(\%), \chi^2$.

Evidence that the In^{3+} sillenite possesses a more distorted framework unit compared with Zn^{2+} and Al^{3+} sillenites can also be observed from the Raman spectra shown in Figure 4.21 and discussed in more detail later in this Chapter. As a result, the R structural model proved to be the most appropriate model for all the experimental characteristics observed in the three studied sillenite analogues. It gave the best solution for stoichiometric Zn^{2+} sillenite; however, it struggles to explain the structural details on the tetrahedral sites for non-stoichiometric sillenites: e.g. sub-stoichiometric Al^{3+} sillenite and super-stoichiometric In^{3+} sillenite.

Due to the fact that fits for the tetrahedral sites of non-stoichiometric sillenites showed difficulties with large thermal parameters, some research groups such as Neov[11] and Mel'nikova[12, 13] claimed the space group should be assigned as $P23$ for these sillenites rather than $I23$. Refinement work on our NPD data with space group $P23$ was attempted but not successful. From peak indexing results of XRPD and NPD data, a space group of $I23$ is always obtained. This result eliminated the possibility of a change in space group.

It is believed that the limitation of the long-range neutron diffraction technique is reached. The subtle atomic arrangements on the tetrahedral sites are not sensitive to be probed by NPD and even by Raman spectroscopy. However, NPD refinements by using the R model did give an averaged result, e.g. bond lengths/angles signifying the distortions of the framework units. Since they are linked and affected by tetrahedral units, useful structural details should be able to revealed and proposed by combined studies of NPD and Raman spectroscopy.

4.2.4 Electron Microscopy

● **Zinc sillenites**

The microstructure and morphology of the cross section at the $Bi_{0.67}Zn_{0.33}$ pellet (relative density ~ 85 %) were examined by SEM, Figure 4.8. The grain size varied from 3 to 10 μm. Grain morphology is uniform and well packed. Grain growth and some porosity can also be observed.
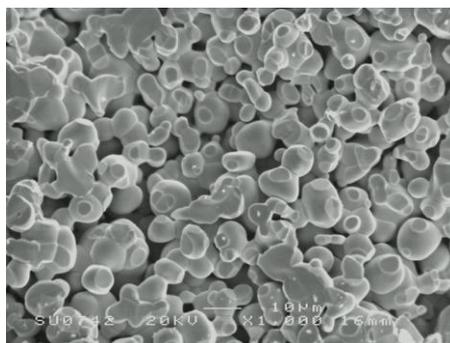
Figure 4.8 SEM image of $Bi_{12}(Bi_{2/3}Zn_{1/3})O_{19.33}$.
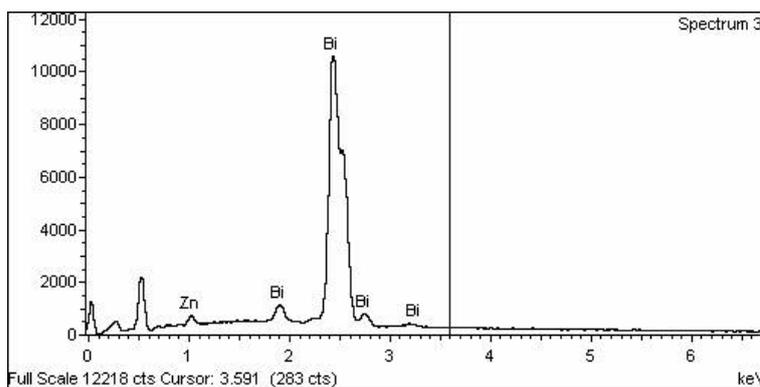
Figure 4.9 EDS spectrum of $Bi_{12}(Bi_{2/3}Zn_{1/3})O_{19.33}$.

The composition was determined by Energy dispersive X-ray spectroscopy (EDS) at the cross section of an un-polished/un-etched pellet of $Bi_{0.67}Zn_{0.33}$. EDS spectra, Figure 4.9, were obtained from ten points selected via the SEM picture. The measured percentage of atomic ratio between Bi and Zn are listed in Table 4.4. The EDS derived composition, $Bi_{12}[Bi_{0.7(1)}Zn_{0.3(1)}]O_{19.35(5)}$ is close to the nominal starting composition, $Bi_{12}(Bi_{0.67}Zn_{0.33})O_{19.33}$.

Table 4.4 Atomic ratios of Bi and Zn obtained via EDS of $Bi_{12}(Bi_{0.67}Zn_{0.33})O_{19.33}$.

$Bi_{12}(Bi_{2/3}Zn_{1/3})O_{19.33}$	Bi (atomic %)	Zn (atomic %)
No.1	97.65	2.35
No.2	97.80	2.20
No.3	97.46	2.54
No.4	99.78	0.22
No.5	97.53	2.47
No.6	99.83	0.17
No.7	98.60	1.40
No.8	99.79	0.21
No.9	98.54	1.46
No.10	97.18	2.82
EDS Averaged Values	**98(1)**	**2(1)**
Theoretical Values	**97.44**	**2.56**
EDS Derived Composition	$Bi_{12}[Bi_{0.7(1)}Zn_{0.3(1)}]O_{19.35(5)}$	

- **Iron sillenites**

The microstructure and morphology of the cross section of an un-polished/un-etched $Bi_{0.5}Fe_{0.5}$ pellet (relative density ~ 87 %) were examined by SEM, Figure 4.10. The grain

size varied from 2 to 10 μm indicating grain growth was occurring. Grains were uniform and some porosity can also be observed.

EDS spectra and the atomic ratio from ten randomly selected points of $Bi_{0.5}Fe_{0.5}$ are given in Figure 4.11 and Table 4.5, respectively. The EDS derived composition, $Bi_{12}[Bi_{0.55(8)}Fe_{0.45(8)}]O_{19.5}$ is close to the nominal starting composition, $Bi_{12}(Bi_{0.5}Fe_{0.5})O_{19.5}$.
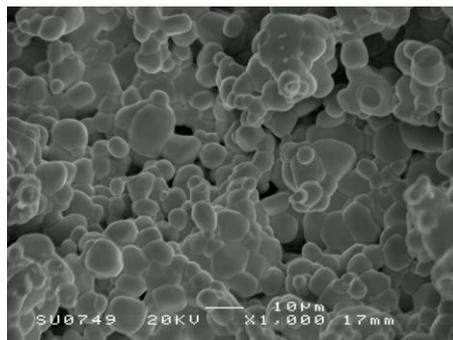
Figure 4.10 SEM image of $Bi_{12}(Bi_{0.5}Fe_{0.5})O_{19.5}$.
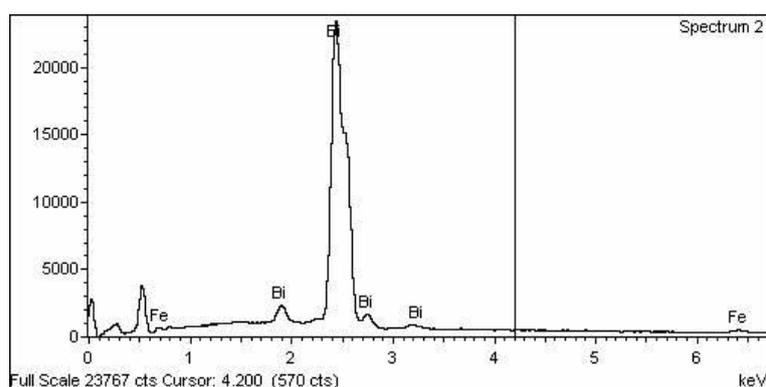
Figure 4.11 EDS spectrum of $Bi_{12}(Bi_{0.5}Fe_{0.5})O_{19.5}$.

Table 4.5 Atomic ratios of Bi and Fe obtained via EDS of $Bi_{12}(Bi_{0.5}Fe_{0.5})O_{19.5}$.

$Bi_{12}(Bi_{1/2}Fe_{1/2})O_{19.5}$	Bi (atomic %)	Fe (atomic %)
No.1	96.95	3.05
No.2	96.56	3.44
No.3	96.6	3.40
No.4	94.92	5.08
No.5	96.40	3.60
No.6	96.61	3.39
No.7	96.73	3.27
No.8	96.85	3.15
No.9	96.96	3.04
No.10	96.54	3.46
EDS Averaged Values	**96.5(6)**	**3.5(6)**
Theoretical Values	**96.15**	**3.85**
EDS Derived Composition	**$Bi_{12}[Bi_{0.55(8)}Fe_{0.45(8)}]O_{19.5}$**	

● **Aluminum sillenites**

SEM images of aluminium sillenites: $Bi_{12}(Bi_{0.4}Al_{0.6})O_{19.5}$ and $Bi_{12}(Bi_{0.3}Al_{0.7})O_{19.5}$ are shown in Figure 4.12 (a) and (b), respectively. Both compounds had a low relative density ~ 56 % but this was due to the low synthesis temperature required to maintain phase-purity. The grain size varied from 1 to 10 μm with a larger grain size (3-10 μm) for $Bi_{0.4}Al_{0.6}$. Some porosity in between the grains can be observed. Elemental analysis of the bismuth/aluminium ratio in aluminium sillenites by EDS was not possible due to the low atomic mass of Al.
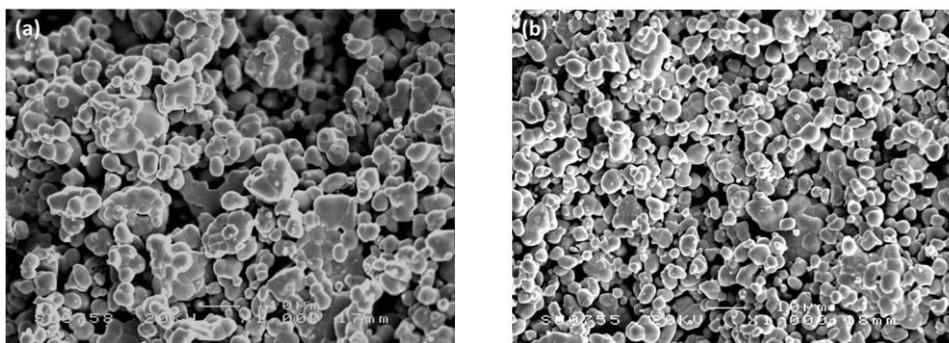
Figure 4.12 SEM image of (a) $Bi_{0.4}Al_{0.6}$ and (b) $Bi_{0.3}Al_{0.7}$.

● **Indium sillenites**

SEM images of indium sillenites $Bi_{12}(Bi_{0.7}In_{0.3})O_{19.5}$ and $Bi_{12}(Bi_{0.6}In_{0.4})O_{19.5}$ are shown in Figures 4.13 (a) and (b), respectively. The morphology of indium sillenites is quite different from the other compositions. The reason might be due to the indium sillenites being sintered above the fluorite phase transition (see DSC results in Figure 4.19) to attain reasonable densities ~ 88 %.

Elemental analysis of indium sillenites were performed on composition $Bi_{0.7}In_{0.3}$ as an example. The EDS spectra and atomic ratio from ten randomly selected points of $Bi_{0.7}In_{0.3}$ are given in Figure 4.14 and Table 4.6, respectively. The EDS derived composition, $Bi_{12}[Bi_{0.64(6)}In_{0.36(6)}]O_{19.5}$ is close to the nominal composition, $Bi_{12}(Bi_{0.7}In_{0.3})O_{19.5}$.
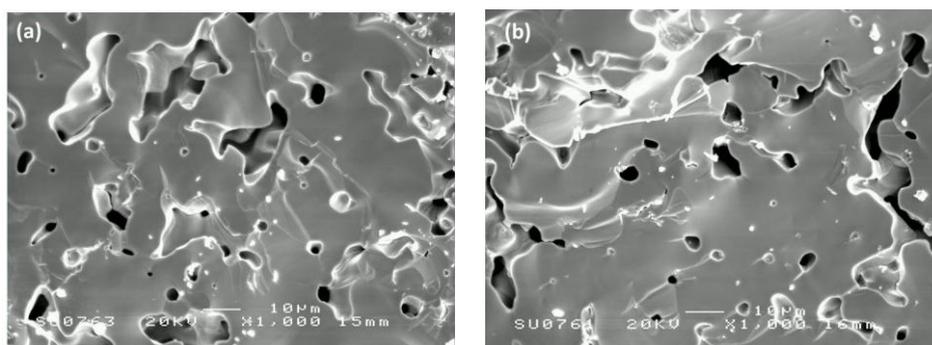
Figure 4.13 SEM image of (a) $Bi_{0.7}In_{0.3}$ and (b) $Bi_{0.6}In_{0.4}$.
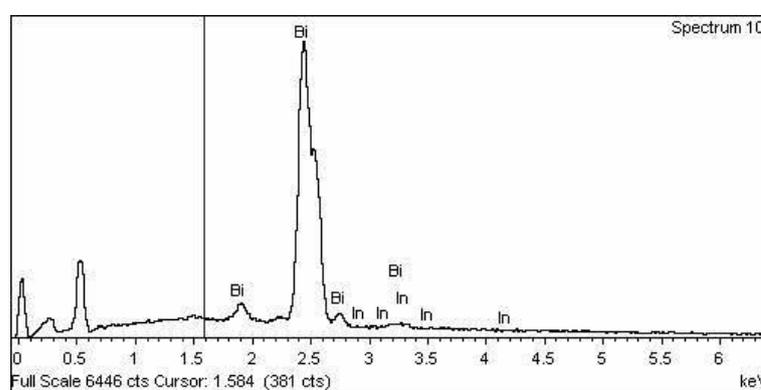
Figure 4.14 EDS spectrum of $Bi_{12}(Bi_{0.7}In_{0.3})O_{19.5}$.

Table 4.6 Atomic ratios of Bi and In obtained via EDS of $Bi_{12}(Bi_{0.7}In_{0.3})O_{19.5}$.

$Bi_{12}(Bi_{0.7}In_{0.3})O_{19.5}$	Bi (atomic %)	In (atomic %)
No.1	96.73	3.27
No.2	97.04	2.96
No.3	96.97	3.03
No.4	96.52	3.48
No.5	97.80	2.20
No.6	97.85	2.15
No.7	97.06	2.94
No.8	96.76	3.24
No.9	97.92	2.08
No.10	97.67	2.33
EDS Averaged Values	**97.2(5)**	**2.8(5)**
Theoretical Values	**97.69**	**2.31**
EDS Derived Composition	$Bi_{12}[Bi_{0.64(6)}In_{0.36(6)}]O_{19.5}$	

4.2.5 DSC

● Zinc sillenites

DSC was performed on $Bi_{0.67}Zn_{0.33}$ from room temperature to 1023 K for three heating and cooling cycles. The enthalpy changes between the sample and reference during the second cycle of heating and cooling are shown in Figure 4.15. This removes any ambiguity associated with water absorbed prior to the first cycle and shows only the intrinsic thermal effects of the sample. From room temperature to 1023 K, there is no obvious thermal event. XRPD data confirmed the sample retained the same sillenite phase after DSC measurements.
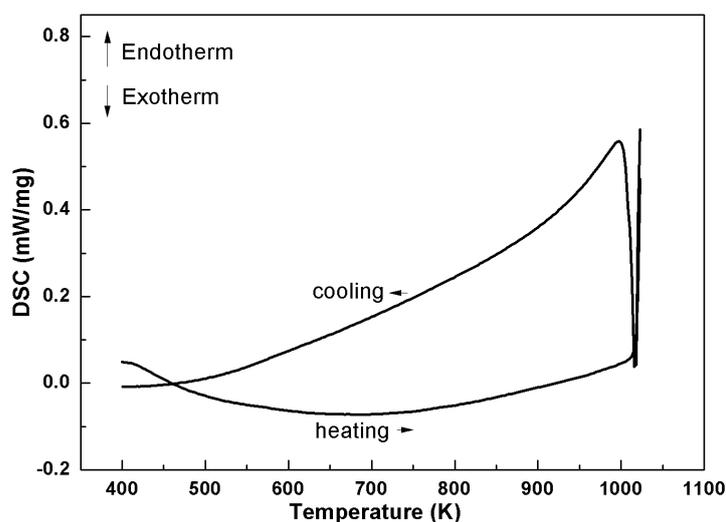
Figure 4.15 DSC trace of $Bi_{12}(Bi_{0.67}Zn_{0.33})O_{19.33.}$

● Iron sillenites

DSC was performed on single phase $Bi_{0.5}Fe_{0.5}$ from room temperature to 1093 K. The enthalpy changes between the sample and reference during heating and cooling are shown in Figure 4.16.
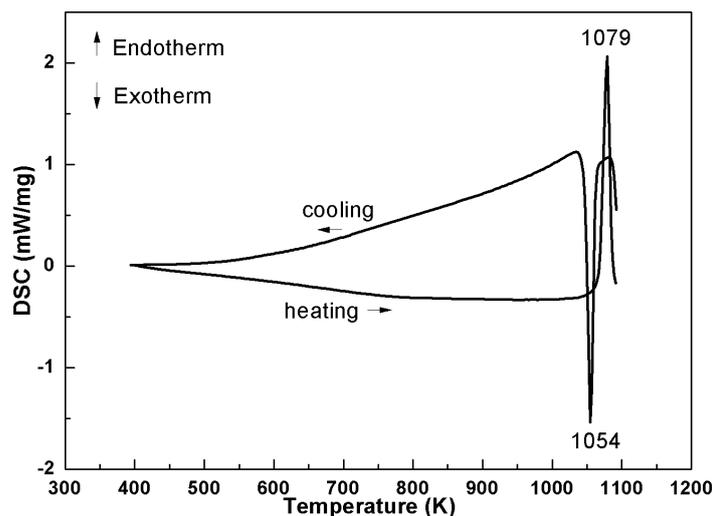
Figure 4.16 DSC trace of $Bi_{12}(Bi_{0.5}Fe_{0.5})O_{19.5}$.

A pair of peaks was shown: an endothermic peak at 1079 K during the heating cycle and a correlated exothermic peak at 1054 K during the cooling cycle. XRPD data on post-DSC measurements showed the sample retained the same sillenite phase and hence inferred a reversible $\gamma \rightarrow \delta \rightarrow \gamma$ phase transition occurred during the DSC measurements.

● **Aluminum sillenites**

DSC was performed on $Bi_{12}(Bi_{0.3}Al_{0.7})O_{19.5}$ and $Bi_{12}(Bi_{0.4}Al_{0.6})O_{19.5}$ from room temperature to 1083 K and they both showed the same thermal behaviour. Here, compound $Bi_{0.3}Al_{0.7}$ is used as an example. The enthalpy changes of the sample during the third heating and cooling cycle are shown in Figure 4.17.

The first two DSC cycles showed complex irreversible enthalpy changes. Therefore, the DSC trace shown here is for the third heating-cooling cycle of the sample when the thermal behaviour becomes repeatable on further cycling. From the DSC trace three main peaks were observed. On the heating cycle there is a large endothermic peak at 1015 K indicating a possible sillenite $\rightarrow \delta$ phase transition occurred. On the cooling cycle, two exothermic peaks occurred at 936 and 813 K indicating possible $\delta \rightarrow \beta$ and $\beta \rightarrow \alpha$ transitions, respectively. The hypothesis for the complicated thermal events was partly

based on the XRPD results on the post-DSC sample: the sillenite phase decomposed to a phase mixture of α-Bi_2O_3 and $Bi_2Al_4O_9$, Figure 4.18.
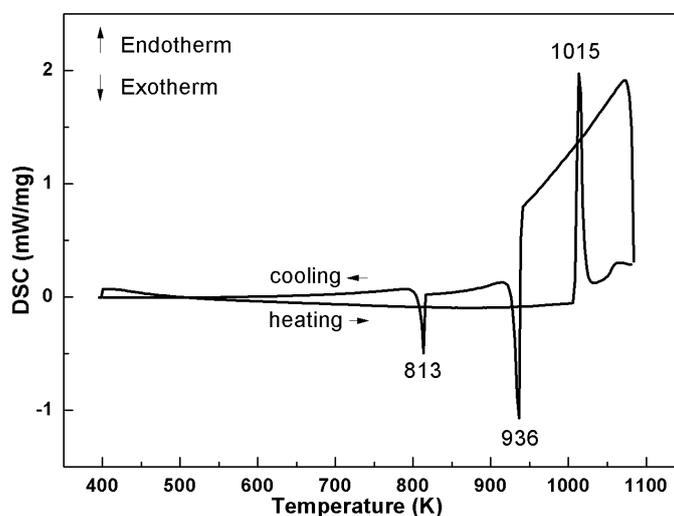
Figure 4.17 DSC trace of $Bi_{12}(Bi_{0.3}Al_{0.7})O_{19.5}$.
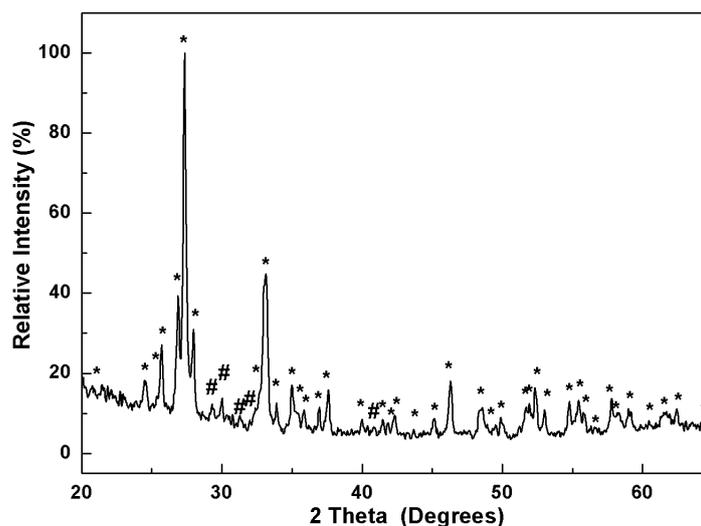
Figure 4.18 XRPD pattern of $Bi_{12}(Bi_{0.3}Al_{0.7})O_{19.5}$ after the DSC measurement. Notations * and # indicate α-Bi_2O_3 (ICCD card [41-1449]) and $Bi_2Al_4O_9$ (ICCD card [25-1048]), respectively.

● **Indium sillenites**

The DSC trace of both indium sillenites: $Bi_{12}(Bi_{0.7}In_{0.3})O_{19.5}$ and $Bi_{12}(Bi_{0.6}In_{0.4})O_{19.5}$ showed the same thermal behaviour in Figure 4.19. A pair of peaks with an endothermic process at 985 K during the heating cycle and a correlated exothermic event at 952 K

during the cooling cycle, indicating a plausible reversible $\gamma \rightarrow \delta \rightarrow \gamma$ phase transition occurs in this sample. XRPD data confirmed the sample retained the same sillenite phase on post-DSC measurements.
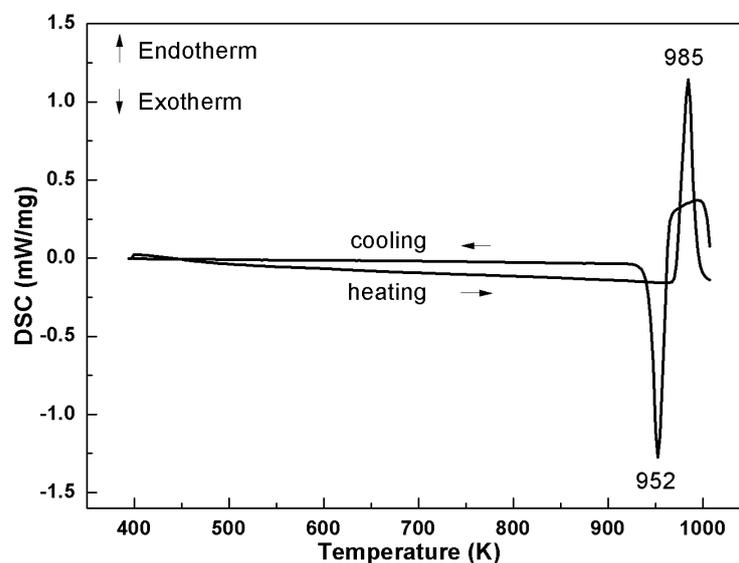
Figure 4.19 DSC trace of $Bi_{0.7}In_{0.3.}$

4.2.6 Thermal Stability Test

A thermal stability test was conducted to test the stability of $Bi_{12}(Bi_{0.67}Zn_{0.33})O_{19.33}$. Two small batches of single-phase $Bi_{0.67}Zn_{0.33}$ were annealed at two different temperatures at 300 and 400 ℃ for 36 hours, respectively. A fast heating rate of 10 ℃/min and a slow cooling rate of 1 ℃/min were applied. XRPD results showed the appearance of a small amount of α-Bi_2O_3 in the sample annealed at 400 ℃ for 36 hours, revealing compound $Bi_{0.67}Zn_{0.33}$ is actually a metastable phase, as shown in Figure 4.20.

Six single-phase batches for $Bi_{12}(Bi_{0.5}Fe_{0.5})O_{19.5}$ were annealed at 250, 300, 400, 500, 600, 650 ℃ for 72 hours, respectively. Examined by XRPD on the post-annealed samples, none of batches decomposed. Therefore, Fe^{3+} sillenite is a thermodynamically stable phase.

Similarly, no decomposition was observed from different batches of single-phase indium sillenites $Bi_{12}(Bi_{0.7}In_{0.3})O_{19.5}$ and $Bi_{12}(Bi_{0.6}In_{0.4})O_{19.5}$ annealed at 300, 400, 500 and

600 ℃ for 72 hours, respectively. This shows In^{3+} sillenites are also thermodynamically stable.
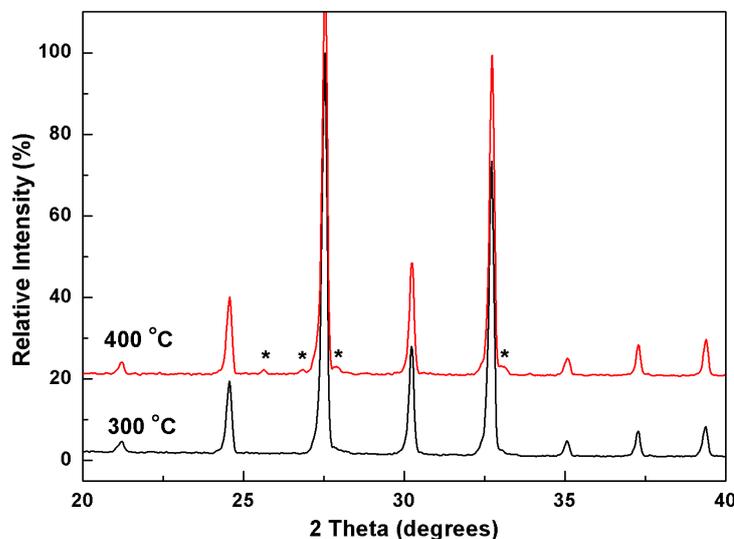
Figure 4.20 XRPD pattern of $Bi_{12}(Bi_{0.67}Zn_{0.33})O_{19.33}$ annealing at 300 and 400 ℃ for 36 hours, respectively. Notation * represents α-Bi_2O_3 phase.

4.2.7 Raman Spectroscopy

Room temperature Raman spectra of the M^{2+}/M^{3+} sillenites compared with that of the 'stoichiometric' sillenite $Bi_{12}SiO_{20}$ are shown in Figure 4.21 and the corresponding Raman peak assignments from literature [14, 15] are listed in Table 4.7. Although M^{2+}/M^{3+} sillenites were classified as stoichiometric sillenites (with a fully occupied oxygen sublattice) by Valant and Suvorov [1], significant differences were revealed from Raman spectra that were not possible from diffraction studies (such as XRPD and NPD) for these small compositional/crystal structural variations caused by different M-cations on the tetrahedral site. The different dopants in the tetrahedral sites (the M cations and the substitution of O3 atom by Bi^{3+} electron lone pairs) have a significant impact on the local structure in the tetrahedra and in the framework of the sillenites.

Significant peak broadening in M^{2+}/M^{3+} sillenites was observed throughout the entire Raman spectra in comparison with the ideal sillenite $Bi_{12}SiO_{20}$, Figure 4.21. Three important features can be captured: (i) A prominent increase in the magnitude of the Raman peak at line 12, which upshifted from ~ 358 cm^{-1} for $Bi_{12}SiO_{20}$ to ~ 380 cm^{-1} for

M^{2+}/M^{3+} sillenites. The Raman peak at line 12 is assigned to O1-Bi-O2 and O1-Bi-O3 bending. [15] (ii) Splitting of the peak at ~ 530 cm^{-1} (e.g. into 516 cm^{-1} and 526 cm^{-1} for $Bi_{0.67}Zn_{0.33}$) was observed in all M^{2+}/M^{3+} sillenites. Peak 516 cm^{-1} (line 15a) was postulated to be related to the concentration of BiO_3LP units in the structure.[15] (iii) The strongest Raman peak changed from ~ 530 cm^{-1} (line 15) for the ideal sillenite $Bi_{12}SiO_{20}$ to ~ 80 cm^{-1} (line 3) for the M^{2+}/M^{3+} sillenites. The Raman peaks at ~ 530 cm^{-1} (line 15) and ~ 80 cm^{-1} (line 3) associated with the O1 vibrations[14, 15] and the Bi, O2 and O3 vibrations elongating the cluster [14], respectively. This indicates the interatomic distances of the framework units are larger and more disordered in M^{2+}/M^{3+}compared with ideal sillenite $Bi_{12}SiO_{20}$.
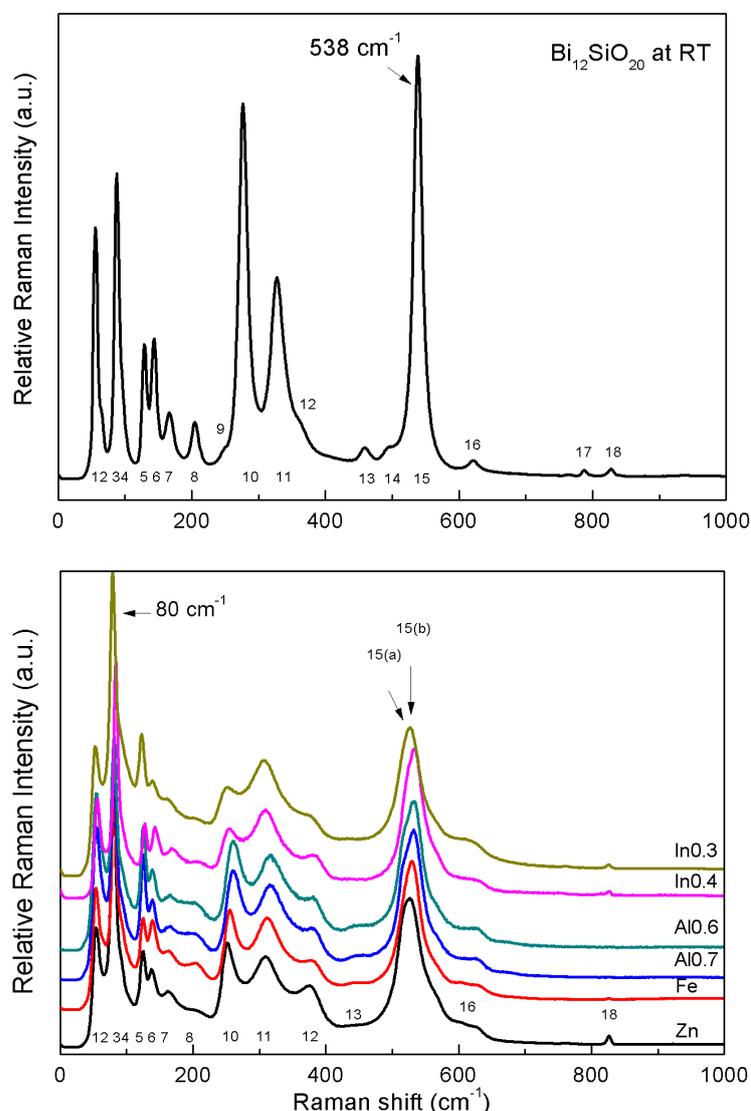
Figure 4.21 Raman Spectra of M^{2+}/M^{3+} sillenites in comparison with $Bi_{12}SiO_{20}$ at room temperature.

Table 4.7 Raman peak positions of M^{2+}/M^{3+} sillenites compared with $Bi_{12}SiO_{20}$.

Line No.	Si	$Zn_{0.33}$	$Fe_{0.5}$	$Al_{0.7}$	$Al_{0.6}$	$In_{0.4}$	$In_{0.3}$	Mode [15]	Type of Vibrations[14, 15]
1	55	54	54	55	55	55	53	F	Bi,O2,O3 and M vibration
2	63	-	-	-	-	-	-	E	Bi,O1,O2 and O3vibrations elongating the cluster along either [100] or [001]
3	88	79*	81*	82*	82*	83*	79*	E	Bi,O2 and O3 vibrations elongating the cluster
4	95	93	90	90	90	95	94	A	Bi-O1 bonds vibration and 'breathing' of O2 atoms
5	129	125	125	125	126	128	123	E	Bi and O2 vibrations elongating the cluster along either [100] or [010]
6	144	137	139	140	140	143	139	A	'breathing' of Bi and O2 atoms
7	166	162	163	169	169	167	161	A	'breathing' of Bi and all O atoms
8	204	205	203	203	203	205	205	F	Bi-O1 stretching & Bi-O2-Bi bending and weak Bi-O1 rocking
9	251	-	-	-	-	-	-	E	Bi-O1 rocking and weak O2 vibrations elongating the cluster along either [100] or [001]
10	276	252	256	263	264	254	252	A	O2 'breathing' and weak Bi-O1 rocking
11	328	309	312	320	322	310	306	A	Bi-O1 rocking and weak O2 'breathing'
12	358	376	376	382	386	381	377	F	O1-Bi-O2 and O1-Bi-O3 bending
13	460	-	443	456	456	-	-	E	O2 vibration elongating the cluster along either [001] or [010] and weak Bi-O1 and Bi-O3 rocking
14	488	-	-	-	-	-	-	F	Bi-O1 stretching and deformation of MO4 tetrahedra
15(a)	538*	516	520	517	521	517	517	A	'breathing' of O1 atoms
15(b)		526	530	533	535	532	527		
16	621	626	626	626	623	625	625	E	O3 vibrations elongating the cluster along either [010] or [100] and weakBi-O1 and Bi-O2 rocking
17	788	-	-	-	-	-	-	A	Symmetric stretching of MO_4 tetrahedra
18	829	826	826	-	-	826	826	FTO	Anti-symmetric stretching of MO_4 tetrahedra

Notation * indicates the strongest peak intensity.

The Raman peak positions are inversely proportional to the mass of the groups of bonded atoms; therefore, the vibrational modes of framework Bi polyhedra, BiO_5LP, dominate the Raman spectra at frequencies below ~ 600 cm^{-1}; whereas the vibrational modes of the MO_4 tetrahedra occur at frequencies above ~ 600 cm^{-1}. Peaks at ~ 826 cm^{-1} (line 18) are associated with MO_4 tetrahedral vibrations. Whether or not the MO_4 tetrahedra vibrations above 700 cm^{-1} can be observed was dependent on the mass of the bonded groups of the atoms involved (MO_4 tetrahedra).

4.2.8 Microwave (MW) Dielectric Properties

MW dielectric measurements were carried out on all phase-pure sillenites using the resonant cavity method. A summary of the results is listed in Table 4.8. The measured sillenite compounds showed similar dielectric properties regardless of the M-dopants, with relative permittivity (ε_r) ~ 30-35; Q ~ 200-400 at resonant frequency f_0 ~ 6-7.5 GHz and τ_f ~ -15 to -202 ppm/K. A strong correlation between pellet density and ε_r was observed, for instance, Al^{3+} sillenites fired at a low temperature (735 °C) to avoid phase decomposition resulted in low pellet density (~ 55 %) and consequently low ε_r.

Table 4.8 MW dielectric properties of M^{2+}/M^{3+} sillenites.

Composition	Sintering Temperature (°C)	Pellet Density (%)	ε_r	Q	f_0 (GHz)	Q.f (GHz)	τ_f (ppm/K)	CM calculated ε_r
$Bi_{12}(Bi_{2/3}Zn_{1/3})O_{19.33}$	740	86	32.5	293	6.503	1905	-31	37
$Bi_{12}(Bi_{0.5}Fe_{0.5})O_{19.5}$	770	87	36.6	407	6.124	2493	-15	38
$Bi_{12}(Bi_{0.3}Al_{0.7})O_{19.5}$	735	56	26.4	205	7.199	1475	-71	33
$Bi_{12}(Bi_{0.4}Al_{0.6})O_{19.5}$	735	57	28.2	220	7.523	1654	-67	35
$Bi_{12}(Bi_{0.6}In_{0.4})O_{19.5}$	780	87	31.8	231	7.031	1624	-202	34
$Bi_{12}(Bi_{0.7}In_{0.3})O_{19.5}$	780	88	34.2	298	6.067	1807	-192	36

● Relative permittivity (ε_r)

All measured ε_r were close to those calculated from the Clausius-Mossotti equation, except for the Al sillenites due to their low pellet density. The similarity of ε_r with different M-dopants in sillenites, ε_r ~ 35, can be explained by the fact that the total polarizability of the sillenite unit cell does not change dramatically with the small concentration of M-cations in these materials. However, the CM calculation can sometimes under-estimate ε_r, e.g. In^{3+} and Fe^{3+} sillenites, due to errors associated with highly polarisable atoms such as Bi^{3+} and/or In^{3+} ions in an unexpected large unit cell.

● Temperature coefficient of resonant frequency (τ_f)

Unlike ε_r, τ_f changes significantly with the composition of the sillenites, i.e. the variation of M-site dopants. The most temperature dependent samples were $Bi_{0.7}In_{0.3}$ and $Bi_{0.6}In_{0.4}$ with $\tau_f \sim -192$ and -202 ppm/K, respectively. Composition $Bi_{0.67}Zn_{0.33}$, $Bi_{0.3}Al_{0.7}$ and $Bi_{0.4}Al_{0.6}$ had τ_f in a range of -30 to -70 ppm/K. The best τ_f value (~ -15 ppm/K) was obtained from $Bi_{0.5}Fe_{0.5}$. Sillenites with similar compositions, i.e. solid solutions, had similar τ_f values. In the M^{2+}/M^{3+} group, Bi contents in the M-sites did not play a vital role in the variation of τ_f; whereas the M-dopants did.

Recent investigations have revealed a structural influence to τ_f in many perovskites due to tilting of the oxygen octahedra and hence, the tolerance factor with different ionic radii combinations of A, B and O ions have a strongly influence on τ_f.[16-18] Valant and Suvorov[19] then reported the oxygen sublattice was also an important factor in influencing the τ_f of sillenites. They stated that the O(3)-O(3) distance in the tetrahedra can be changed by the ionic radii of the M-site cations, therefore, Bi^{3+} ions in the M-site with a distorted structure would also make an impact on τ_f. In the end, they concluded two trends: (i) for large M-site ions ($r > 0.31$ Å), τ_f increases with a decrease in ionic size; (ii) for small M-site ions ($r < 0.31$ Å), τ_f is independent of ionic size with a value of ~ 20 ppm/K. However, the results reported in this thesis have found these statements to be controversial. The τ_f as a function of the M-ion ionic radii of M^{2+}/M^{3+} sillenites from our results, Figure 4.22, reveal that (i) by introducing different concentrations of Bi^{3+} ions in M-site, τ_f did not exhibit a strong dependency on the perturbation of the oxygen sublattice caused by Bi^{3+} ions and their lone electron pairs. For instance, compound $Bi_{0.67}Zn_{0.33}$ and $Bi_{0.7}In_{0.3}$ with similar concentrations of Bi^{3+} interstitial ions (~ 0.7), had τ_f of -31 and -192 ppm/K, respectively; and (ii) the correlations between τ_f and the M-ion ionic radii are more complicated than the two above mentioned trends proposed by Valant and Suvorov[19]. All of our prepared sillenites belong to the large M-site ion ($r > 0.31$ Å) group; however, it is impossible to extract an empirical near linear trend of "increasing τ_f with a decrease in

ionic size"; instead these are scattered data and show no trend. Compound $Bi_{0.5}Fe_{0.5}$ in this large ion group obtained the best τ_f value of -15 ppm/K for near-zero τ_f applications.
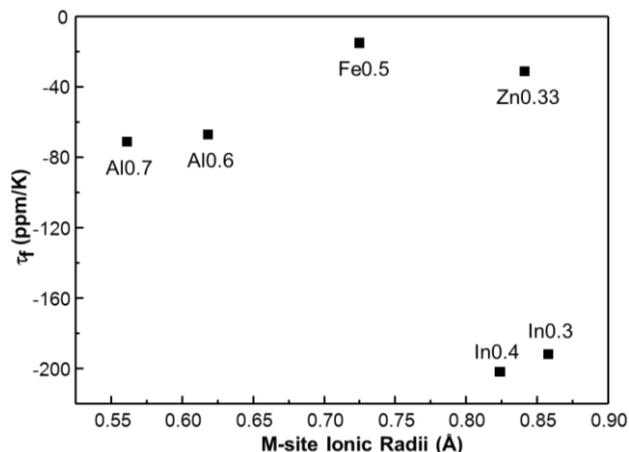
Figure 4.22 τ_f as a function of the M-ions ionic radii of M^{2+}/M^{3+} sillenites. (Note: M-site ionic radii were from Shannon[8] with Bi^{3+} (V) = 0.96 Å, Zn^{2+} (VI) = 0.6 Å, Fe^{3+} (VI) = 0.49 Å, Al^{3+} (VI) = 0.39 Å and In^{3+} (VI) = 0.62 Å)
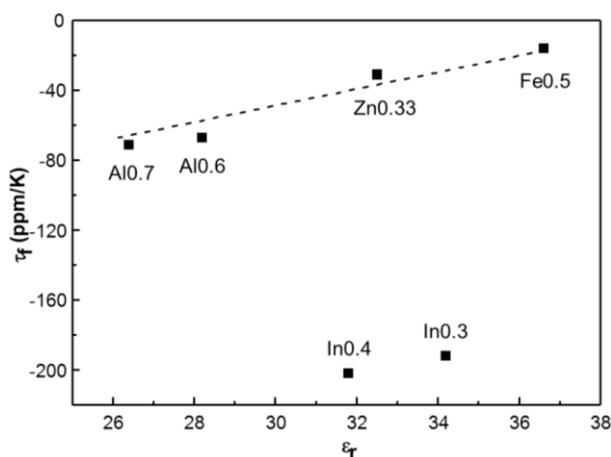
Figure 4.23 The relationship between τ_f and ε_r of M^{2+}/M^{3+} sillenites after Harrop [20].

Another relationship between τ_f and ε_r has been established by Harrop[20] and it is typified by many 3C-type perovskites: τ_f becomes increasingly positive as ε_r increases. τ_f as a function of ε_r for M^{2+}/M^{3+} sillenites is plotted in Figure 4.23. The general trend as expected from Harrop[20] can be observed for most compounds with τ_f close to 0 ppm/K for the highest permittivity compound $Bi_{0.5}Fe_{0.5}$, $\varepsilon_r \sim$ 37. However, indium sillenites disobey the general trend, with an unexpected large and negative $\tau_f \sim$ -200 ppm/K, for a moderate $\varepsilon_r \sim$ 33. The discrepancy of τ_f for In^{3+} sillenites may be related to the temperature- and

frequency-dependent relaxation close to RT observed from *rf* fixed frequency measurement (Session 4.2.9).

- **Dielectric losses (tan δ)**

The dielectric losses are a combination of intrinsic losses arising from the anharmonic vibrations of the material itself[21, 22] and extrinsic losses from processing such as porosity, secondary phases, grain size, grain growth and defects *etc*.[23, 24] It is well-known that oxides with highly ordered cations have less dielectric losses and large Q.f's, for example in the 1:2 B-site ordered perovskites $Ba(Zn_{1/3}Ta_{2/3})O_3$ and related systems.[25-27] Hence, from an intrinsic losses aspect, cation ordering on the M-site of sillenites would be expected to affect the dielectric losses. Our results again showed disagreement with the empirical correlations between Q.f and M-ion size purposed by Valant and Suvorov: Q.f values decreases with increasing M-ion sizes when r > 0.31Å.[19] $Bi_{0.5}Fe_{0.5}$ with a medium M-ion size showed the highest Q.f value of ~ 2500 GHz (measured at 6 GHz) among all M^{2+}/M^{3+} sillenites studied, Figure 4.24.
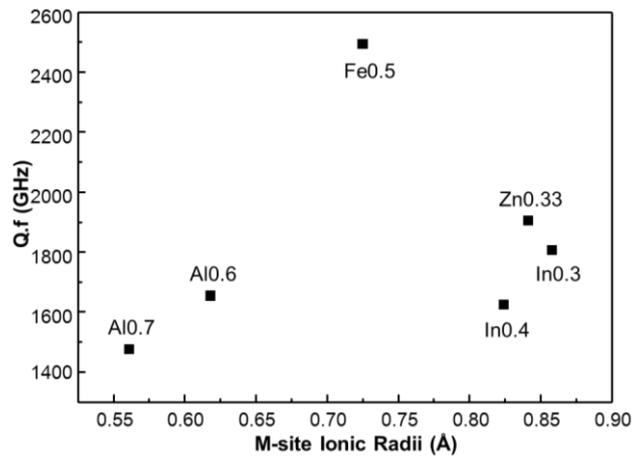
Figure 4.24 Q.f as a function of M-site ionic radii of M^{2+}/M^{3+} sillenites.

The basic formula of ε_r revealed an inversely proportional relationship with resonant frequency f (i.e. $f \approx \frac{c}{\lambda\, \varepsilon^{1/2}} \approx \frac{c}{D\, \varepsilon^{1/2}}$).[28] Therefore, increasing ε_r is expected to have a

fundamental trade-off of Q.f. However, this relationship cannot be observed for either measured ε_r or CM calculated ε_r, Figure 4.25.
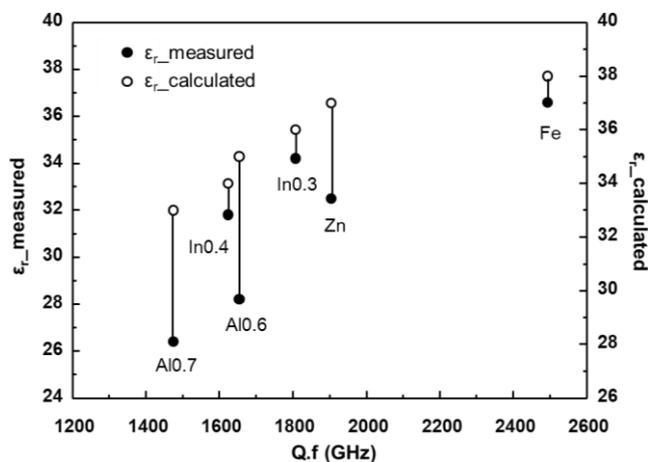
Figure 4.25 Correlation between Q.f and measured ε_r ($\circ$) / CM calculated ε_r ($\bullet$) for M^{2+}/M^{3+} sillenites.

4.2.9 Fixed Frequency Capacitance Measurements

MW dielectric properties of M^{2+}/M^{3+} sillenites performed at 6-7.5 GHz, revealed $\varepsilon_r \sim 30$-35, Q.f~ 1,500-2,500 GHz with τ_f from -15 to -202 ppm/K. In order to correlate the fixed frequency data with MW dielectric properties, variation of ε_r as a function of temperature in the range 10-320 K for all six samples at 1 MHz is shown in Figure 4.26. It is obvious that the negative value of τ_f from MW dielectric property is consistent with the increase of ε_r (due to a positive τ_ε from the relationship $\tau_f = - \left(\frac{\tau\varepsilon}{2} + \alpha_L \right)$) in fixed frequency data. Hence, the negative value of τ_f is influenced by the presence of the temperature- and frequency- dependent relaxation behaviour of sillenites, where a positive trend of τ_ε appeared for all the analogues.
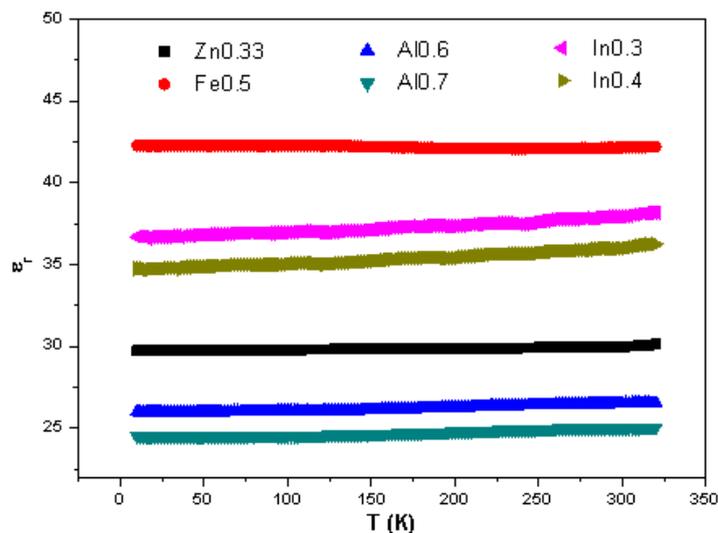
Figure 4.26 ε_r versus T for six sillenites: $Bi_{0.67}Zn_{0.33}$, $Bi_{0.5}Fe_{0.5}$, $Bi_{0.3}Al_{0.7}$, $Bi_{0.4}Al_{0.6}$, $Bi_{0.6}In_{0.4}$ and $Bi_{0.7}In_{0.3}$ extracted from an LCR meter (at 1 MHz) with a Cryocooler (10 – 320 K).

The variation of capacitance (hence, ε_r) and the dielectric loss (tan δ) with temperature were obtained using fixed frequency measurements at 1, 10, 100 K and 1M Hz over 10 – 750 K for M^{2+}/M^{3+} sillenites. Data were obtained from an LCR meter connected with a Cryocooler (10 – 320 K) and a high temperature furnace (> 300 K). The small difference in measured ε_r due to differences in the stray capacitance associated with the different jig settings was corrected by ε_r values measured at 300 K using a "Test Fixture Box" measurement with a minimal stray capacitance. Due to the fragile/low density (~ 57 %) of the aluminium sillenites, where only data from Cryocooler (10 – 320 K) were obtained successfully, a frequency dispersion region of ε_r and tan δ above room temperature (RT) was observed in all other measured samples: $Bi_{0.67}Zn_{0.33}$, $Bi_{0.5}Fe_{0.5}$, $Bi_{0.7}In_{0.3}$ and $Bi_{0.6}In_{0.4}$.

● **Zinc sillenites**

The temperature dependence of the permittivity (ε_r) and dielectric loss (tan δ) at fixed frequencies of 1, 10, 100 k and 1 MHz over the temperature range from 10 to 820 K of $Bi_{12}(Bi_{0.67}Zn_{0.33})O_{19.33}$ is shown in Figure 4.27 (a) and (b). A broad frequency-dispersive region of ε_r was observed above room temperature, with the peak maximum shifting to

higher temperature with increasing frequency. The 1 and 10 kHz data exhibit a peak with ε_r maximum of $\sim$ 83 and 86 at temperatures of $\sim$ 694 and 769 K, respectively. The corresponding capacitance maximum of the 1 and 10 kHz data are 7.35×10^{-12} and 7.61×10^{-12} F.cm^{-1}, respectively. The data at 100 kHz and 1 MHz does not show the presence of a peak maximum within the measured temperature range. In the tan δ plot, the frequency dispersion behaviour is not observed within the measured temperature range.
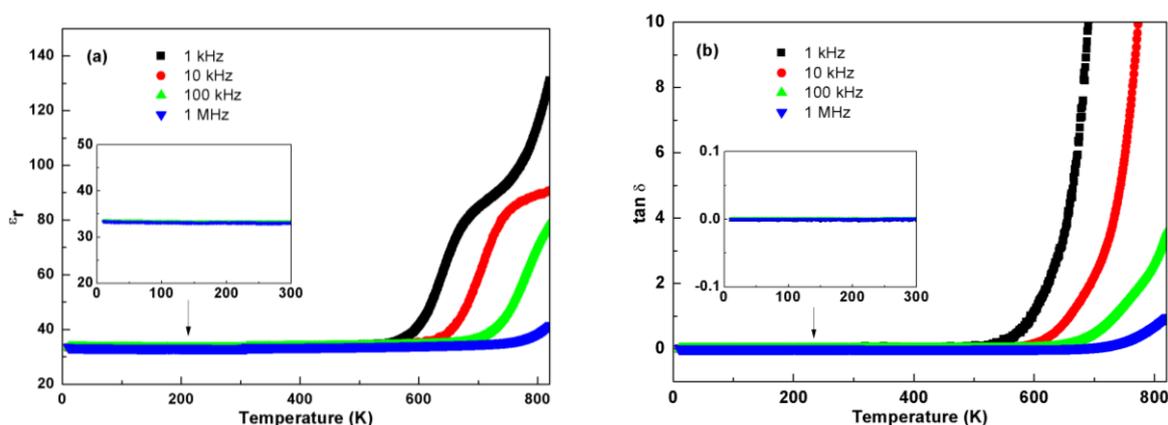
Figure 4.27 Temperature dependence of (a) permittivity and (b) dielectric losses of compound $Bi_{12}(Bi_{0.67}Zn_{0.33})O_{19.33}$. Insets are expanded view of lower temperature data between 10 and 300 K.

● **Iron sillenites**

Temperature dependence of ε_r and tan δ for $Bi_{12}(Bi_{0.5}Fe_{0.5})O_{19.5}$ in the temperature range of 10 – 840 K are shown in Figure 4.28 (a) and (b), respectively. In the ε_r plot, there were two relaxation processes (R1 and R2) observed above 400 K, which correspond to two relaxations in the tan δ plot with the second relaxation (R2) significantly dominating the first relaxation (R1). The magnitude of the R2 tan δ peak at 1 kHz was $\sim$ 65, which was $\sim$ 100 times larger than that of R1 ($\sim$ 0.65) at 1 kHz.

In the first relaxation (R1), the ε_r peak maximum at 1, 10, 100 k and 1 MHz are $\sim$ 150, 136, 78 and 50 at temperatures of $\sim$ 563, 634, 690 and 754 K, with a corresponding capacitance maximum of 1.33×10^{-11}, 1.20×10^{-11}, 6.91×10^{-12} and 4.43×10^{-12} F.cm^{-1}, respectively. Similarly, in the second relaxation (R2), the ε_r peak maximum at 1, 10 and

100 kHz are ~ 226, 155 and 103 at temperatures of ~ 686, 755 and 830 K, with a corresponding capacitance maximum of 2×10^{-11}, 1.37×10^{-11} and 9.12×10^{-12} F.cm^{-1}, respectively. The ε_r peak maximum at 1 MHz for R2 was not observed within the measured temperature range.
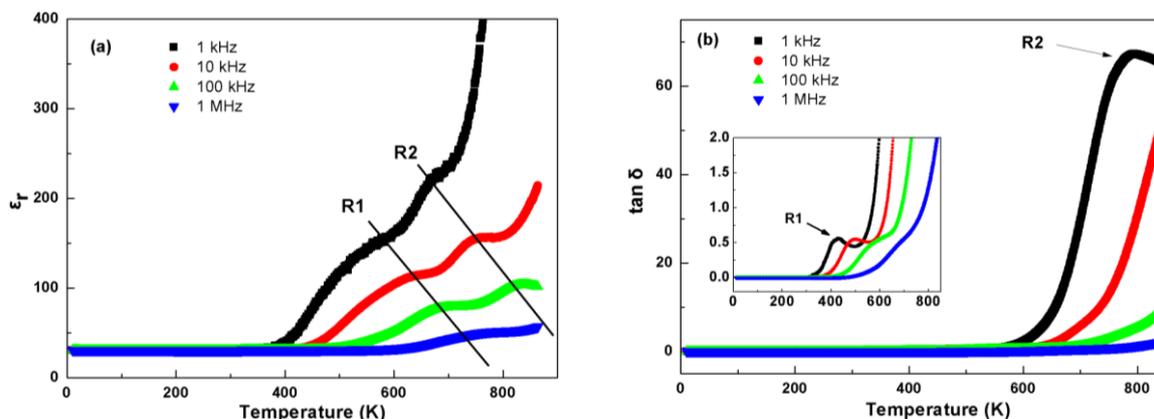
Figure 4.28 Temperature dependence of (a) permittivity and (b) dielectric losses of $Bi_{0.5}Fe_{0.5}$. R1 and R2 indicate two relaxation events. Insets are an expanded view of the y-axis data to show R1.

● **Indium sillenites**

$Bi_{0.6}In_{0.4}$ and $Bi_{0.7}In_{0.3}$ exhibit identical temperature dependence of ε_r and tan δ. Hence, $Bi_{0.7}In_{0.3}$ is used as a representative example. A broad frequency-dispersive region was observed in the ε_r plot, Figure 4.29 (a). The 1, 10, 100 k and 1 MHz data exhibit a peak with an ε_r maximum of ~ 79, 73, 66 and 60 at temperatures of ~ 514, 580, 657 and 749 K, respectively. The corresponding capacitance maximum of the 1, 10 and 100 kHz data are 6.99×10^{-12}, 6.46×10^{-12}, 5.84×10^{-12} and 5.31×10^{-12} F.cm^{-1}, respectively. In the tan δ plot, Figure 4.29 (b), only the corresponding peak maximum at 1 kHz data with a value of ~ 733 at 709 K was observed in the measured temperature range.
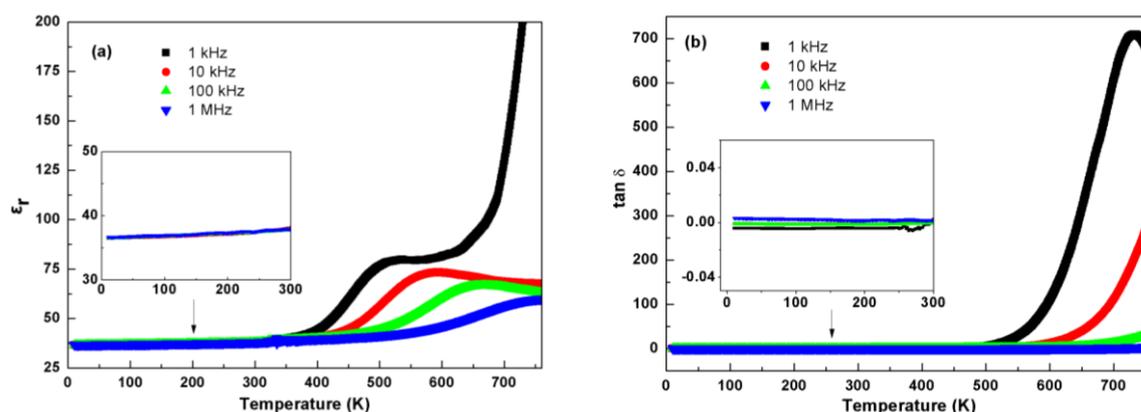
Figure 4.29 Temperature dependence of (a) permittivity and (b) dielectric losses of compound $Bi_{0.7}In_{0.3}$. Insets are expanded view of lower temperature data between 10 and 300 K.

4.2.10 Impedance Spectroscopy (IS)

To investigate the relaxation behaviour observed from *rf* fixed frequency capacitance measurements, IS measurements were performed on single-phase samples. All measured M^{2+}/M^{3+} sample details for low temperature (10-320 K) and high temperature IS measurements (320–800 K) are listed in Table 4.10.

Table 4.9 Details of M^{2+}/M^{3+} sillenite samples from IS measurements. The $Bi_{0.67}Zn_{0.33}$ sample used silver paste electrodes; the rest used gold-sputtered electrodes.

Composition	Sintering Temperature / ℃	Pellet Density / %	Activation Energy (bulk) / eV
$Bi_{12}(Bi_{0.67}Zn_{0.33})O_{19.33}LP_{0.67}$	740	86	1.20
$Bi_{12}(Bi_{0.5}Fe_{0.5})O_{19.5}LP_{0.5}$	770	87	0.57
$Bi_{12}(Bi_{0.3}Al_{0.7})O_{19.5}LP_{0.3}$	735	56	0.80
$Bi_{12}(Bi_{0.4}Al_{0.6})O_{19.5}LP_{0.4}$	735	57	0.84
$Bi_{12}(Bi_{0.6}In_{0.4})O_{19.5}LP_{0.6}$	780	87	0.73
$Bi_{12}(Bi_{0.7}In_{0.3})O_{19.5}LP_{0.7}$	780	88	0.74

Consistent with *rf* fixed frequency results, low temperature IS measurements for all samples did not show any relaxation dispersion of capacitance (ε') and/or dielectric losses (tan δ). All samples were too resistive to observe any arc from Z* impedance plots below RT and required high temperature IS measurements to get reasonable bulk data. $Bi_{12}(Bi_{0.7}In_{0.3})O_{19.5}$ was chosen as an example to show the general IS behaviour of M^{2+}/M^{3+}

sillenites. The IS data for other compounds and the correlated circuit fitting results are shown in Appendix III.

A typical IS data set for $Bi_{12}(Bi_{0.7}In_{0.3})O_{19.5}$ at 573 K is shown in Figure 4.30. The complex impedance (Z*) plot, Figure 4.30 (a), showed the presence of a single semicircle, with a depression angle of ~ 7.2 ° compared with the ideal value of 0 °. The admittance (Y') spectroscopic plot, Figure 4.30 (b), showed a frequency-independent plateau attributed to the *dc* conductivity, R^{-1}, at low frequencies; with frequency-dependent power law behaviour at higher frequency. Similar with the C' spectroscopic plot of ideal sillenite: $Bi_{12}SiO_{20}$ (Chapter 3), the capacitance (C') spectroscopic plots of M^{2+}/M^{3+} sillenites also exhibited two plateaux: one at high frequency and one at low frequency, e.g. $Bi_{0.7}In_{0.3}$ in Figure 4.30 (c). The high-frequency plateau ($f \sim 10^6$ Hz) is temperature-independent with an associated capacitance of ~ 4 pF.cm^{-1} ($\varepsilon_r \sim 45$), which is assigned as a bulk response of the sample; whereas the low frequency plateau ($f \sim 10^4$ Hz) is slightly temperature-dependent with C' ~ 6.5 pF.cm^{-1} ($\varepsilon_r \sim 73$). This capacitance fluctuation, Figure 4.31, is correlated to the large, broad relaxor-liked peaks in the *rf* fixed frequency measurements, Figure 4.29. In the combined –Z", M" spectroscopic plot, Figure 4.30 (d), a single, almost coincident peak is observed in both spectra, with a corresponding Δf ~ 0.2 decades, where Δf = log (f_M) – log (f_Z). (f_M and f_Z are the frequencies at the peak maximum in the Debye peaks of the –Z" and M" spectroscopic plots). Ideally a homogeneous ceramic would have a Δf value of 0 decades. The corresponding FWHM (Full Width Half Maximum) value of the M" peak is ~ 1.34 decades which is higher than the ideal value of 1.14 decades. This relatively wide M" Debye peak indicates the sample is heterogeneous and probably caused by the permittivity fluctuation from the bulk response of the sample.
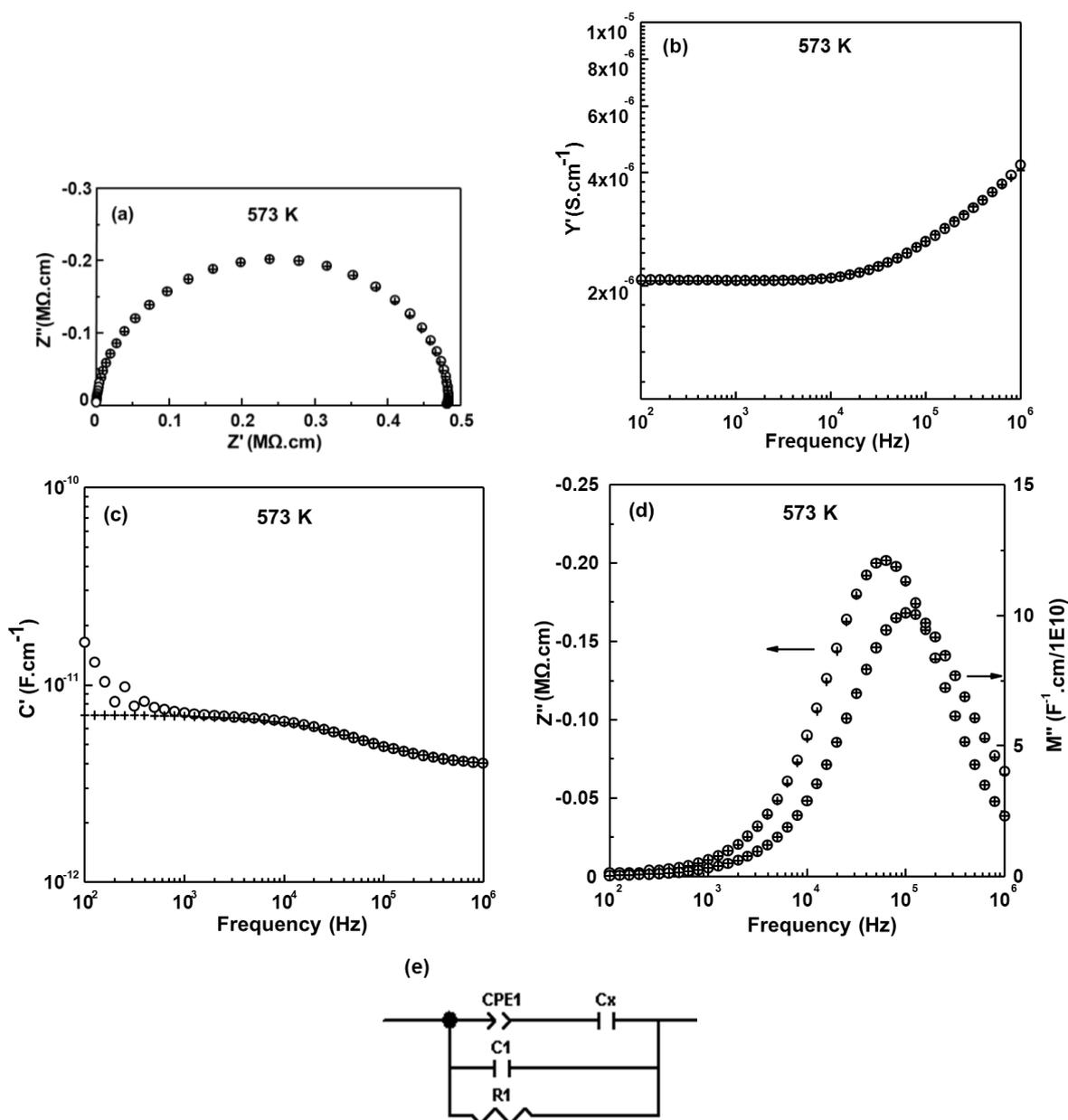
Figure 4.30 Impedance spectroscopy data of the IS experimental data points and the fitting results to equivalent circuit shown in (e) with (a) Z* plot; (b) Y', (c) C', and (d) −Z"/M" spectroscopic plots at 573 K for $Bi_{12}(Bi_{0.7}In_{0.3})O_{19.5}$.
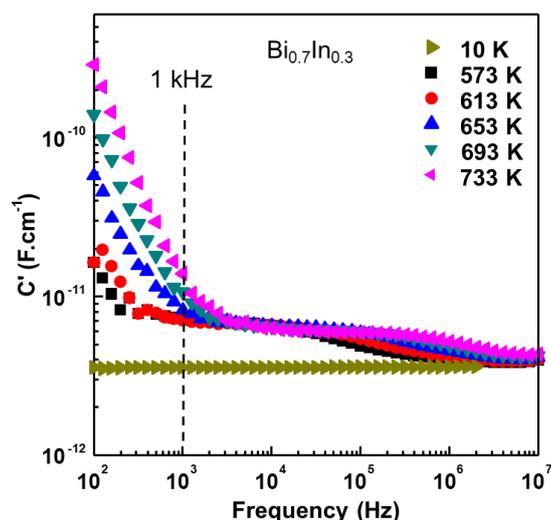
Figure 4.31 C' spectroscopic plot at various temperatures for $Bi_{12}(Bi_{0.7}In_{0.3})O_{19.5}$.

All the fitted results with the circuit parameters are shown in Table 4.11 for $Bi_{0.7}In_{0.3}$ in the temperature range from 573 to 653 K. For IS data above 653 K the proposed equivalent circuit, Figure 4.30 (e), is not suitable to model the impedance response of the sample as it exhibits ionic conductivity above 653 K.

Table 4.10 Fitted values of $Bi_{12}(Bi_{0.7}In_{0.3})O_{19.5}$ from 573 to 653 K. Errors associated with the fitted circuit parameters R_1, C_1, C_x, A and n are $< \pm0.06\%$, $< \pm0.6\%$, $< \pm2.8\%$, $< \pm16.1\%$ and $< \pm3.2\%$, respectively.

Temperature (K)	R_1 (Ω cm)	C_1 (pF cm^{-1})	C_x (pF cm^{-1})	A (Ω^{-1} cm^{-1} rad^{-1})	n
573	484670	3.80	3.24	1.95×10^{-8}	0.31
593	321960	3.80	3.29	2.25×10^{-8}	0.32
613	223940	3.72	3.85	1.39×10^{-8}	0.37
633	123340	3.83	2.98	4.88×10^{-8}	0.31
653	82855	3.83	2.86	6.51×10^{-8}	0.30

4.2.10.1 Ionic Conductivity of Indium Sillenites (T > 653 K)

Indium sillenites: $Bi_{12}(Bi_{0.7}In_{0.3})O_{19.5}LP_{0.7}$ and $Bi_{12}(Bi_{0.6}In_{0.4})O_{19.5}LP_{0.6}$ are the only super-stoichiometric sillenites prepared in M^{2+}/M^{3+} sillenite analogues. At temperature above 653 K, the predominant feature of indium sillenites is the presence of a low frequency spike attached with a single semicircle at high frequency in Z* plots; whereas no spike was observed for other M^{2+}/M^{3+} sillenites in Z* plots. Here, compound $Bi_{0.7}In_{0.3}$ is selected to show this electrical behaviour.

The Z* plot of $Bi_{0.7}In_{0.3}$ at 733 K, Figure 4.32, showed a low frequency spike with an inclined angle of ~ 23 ° to the x-axis. Its associated capacitance was ~ 8.7×10^{-10} $F.cm^{-1}$. At 793 K the low-frequency spike inclined at ~ 45 ° to the x-axis and its associated capacitance was ~ 3.1×10^{-9} $F.cm^{-1}$. The capacitance values of the spike has a tendency of reaching ~ 10^{-7} $F.cm^{-1}$ at elevated temperatures, indicating an ionic polarisation phenomenon at blocking electrodes may be taking place.[29] However, the composition of indium sillenites $Bi_{12}(Bi_{0.7}In_{0.3})O_{19.5}LP_{0.7}$ shows that the excess oxygen sublattice is filled by 0.2 Bi^{3+} electron lone pairs from the tetrahedral site. According to the R model, the excess ions will occupy the crystallographic O(4) site. It might be possible that some of the O(3) oxygen was exchanged by Bi^{3+} electron lone pairs from O(4) site, therefore, some of the O(4) site could be partially occupied by oxygen ions instead of Bi^{3+} electron lone pairs so as to favour ionic conduction.

Super-stoichiometric P^{5+} sillenite analogues: $Bi_{12}P_{0.92}O_{20.3}$ and $Bi_{12}P_{0.86}O_{20.15}$ are reported as mixed electronic and oxide ionic conductors < 750 ℃,[30] the conduction species of indium sillenites might also be mixed, a set of conductivity measurement need to be performed in oxygen free atmosphere to examine whether there is an electronic contribution to the conduction.
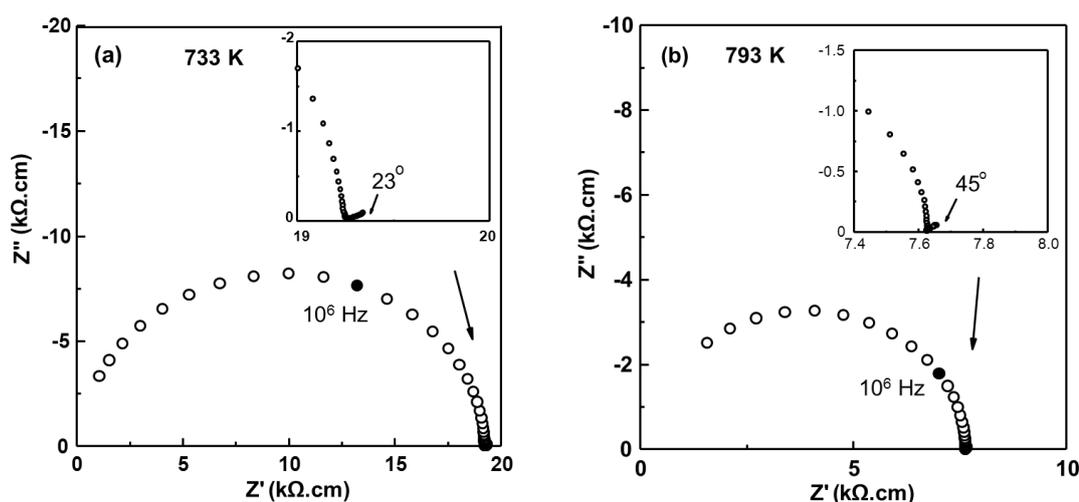
Figure 4.32 Z* plot of $Bi_{0.7}In_{0.3}$ at (a) 733 and (b) 793 K.

4.2.10.2 Arrhenius plot of bulk conductivity

Bulk conductivity data for all measured M^{2+}/M^{3+} sillenites were calculated from the M"
Debye peak and plotted in Arrhenius format, as shown in Figure 4.33. The bulk
conductivity is strongly influenced by the oxygen content of the sillenite. Among the
measured sillenites, stoichiometric sillenite $Bi_{12}(Bi_{0.67}Zn_{0.33})O_{19.33}LP_{0.67}$, with the oxygen
sublattice fully occupied was the most resistive compound and has the highest activation
energy (Ea) for bulk conduction with the value of 1.20 eV. Super-stoichiometric sillenites:
$Bi_{12}(Bi_{0.6}In_{0.4})O_{19.5}LP_{0.6}$ and $Bi_{12}(Bi_{0.7}In_{0.3})O_{19.5}LP_{0.7}$, with excess lone pair electrons in the
oxygen sublattice had Ea of 0.73 and 0.74 eV, respectively. Sub-stoichiometric sillenites:
$Bi_{12}(Bi_{0.3}Al_{0.7})O_{19.5}LP_{0.3}\square_{0.2}$ and $Bi_{12}(Bi_{0.4}Al_{0.6})O_{19.5}LP_{0.4}\square_{0.1}$, with some vacancies in the
oxygen sublattice had Ea of 0.8 and 0.84 eV, respectively. The only exception is
$Bi_{12}(Bi_{0.5}Fe_{0.5})O_{19.5}LP_{0.5}$ which has the stoichiometric formula with a fully filled oxygen
sublattice, but exhibited the lowest Ea of 0.57 eV. This might indicate that the oxygen
sublattice was in fact not fully occupied, but deficient due to the presence of mixed valence
state of Fe^{2+}/Fe^{3+} atoms. Mössbauer spectroscopy has been used to study the oxidation
environments of Fe atoms, but due to the low concentration of Fe atoms in the composition
the data analysis was not successful.
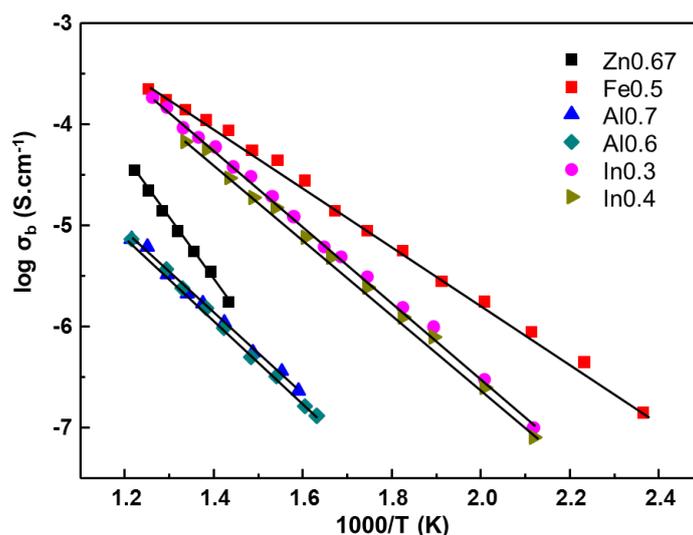
Figure 4.33 Arrhenius plot of bulk conductivity versus reciprocal temperature for all
M^{2+}/M^{3+} sillenites.

4.3   Discussion

4.3.1   Formation of Divalent/Trivalent Cations Doping Sillenites

All prepared single-phase M^{2+}/M^{3+} sillenites with their lattice parameters are listed in Table 4.12. Not all of the formed sillenites obeyed the VS general formula: $Bi_{12}(Bi_{0.67}M^{2+}_{0.33})O_{19.33}$ and $Bi_{12}(Bi_{0.5}M^{3+}_{0.5})O_{19.5}$ for M^{2+} and M^{3+} dopants, respectively.[1] For instance, instead of forming the expected composition $Bi_{12}(Bi_{0.5}M^{3+}_{0.5})O_{19.5}$, Al^{3+} and In^{3+} formed narrow solid solution ranges: $[Bi_{12}(Bi_{0.3}Al_{0.7})O_{19.5} - Bi_{12}(Bi_{0.4}Al_{0.6})O_{19.5}]$s.s. and $[Bi_{12}(Bi_{0.6}In_{0.4})O_{19.5} - Bi_{12}(Bi_{0.7}In_{0.3})O_{19.5}]$s.s, respectively. Consistent with existing literature,[6, 9, 31, 32] transition metals Zn^{2+} and Fe^{3+} obeyed the VS formula. Other reported examples that closely obeyed the VS formula were: $Bi_{12}(Bi_{0.6875}Cd^{2+}_{0.33})O_{19.3645833}$[5]; $Bi_{12.7}Co^{2+}_{0.3}O_{19.35}$[33] and $Bi_{12}(Bi_{0.5}Tl^{3+}_{0.5})O_{19.5}$[34].

This revealed there is a correlation between the size of the dopant ion and the lattice parameter of the resultant sillenite phase, Figure 4.34. A near linear relationship can be observed for prepared M^{2+}/M^{3+} sillenites, which is in general agreement with Poleti *et al.*[31] and Donovan[7].

Table 4.11 Summary of prepared single-phase M^{2+}/M^{3+} sillenites.

VS formula	Single-phase Composition	Reaction Temperature (℃)	Lattice Parameter, a(Å)	Unit Cell Volume (Å³)
M^{2+}:$Bi_{12}(Bi^{3+}_{0.67}M^{2+}_{0.33})O_{19.33}$	$Bi_{12}(Bi_{0.67}Zn_{0.33})O_{19.33}$	735	10.2072(3)	1063.46(6)
M^{3+}: $Bi_{12}(Bi^{3+}_{0.5}M^{3+}_{0.5})O_{19.5}$	$Bi_{12}(Bi_{0.5}Fe_{0.5})O_{19.5}$	745	10.18927(15)	1057.86(3)
	$Bi_{12}(Bi_{0.3}Al_{0.7})O_{19.5}$	730	10.17255(13)	1052.66(2)
	$Bi_{12}(Bi_{0.4}Al_{0.6})O_{19.5}$	730	10.1765(3)	1053.88(5)
	$Bi_{12}(Bi_{0.6}In_{0.4})O_{19.5}$	750	10.2293(2)	1070.37(9)
	$Bi_{12}(Bi_{0.7}In_{0.3})O_{19.5}$	750	10.23583(18)	1072.40(3)
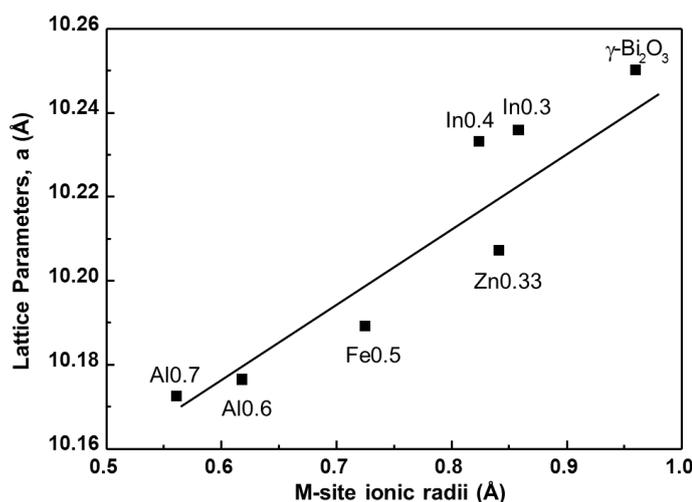
Figure 4.34 The relationship between the unit cell parameters and the M-site ionic radii of M^{2+}/M^{3+} sillenites (as there is lack of data for four-fold coordinated Bi^{3+} ions in a M-site, ionic radius data of Bi^{3+} ions with a coordination number of five was used $rBi^{3+}_{(V)} = 0.96$ Å from Shannon[35]); data for γ-Bi_2O_3[35] is included for comparison.

4.3.2 Thermal Stability of M^{2+}/M^{3+} Sillenites

The metastability of the parent γ-Bi_2O_3 phase made it worthy to study the phase stability of the sillenite phases by DSC and thermal annealing results.

The annealing tests for zinc sillenite at 400 ℃ for 36 hours showed it partially decomposed into sillenite and α-Bi_2O_3 phases, Figure 4.20. The decomposition process is very slow and zinc sillenite is still a kinetically stable phase. DSC was not sensitive enough to show any obvious decomposition process in the sample.

The thermal stability tests for iron sillenite showed it is a thermodynamically stable phase below ~ 780 ℃, it undergoes a reversible $\gamma \rightarrow \delta$ phase transition above ~ 780 ℃, Figure 4.16.

DSC results showed that aluminium sillenites were not thermodynamically stable. The first two DSC cycles of aluminium sillenites showed complex irreversible enthalpy changes, which is outside the scope of this current work. When the thermal behaviour becomes repeatable at/after the third heating cycle, phase transformation to the stable δ phase at high temperature occurred. During the cooling cycle, the δ phase might transform to the metastable β-polymorph and then transform to the stable α-phase. Finally XRPD

137

result, Figure 4.18, revealed that aluminium sillenite was hardly observed from the XRPD results after the DSC measurements, where a phase mixture of α-Bi_2O_3 and $Bi_2Al_4O_9$ was present. Therefore, aluminium sillenites are short-lived metastable phases and rapid decomposition processes can take place.

Based on the heating temperature and heating time of the reported sillenites by the solid state reaction method, Poleti et $al.$[31] summarized a list with increasing phase stability of various dopants, where $Sb^{5+} < Co^{2+} \approx Mn^{4+} < Fe^{3+} \approx Si^{4+} < Ti^{4+} < V^{5+} < Zn^{2+} <$ Pb^{2+}. The reaction temperature and time for Fe^{3+} and Zn^{2+} sillenites was reported as 800 ℃ for 3 hours and 690 ℃ for 3 hours, respectively. However, the current results here showed disagreement with part of the above summary. In the current work Fe^{3+} and Zn^{2+} sillenites were prepared at similar reaction temperatures of 745 and 735 ℃ for 16 and 96 hours, respectively. Thermal annealing test showed Zn^{2+} sillenite is a metastable phase whereas Fe^{3+} is not. Hence, the increasing relative stability of the prepared four dopants should be $Al^{3+} < Zn^{2+} < In^{3+} < Fe^{3+}$.

4.3.3 Structural Features of M^{2+}/M^{3+} Sillenites

Detailed structural variations of M^{2+}/M^{3+} sillenites in comparison with M^{4+} ideal sillenites have been proposed by Radaev and Simonov.[9] In their model, tetrahedral sites are statistically filled by various M^{2+}/M^{3+} cations (including Bi^{3+}) leading to incomplete occupation by O(3) atoms. In contrast to ideal sillenites where the framework units (Bi-octahedral BiO_5LP formed dimers) are linked by "rigid" tetrahedral units ($M^{4+}O_4$), the structure of M^{2+}/M^{3+} sillenites are more complicated with three important types of Bi-polyhedra, Figure 4.35.

(1) Bi(1)O_4LP, Figure 4.36 (a), with the configuration of this polyhedron corresponds to a distorted trigonal bipyramid with an unshared electron pair in the equatorial plane LP-O(1a)-O(1b) and axial vertices O(1c) and O(2). To allow redistribution of the valence forces in this polyhedron, Bi(1) atom displace in the direction opposite to the vacancy of the O(3) atom, giving a shortening of the long Bi-O(1c) bond.

(2) Bi_MO_3LP, Figure 4.36 (b), with one of the missing O(3) atoms occupied by the unshared electron pair of Bi^{3+} atom, forming umbrella-shaped tetrahedral units.

(3) $Bi(3)O_5LP$, Figure 4.36 (c), which are polyhedra connected with regular MO_4 tetrahedra. It is noteworthy that the bond lengths of these polyhedra actually differ from their analogues in ideal sillenites. To achieve local valence balance, (as the valence of cations M^{2+}/M^{3+} is less than 4+) the Bi-O(3) bonds are shortened and the correlated Bi-O(1b) and Bi-O(1c) bonds are lengthened.

All the above structural changes, in terms of the variations of Bi-polyhedron, are "averaged" over the whole structure. Radaev and Simonov[9] reported that the Bi-O(3) bond is 0.05-0.06 Å shorter and Bi-O(1b) bond is 0.02-0.03 Å longer in comparison with that of the ideal sillenite $Bi_{12}GeO_{20}$, Table 4.3.

The most noticeable feature of the RT Raman spectra, Figure 4.21, is the upshift and increase of the magnitude of peak at ~ 380 cm^{-1} (line 12) for M^{2+}/M^{3+} sillenites, compared with that of ideal sillenite $Bi_{12}SiO_{20}$ at ~ 358 cm^{-1}. This peak was assigned as O1-Bi-O2 and O1-Bi-O3 bending.[15] The dramatic increase of the magnitude of this peak is believed to be associated with the influence of distorted tetrahedral unit, BiO_3LP, where one O(3) site is occupied by an electron lone pairs of Bi^{3+}.[15]
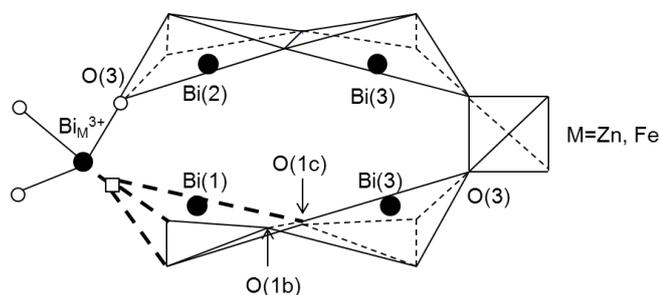
Figure 4.35 Fragment of structure features showing dimers linked with various neighbourhood of tetrahedra in M^{2+}/M^{3+} sillenites.[9]
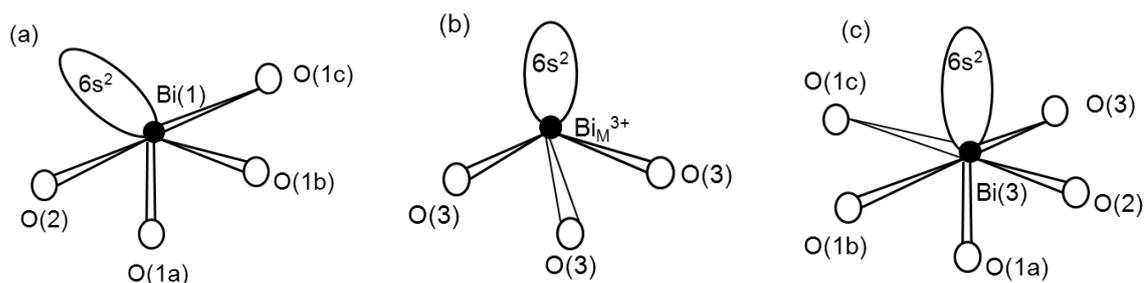
Figure 4.36 Schematic representation of Bi-polyhedron in M^{2+}/M^{3+} sillenites with (a) $Bi(1)O_4LP$; (b) Bi_MO_3LP and (c) $Bi(3)O_5LP$. [9]

As a result, structural distortion can be induced by the defect contents of the O(3) atoms. This increases the concentration of trigonal bipyramid Bi-polyhedra, Bi(1)O4LP in Figure 4.36 (a), which leads to a distorted framework of the sillenites. The numbers of these trigonal bipyramid Bi-polyhedra, Bi(1)O4LP for the studied M^{2+}/M^{3+} sillenites $Bi_{0.67}Zn_{0.3}$, $Bi_{0.5}Fe_{0.5}$, $Bi_{0.3}Al_{0.7}$, $Bi_{0.4}Al_{0.6}$, $Bi_{0.6}In_{0.4}$ and $Bi_{0.7}In_{0.3}$ are 16.67, 12.5, 7.5, 10, 15 and 17.5 % of all polyhedra in the structures, respectively. The way of inducing defect contents of the O(3) atoms in this case is by introducing Bi^{3+} with electron lone pairs into the tetrahedral sites. However, there is an upper limit between the amount of Bi^{3+} and M cations occupying the tetrahedral sites; this may be influenced by the size and charge of both ions. Whether this distortion could cause a change in space group of the sillenite; or how does this distortion develop and hence allow a structural transition to the δ-polymorph at elevated temperatures is still an interesting research topic.

4.3.4 The Correlations Between Bulk Conductivity and Q.f

The origin of the difference in quality factor (Q.f, where $Q \sim \frac{1}{\tan \delta}$ and f = resonant frequency) of all samples was investigated by comparing the electrical conductivity and analysing the onset temperature of γ-δ phase transitions. The correlation of activation energy and Q.f is listed in Table 4.13. Four compounds with similar pellet density (~ 87 ± 2%) were compared, Figure 4.37. It is observed that the increase in activation energy (i.e. decrease of conductivity near room temperature) would cause an increase of Q.f. The only

exception is the Fe^{3+} analogue, which is the most conducting compound and yet has the highest Q.f value. Based on similar pellet density and assuming all four compounds have similar extrinsic loss effects on Q.f (such as porosity, secondary phases, grain size, grain growth and defects), therefore, the intrinsic losses of Q.f arising from the anharmonic vibrations of the material itself must play an important role. A compound with higher Q.f value might indicate it has a more ordered or regular structure. The onset temperature of the γ-δ phase transition for compound $Bi_{0.5}Fe_{0.5}$ was the highest (at 806 ℃), which indicates $Bi_{0.5}Fe_{0.5}$ was the most stable sillenite compound in this series of samples.

Table 4.12 Summary of sintering temperature, pellet density, Ea for bulk conduction, Q.f and polymorphic phase transition temperature for the M^{2+}/M^{3+} sillenites under study.

Composition	Sintering Temperature / ℃	Pellet Density / %	Activation Energy Ea(bulk) / eV	Q.f (GHz)	Temperature of γ to δ phase from DSC/ ℃
$Bi_{12}(Bi_{0.67}Zn_{0.33})O_{19.33}$	740	86	1.20	1905	750
$Bi_{12}(Bi_{0.5}Fe_{0.5})O_{19.5}$	770	87	0.57	2493	806
$Bi_{12}(Bi_{0.3}Al_{0.7})O_{19.5}$	735	56	0.80	1475	742
$Bi_{12}(Bi_{0.4}Al_{0.6})O_{19.5}$	735	57	0.84	1654	740
$Bi_{12}(Bi_{0.6}In_{0.4})O_{19.5}$	780	87	0.73	1624	712
$Bi_{12}(Bi_{0.7}In_{0.3})O_{19.5}$	780	88	0.74	1807	711
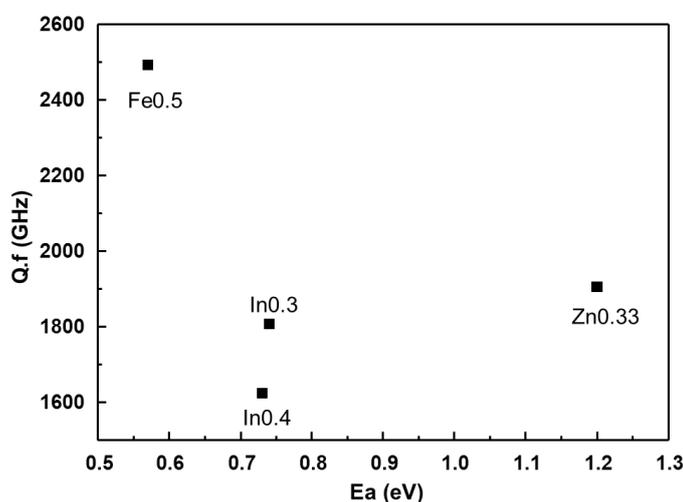
Figure 4.37 Activation energy for bulk conduction versus Q.f for $Bi_{0.67}Zn_{0.33}$, $Bi_{0.7}In_{0.3}$, $Bi_{0.6}In_{0.4}$ and $Bi_{0.5}Fe_{0.5}$.

4.4 Conclusions

Not all of the prepared sillenites obeyed the VS general formula, transition metals Zn^{2+} and Fe^{3+} obeyed the formula and formed sillenites $Bi_{12}(Bi_{0.67}Zn_{0.33})O_{19.33}LP_{0.67}$ and $Bi_{12}(Bi_{0.5}Fe_{0.5})O_{19.5}LP_{0.5}$, respectively in the Bi_2O_3-M_xO_y binary system. p-block cations Al^{3+} and In^{3+} disobeyed the general formula and formed limited solid solutions $[Bi_{12}(Bi_{0.3}Al_{0.7})O_{19.5}LP_{0.3}\square_{0.2}$–$Bi_{12}(Bi_{0.4}Al_{0.6})O_{19.5}LP_{0.4}\square_{0.1}]$ s.s. and $[Bi_{12}(Bi_{0.6}In_{0.4})O_{19.5}LP_{0.6}$ – $Bi_{12}(Bi_{0.7}In_{0.3})O_{19.5}LP_{0.7}]$ s.s, respectively. Consistent with Poleti et al.,[31] a near linear relationship between the average M-site ions and lattice parameters of M^{2+}/M^{3+} sillenites was observed.

The phase stability of the sillenites was studied by combined analysis of DSC and thermal annealing tests. Zn^{2+} and Al^{3+} sillenites were found to be metastable phases, whereas Fe^{3+} and In^{3+} sillenites were thermodynamically stable. The increasing relative stability of the prepared four dopants is $Al^{3+} < Zn^{2+} < In^{3+} < Fe^{3+}$. SEM and EDS results on Zn^{2+}, Fe^{3+} and In^{3+} sillenites confirmed the derived compositions were similar to the theoretical compositions, which proves the Bi-loss was insignificant (if there was any) in these sillenites.

Rietveld refinements were carried out on NPD data of $Bi_{12}(Bi_{0.5}Zn_{0.5})O_{19.25}$, $Bi_{12}(Bi_{0.3}Al_{0.7})O_{19.5}$ and $Bi_{12}(Bi_{0.7}In_{0.3})O_{19.5}$. The starting models were based on Radaev's model (R model) of $Bi_{12}(Bi^{3+}_{0.67}Zn^{2+}_{0.33})O_{19.33}LP_{0.67}$ and $Bi_{12}(Bi^{3+}_{0.5}Fe^{3+}_{0.5})O_{19.5}LP_{0.5}$ for M^{2+} and M^{3+} dopants, respectively.[6] The final refinement results generally agreed with the starting models. Although some authors suggest the possibility of changing the space group in sillenites,[11, 12] our refinement work confirmed the best fits were obtained from space group I23. However, there was probably more than one sillenite structural model: with different M-ions, the final structural model might be different from sillenite to sillenite.

Rietveld refinements of In^{3+} sillenites exhibited a slight distortion in the framework structure. Compound $Bi_{12}(Bi_{0.7}In_{0.3})O_{19.5}LP_{0.7}$ belongs to the super-stoichiometric group and the oxygen sublattice is in excess with oxygen atoms in the voids of the framework.

The slight distortion in the framework of In^{3+} sillenites can also be observed from Raman spectra. Raman spectroscopy highlighted the local structures and showed apparent structural differences, especially for the framework units of studied M^{2+}/M^{3+} sillenites compared with an ideal sillenite such as $Bi_{12}SiO_{20}$, although they have all been classified as stoichiometric sillenites by Valant and Suvorov[1].

Microwave dielectric results revealed compounds $Bi_{0.67}Zn_{0.33}$ and $Bi_{0.5}Fe_{0.5}$ to show promising microwave dielectric properties Due to the metastable nature and long reaction time of $Bi_{0.67}Zn_{0.33}$, compound $Bi_{0.5}Fe_{0.5}$ with $\varepsilon_r \sim 36.6$; Q.f ~ 2500 GHz and $\tau_f \sim -15$ ppm/K is the only suitable commercial candidates for LTCC applications.

The negative values of τ_f observed in all measured M^{2+}/M^{3+} sillenites, which are influenced by the presence of the temperature- and frequency-dependent relaxation behaviour of sillenites, where a positive trend of $\tau\varepsilon$ appeared for all the analogues. Similar with the ideal sillenite $Bi_{12}SiO_{20}$ in Chapter 3, a non-ferroelectric relaxor-like behaviour was observed by a combined study of fixed frequency dielectric measurements and IS above room temperature for all sillenites. IS data were successfully modelled by the equivalent circuit used in Chapter 3. The origin of this relaxor-type behaviour is again attributed to the non-correlated local dipole moments associated with the BiO_5LP units in the framework.

High temperature IS measurements revealed super-stoichiometric In^{3+} sillenites: $Bi_{0.6}In_{0.4}$ and $Bi_{0.7}In_{0.3}$ to exhibit detectable levels of oxide ion conductivity at temperature > 653 K.

The concentration of oxygen-deficiency and/or lone-electron pairs of Bi^{3+} in the oxygen sublattice affects the conductivity (σ_b) of the sillenites. Except for compound $Bi_{0.5}Fe_{0.5}$, it is observed that the increase of activation energy for bulk conduction (i.e. a decrease of conductivity near RT) results in an increase of Q.f at RT.

4.5 References

[1]   M. Valant and D. Suvorov, A stoichiometric model for sillenites, Chemistry of Materials, 2002. **14**: p. 3471-3476.

[2]   S. F. Radaev, V. I. Simonov and Y. F. Kargin, Structural features of γ-phase Bi_2O_3 and its place in the sillenite family, Acta Crystallographica Section B-Structural Science, 1992. **48**: p. 604-609.

[3]   S. F. Radaev and V. I. Simonov, Structure of sillenites and atomic mechanisms of isomorphous substitutions, Kristallografiya, 1992. **37**: p. 914-941.

[4]   R. N. Vannier, F. Abraham, G. Nowogrocki and G. Mairesse, New structural and electrical data on Bi-Mo mixed oxides with a structure based on $[Bi_{(12)}O_{(14)}]^{(\infty)}$ columns, Journal of Solid State Chemistry, 1999. **142**: p. 294-304.

[5]   J. C. Champarnaud-Mesjard and B. Frit, A structural model for the $Bi_{1-x}Cd_xO_{1.5-x/2}$ (0 <= x <= 0.0256) sillenite-type solid solution, Comptes Rendus De L Academie Des Sciences Serie Ii Fascicule C-Chimie, 1999. **2**: p. 369-374.

[6]   S. F. Radaev, L. A. Muradyan and V. I. Simonov, Atomic structure and crystal chemistry of sillenites $Bi_{12}(Bi^{3+}_{0.50}Fe^{3+}_{0.50})O_{19.50}$ and $Bi_{12}(Bi^{3+}_{0.67}Zn^{2+}_{0.33})O_{19.33}$, Acta Crystallographica Section B-Structural Science, 1991. **47**: p. 1-6.

[7]   A. G. Donovan, "Synthesis and characterisation of Bi-based electroceramics," Ph.D. Thesis, University of Sheffield, 2009.

[8]   R. D. Shannon, Revised effective ionic radii and systematic studies of interatomic distances in halides and chalcogenides, Acta Crystallographica Section A, 1976. **32**: p. 751-767.

[9]   S. F. Radaev and V. I. Simonov, Structure of sillenites and atomic mechanisms of their isomorphic substitutions, Kristallografiya, 1992. **37**: p. 484-499.

[10]   N. E. Brese and M. Okeeffe, Bond-valence parameters for solids, Acta Crystallographica Section B-Structural Science, 1991. **47**: p. 192-197.

[11]   S. Neov, V. Marinova, M. Reehuis and R. Sonntag, Neutron-diffraction study of $Bi_{12}MO_{20}$ single crystals with sillenite structure (M = Si, $Si_{0.995}Mn_{0.005}$, $Bi_{0.53}Mn_{0.47}$), Applied Physics a-Materials Science & Processing, 2002. **74**: p. S1016-S1018.

[12]   T. I. Mel'nikova, G. M. Kuz'micheva, V. B. Rybakov, N. B. Bolotina and A. B. Dubovsky, On symmetry of sillenites, Crystallography Reports, 2010. **55**: p. 229-232.

[13]   T. I. Mel'nikova, G. M. Kuz'micheva, V. B. Rybakov, N. B. Bolotina, A. B. Dubovskii and A. Cousson, Composition and structure of solid solutions in the Bi_2O_3-SiO_2-$V_2^{5+}O_5$ system with the structure sillenite, Journal of Structural Chemistry, 2011. **52**: p. 510-516.

[14]   B. Mihailova, M. Gospodinov and L. Konstantinov, Raman spectroscopy study of sillenites. I. Comparison between $Bi_{12}(Si,Mn)O_{20}$ single crystals, Journal of Physics and Chemistry of Solids, 1999. **60**: p. 1821-1827.

[15]   A. V. Egorysheva, V. I. Burkov, Y. F. Kargin, V. G. Plotnichenko, V. V. Koltashev, E. D. Obraztsova and S. V. Terekhov, Atomic structure features of sillenite crystals as probed by Raman spectroscopy, Russian Journal of Inorganic Chemistry, 2005. **50**: p. 238-245.

[16]   E. L. Colla, I. M. Reaney and N. Setter, Effect of structural changes in complex perovskites on the temperature-coefficient of the relative permittivity, Journal of Applied Physics, 1993. **74**: p. 3414-3425.

[17]   I. M. Reaney, E. L. Colla and N. Setter, Dielectric and structural characteristics of Ba-based and Sr-based complex perovskites as a function of tolerance factor, Japanese Journal of Applied Physics Part 1-Regular Papers Short Notes & Review Papers, 1994. **33**: p. 3984-3990.

[18]   R. Rawal, A. J. McQueen, L. J. Gillie, N. C. Hyatt, E. E. McCabe, K. Samara, N. M. Alford, A. Feteira, I. M. Reaney and D. C. Sinclair, Influence of octahedral tilting on the microwave dielectric properties of $A_3LaNb_3O_{12}$ hexagonal perovskites (A=Ba, Sr), Applied Physics Letters, 2009. **94**.

[19]   M. Valant and D. Suvorov, Processing and dielectric properties of sillenite compounds $Bi_{12}MO_{20-\delta}$ (M = Si, Ge, Ti, Pb, Mn, $B_{1/2}P_{1/2}$), Journal of the American Ceramic Society, 2001. **84**: p. 2900-2904.

[20]   P. J. Harrop, Temperature coefficients of capacitance of solids, Journal of Materials Science, 1969. **4**: p. 370-374.

[21]   V. L. Gurevich and A. K. Tagantsev, Intrinsic dielectric loss in crystals, Advances in Physics, 1991. **40**: p. 719-767.

[22]   A. K. Tagantsev, J. Petzelt and N. Setter, Relation between intrinsic microwave and submillimeter losses and permittivity in dielectrics, Solid State Communications, 1993. **87**: p. 1117-1120.

[23]   S. J. Penn, N. M. Alford, A. Templeton, X. R. Wang, M. S. Xu, M. Reece and K. Schrapel, Effect of porosity and grain size on the microwave dielectric properties of sintered alumina, Journal of the American Ceramic Society, 1997. **80**: p. 1885-1888.

[24]   M. Valant and D. Suvorov, Microstructural phenomena in low-firing ceramics, Materials Chemistry and Physics, 2003. **79**: p. 104-110.

[25]   S. Kawashima, M. Nishida, I. Ueda and H. Ouchi, $Ba(Zn_{1/3}Ta_{2/3})O_3$ ceramics with low dielectric loss at microwave frequencies, Journal of the American Ceramic Society, 1983. **66**: p. 421-423.

[26]   S. B. Desu and H. M. Obryan, Microwave loss quality of $Ba(Zn_{1/3}Ta_{2/3})O_3$ ceramics, Journal of the American Ceramic Society, 1985. **68**: p. 546-551.

[27]   R. Zurmuhlen, J. Petzelt, S. Kamba, G. Kozlov, A. Volkov, B. Gorshunov, D. Dube, A. Tagantsev and N. Setter, Dielectric spectroscopy of $Ba(B'_{1/2}B''_{1/2})O_3$ complex perovskite ceramics: correlations between ionic parameters and microwave dielectric properties. II. Studies below the phonon Eigenfrequencies (102-1012 Hz). Journal of Applied Physics, 1995. **77**: p. 5351-5364.

[28]   A. J. Moulson and J. M. Herbert, *Electroceramics: materials, properties, applications. (Second Edition).* Chichester, England: John Wiley & Sons Ltd., 2003.

[29]   J. T. S. Irvine, D. C. Sinclair and A. R. West, Electroceramics: Characterization by impedance spectroscopy, Advanced Materials, 1990. **2**: p. 132-138.

[30]   S. L. Lee, C. K. Lee and D. C. Sinclair, Synthesis and characterisation of bismuth phosphate-based sillenites, Solid State Ionics, 2005. **176**: p. 393-400.

[31]   D. Poleti, L. Karanovic and A. Hadzi-Tonic, Doped gamma-Bi_2O_3: synthesis of microcrystalline samples and crystal chemical analysis of structural data, Zeitschrift Fur Kristallographie, 2007. **222**: p. 59-72.

[32]   J. P. Guha, S. Kune and D. Suvorov, Phase equilibrium relations in the binary system Bi_2O_3-ZnO, Journal of Materials Science, 2004. **39**: p. 911-918.

[33]   T. A. Mary, R. Mackay, P. Nguyen and A. W. Sleight, Crystal structure of $Bi_{12.7}Co_{0.3}O_{19.35}$, European Journal of Solid State and Inorganic Chemistry, 1996. **33**: p. 285-293.

[34]   S. F. Radaev, M. Tromel, Y. F. Kargin, A. A. Marin, E. E. Rider and V. A. Sarin, $Bi_{12}(Bi_{0.5}Tl^{3+}_{0.5})O_{19.50}$, Acta Crystallographica Section C-Crystal Structure Communications, 1994. **50**: p. 656-659.

[35]   H. A. Harwig and A. G. Gerards, Polymorphism of bismuth sesquioxide, Thermochimica Acta, 1979. **28**: p. 121-131.

5 Investigation of Boron (B^{3+}) Containing Sillenites

5.1 Introduction

Among the trivalent cations used to dope sillenite analogues, boron is the smallest ion with an ionic radius of $B^{3+}_{(III)} = 0.01$ Å and $B^{3+}_{(IV)} = 0.11$ Å.[1] $Bi_{24}B^{3+}_2O_{39}$ was first reported by Levin *et al.*[2] in 1962, which melted incongruently at 650 °C. However, formation of the sillenite compound $Bi_{24}BO_{39}$ was reported to be difficult due to: (i) the very small field of crystallization in the Bi_2O_3-B_2O_3 binary system, which particularly affects the single-crystal formation; (ii) the high density differences between Bi_2O_3 ($\rho = 9.3$ g/cm^3) and B_2O_3 ($\rho = 2.46$ g/cm^3), which challenged compositional homogeneity formation; (iii) the nearly simultaneous formation of the 2:1 compound $Bi_4B_2O_9$ and the 12:1 compound $Bi_{24}B_2O_{39}$ and (iv) the uncertainty of the exact composition for boron sillenites due to the disobedience of the Valant and Suvorov general formula[3] as a guide (as mentioned in Chapter 4, VS formula for trivalent dopants – $Bi_{12}(Bi^{3+}_{0.5}M^{3+}_{0.5})O_{19.5}[LP]_{0.5}$). Although the boron sillenite was known as a 12:1 compound $Bi_{24}B_2O_{39}$[2, 4], several authors have suggested different nBi_2O_3-mB_2O_3 stoichiometries for boron sillenite. Burianek *et al.* agreed with the 12:1 formula in their first paper[5] but after a careful follow-up investigation they suggested the exact stoichiometry for single-crystal boron sillenite should be $Bi_{24.5}BO_{38.25} = Bi_{12}(Bi_{0.25}B_{0.5})O_{19.125}$ [6, 7]. In addition, Kuzmicheva *et al.* reported a slightly B-riched composition of $Bi_2B_{0.167}O_{3.25} = Bi_{12}B_{1.002}O_{19.5}$[8]. Nevertheless, the true stoichiometry of boron sillenite(s) is still debateable.

Structurally, Kargin and Egorysheva[4] used crystal-chemical analysis and infrared (IR) studies and reported that in boron-containing sillenites (e.g. $Bi_{24}B^{3+}_2O_{39}$, $Bi_{24}B^{3+}P^{5+}O_{40}$, $Bi_{24}B^{3+}V^{5+}O_{40}$), the boron atom is coordinated mainly by three oxygen atoms to form $BO(3)_3$ groups in the tetrahedral site of the structure, as shown in Figure 5.1. This unique structural feature of boron containing sillenites permits a distorted structure with considerable local structural fluctuation, and it is not surprising to observe interesting electrical properties in these sillenite analogues.
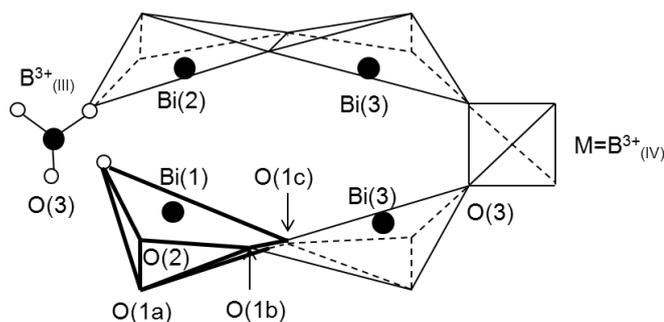
Figure 5.1 Fragment of the structure showing two different types of boron coordination $BO(3)_3$ and $BO(3)_4$ units in the M-sites of B^{3+} containing sillenites.

The peculiarity of the relaxor-like behaviour in the electrical properties of $Bi_{12}(B_{0.5}P_{0.5})O_{20}$ over the temperature range ~ 200 to 400 K found by Valant and Suvorov[9] is of interest to us to comprehensively investigate its origin. Valant and Suvorov[9] attributed this relaxor-behaviour to random occupation of B and P atoms over the M-site. This unique electrical behaviour below room temperature (RT) was not present in any sillenites studied in Chapters 3 and 4. In the case of the sillenites in Chapters 3 and 4, the origin of the relaxor-behaviour above RT is associated with random dipole moments from BiO_5LP units in the sillenite Bi-O framework. The associated dielectric loss is more than an order of magnitude greater than that reported by Valant and Suvorov for $Bi_{12}(B_{0.5}P_{0.5})O_{20}.$[9] Hence, the origin of the two relaxor-like behaviours may be different. To assess whether a mixed occupation of B and P atoms on the tetrahedral site could be the origin of the relaxation behaviour at low temperature, a series of relevant sillenites (13 compositions) were systematically investigated, with compounds containing mainly boron or phosphorus ions being reported in Chapters 5 and 6, respectively.

In this chapter, several new B^{3+} containing sillenites were prepared based on the general formula $(1-x)Bi_{12}BO_{19.5}-xBi_{12}MO_{20+\delta}$, leading to a new group of boron (B^{3+}) sillenite analogues. With the assumption that $Bi_{12}BO_{19.5}$ is single-phase, four different formulae were developed from the general formula $(1-x)Bi_{12}BO_{19.5}-xBi_{12}MO_{20+\delta}$, which are $Bi_{12}(B^{3+}_{1-x}P^{5+}_{x})O_{19.5+x}$; $Bi_{12}(B^{3+}_{1-x}Si^{4+}_{x})O_{19.5+x/2}$; $Bi_{12}(B^{3+}_{0.5}M^{3+}_{0.5})O_{19.5}$ (M^{3+} = Fe^{3+}, Al^{3+} and Ga^{3+}) and $Bi_{12}(B^{3+}_{0.5}M^{5+}_{0.5})O_{20}$ ($M^{5+} = V^{5+}$). The first two formulae were aimed to investigate the solid solubility limits for the $Bi_{12}BO_{19.5}-Bi_{12}P^{5+}O_{20.5}$ and $Bi_{12}BO_{19.5}-Bi_{12}SiO_{20}$ series, respectively. The validity of the VS formula[3] for B^{3+}

containing sillenites were testified for all prepared compounds.

The aim of this chapter was to explore new boron containing sillenite phases, investigate the relationships between the lattice parameter and the M-cation ionic radius, and hence the influence of the ionic radius on the stability of the sillenite phase. Structural analysis has been performed by X-ray Powder Diffraction (XRPD), Neutron Powder Diffraction (NPD); Nuclear Magnetic Resonance (NMR) and Raman Spectroscopy (RS). Electrical properties were measured using *rf* fixed frequency capacitance measurements, Impedance Spectroscopy (IS) and microwave (MW) dielectric resonance measurements. Modelling of the IS data was undertaken using equivalent circuit analysis. Finally, the origin(s) of the peculiar electrical properties are discussed and correlated to the crystal structure.

5.2   Results

5.2.1 Synthesis of Boron Containing Sillenites

~ 10g of various compositions of the B^{3+} sillenites based on the four formulae: $Bi_{12}(B^{3+}_{1-x}P^{5+}_{x})O_{19.5+x}$; $Bi_{12}(B^{3+}_{1-x}Si^{4+}_{x})O_{19.5+x/2}$; $Bi_{12}(B^{3+}_{0.5}M^{3+}_{0.5})O_{19.5}$ (M^{3+} = Fe^{3+}, Al^{3+} and Ga^{3+}) and $Bi_{12}(B^{3+}_{0.5}M^{5+}_{0.5})O_{20}$ (M^{5+} = V^{5+}) were prepared by the solid state reaction method. Precursors were dried at appropriate temperatures, as listed in Table 2.1 in Chapter 2: Experimental Procedure. Samples were ground together with acetone using a mortar and pestle and heated in Au foil boats from room temperature to 400 ℃ for 2 hours with a heating rate of 1 ℃/min to evaporate any H$_2$O and/or NH$_3$ in the reagents and then heated at 600 ℃ for 6 hours with a heating and cooling rate of 10 ℃/min. The samples were eventually reacted between 625 and 740 ℃ with intermediate grinding until an equilibrium state was detected by X-ray powder diffraction. The single-phase compositions based on XRPD results are listed in Table 5.1.

Table 5.1 Summary of single-phase boron sillenites examined by XRPD.

Formula	Single-phase Composition	Reaction Temperature / °C	Reaction Time / h	Sintering Temperature / °C
$Bi_{12}(B^{3+}_{1-x}P^{5+}_{x})O_{19.5+x}$	$Bi_{12}(B_{0.5}P_{0.5})O_{20}$	730	36	790
	$Bi_{12}(B_{0.75}P_{0.25})O_{19.75}$	730	48	787
$Bi_{12}(B^{3+}_{1-x}Si^{4+}_{x})O_{19.5+x/2}$	$Bi_{12}(B_{0.25}Si_{0.75})O_{19.875}$	730	72	730
$Bi_{12}(B^{3+}_{0.5}M^{3+}_{0.5})O_{19.5}$	$Bi_{12}(B_{0.5}Al_{0.5})O_{19.5}$	680	72	715
	$Bi_{12}(B_{0.5}Ga_{0.5})O_{19.5}$	700	48	770
$Bi_{12}(B^{3+}_{0.5}M^{5+}_{0.5})O_{20}$	$Bi_{12}(B_{0.5}V_{0.5})O_{20}$	740	48	780

5.2.2 XRPD

- **$Bi_{12}(B^{3+}_{1-x}P^{5+}_{x})O_{19.5+x}$**

Valant and Suvorov[9] were the first to report single-phase sillenite $Bi_{12}(B_{0.5}P_{0.5})O_{20}$ (i.e. as x = 0.5 in formula $Bi_{12}(B^{3+}_{1-x}P^{5+}_{x})O_{19.5+x}$) that was prepared by the solid state reaction method. To explore the solid solubility of the formula, compounds: $Bi_{12}(B_{0.25}P_{0.75})O_{20.25}$, $Bi_{12}(B_{0.5}P_{0.5})O_{20}$ and $Bi_{12}(B_{0.75}P_{0.25})O_{19.75}$ with x = 0.75, 0.50 and 0.25 were prepared, respectively. The end-members of the formula $Bi_{12}(B^{3+}_{1-x}P^{5+}_{x})O_{19.5+x}$ are $Bi_{12}BO_{19.5}$ and $Bi_{12}P^{5+}O_{20.5}$. However, both of the end-members were difficult to synthesis by the solid state reaction method.[10, 11] Attempts were made to explore the true stoichiometry of the end-members and are shown in Appendix I.

X-ray powder diffraction (XRPD) was carried out using a Stoë STADI P diffractometer (Cu$K\alpha_1$ radiation, 1.54059 Å) with a small linear position sensitive detector operating in transmission mode, step size 0.01° and 2θ range 15-85°. XRPD results, Figure 5.2, detected that $Bi_{12}(B_{0.75}P_{0.25})O_{19.75}$ was single-phase, whereas $Bi_{12}(B_{0.25}P_{0.75})O_{20.25}$ and $Bi_{12}(B_{0.5}P_{0.5})O_{20}$ were not. Besides the existence of the secondary phase $Bi_4B_2O_9$ in $B_{0.25}P_{0.75}$, XRPD results detected both $B_{0.25}P_{0.75}$ and $B_{0.5}P_{0.5}$ to be phase-mixtures of two coexisting sillenite phases, shown in the inset of Figure 5.2. The XRPD data over the 2θ range of 5-70° could be indexed on a single cell, however, clear splitting of the peaks could be observed at higher 2θ values indicating evidence for the presence of a second sillenite phase with a different but similar lattice parameter based on space group $I23$.
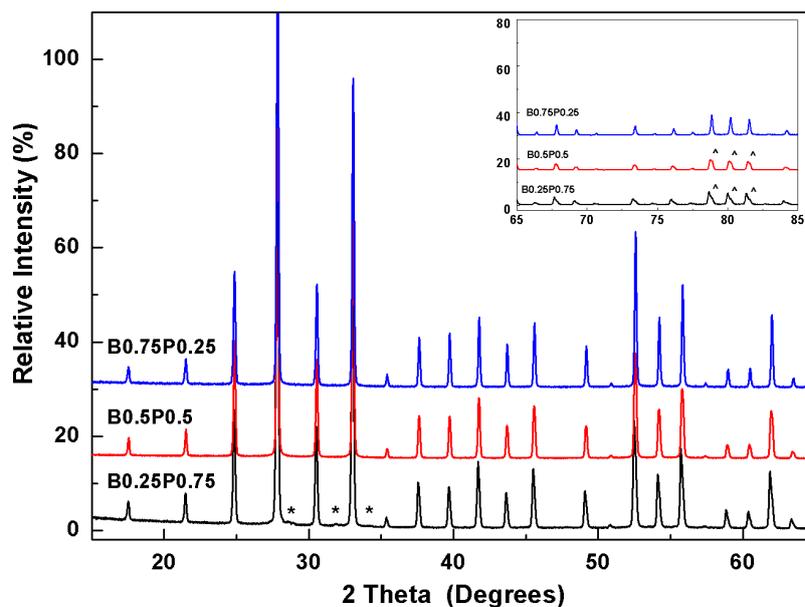
Figure 5.2 XRPD results of $Bi_{12}(B_{0.25}P_{0.75})O_{20.25}$, $Bi_{12}(B_{0.5}P_{0.5})O_{20}$ and $Bi_{12}(B_{0.75}P_{0.25})O_{19.75}$ with x = 0.75, 0.50 and 0.25 from the formula $Bi_{12}(B^{3+}_{1-x}P^{5+}_{x})O_{19.5+x}$, respectively. Inset shows XRPD patterns at higher 2θ angles 65-85 °, where peak splitting was observed. Notations * and ^ indicate impurity $Bi_4B_2O_9$ (ICCD card [70-1458]) and unknown sillenite phase, respectively.

- **$Bi_{12}(B^{3+}_{1-x}Si^{4+}_{x})O_{19.5+x/2}$**

The formula $Bi_{12}(B^{3+}_{1-x}Si^{4+}_{x})O_{19.5+x/2}$ was used to investigate the solid solubility limits between $Bi_{12}BO_{19.5}$ and $Bi_{12}SiO_{20}$. The compositions $Bi_{12}(B_{0.1}Si_{0.9})O_{19.95}$, $Bi_{12}(B_{0.25}Si_{0.75})O_{19.875}$, $Bi_{12}(B_{0.5}Si_{0.5})O_{19.75}$ and $Bi_{12}(B_{0.75}Si_{0.25})O_{19.625}$ were initially heated between 650 and 750 °C until equilibrium was reached, however, none of them were single-phase based on XRPD, Figure 5.3. It is noteworthy that the peak splitting shown here in all the XRPD patterns at 2θ angles > 55 ° was an extrinsic effect due to the Cu$K\alpha_2$ radiation from the Philips D500 Diffractometer.
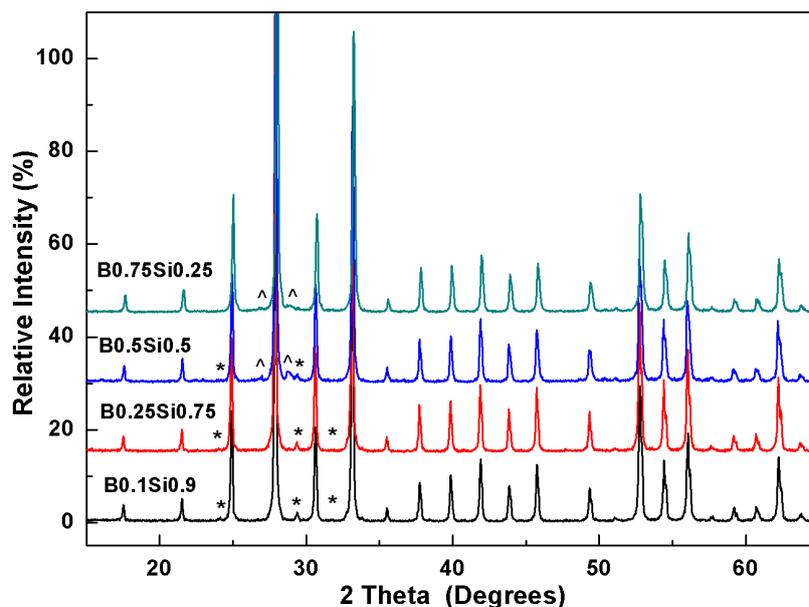
Figure 5.3 XRPD results of sample Bi$_{12}$(B$_{0.1}$Si$_{0.9}$)O$_{19.95}$, Bi$_{12}$(B$_{0.25}$Si$_{0.75}$)O$_{19.875}$, Bi$_{12}$(B$_{0.5}$Si$_{0.5}$)O$_{19.75}$ and Bi$_{12}$(B$_{0.75}$Si$_{0.25}$)O$_{19.625}$ prepared directly from reagents Bi$_2$O$_3$, B(OH)$_3$ and SiO$_2$. Notations * and ^ indicate the presence of secondary phases Bi$_2$SiO$_5$ (ICCD card [75-1483]) and Bi$_4$B$_2$O$_9$ (ICCD card [70-1458]), respectively.

The nearly simultaneous formation of compound Bi$_2$SiO$_5$ and Bi$_4$B$_2$O$_9$ along with the sillenite phase impede the synthesis of phase pure compounds from powdered reagents Bi$_2$O$_3$, B(OH)$_3$ and SiO$_2$. Another method was attempted: prior to the synthesis of boron silicate sillenites, two end-member phases: Bi$_{12}$BO$_{19.5}$ and Bi$_{12}$SiO$_{20}$ were prepared from powder mixtures of high purity Bi$_2$O$_3$ with either B(OH)$_3$ or SiO$_2$ in stoichiometric amounts and reacted at 625 and 840 °C, respectively. Bi$_{12}$SiO$_{20}$ was phase-pure by XRPD (shown in chapter 3) whereas Bi$_{12}$BO$_{19.5}$ was not, but contained a small amount of impurity phase of Bi$_4$B$_2$O$_9$ (shown in Appendix I). Then the boron silicate sillenites Bi$_{12}$(B$_{0.25}$Si$_{0.75}$)O$_{19.875}$, Bi$_{12}$(B$_{0.5}$Si$_{0.5}$)O$_{19.75}$ and Bi$_{12}$(B$_{0.75}$Si$_{0.25}$)O$_{19.625}$ were synthesised by mixing the two end-members in the corresponding molar ratios and a subsequent cycle of regrinding and reheating were operated to obtain single-phase products.

---

* The peak splitting caused by an intrinsic effect of the sample will be mentioned exclusively in the text and is confirmed by using a Stoë STADI P diffractometer (Cu$K\alpha_1$ radiation, 1.54059 Å) with a small linear position sensitive detector operating in transmission mode, step size 0.01° and 2θ range 10-90°. Otherwise, all XRPD patterns in this thesis show the extrinsic effect due to the Cu$K\alpha_2$ radiation from the Philips D500 Diffractometer.

XRPD results, Figures 5.4 (a) and (b), confirmed that $Bi_{12}(B_{0.25}Si_{0.75})O_{19.875}$ formed a single phase compound, whereas $Bi_{12}(B_{0.5}Si_{0.5})O_{19.75}$ and $Bi_{12}(B_{0.75}Si_{0.25})O_{19.625}$ contained an impurity phase, $Bi_4B_2O_9$. A scrutinized examination of the XRPD pattern for $Bi_{12}(B_{0.25}Si_{0.75})O_{19.875}$ confirmed that the sample was not a mixture of two sillenite phases, Figure 5.4 (b) inset.

The exact stoichiometry of $Bi_{12}(B_{0.25}Si_{0.75})O_{19.875}$ is unclear due to the impurity present in the 'parent' $Bi_{12}BO_{19.5}$ powder, further investigation of sample stoichiometry is still required. Nevertheless, a solid solution from formula $Bi_{12}(B^{3+}_{1-x}Si^{4+}_{x})O_{19.5+x/2}$, where $x = 1$ to $x \approx 0.75$ is established.
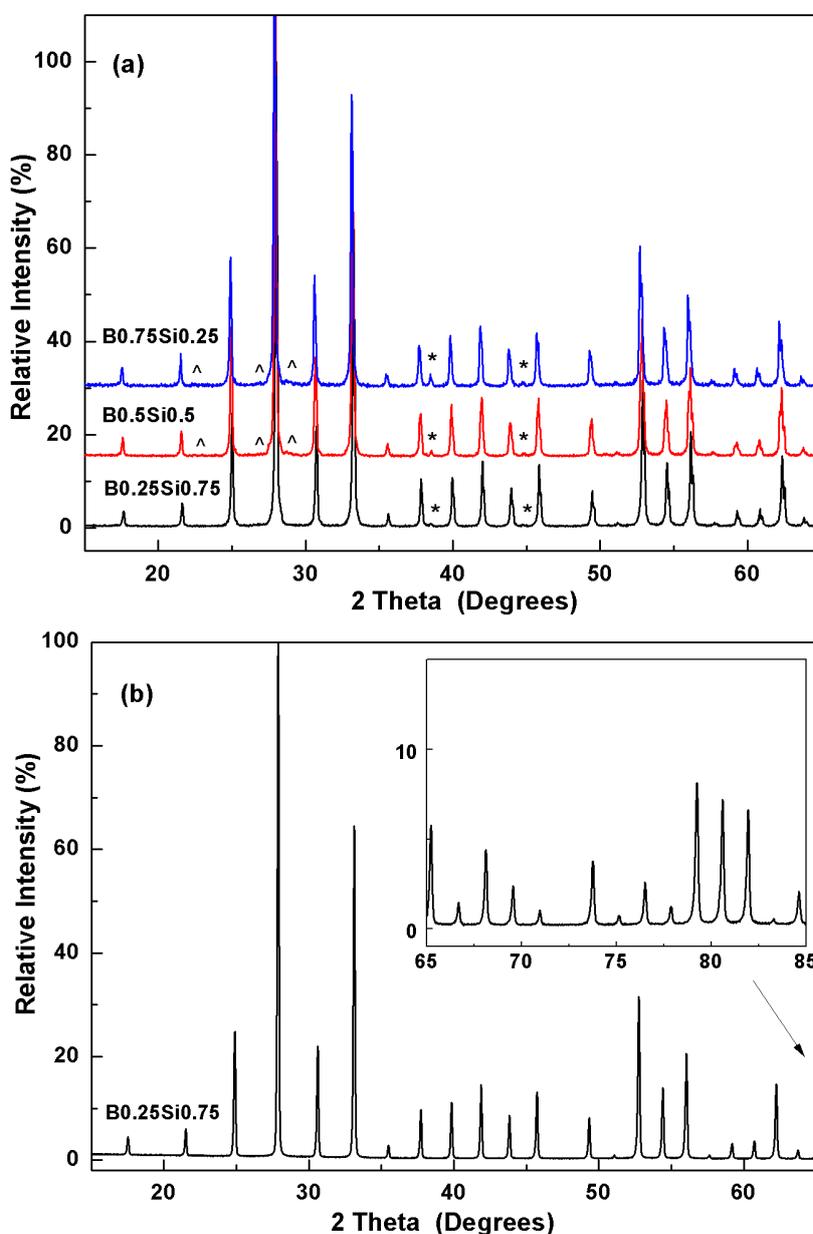
Figure 5.4 XRPD results of (a) $Bi_{12}(B_{0.25}Si_{0.75})O_{19.875}$, $Bi_{12}(B_{0.5}Si_{0.5})O_{19.75}$ and $Bi_{12}(B_{0.75}Si_{0.25})O_{19.625}$ prepared from mixing of two end-members $Bi_{12}BO_{19.5}$ and $Bi_{12}SiO_{20}$.

Notation ^ and * indicate the presence of secondary phases $Bi_4B_2O_9$ (ICCD card [70-1458]) and Al metal (ICCD card [4-787]) from the Philips D500 diffractometer sample holder, respectively. (b) single-phase $Bi_{12}(B_{0.25}Si_{0.75})O_{19.875}$. The inset shows the XRPD pattern at higher 2θ angles, ~ 65 to 85 º.

- **$Bi_{12}(B^{3+}_{0.5}M^{3+}_{0.5})O_{19.5}$, where M^{3+} = Fe, Al and Ga**

XRPD results of $Bi_{12}(B^{3+}_{0.5}M^{3+}_{0.5})O_{19.5}$, where M^{3+} = Fe, Al and Ga, showed that $Bi_{12}(B_{0.5}Al_{0.5})O_{19.5}$ and $Bi_{12}(B_{0.5}Ga_{0.5})O_{19.5}$ were single phase; whereas $Bi_{12}(B_{0.5}Fe_{0.5})O_{19.5}$ contained an impurity phase, $Bi_2Fe_4O_9$, Figure 5.5. XRPD patterns did not reveal any peak splitting at 2θ angles over the range ~ 65 to 85 º and therefore the presence of any bi-phasic sillenite mixtures could be eliminated.
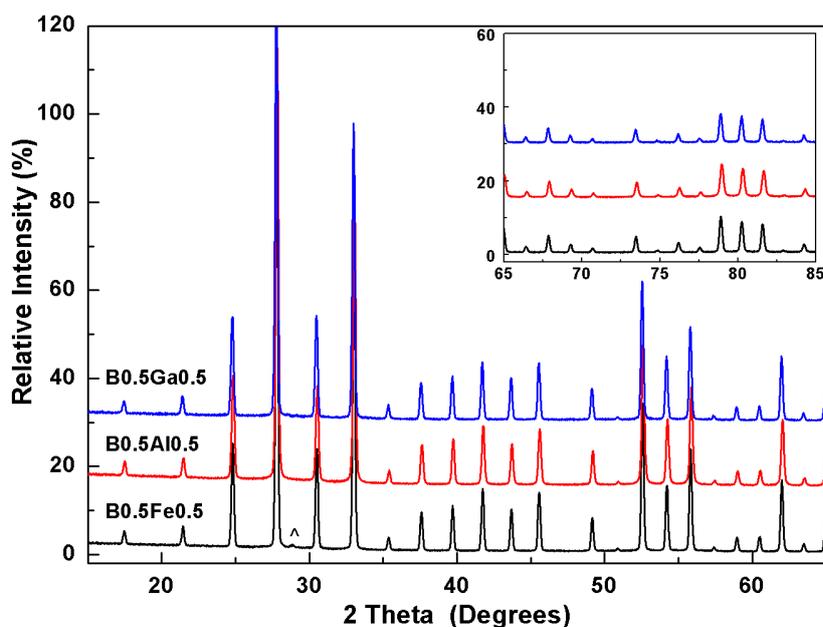
Figure 5.5 XRPD results of $Bi_{12}(B_{0.5}Fe_{0.5})O_{19.5}$, $Bi_{12}(B_{0.5}Al_{0.5})O_{19.5}$ and $Bi_{12}(B_{0.5}Ga_{0.5})O_{19.5}$. Notation ^ indicates an impurity phase of $Bi_2Fe_4O_9$ (ICCD card [25-90]).

- **$Bi_{12}(B^{3+}_{0.5}M^{5+}_{0.5})O_{20}$, where M^{5+} = V^{5+}**

The XRPD results of $Bi_{12}(B_{0.5}V_{0.5})O_{20}$ were similar to $Bi_{12}(B_{0.5}P_{0.5})O_{20}$. A phase mixture of two sillenite phases with clear peak splitting over 2θ angles of 65-85 º was observed, Figure 5.6 inset.
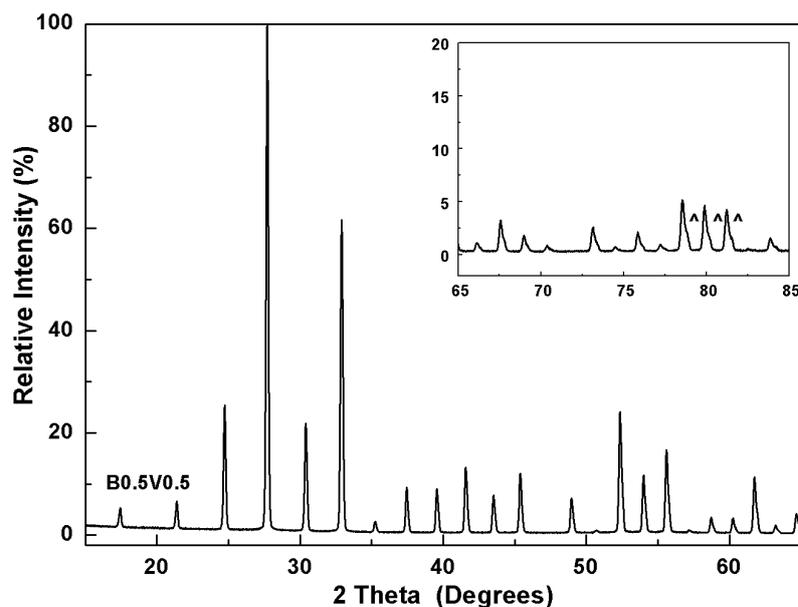
Figure 5.6 XRPD results of $Bi_{12}(B_{0.5}V_{0.5})O_{20}$.

5.2.3 Thermal Stability Test

To investigate the bi-phasic nature of coexisting sillenite phases with similar but different lattice parameters for $Bi_{12}(B_{0.5}P_{0.5})O_{20}$ and $Bi_{12}(B_{0.5}V_{0.5})O_{20}$, the effects of different cooling rates were tested. Each batch of $Bi_{12}(B_{0.5}P_{0.5})O_{20}$ and $Bi_{12}(B_{0.5}V_{0.5})O_{20}$ (synthesized at a standard cooling rate of 10 ℃/min) was separated into two different batches, heated to the reaction temperatures for 30 minutes and then cooled with either a fast (i.e. air quenching by taking the sample out of the furnace from the reaction temperatures and allowed to cool in air) or a slow (i.e. 1 ℃/min) cooling rate. For a fast cooling rate (air quenching), both $B_{0.5}P_{0.5}$ and $B_{0.5}V_{0.5}$ were phase-pure with no detectable peak splitting at higher 2θ angles in the XRPD patterns; whereas at a slow cooling rate (1 ℃/min), the phases decomposed with secondary phase $Bi_4B_2O_9$ present in both samples, Figure 5.7 (a) and (b).
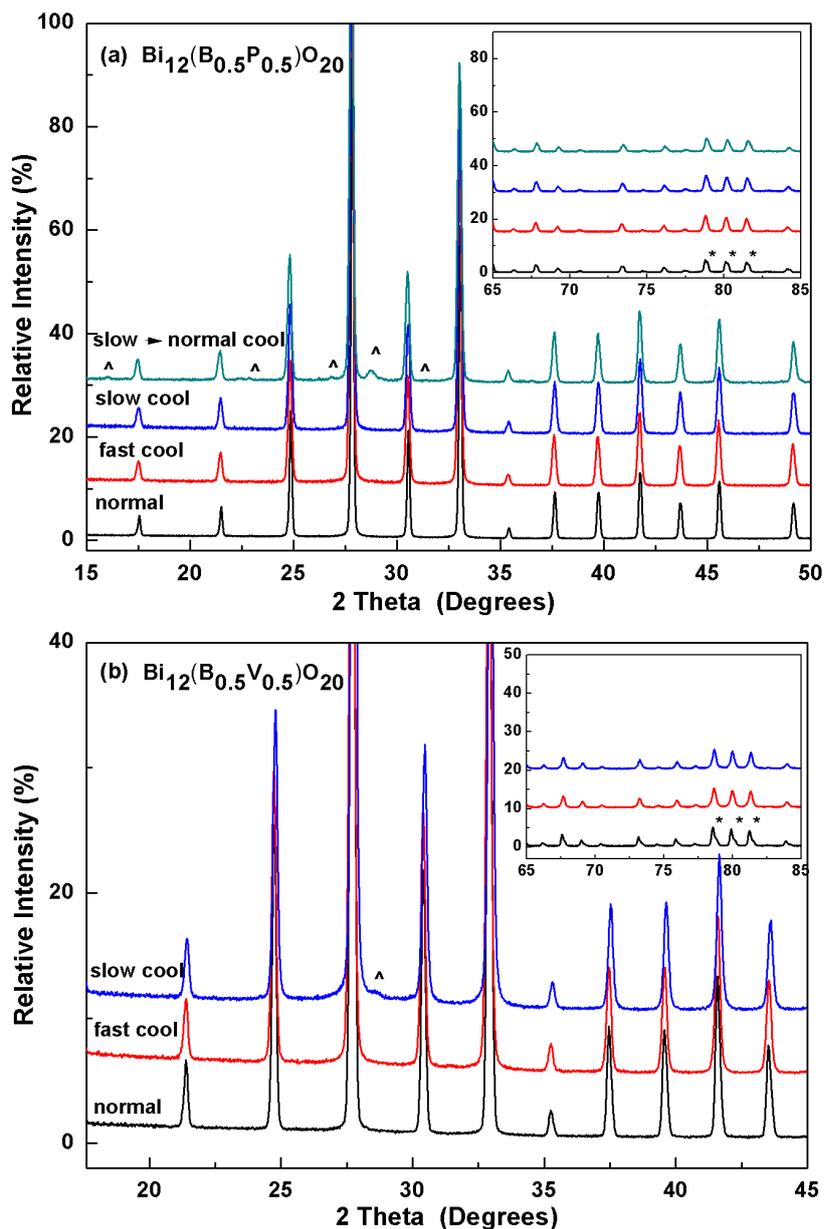
Figure 5.7 XRPD results of (a) Bi$_{12}$(B$_{0.5}$P$_{0.5}$)O$_{20}$ reacted at 730 ℃ for 36h and (b) Bi$_{12}$(B$_{0.5}$V$_{0.5}$)O$_{20}$ at 740 ℃ for 48h with a normal (standard) cooling rate of 10 ℃/min; a fast cooling rate (i.e. air quenching) and a slow cooling rate of 1 ℃/min, respectively. Notation * and ^ indicate the second sillenite phase with a smaller unit cell and a secondary phase of Bi$_4$B$_2$O$_9$ (ICCD card [70-1458]), respectively.

Valant and Suvorov[9] reported that single-phase Bi$_{12}$(B$_{0.5}$P$_{0.5}$)O$_{20}$ was obtained at a fast heating rate of 20 ℃/min; whereas at a slow heating rate of 3 ℃/min, significant P^{5+} and/or B^{3+} losses are detected with the presence of a γ-Bi$_2$O$_3$ impurity phase. The results present here are contradictory to Valant and Suvorov[9]: (i) the formation of single-phase B$_{0.5}$P$_{0.5}$ and B$_{0.5}$V$_{0.5}$ depends mainly on the effect of the cooling rate, regardless of the heating rates; (ii) significant P and/or B losses was not observed experimentally; and (iii) the lattice

parameters of two coexisting sillenites eliminated the possibility of the formed sillenites to be γ-Bi$_2$O$_3$, Table 5.2.

Table 5.2 Lattice parameters for Bi$_{12}$(B$_{0.5}$P$_{0.5}$)O$_{20}$ and Bi$_{12}$(B$_{0.5}$V$_{0.5}$)O$_{20}$ at a normal (standard) cooling rate of 10 ℃/min (two sillenite phases) and at a fast cooling rate i.e. air quenching (single-phase). For comparison, the lattice parameter of γ-Bi$_2$O$_3$ with a =10.2501(5) Å[12] is given.

Composition	Reaction Temperature / ℃	Normal Cooling Rate (i.e. 10 ℃/min)		Fast Cooling Rate (i.e. Air Quench)
		Lattice Parameter/Å (Sillenite I)	Lattice Parameter/Å (Sillenite II)	Lattice Parameter/Å (Single-phase)
Bi$_{12}$ (B$_{0.5}$P$_{0.5}$) O$_{20}$	730	10.1454(5)	10.1346(5)	10.1527(6)
Bi$_{12}$ (B$_{0.5}$V$_{0.5}$) O$_{20}$	740	10.1792(3)	10.1545(15)	10.1709(4)

5.2.4 NPD

NPD data of Bi$_{12}$(Bi$_{0.02}$B$_{0.98}$)O$_{19.5}$ were collected by Donovan[9] at room temperature on the D2B diffractometer at the Institut Laue-Langevin (ILL) in Grenoble, France. ~ 10 g of powder in a vanadium can was placed under a neutron beam generated continuously from a nuclear reactor. Data were collected by using a Ge monochromator over a range of 5º < 2θ < 160 ºwith a step size of 0.05 ºand plotted against intensity.

Rietveld refinement of the NPD data was carried out using a structure reported by Radaev and coworkers' (R model)[13, 14] as an initial model. Both XRPD and NPD patterns were indexed on a centrosymmetric body-centred cubic unit cell, $a \approx 10.125$ Å with space group I23. Preliminary work by Donovan[9] reported Bi$_{12}$(Bi$_{0.02}$B$_{0.98}$)O$_{19.5}$ to be phase pure by XRPD. However, NPD detected an impurity phase Bi$_4$B$_2$O$_9$ in the sample shown as red tick marks in Figure 5.8. A two-phase Rietveld refinement with fixed composition Bi$_{12}$BO$_{19.5}$ (primary phase) suggested a 2.62 weight% of the impurity phase Bi$_4$B$_2$O$_9$ (secondary phase) in the Bi$_{12}$(Bi$_{0.02}$B$_{0.98}$)O$_{19.5}$ sample. The final refinement profiles are shown in Figure 5.8 with overall fitting parameters R$_{wp}$(%), R$_p$(%), χ^2 of 5.18, 3.97, 6.551, respectively.
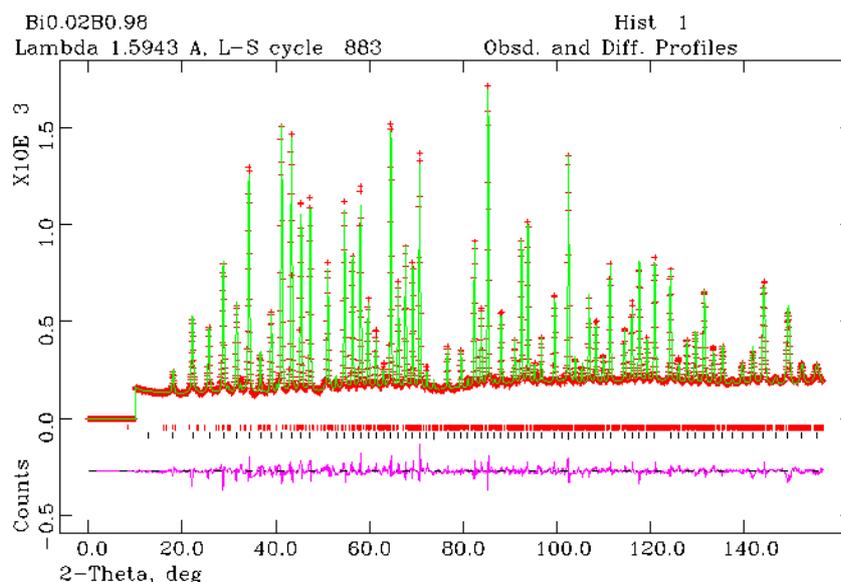
Figure 5.8 Calculated, experimental and difference profile plot from Rietveld refinement of Bi$_{12}$(Bi$_{0.02}$B$_{0.98}$)O$_{19.5}$ using NPD data at room temperature to show the goodness of the fit between the R structural model (+) and the observed data (-). Black ticks (|) indicate Bragg reflections of the sillenite phase, whereas red ticks indicates reflection positions of secondary phase Bi$_4$B$_2$O$_9$.

Table 5.3 Structural parameters from refined room temperature NPD data for fixed composition Bi$_{12}$BO$_{19.5}$, space group I23.

Atom	Wyckoff site	x	y	z	Fractional occupancy	Uiso $\times$ 100/Å^2
Bi(1)	24f	0.1751(2)	0.3179(1)	0.0157(1)	1	U$_{11}$ = 2.1(1)
						U$_{22}$ = 2.4(1)
						U$_{33}$=1.55(9)
						U$_{12}$=0.44(7)
						U$_{13}$=-0.36(9)
						U$_{23}$=0.50(7)
B	8c	0.0235(7)	0.0235(7)	0.0235(7)	0.25	0.9(5)
O(1)	24f	0.1337(2)	0.2539(3)	0.4868(2)	1	1.61(4)
O(2)	8c	0.1958(2)	0.1958(2)	0.1958(2)	1	1.64(9)
O(3)	8c	0.9099(3)	0.9099(3)	0.9099(3)	0.875	3.8(2)
a = 10.1248(1) Å ; χ^2 = 6.551 (47 variables), R$_{wp}$ = 5.18 %, R$_p$ = 3.97 %						

In the initial model, the M atoms occupied the centre of the tetrahedral 2a site, but this did not give a sensible Uiso value for the B atom. According to Kargin and Egorysheva[4] and our NMR results on Bi$_{12}$(B$_{0.5}$P$_{0.5}$)O$_{20}$ (Figure 5.9 in Section 5.2.5), the boron atoms mainly form trigonal planar coordination with three oxygen atoms. Subsequent refinement results showed the B atoms preferentially moved from the 2a site to the lower symmetry 8c site. The fractional occupancies of the three oxygen sites were fixed as 19.5 per formula

unit, with vacancies located predominantly on the O(3) site in the tetrahedra. Details of the refinement results are listed in Table 5.3 and selected bond lengths/angles compared with the ideal sillenite $Bi_{12}GeO_{20}$[13] are given in Table 5.4.

Table 5.4 Selected bond distances (Å), bond angles (°) and calculated bond valence sums ($\sum$BVS) for $Bi_{12}BO_{19.5}$ from Rietveld refinement using NPD data. Bond length values of the ideal sillenite $Bi_{12}GeO_{20}$ reported by Radaev and Simonov[13] are added as a comparison.

Bond length / Å	M = B^{3+}	M=Ge^{4+} [13]	Bond Angles / °	M = B^{3+}
Bi1-O1(a)	2.0884(26)	2.072(1)	Bi1-O2-Bi1	115.81(6)
Bi1-O1(b)	2.2331(25)	2.221(1)	Bi1-O1-Bi1	118.61913)
Bi1-O1(c)	2.6141(26)	2.622(1)	O3-B-O3	119.33(15)
Bi1-O2	2.2131(15)	2.2146(6)		
Bi1-O3	2.6845(29)	2.6241(8)		
M-O3	1.495(5)×3	1.764(2)×4		
	1.993(14)			
$\sum$BVS_calc. Bi1= 2.84; $\sum$BVS_calc. B = 2.15				

5.2.5 Nuclear Magnetic Resonance (NMR) Spectroscopy

NMR spectroscopy was performed by Dr. John V. Hanna from University of Warwick to provide evidence of the short range structure around B atoms in the sillenite $Bi_{12}(B_{0.5}P_{0.5})O_{20}$. Usually boron atoms of compounds e.g. borates are either three- or four-fold coordinated to oxygen atoms, forming BO_3 trigonal planar units or BO_4 tetrahedra, respectively. [11]B one pulse spectra of $Bi_{12}(B_{0.5}P_{0.5})O_{20}$ were measured at magnetic field of 14.1 T (12.5 kHz MAS). Two peaks with chemical environments of BO_3 and BO_4 were detected, which directly proves the existence of BO_3 trigonal planar units in $Bi_{12}(B_{0.5}P_{0.5})O_{20}$, Figure 5.9 and Table 5.5. Based on the NMR intensities of the total transitions ($m = -3/2 \leftrightarrow -1/2$, $m = -1/2 \leftrightarrow 1/2$, and $1/2 \leftrightarrow 3/2$) for the ^{11}B NMR line of BO_3 and BO_4 units contained in $Bi_{12}(B_{0.5}P_{0.5})O_{20}$, the relative percentages of BO_3 and BO_4 units were 91.8 and 8.2 %, respectively.
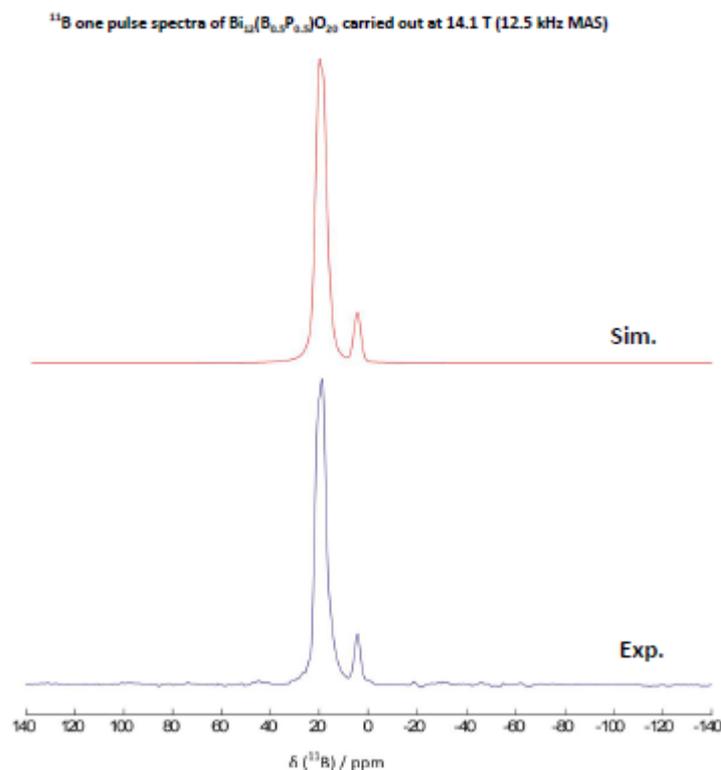
Figure 5.9 Simulated (red) and Experimental (black) NMR spectra of isotope ^{11}B one pulse spectra of $Bi_{12}(B_{0.5}P_{0.5})O_{20}$ at magnetic field of 14.1 T (12.5 kHz MAS).

Table 5.5 Relative percentages of BO_3 and BO_4 structural units with their chemical shift values (δ), quadrupole coupling constant (C_Q) and asymmetry parameter (η) from isotope ^{11}B of $Bi_{12}(B_{0.5}P_{0.5})O_{20}$.

Peak	Isotropic Shift δ (ppm)	C_Q (MHz)	η	Intensity (%)	Environment
1	5.4	1.1	0.78	8.2	BO_4
2	22.3	2.1	0.41	91.8	BO_3

5.2.6 Raman Spectroscopy

● Room Temperature (RT) Raman Spectroscopy

Room temperature Raman spectra for all single-phase B containing sillenites are shown in Figure 5.10 with the corresponding Raman peak assignment listed in Table 5.6. The peak intensity of all Raman spectra were normalized by the peak at ~ 530 cm^{-1} (line 15), which was the strongest peak in the ideal sillenite, $Bi_{12}SiO_{20}$. One unique Raman feature for B^{3+}

sillenite analogues is the two extra vibrations at ~ 850 (line 18) and 900 cm^{-1} (line 19), assigned as vibrations of BO_4 and BO_3 units, respectively.
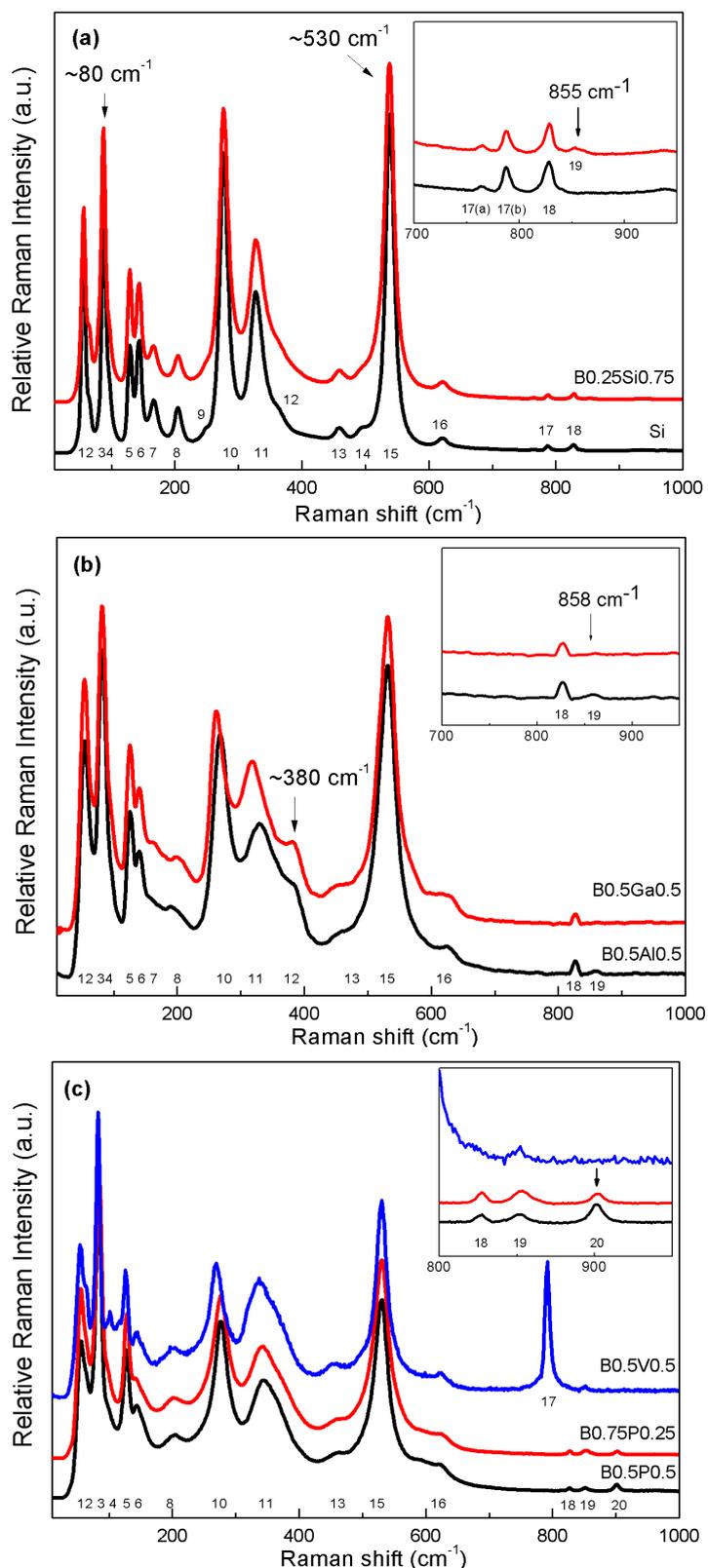
Figure 5.10 Room temperature Raman Spectra of (a) $Bi_{12}(B_{0.25}Si_{0.75})O_{19.875}$ in comparison with $Bi_{12}SiO_{20}$; (b) $Bi_{12}(B_{0.5}Ga_{0.5})O_{19.5}$ and $Bi_{12}(B_{0.5}Al_{0.5})O_{19.5}$ and (c) $Bi_{12}(B_{0.5}P_{0.5})O_{20}$, $Bi_{12}(B_{0.75}P_{0.25})O_{19.75}$ and $Bi_{12}(B_{0.5}V_{0.5})O_{20}$.

Table 5.6 Raman peak positions of B^{3+} containing sillenites compared with Bi$_{12}$SiO$_{20}$.

Line No.	Si	Si$_{0.75}$	P$_{0.5}$	P$_{0.25}$	Al$_{0.5}$	Ga$_{0.5}$	V$_{0.5}$	Mode [15]	Type of Vibrations[15, 16]
1	55	57	55	55	54	54	54	F	Bi,O2,O3 and M vibration
2	63	61	63	-	-	-	58	E	Bi,O1,O2 and O3vibrations elongating the cluster along either [100] or [001]
3	88	88	84*	84*	81*	81*	82*	E	Bi,O2 and O3 vibrations elongating the cluster
4	95	-	99	-	-	95	101	A	Bi-O1 bonds vibration and 'breathing' of O2 atoms
5	129	129	128	128	126	126	126	E	Bi and O2 vibrations elongating the cluster along either [100] or [010]
6	144	144	144	141	140	139	145	A	'breathing' of Bi and O2 atoms
7	166	166	-	-	-	162	-	A	'breathing' of Bi and all O atoms
8	204	205	204	202	193	202	202	F	Bi-O1 stretching & Bi-O2-Bi bending and weak Bi-O1 rocking
9	251	251	-	-	-	-	-	E	Bi-O1 rocking and weak O2 vibrations elongating the cluster along either [100] or [001]
10	276	276	275	277	270	260	269	A	O2 'breathing' and weak Bi-O1 rocking
11	328	328	342	343	332	319	337	A	Bi-O1 rocking and weak O2 'breathing'
12	358	359	360	364	378	382	359	F	O1-Bi-O2 and O1-Bi-O3 bending
13	460	459	461	461	458	455	452	E	O2 vibration elongating the cluster along either [001] or [010] and weak Bi-O1 and Bi-O3 rocking
14	488	495	-	-	-	-	-	F	Bi-O1 stretching and deformation of MO4 tetrahedra
15	538*	538*	531	531	533	534	531	A	'breathing' of O1 atoms
16	621	621	621	621	626	620	625	E	O3 vibrations elongating the cluster along either [010] or [100] and weakBi-O1 and Bi-O2 rocking
17	788	788	-	-	-	-	792	A	Symmetric stretching of MO$_4$ tetrahedra
18	829	829	827	828	827	827	852	FTO	Stretching of MO$_4$ or BO$_4$ tetrahedra
19	-	855	851	854	858	-	-	-	Stretching of BO$_3$ unit
20	-	-	902	901	-	-	-	-	Stretching of PO$_4$ unit

Notation * indicates the strongest peak intensity.

In general, Raman spectra for B^{3+} containing sillenites can be separated into the following three groups:

(i)   Raman spectrum of Bi$_{12}$(B$_{0.25}$Si$_{0.75}$)O$_{19.875}$, Figure 5.10 (a), was almost identical with its parent compound Bi$_{12}$SiO$_{20}$, except for the appearance of a small peak at ~

855 cm^{-1} (line 19) for $B_{0.25}Si_{0.75}$ corresponding to vibrations of the BO_3 group. This confirms boron partially occupied the tetrahedral site with three-fold oxygen coordination. There is no direct evidence for the existence of the BO_4 units in the Raman spectra of $B_{0.25}Si_{0.75}$, if there is any, it is too low to detect. The strongest peak of $B_{0.25}Si_{0.75}$ remained at ~ 530 cm^{-1} (line 15), although the magnitude of the peak intensity ~ 80 cm^{-1} (line 3) is larger than that of $Bi_{12}SiO_{20}$. The peak at ~530 cm^{-1} (line 15) was assigned as a fully symmetric Bi-O(1) framework vibration; whereas the peak at ~ 80 cm^{-1} associated with Bi, O2 and O3 vibrations elongating the cluster[15, 16], signifying the distorted framework polyhedra with incorporation of boron atoms in sillenites. Compared with other B^{3+} sillenites, the Raman Spectroscopy results revealed $B_{0.25}Si_{0.75}$ is the most regular of these sillenites and possessed the closest local structure to the ideal sillenite, $Bi_{12}SiO_{20}$.

(ii)   Raman spectra of $Bi_{12}(B_{0.5}Al_{0.5})O_{19.5}$ and $Bi_{12}(B_{0.5}Ga_{0.5})O_{19.5}$, Figure 5.10 (b), showed a prominent peak at ~ 380 cm^{-1} (line 12), which was assigned as O1-Bi-O2 and O1-Bi-O3 bending[15]. The magnitude and peak position of the ~ 380 cm^{-1} is similar to that obtained for M^{2+}/M^{3+} sillenites (Chapter 4), structural interpretations will be mentioned later in Section 5.3.2.

(iii)   Raman spectra of $Bi_{12}(B_{0.5}P_{0.5})O_{20}$, $Bi_{12}(B_{0.75}P_{0.25})O_{19.75}$ and $Bi_{12}(B_{0.5}V_{0.5})O_{20}$ are shown in Figure 5.10 (c). Solid solutions $B_{0.5}P_{0.5}$ and $B_{0.75}P_{0.25}$ had similar Raman spectra with peaks at ~ 827 cm^{-1} (line 18), ~ 851 cm^{-1} (line 19) and ~ 900 cm^{-1} (line 20) and assigned as vibrations of BO_4, BO_3 and PO_4 units, respectively. Raman spectra of $B_{0.5}V_{0.5}$ presented a characteristic peak at ~ 790 cm^{-1} probably related with stretching of VO_4 tetrahedra. [15] In the pentavalent doped boron sillenite analogues, the peak at ~ 380 cm^{-1} (line 12) increased and downshifted to ~ 360 cm^{-1}, representing an increase of vibration of O1-Bi-O2 and O1-Bi-O3 bending and therefore a more disordered local structure compared with trivalent doped boron sillenites in (ii) group.

• **Low Temperature Raman Spectroscopy**

Low temperature Raman spectroscopy was performed to investigate the subambient relaxation phenomenon observed from the *rf* fixed frequency capacitance measurements (Section 5.2.8) and the low temperature IS measurements (Section 5.2.9.3). In this chapter, to correlated with NMR results for $Bi_{12}(B_{0.5}P_{0.5})O_{20}$, subambient RS results (i.e. 80 – 420 K) for the same compound are chosen as an example and selected RS data are shown in Figure 5.11. A laser power of 10 mW was focused on the same grain ~ 2 μm spot of the sample while various temperature measurements were performed and data recorded in back-scattering geometry.
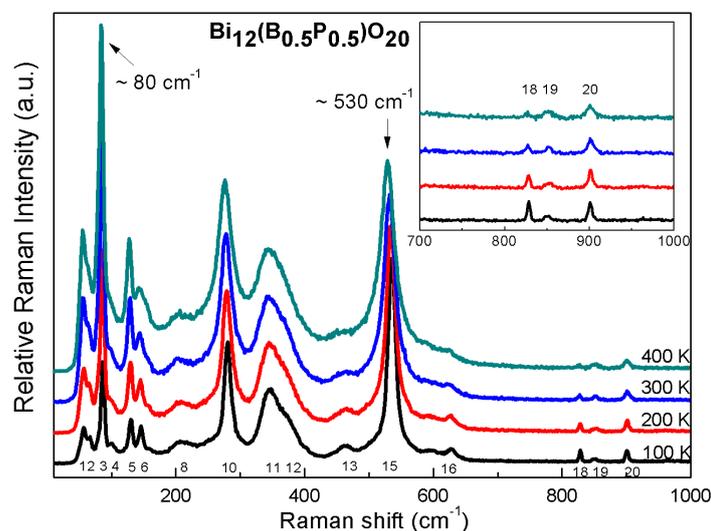
Figure 5.11 Raman spectra of $Bi_{12}(B_{0.5}P_{0.5})O_{20}$ at 100, 200, 300 and 400 K.

All peak intensities of the data were normalised by the strongest peak at ~530 cm^{-1} at 100 K. A switchover in the most intense peak from ~ 530 cm^{-1} to ~ 80 cm^{-1} in the Raman spectra at temperatures above 300 K was observed. The Raman peak positions are inversely proportional to the mass of the groups of the bonded atoms; therefore, the vibrational modes associated with tetrahedral units occur above 700 cm^{-1} (i.e. at ~ 820 cm^{-1} (line 18), 850 cm^{-1} (line 19) and 900 cm^{-1} (line 20) for BO_4, BO_3 and PO_4, respectively), Figure 5.11 inset. It is remarkable that with increasing temperature the magnitude of the peak at ~ 820 cm^{-1} (line 18) decreases; whereas the magnitude of the peak at ~ 850 cm^{-1} (line 19) increases. As the intensity of the Raman peak indicates the strength of the

correlated vibrations, this result showed the strength of BO_3 vibrations is increasing while that of BO_4 vibrations is decreasing at elevated temperatures.

5.2.7 Microwave (MW) Dielectric Properties

Microwave dielectric measurements performed on six B^{3+} sillenite ceramics (pellet density ~ 86–92 (±2) % of the theoretical X-ray density) at ~ 6-7.7 GHz revealed similar mw properties with relative permittivity (ε_r) ~ 30-38; Q ~ 35-60 and τ_f ~ 0 ppm/K, Table 5.6.

The observed relative permittivity (ε_r ~ 35) for all measured B^{3+} sillenites is close to the Clausius-Mossotti calculated ε_r, which is a typical value for sillenites as the polarizability of the sillenite unit cell does not change significantly with the small concentration of M-site dopants. Q.f values ranging from ~ 220-400 GHz were low compared with sillenites in Chapters 2 and 3, which may be due to the anharmonic vibrations from the locally disordered dipolar moments (relaxation behaviour) near/at room temperature. The temperature coefficient of resonant frequency, τ_f, was close to 0 ppm/K over the temperature range of 20 – 80 ℃ for all boron containing sillenites.

Table 5.7 MW dielectric properties of boron containing sillenites.

Composition	Sintering Temperature (℃)	Pellet Density (%)	ε_r	Q	f_0 (GHz)	Q.f (GHz)	τ_f (ppm /K)	CM calculated ε_r
Bi_{12} $(B_{0.5}P_{0.5})$ O_{20}	790	92	35	54	7.561	408	0	35
Bi_{12} $(B_{0.75}P_{0.25})$ $O_{19.75}$	787	90	33	51	7.060	360	0	33
Bi_{12} $(B_{0.25}Si_{0.75})$ $O_{19.875}$	730	92	38	56	7.182	402	0	38
$Bi_{12}(B_{0.5}Al_{0.5})O_{19.5}$	715	91	37	35	6.468	226	0	31
$Bi_{12}(B_{0.5}Ga_{0.5})O_{19.5}$	775	86	31	39	7.058	275	0	31
Bi_{12} $(B_{0.5}V_{0.5})$ O_{20}	780	86	30	44	7.732	340	0	33

5.2.8 Fixed Frequency Capacitance Measurements

The frequency dependence of ε_r and tan δ for boron containing sillenites over the measured temperature range are shown in Figure 5.12 (a)–(l). All samples revealed two main broad, highly frequency-dispersive regions in ε_r as a function of temperature with one present

above room temperature (> 500 K) and one present below/at room temperature (i.e. ~ 100 – 400 K). The peak maxima of both relaxor-like regions shifted to higher temperature with increasing frequency.

The frequency-dispersive region above RT (> 500 K) was also observed in ideal sillenite $Bi_{12}SiO_{20}$ (Chapter 3) and M^{2+}/M^{3+} doping sillenites (Chapter 4) and was attributed to local dipole moments associated with the BiO_5LP units in the framework from combined Raman and Impedance spectroscopy studies.

Subambient RS results (80 - 420 K), Figure 5.11, revealed the low temperature frequency-dispersive region for boron containing sillenite analogues was possibly related to the switchover from BO_4 to BO_3 units on the tetrahedral sites with increasing temperature.

Some of the compounds, e.g. $Bi_{12}(B_{0.75}P_{0.25})O_{19.75}$, $Bi_{12}(B_{0.25}Si_{0.75})O_{19.875}$, $Bi_{12}(B_{0.5}Al_{0.5})O_{19.5}$ and $Bi_{12}(B_{0.5}Ga_{0.5})O_{19.5}$ exhibited two subambient dielectric relaxation processes in the *rf* fixed frequency measurement ranging from 1 k to 1 M Hz, Figure 5.12 (d)-(j). For instance, the tan δ peak maxima of $Bi_{12}(B_{0.25}Si_{0.75})O_{19.875}$, Figure 5.12 (f), showed relaxation processes occurred at ~ 84 and 204 K (for a frequency of 10 kHz) with different activation energies (obtained from log f_{max} versus 1000/T of the tan δ peak maxima). The activation energy of the lower temperature (~ 100 - 400 K) relaxations for all boron sillenites is listed in Table 5.8.
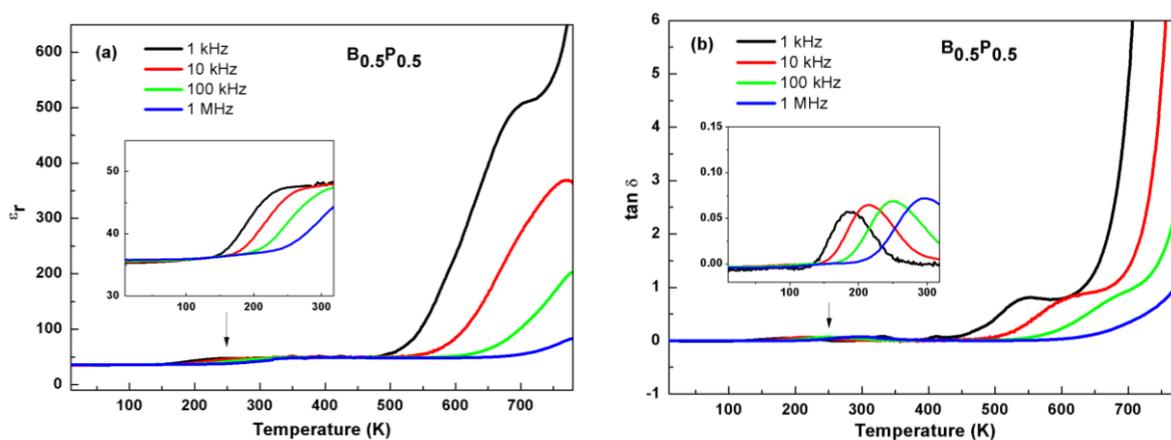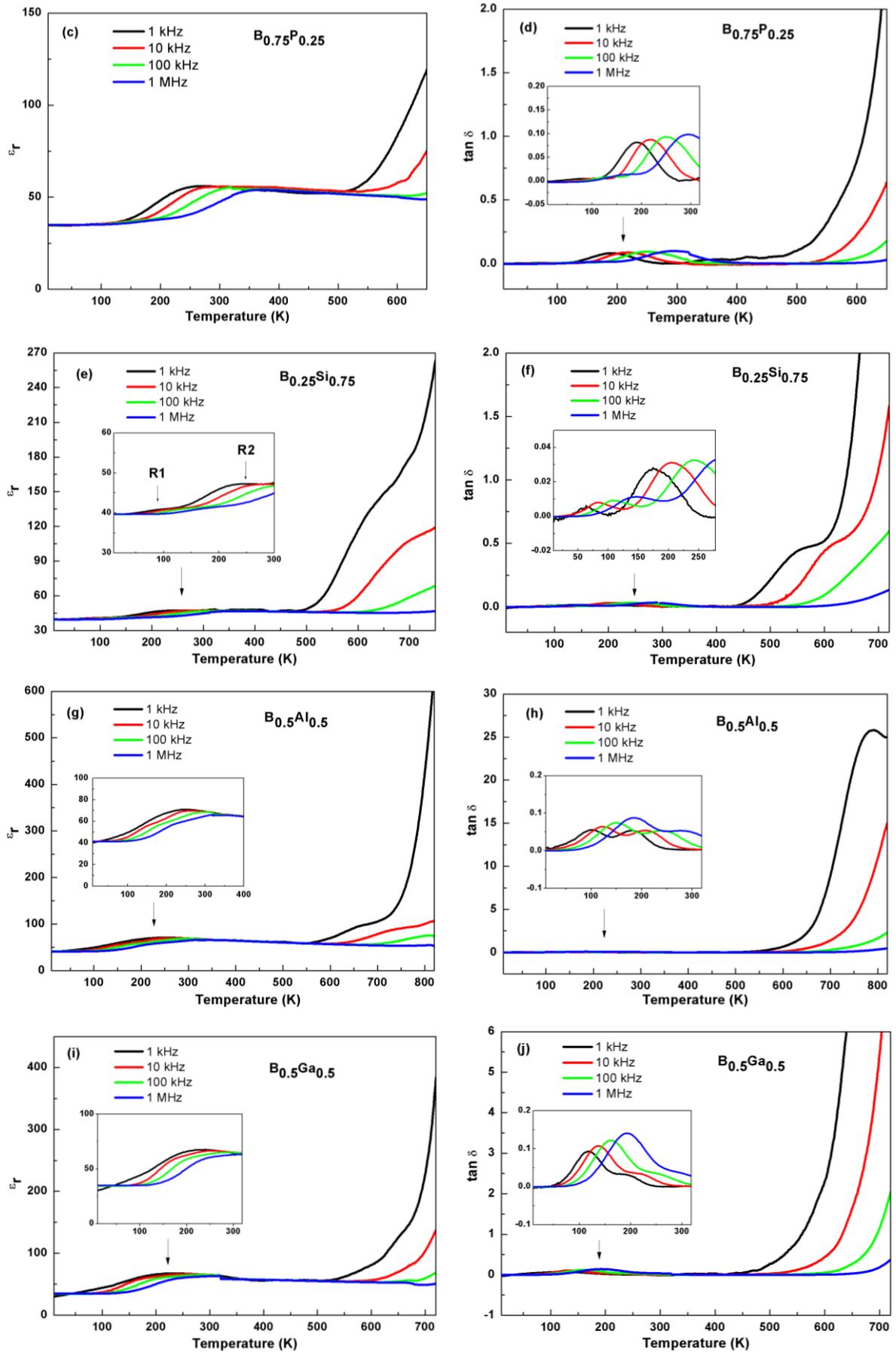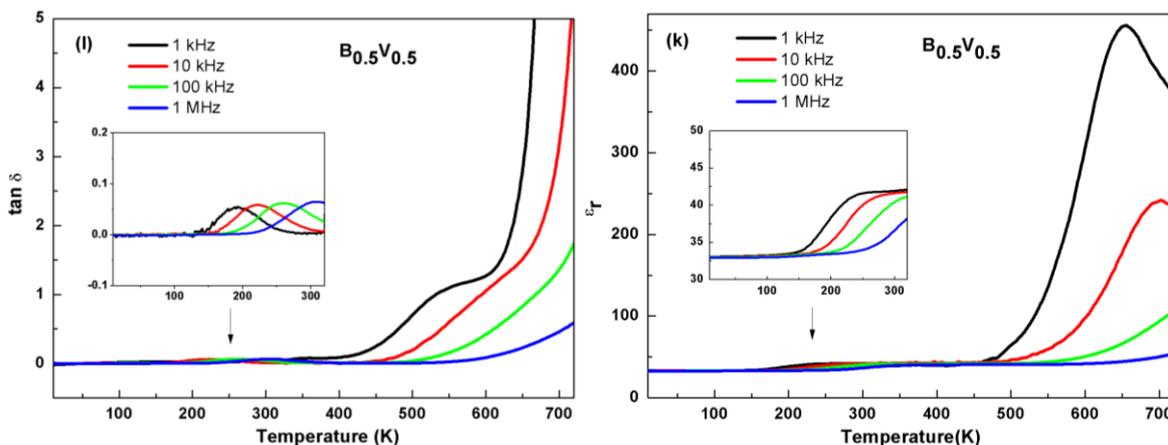
Figure 5.12 Temperature dependence of permittivity (ε_r) and dielectric loss (tan δ) of (a) and (b) $Bi_{12}(B_{0.5}P_{0.5})O_{20}$; (c) and (d) $Bi_{12}(B_{0.75}P_{0.25})O_{19.75}$; (e) and (f) $Bi_{12}(B_{0.25}Si_{0.75})O_{19.875}$; (g) and (h) $Bi_{12}(B_{0.5}Al_{0.5})O_{19.5}$; (i) and (j) $Bi_{12}(B_{0.5}Ga_{0.5})O_{19.5}$; (k) and (l) $Bi_{12}(B_{0.5}V_{0.5})O_{20}$; respectively.

Table 5.8 Temperature of tan δ peak maximum (at 10 kHz) and activation energy (Ea) (obtained from log f_{max} versus 1000/T of the tan δ peak maxima) of the lower temperature relaxation process(es) for boron containing sillenites.

Composition	Temperature of tan δ peak maxima at 10 kHz / K		Activation Energy (Ea_relaxation) / eV	
	1st	2nd	1st	2nd
$Bi_{12}(B_{0.5}P_{0.5})O_{20}$	-	216	-	0.28
$Bi_{12}(B_{0.75}P_{0.25})O_{19.75}$	112	218	0.09	0.33
$Bi_{12}(B_{0.25}Si_{0.75})O_{19.875}$	84	206	0.07	0.26
$Bi_{12}(B_{0.5}Al_{0.5})O_{19.5}$	124	208	0.13	0.31
$Bi_{12}(B_{0.5}Ga_{0.5})O_{19.5}$	138	216	0.19	0.32
$Bi_{12}(B_{0.5}V_{0.5})O_{20}$	-	222	-	0.30

5.2.9 Impedance Spectroscopy (IS)

Low (10-320 K) and high (320-800 K) temperature IS measurements were performed on all B^{3+} sillenites to probe the two main relaxation phenomena observed from *rf* fixed frequency capacitance measurements. Gold-sputtered electrodes were applied on opposite pellet faces for all samples. Table 5.9 lists the measured sample details for IS measurements. All of the boron containing sillenite samples showed similar low/high temperature IS behaviour, therefore, $Bi_{12}(B_{0.75}P_{0.25})O_{19.75}$ was selected as an example. The IS data for the rest of the compounds and circuit fitting results are shown in Appendix III.

Table 5.9 Details of boron containing sillenites from IS measurements. All samples had gold-sputtered electrodes.

Formula	Single-phase Composition	Sintering Temperature / °C	Pellet Density / %	Activation Energy (buk) / eV
$Bi_{12}(B^{3+}_{1-x}P^{5+}_x)O_{19.5+x}$	$Bi_{12} (B_{0.5}P_{0.5}) O_{20}$	790	92	0.94
	$Bi_{12} (B_{0.75}P_{0.25}) O_{19.75}$	787	90	1.26
$Bi_{12}(B^{3+}_{1-x}Si^{4+}_x)O_{19.5+x/2}$	$Bi_{12} (B_{0.25}Si_{0.75}) O_{19.875}$	730	92	0.85
$Bi_{12}(B^{3+}_{0.5}M^{3+}_{0.5})O_{19.5}$	$Bi_{12}(B_{0.5}Al_{0.5})O_{19.5}$	715	91	1.22
	$Bi_{12}(B_{0.5}Ga_{0.5})O_{19.5}$	770	86	1.20
$Bi_{12}(B^{3+}_{0.5}M^{5+}_{0.5})O_{20}$	$Bi_{12} (B_{0.5}V_{0.5}) O_{20}$	780	86	0.71

5.2.9.1   High Temperature IS Data (above RT)

High temperature IS data for $Bi_{12}(B_{0.75}P_{0.25})O_{19.75}$ at 723 K, Figure 5.13 (a)-(d), revealed similar relaxation behaviour as the ideal sillenite $Bi_{12}SiO_{20}$ (Chapter 3) and M^{2+}/M^{3+} doped sillenites (Chapter 4). The direct evidence is the existence of two capacitance (C') plateaux: one at high frequency and one at low frequency, Figure 5.14. The high-frequency plateau ($f > 10^6$ Hz) is frequency-independent and assigned as a bulk component with an associated capacitance of ~ 4.8 pF.cm^{-1}; whereas the low frequency plateau ($f < 10^6$ Hz) is frequency-dependent with fluctuated capacitance values, corresponding to the large, broad relaxor-liked ε_r peaks in the *rf* fixed frequency measurements, Figure 5.12 (c).

The same equivalent circuit consisting of a parallel connection of R, C and Cole-Cole branch (CPE in series with a C), Figure 5.13 (e), was used and successfully modelled the high temperature IS data from 648 to 773 K over the frequency range of 10^3-10^6 Hz. At f < 10^3 Hz, there is a continuous rising in the C' spectroscopic data with decreasing frequency, which is attirbuted to space-charge polarization from the sample-electrode interface[17, 18]. This response is beyond the scope of the present work and no attempt has been made to include it in the equivalent circuit analysis/fitting and hence the poor agreement between the low frequency experimental and fit data in Figure 5.13 (c). The fitted results of the circuit parameters R_1, C_1, C_x and CPE (A and *n*) for $B_{0.75}P_{0.25}$ over $648 - 773$ K are listed in Table 5.10.

Table 5.10 Fitted high temperature IS values of $Bi_{12}(B_{0.75}P_{0.25})O_{19.75}$ from 573 to 653 K. Errors associated with the fitted circuit parameters R_1, C_1, C_x, A and n are $< \pm0.3$ %, $< \pm0.8$ %,$< \pm3.7$ %,$< \pm18.8$ % and $< \pm3.8$ %, respectively.

Temperature (K)	R_1 (Ω cm)	C_1 (pF cm^{-1})	C_x (pF cm^{-1})	A (Ω^{-1} cm^{-1} rad^{-1})	n
648	9827500	4.67	8.74	4.49×10^{-9}	0.33
673	3740500	4.63	9.28	6.54×10^{-9}	0.35
698	1116100	4.68	9.51	1.12×10^{-8}	0.36
723	679110	4.57	5.85	1.96×10^{-8}	0.31
748	338780	4.51	5.97	2.19×10^{-8}	0.33
773	157500	4.39	6.20	2.06×10^{-8}	0.37
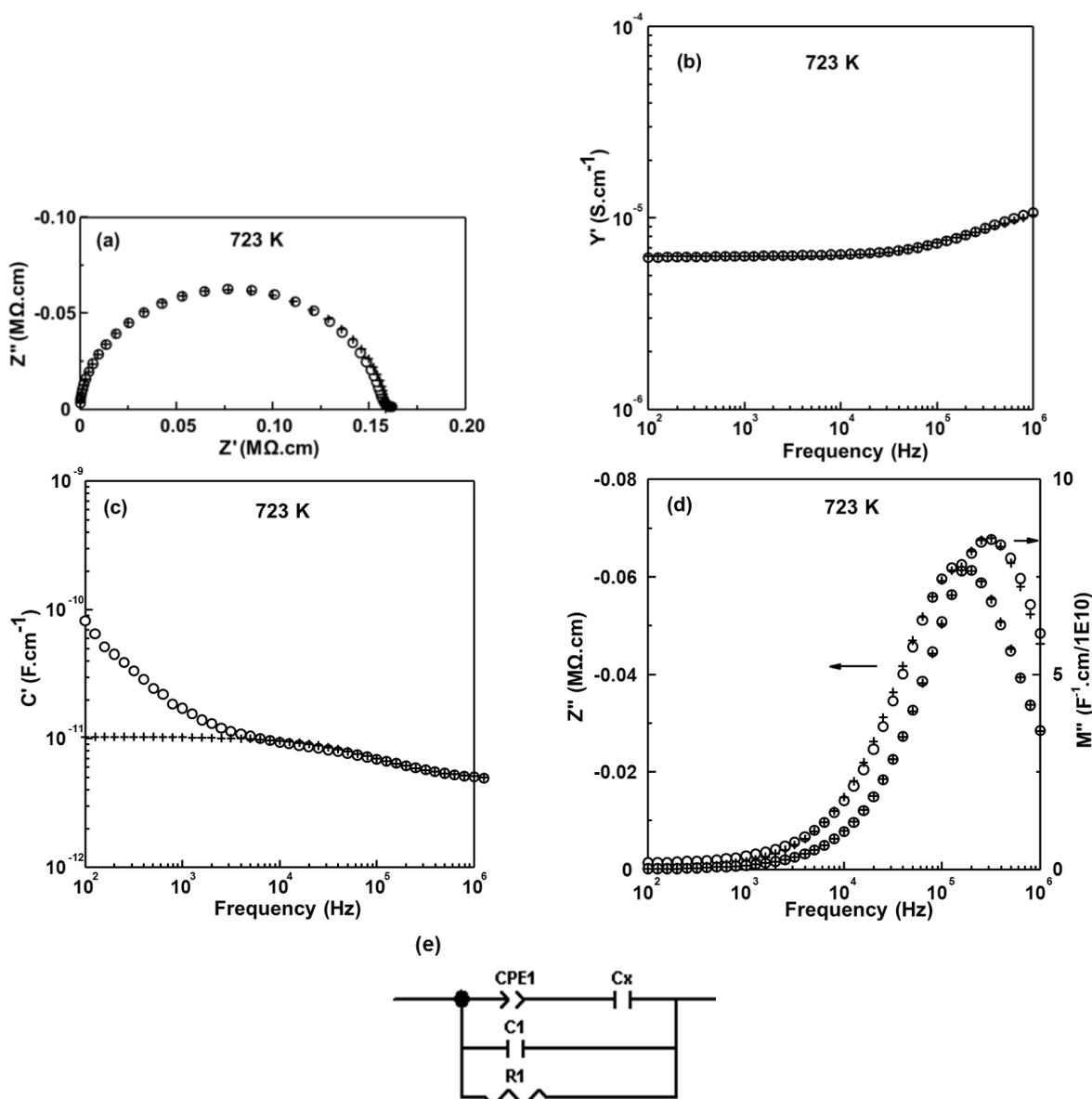
Figure 5.13 High temperature IS experimental data points (○) and the fitting results (+) to equivalent circuit shown in (e) with (a) Z* plot; (b) Y', (c) C', and (d) –Z"/M" spectroscopic plots at 723 K for $Bi_{12}(B_{0.75}P_{0.25})O_{19.75}$.
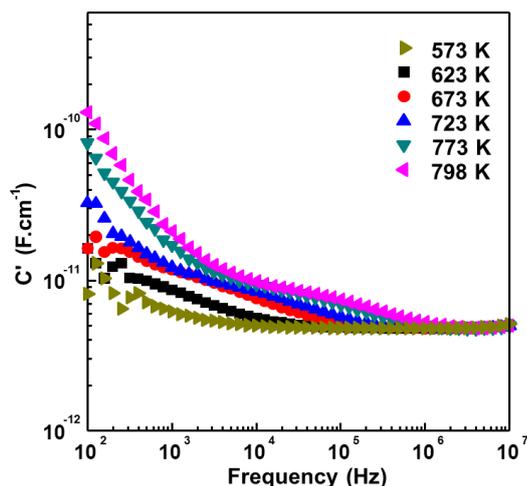
Figure 5.14 C' spectroscopic plot at various temperatures for $Bi_{12}(B_{0.75}P_{0.25})O_{19.75}$.

5.2.9.2 Arrhenius plot of bulk conductivity

Bulk conductivity data for all measured B^{3+} containing sillenites were calculated from the M" Debye peak and plotted in Arrhenius format, as shown in Figure 5.15. The bulk conductivity is not dependent on the oxygen content for boron containing sillenites. Among the measured sillenites, the three most resistive compounds were substoichiometric sillenites $Bi_{12}(B_{0.75}P_{0.25})O_{19.75}$, $Bi_{12}(B_{0.5}Al_{0.5})O_{19.5}$ and $Bi_{12}(B_{0.5}Ga_{0.5})O_{19.5}$ with the highest activation energy of 1.26, 1.22 and 1.20 eV, respectively. The activation energy for the other three compound $Bi_{12}(B_{0.5}P_{0.5})O_{20}$, $Bi_{12}(B_{0.25}Si_{0.75})O_{19.875}$ and $Bi_{12}(B_{0.5}V_{0.5})O_{20}$ were 0.94, 0.85 and 0.71 eV, respectively.
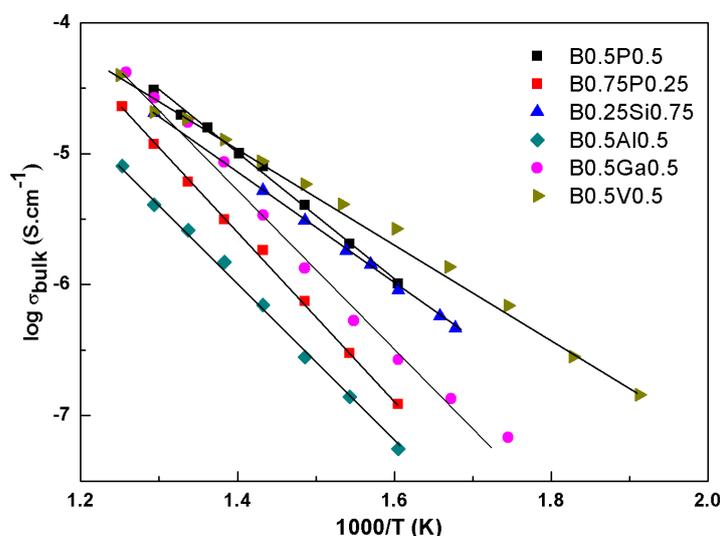
Figure 5.15 Arrhenius plot of bulk conductivity versus reciprocal temperature for B^{3+} containing sillenites.

5.2.9.3   Low Temperature IS Data

Subambient IS data for $Bi_{12}(B_{0.75}P_{0.25})O_{19.75}$ at 240 K, Figure 5.16 (a)-(d), presented in different formats is selected to show the general low temperature relaxation behaviour for B^{3+} containing sillenite analogues.

The sample was too resistive to show any arc (i.e. *dc* conductivity) from Z* impedance plots. Y' spectroscopic data also did not show any frequency-independent plateau at low frequency corresponding to *dc* conduction, R^{-1} through the sample; only frequency-dependent *ac* conduction is observed, e.g. at 240 K in Figure 5.16 (a). Similar with high temperature C' data, subambient C' spectroscopic plot again revealed two C' plateaux (with one at higher frequency and one at lower frequency) at temperatures ranging from ~ 150 to 320 K, corresponding to the subambient relaxation peaks from *rf* fixed frequency results. Below 150 K, the C' data were independent of frequency over the entire measurement range, Figure 5.17(c).

Table 5.11 Fitted subambient IS values of $Bi_{12}(B_{0.75}P_{0.25})O_{19.75}$ from 220 to 320 K (for the 2nd low temperature relaxation). Errors associated with the fitted circuit parameters C_1, C_x, A and *n* are $< \pm 0.6$ %,$< \pm 2.1$ %,$< \pm 11.8$ % and $< \pm 4.2$ %, respectively.

Temperature (K)	C_1 (pF cm^{-1})	C_x (pF cm^{-1})	A (Ω^{-1} cm^{-1} rad^{-1})	*n*
220	3.76	1.86	5.34×10^{-10}	0.48
230	3.76	1.88	8.36×10^{-10}	0.47
240	3.77	1.86	1.46×10^{-9}	0.46
250	3.79	1.82	2.71×10^{-9}	0.44
260	3.82	1.76	5.25×10^{-9}	0.41
270	3.86	1.70	1.04×10^{-8}	0.38
280	3.90	1.63	2.09×10^{-8}	0.36
290	3.97	1.56	4.18×10^{-8}	0.32
300	4.04	1.47	8.47×10^{-8}	0.29
310	4.12	1.38	1.69×10^{-7}	0.26
320	4.22	1.27	3.45×10^{-8}	0.22
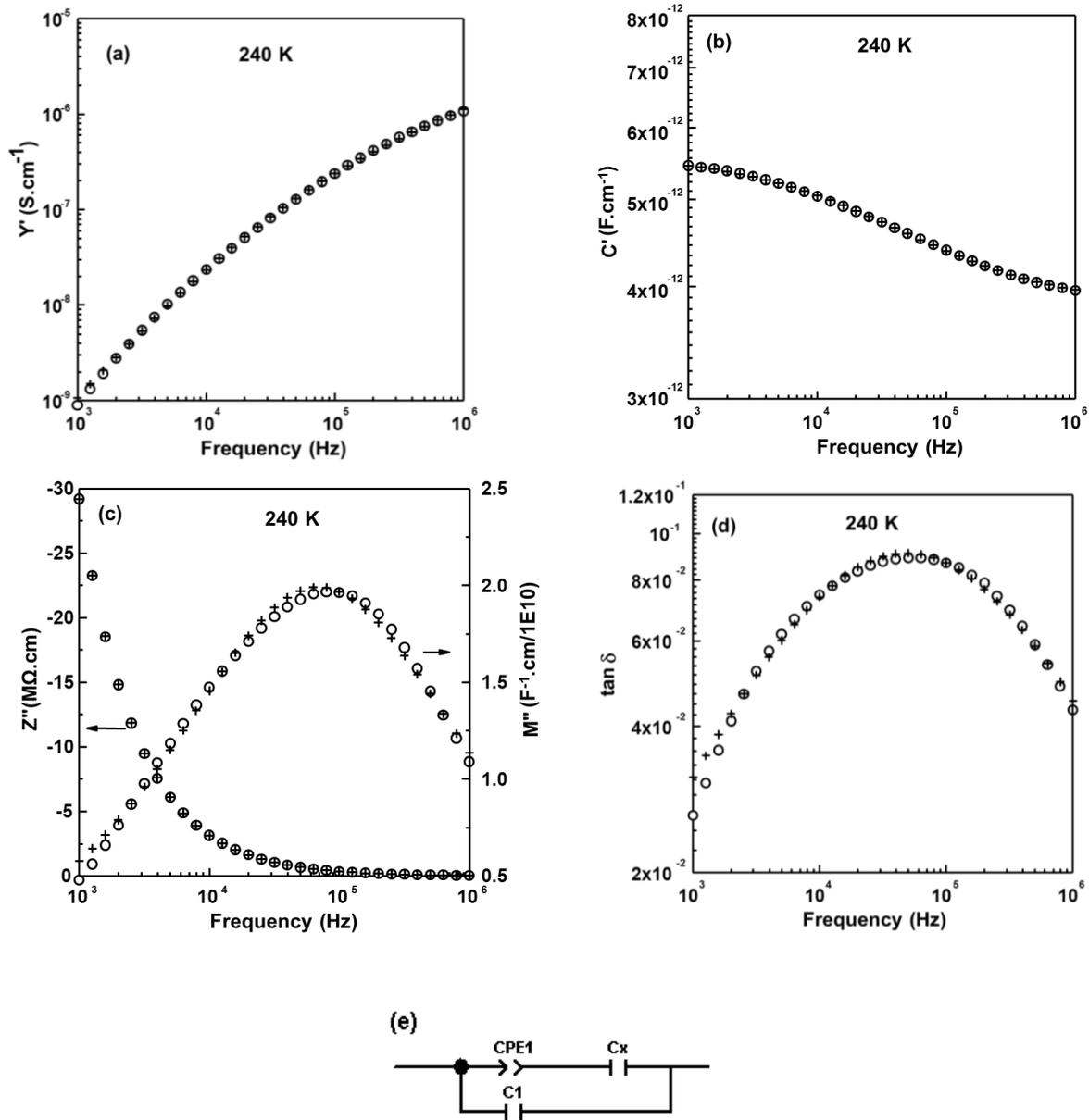
Figure 5.16 Low temperature IS experimental data points (O) and the fitting results (+) to equivalent circuit shown in (e) with (a) Y'; (b) C', (c) –Z"/M", and (d) tan δ spectroscopic plots at 240 K for Bi$_{12}$(B$_{0.75}$P$_{0.25}$)O$_{19.75}$.

A modified equivalent circuit, Figure 5.16 (e), consisting of a parallel connection of C and Cole-Cole branch (CPE in series with a C) was used. *dc* resistance R was eliminated from the equivalent circuit due to the sample being too resistive (R values are too large) to measure. The modified equivalent circuit gave a reasonable fit to the IS data of B$_{0.75}$P$_{0.25}$, in the range of 220-320 K and measured frequency of 10^{3}-10^{6} Hz, as shown in examples for the IS data set at 240 K, Figure 5.16 (a)-(d). All the fitted values of the circuit parameters, C$_1$, C$_x$ and CPE (A and *n*) are listed in Table 5.11.
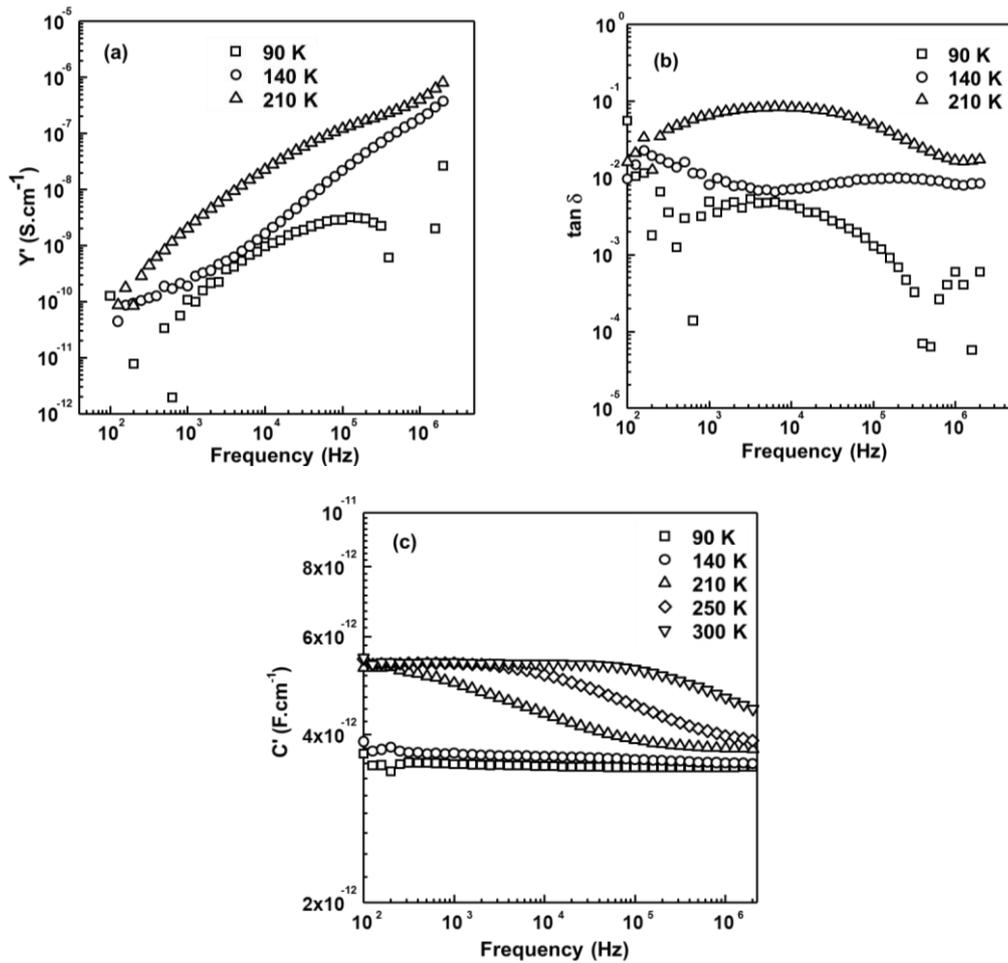
Figure 5.17 (a)Y' , (b) tan δ and (c) C' spectroscopic plots of B$_{0.75}$P$_{0.25}$ at various temperatures.

IS data for B$_{0.75}$P$_{0.25}$ at temperature < 210 K cannot be modelled successfully using the above equivalent circuit, Figure 5.16 (e). Y' spectroscopic data, Figure 5.17 (a), at lower temperature (e.g. at 90 K) revealed a smaller frequency-dependent *ac* conduction. At 140 K, approximate linear, power law dependent *ac* conduction was observed. At 210 K, the second *ac* conduction process (as mentioned above) was observed. Similar behaviour can also be observed from the tan δ spectroscopic plots, where two sets of loss peaks were clearly present, Figure 5.17 (b). C' spectroscopic plot only revealed the permittivity fluctuation for the second relaxation process, Figure 5.17 (c). Activation energy values for the subambient relaxation process(es) of B^{3+} sillenites were obtained from log f$_{max}$ versus 1000/T of the tan δ peak maxima from *rf* fixed frequency measurements and are listed in Table 5.8.

5.3   Discussion

5.3.1   Formation of Boron Containing Sillenites

All formed single-phase boron containing sillenites with their lattice parameters are listed in Table 5.12. Solid solubility for $Bi_{12}(B^{3+}_{1-x}P^{5+}_{x})O_{19.5+x}$ with ~0 ≤ x ≤ ~0.25 and for $Bi_{12}(B^{3+}_{1-x}Si^{4+}_{x})O_{19.5+x/2}$ with ~0.75 ≤ x ≤ 1 were established. Single-phase compounds, except for M = Fe^{3+} were also formed from formulae $Bi_{12}(B^{3+}_{0.5}M^{3+}_{0.5})O_{19.5}$ (M^{3+} = Fe^{3+}, Al^{3+} and Ga^{3+}) and $Bi_{12}(B^{3+}_{0.5}M^{5+}_{0.5})O_{20}$ (M^{5+} = V^{5+}). Among all prepared boron sillenites, "stoichiometric" $Bi_{12}(B_{0.5}P_{0.5})O_{20}$ and $Bi_{12}(B_{0.5}V_{0.5})O_{20}$ were bi-phasic mixtures of two coexisting sillenites with a slightly different unit cell parameter. Similar results for vanadate sillenites was also reported by Devalette et al.[19, 20] They assumed the tetrahedral sites for vanadate sillenites were occupied by either vanadium only or by mixed Bi^{5+} and V^{5+}. The chemical formulae were $Bi_{12}(V_{4/5}^{5+}\square_{1/5})O_{20}$ and $Bi_{12}(V_{0.03}^{5+}Bi_{0.77}^{5+}\square_{1/5})O_{20}$ with lattice parameters of 10.203(1) and 10.255(1)Å, respectively. In addition, they suggested a general formula: $Bi_{12}(B_{4/5-x}^{5+}Bi_{x}^{5+}\square_{1/5})O_{20}$ for solid solution compounds between the above mentioned end-members of the Bi_2O_3-V_2O_5 series. However, single-phase compounds of $B_{0.5}P_{0.5}$ and $B_{0.5}V_{0.5}$ can be achieved by using a fast cooling rate (i.e. air quenching). In contradiction to Valant and Suvorov[9], it is found that altering the heating rate had an insignificant effect on the resultant sillenite phases. The effect of cooling rate on the phase formation indicated the metastability of both compounds: $B_{0.5}P_{0.5}$ and $B_{0.5}V_{0.5}$. Whether the rest of the prepared boron containing sillenites are metastable is still worthy of investigation.

The relationship between the size of the M-site ion(s) and the lattice parameters of the B^{3+} containing sillenites is shown Figure 5.18. Data for the ideal sillenite, $Bi_{12}SiO_{20}$ (Chapter 3); M^{2+}/M^{3+} doped sillenites (Chapter 4) and the parent γ-Bi_2O_3 from Harwig and Gerards[21] are included in the figure for comparison. According to Poleti et al.[22], mixed M-cations sillenites (e.g. $B_{0.5}P_{0.5}$) are intermediate in the plot and should show no systematic trend(s). Our results showed similar results for boron containing sillenites. It seems that smaller dopants (e.g. B^{3+}) in the tetrahedral site can have much more flexible

lattice parameter values than larger dopants (e.g. M^{2+}/M^{3+} sillenites from Chapter 4) where only an approximately linear trend is observed.

Table 5.12 Summary of single-phase B^{3+} containing sillenites.

VS formula	Single-phase Composition	Reaction Temperature / ℃	Lattice Parameter, a(Å)	Unit Cell Volume (Å³)
$Bi_{12}(B^{3+}_{1-x}P^{5+}_x)O_{19.5+x}$	$Bi_{12} (B_{0.5}P_{0.5}) O_{20}$	730	10.1527(6)	1046.49(16)
	$Bi_{12} (B_{0.75}P_{0.25}) O_{19.75}$	730	10.13364(12)	1040.630(22)
$Bi_{12}(B^{3+}_{1-x}Si^{4+}_x)O_{19.5+x/2}$	$Bi_{12} (B_{0.25}Si_{0.75}) O_{19.875}$	730	10.10689(10)	1032.410(18)
$Bi_{12}(B^{3+}_{0.5}M^{3+}_{0.5})O_{19.5}$	$Bi_{12}(B_{0.5}Al_{0.5})O_{19.5}$	680	10.1344(3)	1040.88(5)
	$Bi_{12}(B_{0.5}Ga_{0.5})O_{19.5}$	700	10.1447(4)	1044.03(6)
$Bi_{12}(B^{3+}_{0.5}M^{5+}_{0.5})O_{20}$	$Bi_{12} (B_{0.5}V_{0.5}) O_{20}$	740	10.1709(4)	1052.15(12)
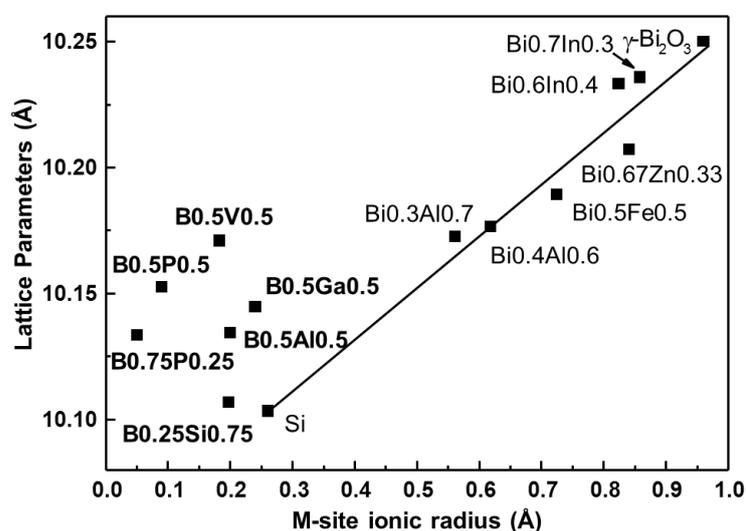
Figure 5.18 The relationship between the unit cell parameters and the M-site ionic radii of B^{3+} containing sillenites (shown as bold letters); data for $Bi_{12}SiO_{20}$ (Chapter 3) and M^{2+}/M^{3+} sillenites (Chapter 4) and γ-Bi_2O_3 from literature[21] are included for comparison. Note: ionic radius for B^{3+} and Bi^{3+} was from Shannon[1] with $B^{3+}_{(III)} = 0.01$ and $Bi^{3+}_{(V)} = 0.96$ Å, respectively.

5.3.2 Structural Features of Boron Containing Sillenites

Consistent with Kargin and Egorysheva[4], NMR results of $Bi_{12}(B_{0.5}P_{0.5})O_{19.5}$, Figure 5.9, showed evidence of coexistence of boron three- and four-fold coordination to oxygen with a relative percentage of 91.8 and 8.2 %, respectively. RS spectra showed BO_3 units (peak ~ 850 cm^{-1}, line 19) were present in all boron containing sillenites, Figure 5.10.

Rietveld refinement results on NPD data of $Bi_{12}(Bi_{0.02}B_{0.98})O_{19.5}$ by using a fixed

composition of $Bi_{12}BO_{19.5}$ for the sillenite phase, Table 5.4, showed three equal B-O bonds (i.e. B-O = 1.495(5) Å) and one longer B-O bond (i.e. B-O = 1.993(14) Å). This indicates the B atoms adopt a three-fold coordination on the tetrahedral site with a similar B-O bond length to the ideal BO_3 trigonal planar unit (i.e. $B-O_{(III)}$ = 1.42 Å[23]). The small concentration of B atoms in the composition considerably lowers the reliability of any determination of crystallographic site occupancy/splitting by B cations and makes the observation of the minority BO_4 groups impossible.
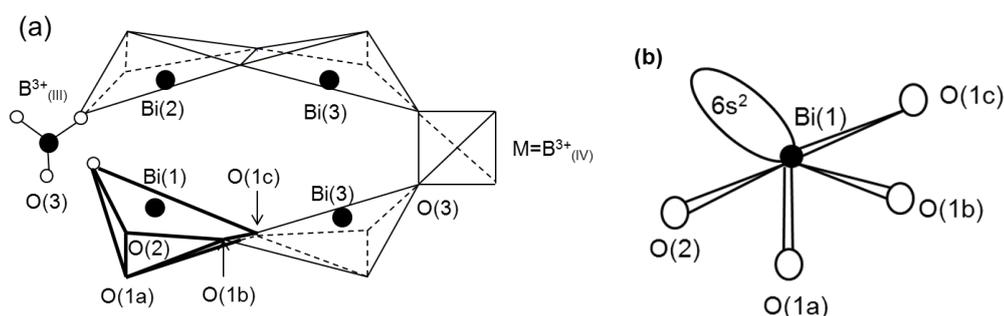
Figure 5.19 Fragment of structure for (a) B^{3+} containing sillenites with unshared O(3) atom in Bi(1)O_5LP polyhedra; (b) distorted trigonal bipyramid Bi(1)O_4LP with unshared Bi^{3+} electron lone pairs in M^{2+}/M^{3+} sillenites.

Compared with the ideal $Bi_{12}SiO_{20}$ sillenite with "rigid" tetrahedral units (SiO_4), structural distortion is inevitably induced by BO_3 units in boron containing sillenites, where one oxygen is not a bridging atom to link between tetrahedral and framework units (i.e. BO_3 and Bi(1)O_5LP), Figure 5.19. This non-bridging oxygen atom is part of the Bi(1)O_5LP polyhedra from the framework of the structure. To achieve local valence balance by introducing pentavalent cations into the structure, the Bi-O(3) bonds of the adjacent BiO_5LP polyhedra are lengthened and the correlated Bi-O(1b) and Bi-O(1c) bonds are shortened; oppositely, for BiO_5LP polyhedra near the BO_3 units Bi(1)-O(3) bonds are shortened and Bi-O(1b) and Bi-O(1c) bonds are lengthened.

Room temperature RS spectra, Figure 5.10, showed that with the incorporation of pentavalent cations (e.g. P^{5+} and V^{5+}) in boron sillenites, a more distorted sillenite structure was attained. The asymmetry of peak at ~ 340 cm^{-1} (line 11) in pentavalent boron sillenites (i.e. $B_{0.5}P_{0.5}$, $B_{0.75}P_{0.25}$ and $B_{0.5}V_{0.5}$) designated the presence of a peak at ~ 360 cm^{-1} (line 12). The increasing magnitude and downshifting of the ~ 360 cm^{-1} peak in pentavalent

boron sillenites compared with the same ~ 380 cm^{-1} peak in trivalent boron sillenites (i.e. B$_{0.5}$Al$_{0.5}$ and B$_{0.5}$Ga$_{0.5}$) showed that the vibrations of O1-Bi-O2 and O1-Bi-O3 bending are stronger and the local structure is more distorted. The larger unit cell for pentavalent boron sillenites promotes the stronger vibration of O1-Bi-O2 and O1-Bi-O3 bending, whereas for trivalent boron sillenites (i.e. B$_{0.5}$Al$_{0.5}$ and B$_{0.5}$Ga$_{0.5}$), the upshifting of the same peak from ~360 cm^{-1} to ~ 380 cm^{-1} (line 12) indicates a weaker vibration of O1-Bi-O2 and O1-Bi-O3 bending that is probably due to limited space/smaller unit cell. Similar vibrations associated with the ~ 380 cm^{-1} peak for trivalent boron sillenites was also observed in M^{2+}/M^{3+} sillenites in Chapter 4. This suggests that the unshared O(3) atom in BiO$_5$LP polyhedra in trivalent boron sillenites is somewhat similar to the unshared Bi^{3+} lone electron pair in the distorted trigonal bipyramid, Bi(1)O$_4$LP, in M^{2+}/M^{3+} sillenites, Figure 5.19 (b).

5.3.3 Origin of Low Temperature Relaxation Behaviour

Fixed frequency measurements of boron containing sillenites ranging from 1 k to 1 MHz, Figure 5.12, revealed a broad frequency-dispersive region of ε_r and tan δ at low temperature (100-400 K). The previous reported relaxor-behaviour in ideal Bi$_{12}$SiO$_{20}$ and M^{2+}/M^{3+} (Chapter 3 and 4) at much higher temperatures (~ 600 -750 K) was also observed in all the boron containing sillenites prepared in this study, which is attributed to dipole moments of the BiO$_5$LP units by the thermal expansion of the framework at elevated temperature. The dielectric loss of the low temperature relaxor behaviour in boron containing sillenites shown here is ~ an order of magnitude less than that of the high temperature relaxation, therefore, the origin of the two relaxations should be different. Valant and Suvorov reported the low temperature relaxation behaviour for Bi$_{12}$(B$_{0.5}$P$_{0.5}$)O$_{20}$ occurring between 200 and 400 K was attributed to random occupation of B and P atoms over the M-sites.[9] Our RS data for Bi$_{12}$(B$_{0.5}$P$_{0.5}$)O$_{20}$ at 100-400 K, Figure 5.11, revealed the strength of BO$_3$ units vibration (i.e. peak 820 cm^{-1} or line 18) increases significantly whereas that of BO$_4$ vibration (i.e. peak 850 cm^{-1} or line 19) decreases with elevated temperature. At 100 K (i.e. "freezing" temperature) most of tetrahedral vibration is from

symmetric BO_4 units; whereas at 400 K, most boron atoms preferentially moved off-centred with a lower symmetric BO_3 coordination, therefore, vibration associated with BO_3 units dominates the tetrahedral vibration at higher temperatures. The randomness and switching between BO_4 and BO_3 units on the tetrahedral site cause Bi^{3+} from adjacent $Bi(1)O_5LP$ octahedra to displace toward BO_3 groups for redistribution of the charge balance. It therefore disrupts the long-range interaction of the electric dipoles and develops random polar regions, which is believed as the origin of the low temperature relaxation behaviour.

This low temperature relaxor-type effect was successfully modelled by the equivalent circuit, Figure 5.17 (e), where a parallel connection of C and Cole-Cole branch (CPE in series with a C) was used. *dc* resistance R was not included in the circuit due to the sample being too resistive (R > 10 GΩ) to measure, only *ac* current can flow through the circuit, the Cole-Cole branch is used to represent the relaxation process associated with short-range orientation of the dipoles from the BiO_5LP units incorporated with movements of B atoms forming BO_3 units. The resistive component of the CPE becomes larger (*n* close to zero) once the co-operative displacements of Bi^{3+} atoms and the rotational BO_4 to BO_3 units are completed, which eventually impedes any displacement of Bi^{3+} atoms from BiO_5LP units.

5.3.4 Microwave Dielectric Properties

The microwave dielectric measurements for B^{3+} sillenite ceramics with similar pellet density ~ 86–92 (±2) % revealed similar microwave dielectric properties with relative permittivity (ε_r) ~ 30 to 38; Q ~ 35 to 60 and τ_f ~ 0 ppm/K at resonant frequency *f* ~ 6 to 7.7 GHz, Table 5.6. As a systematic loss decreases with optimal packing from the close-packed arrangement of the ions in the crystal structure, suggesting the ionic size is important for intrinsic loss[24, 25], it is expected that sillenites with a close-packed tetrahedral arrangement (i.e. a geometrically regular $M^{4+}O_4$ tetrahedral with $r_{(M4+)} = 0.31$ Å [1] and a fully occupied oxygen sublattice) should have the highest Q.f values, for example,

~ 7000 GHz for $Bi_{12}SiO_{20}$, Figure 5.20. B^{3+} containing sillenite analogues exhibit the smallest Q.f values and the highest dielectric losses (tan δ), where the relaxation behaviour was observed from fixed *rf* frequency measurements, Figure 5.12. In addition, a near zero τ_f was observed for all B^{3+} containing sillenites, which also correlated with the broad relaxation peaks over a wide temperature range from 80 to 420 K. The typical property for a non-ferroelectric relaxor with a small value of τ_f and a high permittivity are important factors for possible applications in multilayer ceramic capacitors; however, the permittivity values for the sillenites in this study are too low to be considered for such applications.[26]
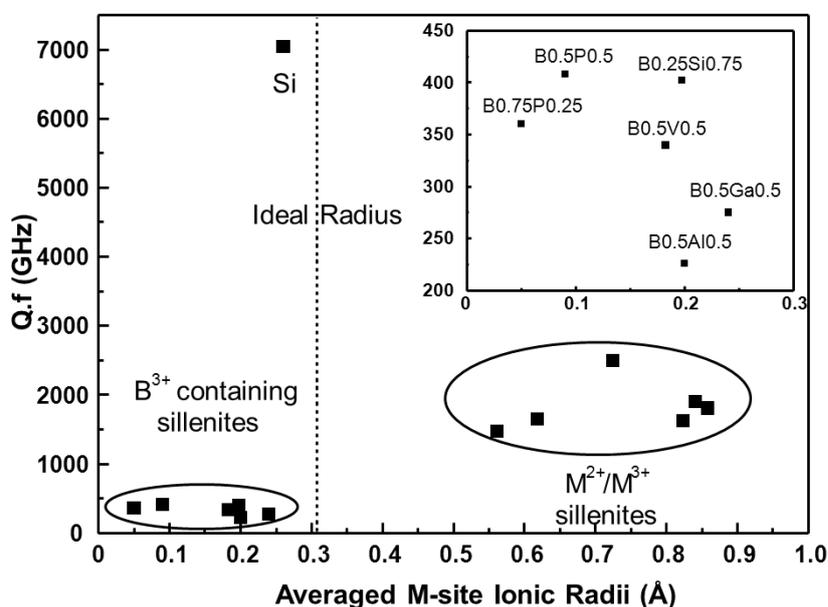
Figure 5.20 Q.f values versus the M-site ionic radii of ideal sillenite ($Bi_{12}SiO_{20}$), M^{2+}/M^{3+} sillenites and B^{3+} containing sillenites. Inset is an expanded view for all B^{3+} containing sillenites.

5.4 Conclusions

Five new phases based on the general formula $(1-x)Bi_{12}BO_{19.5}–xBi_{12}MO_{20+\delta}$, where M = Al^{3+}, Ga^{3+}, Si^{4+}, P^{5+} and V^{5+} have been synthesised and shown to have body-centred cubic structures with space group *I*23 by indexing of XRPD results. Solid solubility for $Bi_{12}(B^{3+}_{1-x}P^{5+}_x)O_{19.5+x}$ with ~0 ≤ x ≤ ~0.25 and for $Bi_{12}(B^{3+}_{1-x}Si^{4+}_x)O_{19.5+x/2}$ with ~0.75 ≤ x ≤ 1 were established. All single-phase boron containing compounds showed VS general formula can be expanded as a baseline for synthesizing new "composite" sillenite phases

with/out Bi^{3+} atoms on the tetrahedral site. It is possible that a large number of related phases may be synthesised. Consistent with Poleti *et al.*[22], mixed M-cation sillenites (e.g. B$_{0.5}$P$_{0.5}$) are intermediate in the plot and should show no systematic trend(s). Our results showed similar results for boron containing sillenites. No linear relationship between the average M-site ions and lattice parameters of B^{3+} containing sillenites was observed, Figure 5.18.

The bi-phasic nature of "stoichiometric" Bi$_{12}$(B$_{0.5}$P$_{0.5}$)O$_{20}$ and Bi$_{12}$(B$_{0.5}$V$_{0.5}$)O$_{20}$ with two coexisting sillenites was detected by XRPD, however, single-phase compounds can be achieved by using a fast cooling rate (i.e. air quenching), which revealed the metastability of both compounds.

Structural refinement for NPD data of Bi$_{12}$(Bi$_{0.02}$B$_{0.98}$)O$_{19.5}$ showed an impurity phase of 2.62 weight % Bi$_4$B$_2$O$_9$ in this end-member composition. Rietveld refinements with fixed composition Bi$_{12}$BO$_{19.5}$ for the sillenite phase showed that B^{3+} preferentially occupies the lower symmetry 8*c* tetrahedral site with three B-O bond length of 1.495(5) Å and one longer B-O bond of B-O = 1.993(14) Å. The near ideal B-O bond length to that of BO$_3$ trigonal planar unit (i.e. B-O$_{(III)}$ = 1.42 Å[23]), confirmed the B^{3+} atom to preferentially adopt three-fold coordination on the tetrahedral site. NMR results for Bi$_{12}$(B$_{0.5}$P$_{0.5}$)O$_{19.5}$, Figure 5.9, showed evidence for the coexistence of boron three- and four-fold coordination with relative percentage of 91.8 and 8.2 %, respectively. RS spectra showed BO$_3$ trigonal planar units (peak ~ 850 cm^{-1}, line 19) were present in all the boron containing sillenites investigated in this study, Figure 5.10.

Microwave dielectric properties of boron containing sillenites showed ε_r ~ 30-38; Q.f ~ 220-400 GHz and τ_f ~ 0 ppm/K at a resonant frequency of ~ 6-7.7 GHz. A high permittivity, low Q.f values and near zero temperature coefficient of resonant frequency τ_f were affected by the frequency- and temperature-dependent relaxation behaviour within the measured microwave range, where the *ac* conductivity possessed quite high tan δ values from fixed frequency and IS results. Low values of Q.f and high dielectric losses of boron containing sillenite analogues eliminate the possibility for LTCC applications. It is found that the M-site ion size and close-packing environment significantly influenced the dielectric losses. A near ideal M-site ionic radius for Bi$_{12}$SiO$_{20}$ (Si$^{4+}_{(VI)}$ = 0.26 Å) gave the

highest Q.f of ~ 7000 GHz.

The characteristic, low temperature relaxation behaviour for boron containing sillenites was probed by subambient *rf* fixed frequency, RS and IS measurements. Subambient RS results of $Bi_{12}(B_{0.5}P_{0.5})O_{20}$, Figure 5.11 , showed a switching from BO_4 to BO_3 units occurs with increasing temperature. The randomness and switching between BO_4 and BO_3 units on the tetrahedral site caused Bi^{3+} from adjacent $Bi(1)O_5LP$ polyhedra to displace toward BO_3 groups for charge redistribution to obtain electroneutrality. It therefore disrupts the long-range interaction of the electric dipoles and develops random polar microregions, which is believed to be the origin of the low temperature relaxation behaviour.

5.5   References

[1]   R. D. Shannon, Revised effective ionic radii and systematic studies of interatomic distances in halides and chalcogenides, Acta Crystallographica Section A*, 1976. **32**: p. 751-767.

[2]   E. M. Levin and C. L. Mcdaniel, The System Bi_2O_3-B_2O_3, Journal of the American Ceramic Society*, 1962. **45**: p. 355-360.

[3]   M. Valant and D. Suvorov, A stoichiometric model for sillenites, Chemistry of Materials*, 2002. **14**: p. 3471-3476.

[4]   Y. F. Kargin and A. V. Egorysheva, Synthesis and structure of the $Bi_{24}B_2O_{39}$ sillenite, Inorganic Materials*, 1998. **34**: p. 714-718.

[5]   M. Burianek and M. Muhlberg, Crystal growth of boron sillenite $Bi_{24}B_2O_{39}$, Crystal Research and Technology*, 1997. **32**: p. 1023-1027.

[6]   M. Burianek, P. Held and A. Muhlberg, Improved single crystal growth of the boron sillenite "$Bi_{24}B_2O_{39}$" and investigation of the crystal structure, Crystal Research and Technology*, 2002. **37**: p. 785-796.

[7]   M. Burianek, S. Haussuhl, M. Kugler, V. Wirth and M. Muhlberg, Some physical properties of boron sillenite: $Bi_{24.5}BO_{38.25}$, Crystal Research and Technology*, 2006. **41**: p. 375-378.

[8]   G. M. Kuzmicheva and T. I. Mel'nikova, Structural features of bismuth borates in

the system nBi_2O_3-mB_2O_3, Russian Journal of Inorganic Chemistry, 2009. **54**: p. 73-80.

[9] M. Valant and D. Suvorov, Synthesis and characterization of a new sillenite compound $Bi_{12}(B_{0.5}P_{0.5})O_{20}$, Journal of the American Ceramic Society, 2002. **85**: p. 355-358.

[10] A. G. Donovan, "Synthesis and characterisation of Bi-based electroceramics," Ph.D. Thesis, University of Sheffield, 2009.

[11] S. L. Lee, C. K. Lee and D. C. Sinclair, Synthesis and characterisation of bismuth phosphate-based sillenites, Solid State Ionics, 2005. **176**: p. 393-400.

[12] S. F. Radaev, V. I. Simonov and Y. F. Kargin, Structural features of g-phase Bi_2O_3 and its place in the sillenite family, Acta Crystallographica Section B-Structural Science, 1992. **48**: p. 604-609.

[13] S. F. Radaev and V. I. Simonov, Structure of sillenites and atomic mechanisms of their isomorphic substitutions, Kristallografiya, 1992. **37**: p. 484-499.

[14] S. F. Radaev, L. A. Muradyan and V. I. Simonov, Atomic structure and crystal chemistry of sillenites $Bi_{12}(Bi^{3+}_{0.50}Fe^{3+}_{0.50})O_{19.50}$ and $Bi_{12}(Bi^{3+}_{0.67}Zn^{2+}_{0.33})O_{19.33}$, Acta Crystallographica Section B-Structural Science, 1991. **47**: p. 1-6.

[15] A. V. Egorysheva, V. I. Burkov, Y. F. Kargin, V. G. Plotnichenko, V. V. Koltashev, E. D. Obraztsova and S. V. Terekhov, Atomic structure features of sillenite crystals as probed by Raman spectroscopy, Russian Journal of Inorganic Chemistry, 2005. **50**: p. 238-245.

[16] B. Mihailova, M. Gospodinov and L. Konstantinov, Raman spectroscopy study of sillenites. I. Comparison between $Bi_{12}(Si,Mn)O_{20}$ single crystals, Journal of Physics and Chemistry of Solids, 1999. **60**: p. 1821-1827.

[17] M. Valant and D. Suvorov, Dielectric characteristics of bismuth oxide solid solutions with a fluorite-like crystal structure, Journal of the American Ceramic Society, 2004. **87**: p. 1056-1061.

[18] A. J. Moulson and J. M. Herbert, *Electroceramics: materials, properties, applications. (Second Edition)*. Chichester, England: John Wiley & Sons Ltd., 2003.

[19] M. Devalette, G. Meunier, J. P. Manaud and P. Hagenmuller, New cationic deficient phases $Bi_{12}(B^{5+}_{4/5-x}Bi^{5+}_x p_{1/5})O_{20}$ with sillenite structure, Comptes Rendus De L Academie Des Sciences Serie Ii, 1983. **296**: p. 189-191.

[20]   N. Khachani, M. Devalette and P. Hagenmuller, On the stoichiometry of the allotropic variation γ-Bi_2O_3, Zeitschrift Fur Anorganische Und Allgemeine Chemie, 1986. **533**: p. 93-98.

[21]   H. A. Harwig and A. G. Gerards, Polymorphism of bismuth sesquioxide, Thermochimica Acta, 1979. **28**: p. 121-131.

[22]   D. Poleti, L. Karanovic and A. Hadzi-Tonic, Doped gamma-Bi_2O_3: synthesis of microcrystalline samples and crystal chemical analysis of structural data, Zeitschrift Fur Kristallographie, 2007. **222**: p. 59-72.

[23]   A. R. West, *Solid state chemistry and its applications*. Aberdeen: John Wiley & Sons, 1989.

[24]   M. Valant and D. Suvorov, Processing and dielectric properties of sillenite compounds $Bi_{12}MO_{20-d}$ (M = Si, Ge, Ti, Pb, Mn, $B_{1/2}P_{1/2}$), Journal of the American Ceramic Society, 2001. **84**: p. 2900-2904.

[25]   R. Zurmuhlen, J. Petzelt, S. Kamba, G. Kozlov, A. Volkov, B. Gorshunov, D. Dube, A. Tagantsev and N. Setter, Dielectric spectroscopy of $Ba(B'_{1/2}B''_{1/2})O_3$ complex perovskite ceramics: Correlations between ionic parameters and microwave dielectric properties. II. Studies below the phonon Eigenfrequencies (10^2-10^{12} Hz). Journal of Applied Physics, 1995. **77**: p. 5351-5364.

[26]   J. C. Nino, M. T. Lanagan and C. A. Randall, Dielectric relaxation in Bi_2O_3-ZnO-Nb_2O_5 cubic pyrochlore, Journal of Applied Physics, 2001. **89**: p. 4512-4516.

6 Investigation of Phosphorus (P^{5+}) Containing Sillenites

6.1 Introduction

The Valant and Suvorov (VS) general formula $Bi_{12}(Bi^{3+}_{4/5-nx}M^{n+}_{5x})O_{19.2+nx}$[1] states the mechanism for pentavalent cation (M^{5+}) doping is that each Bi^{3+} ion on the tetrahedral site is substituted by one M^{5+} ion and one oxygen ion. The oxygen ion fills the space previously occupied by the Bi^{3+} lone electron pairs. The upper substitution limit is when there is no Bi^{3+} ion on the tetrahedral site, i.e. $Bi_{12}(M^{5+}_{4/5}\square_{1/5})O_{20}$.[1] Beyond this limit, additional oxygen ions are sometimes accommodated in the structure for M^{5+} dopants to achieve electroneutrality, leading to the formation of superstoichiometric sillenites with an excess of oxygen on the anion sublattice (i.e. > 20), e.g. $Bi_{12}(Bi^{3+}_{0.03}V_{0.89}\square_{0.08})O_{20.27}[LP]_{0.03}$[2]. Three representative M^{5+} sillenites from the literature are $M^{5+} = P^{5+}$, V^{5+} and As^{5+}.[2-6] Consistent with the VS formula, Soubeyroux *et al.*[6] and Devalette *et al.*[7] reported the end member for M^{5+} sillenites is $Bi_{12}(M^{5+}_{4/5}\square_{1/5})O_{20}$. However, Radaev and Simonov[2]; Watanabe *et al.*[8, 9] and Lee and Sinclair[4] found the solid solubility limits for V, As and P dopants were up to 6.74, 6.88 and 7.69 mol %, respectively, which all exceed that reported in the VS formula (i.e. 6.67 mol %).

The crystal chemistry of M^{5+} superstoichiometric sillenites possesses distinct deformation of the Bi-O framework structure. Radaev and coworkers (R model)[2, 10] disproved the existence of Bi^{5+} [6][7, 11][12] and proposed a structural model, where voids in the sillenite framework (6*b* site) are occupied by excess oxygen ions (O4 atoms), Figure 6.1. With the incorporation of O4 atoms, the Bi-O framework polyhedra undergo the greatest distortion with Bi(1) and O(3) atoms practically disconnected from each other. The additional oxygen atoms O(4) become part of the coordination environment of the Bi-O framework polyhedra, which is a distorted octahedron with an equatorial plane of O(1a), O(1c), O(2), O(4) and apical vertices of O(1b) and the unshared $6s^2$ lone electron pairs of Bi^{3+} atom. Two adjacent polyhedra are face-sharing via O(1b), O(1c) and O(4) and then

corner-sharing via O(4) to another pair. Equally probable vacancies in any of the four tetrahedra and statistically random occupation of *6b* sites by O(4) atoms release the local stress/strain near O(4) atoms and preserve an average cubic structure with space group of *I*23.
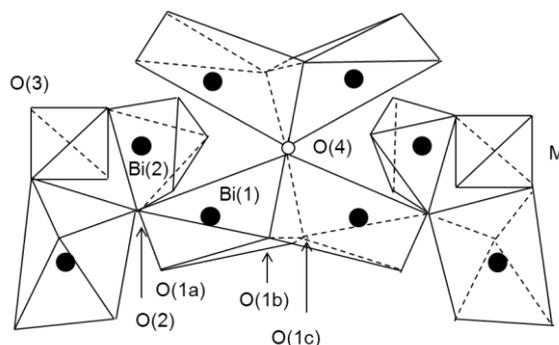
Figure 6.1 Structural feature of superstoichiometric sillenite with additional oxygen O(4) atom occupied the *6b* site to show distinct Bi-O framework polyhedra.

The aim of this chapter is to continue the investigation of the low temperature relaxation behaviour in P^{5+} containing sillenites: whether P^{5+} containing sillenites would exhibit the peculiar relaxation phenomenon at low temperature ($\sim 200 - 400$ K) as reported for $Bi_{12}(B_{0.5}P_{0.5})O_{20}$[13]. Four phosphorus containing sillenites: $Bi_{12}(Bi^{3+}_{0.03}P^{5+}_{0.89}\square_{0.08})O_{20.27}$, $Bi_{12}(P^{5+}_{0.86}\square_{0.14})O_{20.15}$, $Bi_{12}(Fe^{3+}_{0.5}P^{5+}_{0.5})O_{20}$ and $Bi_{12}(Mg^{2+}_{0.33}P^{5+}_{0.67})O_{20}$ were synthesised by the solid state reaction method. Structural and electrical property analysis were investigated by using X-ray Powder Diffraction (XRPD), Raman Spectroscopy (RS), Nuclear Magnetic Resonance (NMR), microwave (MW) dielectric resonance, *rf* fixed frequency capacitance and Impedance Spectroscopy (IS) measurements. A correlation between the M-ion ionic radius and the sillenite lattice parameter is discussed. A possible origin of the low temperature (LT) relaxation phenomenon for P^{5+} containing sillenites is suggested.

6.2   Results

6.2.1 Synthesis of Phosphorus Containing Sillenites

~ 10 g each of the following four P^{5+} containing sillenites: $Bi_{12}(Bi^{3+}_{0.03}P^{5+}_{0.89}\square_{0.08})O_{20.27}$, $Bi_{12}(P^{5+}_{0.86}\square_{0.14})O_{20.15}$, $Bi_{12}(Fe^{3+}_{0.5}P^{5+}_{0.5})O_{20}$ and $Bi_{12}(Mg^{2+}_{0.33}P^{5+}_{0.67})O_{20}$ were synthesised by the traditional solid state reaction method. Precursors were dried at appropriate temperatures, as listed in Table 2.1 in Chapter 2: Experimental Procedure. Samples were ground together with acetone using a mortar and pestle and heated in Au foil boats from room temperature to 400 ℃ for 2 hours with a heating rate of 1 ℃/min to evaporate any H_2O and/or NH_3 in the reagents and then heated at 700 ℃ for 6 hours with a heating and cooling rate of 10 ℃/min. The samples were eventually reacted between 730 and 780 ℃ with intermediate grinding until an equilibrium state was detected by X-ray powder diffraction. The single-phase compositions based on XRPD results are listed in Table 6.1.

Table 6.1 Summary of single-phase P^{5+} containing sillenites examined by XRPD.

Single-phase Composition	Reaction Temperature / ℃	Reaction Time / h	Sintering Temperature / ℃
$Bi_{12}(Bi_{0.03}P_{0.89}\square_{0.08})O_{20.27}$	730	48	850
$Bi_{12}(P_{0.86}\square_{0.14})O_{20.15}$	780	48	855
$Bi_{12}(Fe^{3+}_{0.5}P^{5+}_{0.5})O_{20}$	790	36	870
$Bi_{12}(Mg^{2+}_{0.33}P^{5+}_{0.67})O_{20}$	780	48	864

6.2.2 XRPD

XRPD results, Figure 6.2, showed four single-phase P^{5+} containing sillenites: $Bi_{12}(Bi^{3+}_{0.03}P^{5+}_{0.89}\square_{0.08})O_{20.27}$, $Bi_{12}(P^{5+}_{0.86}\square_{0.14})O_{20.15}$, $Bi_{12}(Fe^{3+}_{0.5}P^{5+}_{0.5})O_{20}$ and $Bi_{12}(Mg^{2+}_{0.33}P^{5+}_{0.67})O_{20}$. All the XRPD data could be indexed on a single cell (space group of $I23$) with no splitting of peaks observed at higher 2θ values over 65-85 ﹔ as shown in the inset of Figure 6.2.
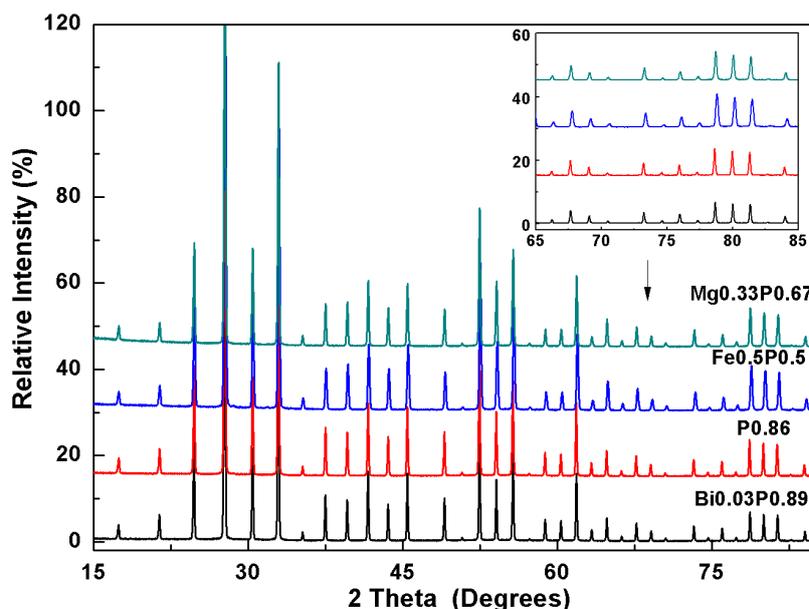
Figure 6.2 XRPD results of single-phase P^{5+} containing sillenites Bi$_{12}$(Bi$^{3+}_{0.03}$P$^{5+}_{0.89}\square_{0.08}$)O$_{20.27}$, Bi$_{12}$(P$^{5+}_{0.86}\square_{0.14}$)O$_{20.15}$, Bi$_{12}$(Fe$^{3+}_{0.5}P^{5+}_{0.5}$)O$_{20}$ and Bi$_{12}$(Mg$^{2+}_{0.33}$P$^{5+}_{0.67}$)O$_{20}$.

6.2.3 Raman Spectroscopy

● Room Temperature (RT) Raman Spectroscopy

Room temperature Raman spectra for P^{5+} containing sillenites are shown in Figure 6.3 and the corresponding Raman peak assignments are listed in Table 6.2. The unique Raman feature for all P^{5+} containing sillenites is the presence of peak at ~ 901 cm^{-1} (line 20), assigned as vibrations of the PO$_4$ tetrahedral unit. The Raman spectra for P^{5+} containing sillenites can be divided into two groups:

(i)   Raman spectra of Bi$_{0.03}$P$_{0.89}$ and P$_{0.86}$ were almost identical with M^{5+} doping boron containing sillenites, e.g. B$_{0.5}$P$_{0.5}$ and B$_{0.5}$V$_{0.5}$ in Chapter 5, except for the absence of a peak at ~ 850 cm^{-1} (line 19) which corresponds to vibrations of the BO$_3$ group. As superstoichiometric sillenites, the downshift of Raman peak ~ 350 cm^{-1} (line 11) is assigned as shortening of the Bi-O(1b) bonds; whereas the upshift of Raman peak ~ 85 cm^{-1} (line 3) indicates lengthening of the Bi-O(3) bonds.

(ii)   Raman spectra of Fe$_{0.5}$P$_{0.5}$ and Mg$_{0.33}$P$_{0.67}$ between 200 and 400 cm^{-1} were similar to those of M^{2+}/M^{3+} sillenites (Chapter 4) with corresponding peaks at ~ 265 cm^{-1}

(line 10), ~ 320 cm^{-1} (line 11) and ~ 380 cm^{-1} (line 12), respectively.
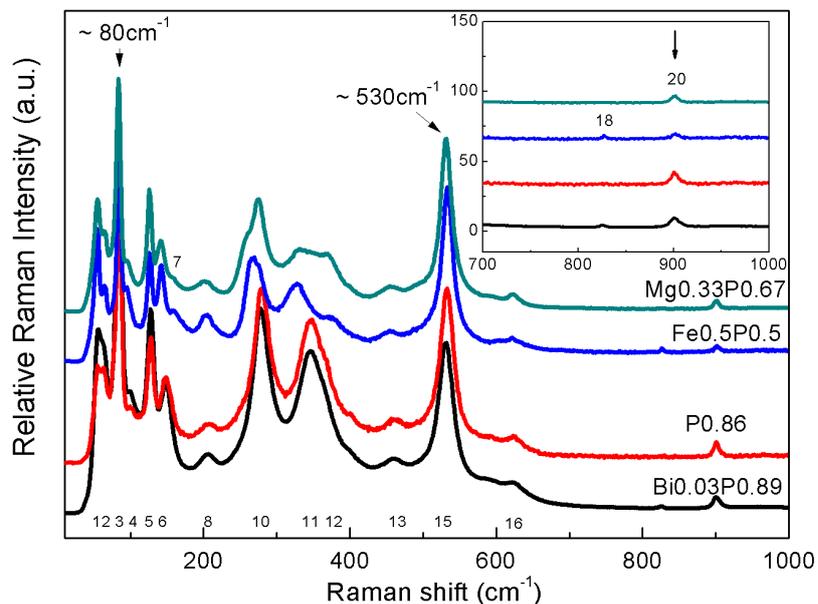
Figure 6.3 Room temperature Raman Spectra of $Bi_{12}(Bi^{3+}_{0.03}P^{5+}_{0.89}\square_{0.08})O_{20.27}$, $Bi_{12}(P^{5+}_{0.86}\square_{0.14})O_{20.15}$, $Bi_{12}(Fe^{3+}_{0.5}P^{5+}_{0.5})O_{20}$ and $Bi_{12}(Mg^{2+}_{0.33}P^{5+}_{0.67})O_{20}$. Peak intensities are normalized by peak ~ 530 cm^{-1}.
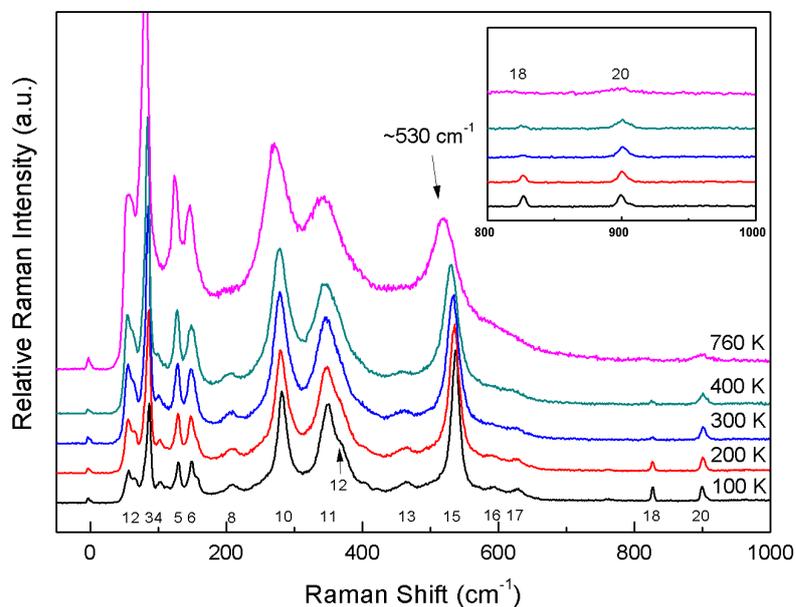
Figure 6.4 Raman spectra of $Bi_{0.03}P_{0.89}$ at 100, 200, 300, 400 and 760 K. Peak intensities are normalized by peak ~ 530 cm^{-1}. Inset is the enlarged version of showing Raman peak ~825 cm^{-1} (line 18) and ~ 901cm^{-1} (line 20).

Table 6.2 Raman peak positions of P^{5+} containing sillenites, data of ideal sillenite $Bi_{12}SiO_{20}$ was used for comparison.

Line No.	Si	$Bi_{0.03}P_{0.89}$	$P_{0.86}$	$Fe_{0.5}P_{0.5}$	$Mg_{0.33}P_{0.67}$	Mode[14]	Type of Vibrations[14, 15]
1	55	56	55	55	55	F	Bi,O2,O3 and M vibration
2	63	64	63	64	64	E	Bi,O1,O2 and O3vibrations elongating the cluster along either [100] or [001]
3	88	85*	84*	85*	84*	E	Bi,O2 and O3 vibrations elongating the cluster
4	95	99	99	95	94	A	Bi-O1 bonds vibration and 'breathing' of O2 atoms
5	129	122	128	126	126	E	Bi and O2 vibrations elongating the cluster along either [100] or [010]
6	144	149	148	142	141	A	'breathing' of Bi and O2 atoms
7	166	-	-	158	158	A	'breathing' of Bi and all O atoms
8	204	207	208	205	198	F	Bi-O1 stretching & Bi-O2-Bi bending and weak Bi-O1 rocking
9	251	-	-	-	-	E	Bi-O1 rocking and weak O2 vibrations elongating the cluster along either [100] or [001]
10	276	278	280	265	275	A	O2 'breathing' and weak Bi-O1 rocking
11	328	347	348	327	331	A	Bi-O1 rocking and weak O2 'breathing'
12	358	358	363	373	366	F	O1-Bi-O2 and O1-Bi-O3 bending
13	460	460	463	455	455	E	O2 vibration elongating the cluster along either [001] or [010] and weak Bi-O1 and Bi-O3 rocking
14	488	-	-	-	-	F	Bi-O1 stretching and deformation of MO4 tetrahedra
15	538*	532	533	534	532	A	'breathing' of O1 atoms
16	621	621	623	621	622	E	O3 vibrations elongating the cluster along either [010] or [100] and weakBi-O1 and Bi-O2 rocking
17	788	788	-	-	-	A	Symmetric stretching of MO_4 tetrahedra
18	829	825	-	826	-	FTO	Asymmetric stretching of MO_4 tetrahedra
19	-	-	-	-	-	-	-
20	-	901	901	902	902	-	Stretching of PO_4 unit

Notation * indicates the strongest peak intensity.

The *rf* fixed frequency measurements (Section 6.2.6) showed that low temperature (10-400 K) relaxation behaviour was only present in $Bi_{0.03}P_{0.89}$ and $P_{0.86}$. Variable temperature Raman spectra for the same grain of sample $Bi_{0.03}P_{0.89}$ at selected temperature 100, 200, 300, 400 and 760 K, Figure 6.4, showed the magnitude of the Raman peak at ~ 825 cm^{-1} (line 18) to vary with a value of 10.59, 7.48, 3.82 and 8.95 at 100, 200, 300 and 400 K,

respectively. The Raman peak ~ 825 cm^{-1} (line 18) is assigned as asymmetric stretching of MO_4 tetrahedra. The peak intensity indicates the strength of the associated vibrations. The weakest peak ~825 cm^{-1} vibration was observed at 300 K and it became stronger at 400 K. The peak intensity at 400 K is suppressed in Figure 6.4, as the strongest peak switched over from peak 530 cm^{-1} at 300 K to peak 80 cm^{-1} at 400 K. Associated with MO_4 tetrahedral vibrations, the Raman peak ~ 530 cm^{-1} (line 15) assigned as the vibrations of the framework units were downshifted with values of 537, 536, 534 and 531 cm^{-1}, respectively. This might be related to the origin of the LT relaxation behaviour in the sample. In addition, a further broadening/downshifting of peak ~530 cm^{-1} to 520 cm^{-1} was observed at 760 K. The differences between the associated activation energy for LT and HT relaxation processes of $Bi_{0.03}P_{0.89}$ (i.e. 0.48 and 1.21 eV, respectively) indicate the origin of both relaxations are different, as discussed in Chapter 7.

6.2.4 Nuclear Magnetic Resonance (NMR) Spectroscopy

NMR spectroscopy was used to investigate detailed information about the PO_4 tetrahedral environments of $Bi_{12}(B_{0.5}P_{0.5})O_{20}$ and $Bi_{12}(Bi_{0.03}P_{0.89}\square_{0.08})O_{20.27}$, both of which exhibit relaxation behaviour at room temperature (300 K). ^{31}P one pulse spectra of $Bi_{12}(B_{0.5}P_{0.5})O_{20}$ and $Bi_{12}(Bi_{0.03}P_{0.89}\square_{0.08})O_{20.27}$ were carried out under a magnetic field of 7.05 T (12.5 kHz MAS) with a one peak chemical environment of PO_4 detected, Figure 6.5 and Table 6.3. Compared with $B_{0.5}P_{0.5}$, a broadening of the NMR peak width at its half height was observed for $Bi_{0.03}P_{0.89}$. This indicates a disordered distribution of P/Bi/$\square$ over the tetrahedral sites, which may be responsible for the LT dielectric relaxation phenomena.
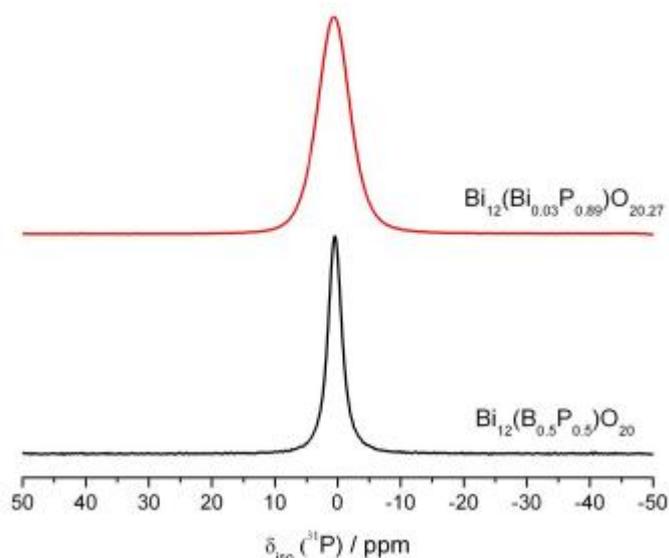
Figure 6.5 NMR spectra of isotope ^{31}P one pulse signal of $Bi_{12}(B_{0.5}P_{0.5})O_{20}$ and $Bi_{12}(Bi_{0.03}P_{0.89}\square_{0.08})O_{20.27}$ carried out at 7.05 T (12.5 kHz MAS).

Table 6.3 Details of NMR isotope ^{31}P peak from $Bi_{12}(B_{0.5}P_{0.5})O_{20}$ and $Bi_{12}(Bi_{0.03}P_{0.89}\square_{0.08})O_{20.27}$.

Sample	Isotropic Shift (ppm)	Width (ppm)
$Bi_{12}(Bi_{0.03}P_{0.89})O_{20.27}$	0.61	5.84
$Bi_{12}(B_{0.5}P_{0.5})O_{20}$	0.42	2.35

6.2.5 Microwave (MW) Dielectric Properties

Microwave dielectric measurements performed on P^{5+} containing sillenites showed that $Bi_{0.03}P_{0.89}$ and $P_{0.86}$ did not resonant at MW frequencies; whereas $Fe_{0.5}P_{0.5}$ and $Mg_{0.33}P_{0.67}$ resonated at ~ 7 GHz with relative permittivity (ε_r) ~ 30; Q ~ 150-180 and τ_f ~ from -15 to +43 ppm/K over the temperature range 20-80 °C, Table 6.4.

Table 6.4 MW dielectric properties of P^{5+} containing sillenites.

Composition	Sintering Temperature / °C	Pellet Density /%	ε_r	Q	f_0 /GHz	Q.f /GHz	τ_f /ppm/K	CM_ calc. ε_r
$Bi_{12}(Bi_{0.03}P_{0.89}\square_{0.08})O_{20.27}$	850	90		Too lossy to be measured				36
$Bi_{12}(P_{0.86}\square_{0.14})O_{20.15}$	855	93		Too lossy to be measured				34
$Bi_{12}(Fe^{3+}_{0.5}P^{5+}_{0.5})O_{20}$	850	83	31	150	7.058	1059	-15	38
$Bi_{12}(Mg^{2+}_{0.33}P^{5+}_{0.67})O_{20}$	864	83	32	179	7.215	1291	43	34

6.2.6 Fixed Frequency Capacitance Measurements

The frequency dependence of ε_r and tan δ for P^{5+} containing sillenites over the measured temperature range are shown in Figure 6.6 (a)–(h). All measured P^{5+} containing sillenites revealed a broad, highly frequency-dispersive region at high temperature (T > 400 K), which is similar to what is seen in all other groups of sillenites (in Chapter 3-5). However, only Bi$_{0.03}$P$_{0.89}$ and P$_{0.86}$ exhibited a low temperature relaxation region at ~ 100 – 400 K. This result indicated that the low temperature (LT) relaxation behaviour is not only present in B^{3+} containing sillenites, but also in some of P^{5+} containing sillenites. Activation energy values of the low temperature relaxation process for P^{5+} containing sillenites: Bi$_{0.03}$P$_{0.89}$ and P$_{0.86}$ were obtained from log f$_{max}$ versus 1000/T of the tan δ peak maxima from *rf* fixed frequency measurements and are listed in Table 6.5.
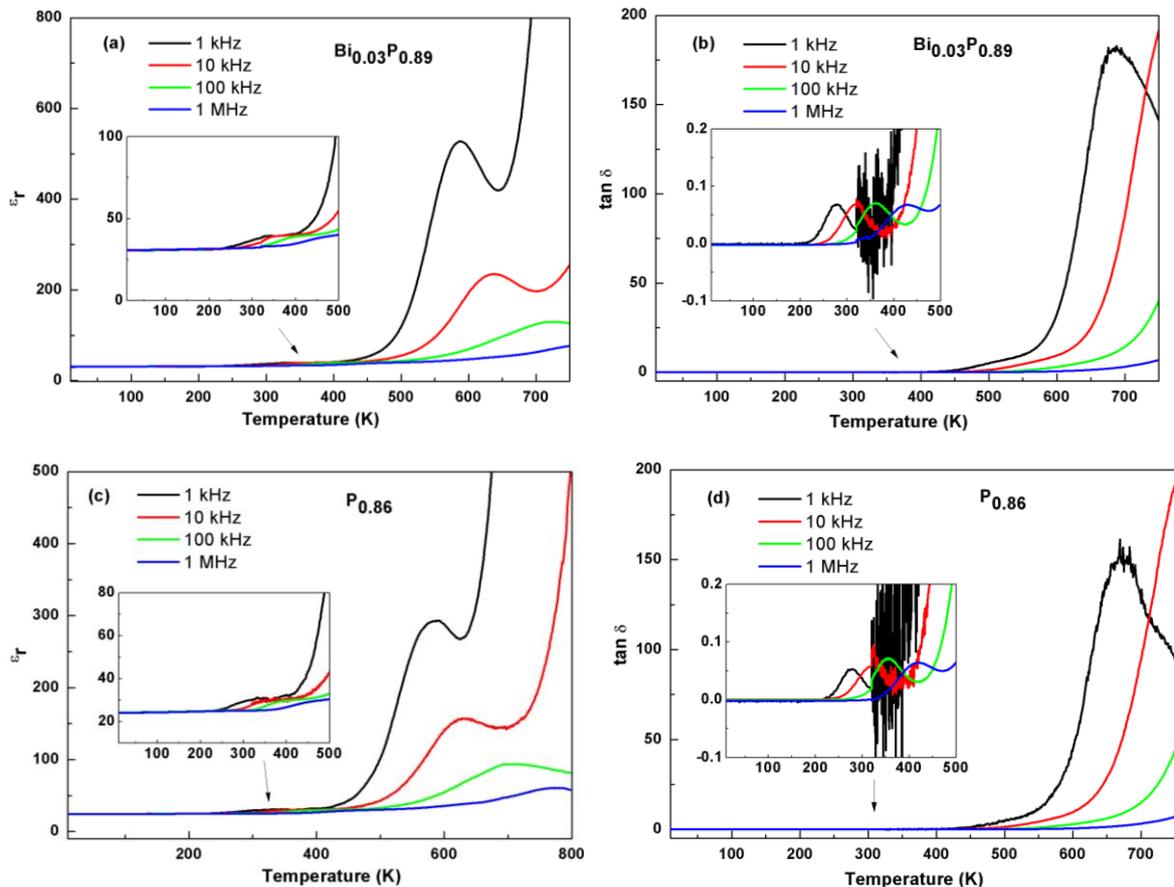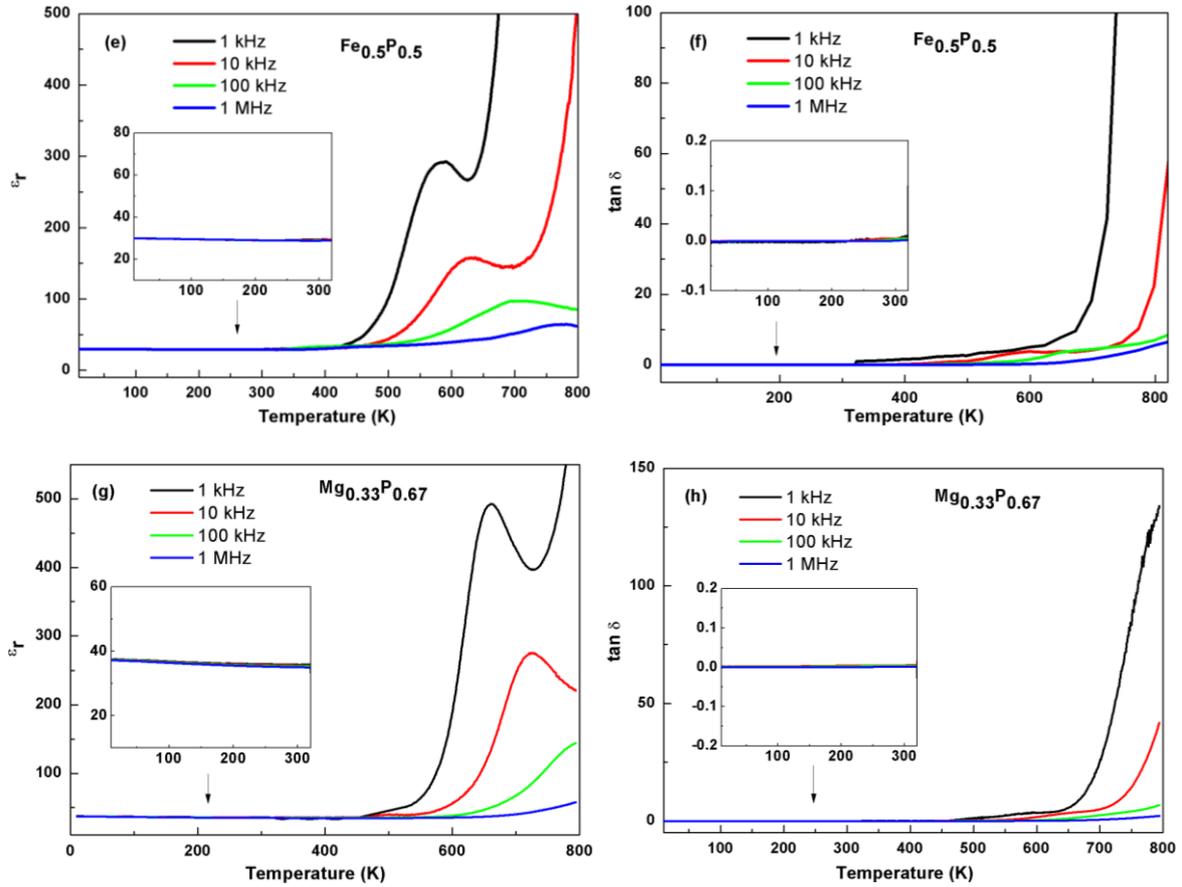
Figure 6.6 Temperature dependence of permittivity (ε_r) and dielectric loss (tan δ) of (a) and (b) $Bi_{12}(Bi_{0.03}P_{0.89}\square_{0.08})O_{20.27}$; (c) and (d) $Bi_{12}(P_{0.86}\square_{0.14})O_{20.15}$; (e) and (f) $Bi_{12}(Fe_{0.5}P_{0.5})O_{20}$; (g) and (h) $Bi_{12}(Mg_{0.33}P_{0.67})O_{20}$, respectively.

Table 6.5 Temperature of tan δ peak maximum (at 10 kHz) and activation energy (Ea) (obtained from log f_{max} versus 1000/T of the tan δ peak maxima) of the lower temperature relaxation process(es) for P^{5+} containing sillenites: $Bi_{0.03}P_{0.89}$ and $P_{0.86}$.

Composition	Temperature of tan δ peak maxima at 10 kHz / K	Activation Energy (Ea_relaxation) / eV
$Bi_{12}(Bi_{0.03}P_{0.89}\square_{0.08})O_{20.27}$	320	0.46
$Bi_{12}(P_{0.86}\square_{0.14})O_{20.15}$	320	0.50

6.2.7 Impedance Spectroscopy (IS)

Low (10-400 K) and high (400-800 K) temperature IS measurements were performed on gold-sputtered P^{5+} containing sillenite samples, Table 6.6, to probe the LT and HT relaxation phenomenon observed from *rf* fixed frequency measurements. LT relaxation

behaviour was not present in the $Mg_{0.33}P_{0.67}$ sample. HT IS results for $Bi_{0.03}P_{0.89}$ were used to show the higher temperature relaxation phenomenon as well as the oxide ionic conductivity for superstoichiometric sillenites. The IS data for the rest of the compounds and circuit fitting results are shown in Appendix III.

Table 6.6 Details of phosphorus containing sillenites from IS measurements. All samples had gold-sputtered electrodes.

Single-phase Composition	Sintering Temperature / °C	Pellet Density / %
$Bi_{12}(Bi_{0.03}P_{0.89}\square_{0.08})O_{20.27}$	850	90
$Bi_{12}(P_{0.86}\square_{0.14})O_{20.15}$	855	93
$Bi_{12}(Fe^{3+}_{0.5}P^{5+}_{0.5})O_{20}$	870	83
$Bi_{12}(Mg^{2+}_{0.33}P^{5+}_{0.67})O_{20}$	864	83

6.2.7.1 Low Temperature IS Data for $Bi_{12}(Mg_{0.33}P_{0.67})O_{20}$ (10 − 400 K)

Low temperature IS data of $Mg_{0.33}P_{0.67}$ at 320 K, Figure 6.7 (a)-(d), is used to show that no relaxation behaviour was observed at the measured temperature range of 10-400 K, which is similar with fixed frequency results in Figure 6.6 (g) and (h). A C' spectroscopic plot, Figure 6.7 (a), showed only one frequency-independent C' plateau existed throughout the measured temperature range. Y' spectroscopic plot, Figure 6.7 (b), showed power-law *ac* conductivity. In addition, no relaxation loss peaks was observed in either Z''/M'' or tan δ spectroscopic plots, Figure 6.7 (c) and (d).
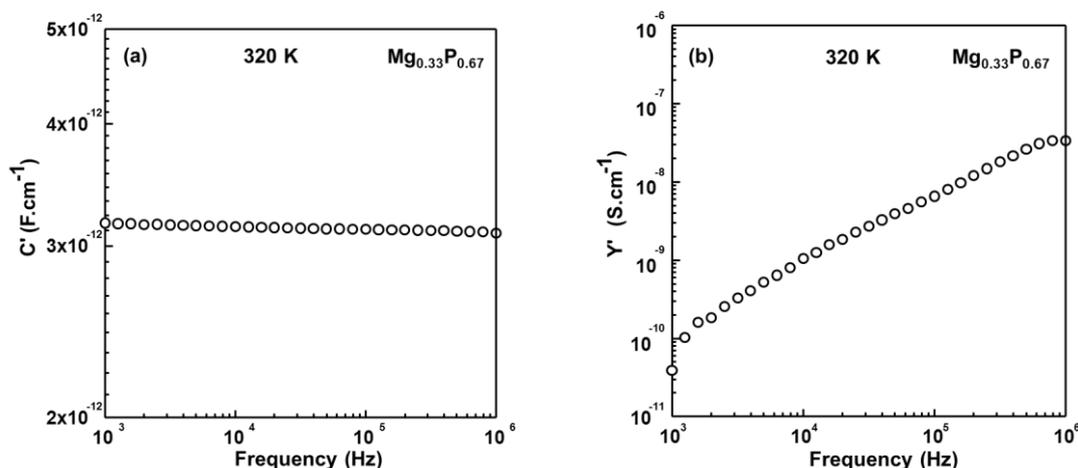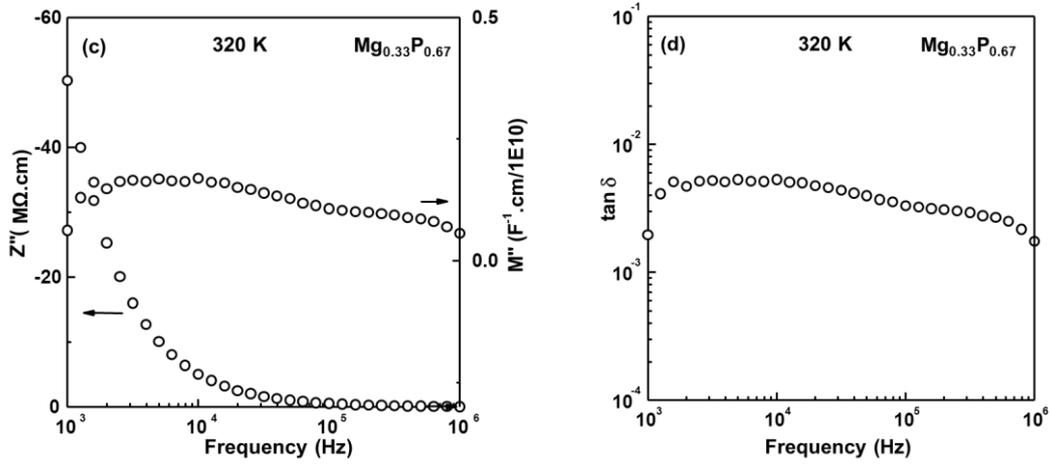
Figure 6.7 (a) C'; (b) Y'; (c) –Z"/M" and (d) tan δ spectroscopic plots for $Bi_{12}(Mg_{0.33}P_{0.67})O_{20}$ at 320 K to show that no low temperature relaxation behaviour was present.

6.2.7.2 IS data for $Bi_{12}(Bi_{0.03}P_{0.89})O_{20.27}$

- **Low temperature IS data (10 – 400 K)**

LT IS data for $Bi_{12}(Bi_{0.03}P_{0.89})O_{20.27}$ at 328 K presented in different formats is selected to show the general low temperature relaxation behaviour for P^{5+} containing sillenite analogues, Figure 6.8 (a)-(d). The modified equivalent circuit without *dc* resistance R, Figure 6.8 (e), gave a reasonable fit to the IS data in the measured frequency of 10^3-10^6 Hz, as shown in the example for $Bi_{0.03}P_{0.89}$ in the range of 290-373 K and the fitted values of the circuit parameters, C_1, C_x and CPE (A and *n*) are listed in Table 6.7.

Table 6.7 Fitted subambient IS values of $Bi_{12}(Bi_{0.03}P_{0.89})O_{20.27}$ from 270 to 373 K for the low temperature relaxation. Errors associated with the fitted circuit parameters C_1, C_x, A and *n* are $< \pm0.21$ %,$< \pm1.89$ %,$< \pm11.86$ % and $< \pm17.32$ %, respectively.

Temperature (K)	C_1 (pF cm^{-1})	C_x (pF cm^{-1})	A (Ω^{-1} cm^{-1} rad^{-1})	*n*
290	2.77	0.56	1.83×10^{-9}	0.12
310	2.77	0.59	2.99×10^{-9}	0.15
328	3.03	0.60	1.06×10^{-8}	0.17
348	3.03	0.61	1.60×10^{-8}	0.20
373	3.02	0.64	2.29×10^{-8}	0.23
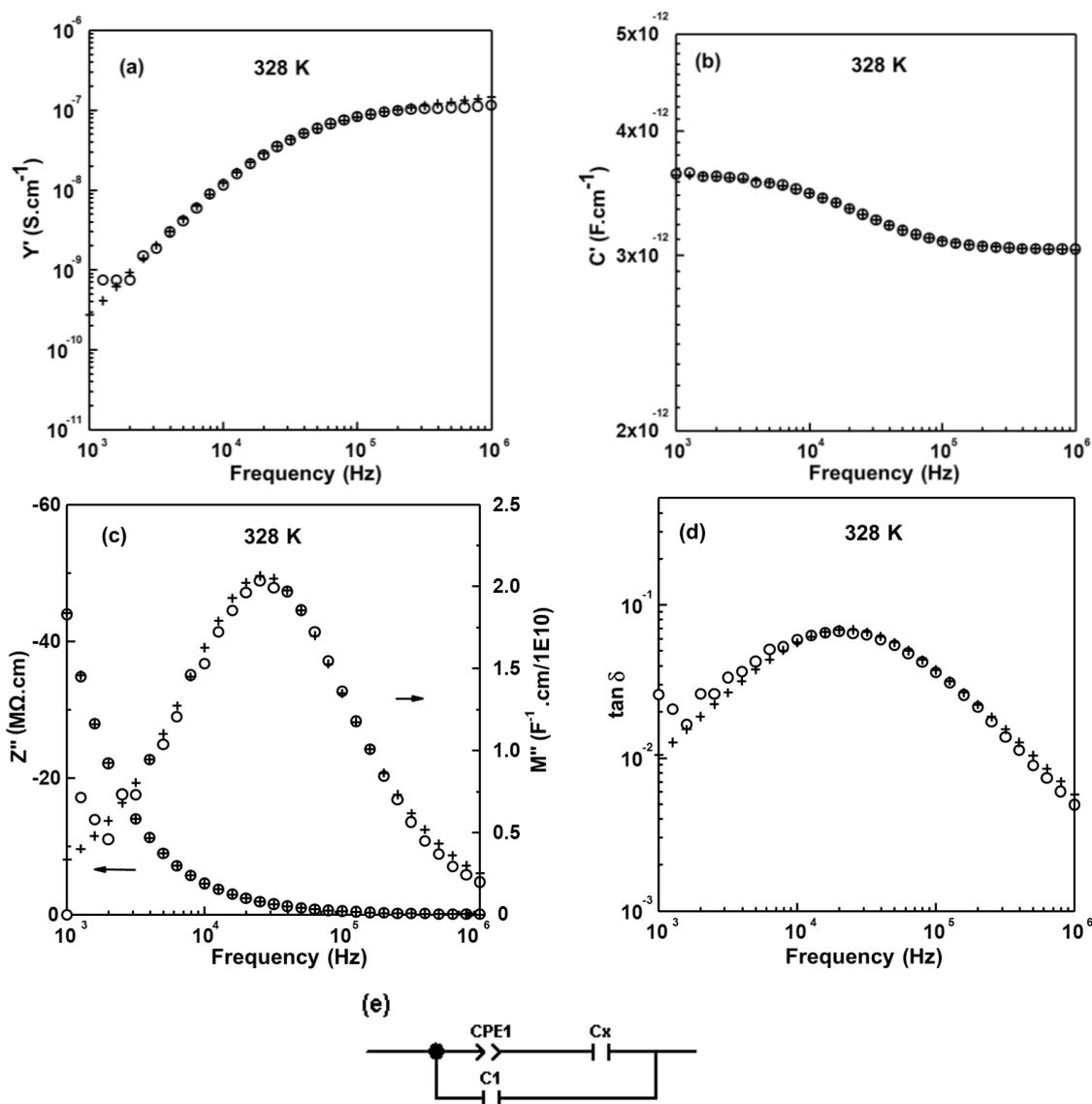
Figure 6.8 Low temperature IS experimental data points (○) and the fitting results (+) to equivalent circuit shown in (e) with (a) Y'; (b) C', (c) –Z"/M", and (d) tan δ spectroscopic plots at 328 K for $Bi_{12}(Bi_{0.03}P_{0.89})O_{20.27}$.

The sample was too resistive to show any semicircular arc in Z* plots below 373 K. Y' spectroscopic plots, Figure 6.8 (a), also did not show a low frequency-independent plateau consistent with any *dc* conductivity of the sample; instead a curved, frequency-dependent non-power law dispersive *ac* conduction was observed. A C' spectroscopic plot, Figure 6.8 (b), showed two typical C' plateaux with one at higher frequency and one at lower frequency.

● High Temperature IS Data (T > 400 K)

A high temperature IS data set of $Bi_{12}(Bi_{0.03}P_{0.89})O_{20.27}$ at 723 K is used as an example to show the universal HT relaxation behaviour in all P^{5+} containing sillenites, Figure 6.9 (a)-(d). Z* plots showed two semicircular arcs; both of which are related to the bulk response of the sample, Figure 6.9 (a). (Evidence refers to Section 3.2.3: equivalent circuit analysis for $Bi_{12}SiO_{20}$). The real admittance (Y') spectroscopic plot, Figure 6.9 (b), showed a frequency-independent low frequency plateau attributed to the *dc* conductivity and a frequency-dependent power law behaviour at higher frequency. Two C' plateaux with one at high frequency and one at low frequency were observed, Figure 6.9 (c). The high-frequency plateau ($f > 10^5$ Hz) is frequency-independent with an associated capacitance of ~ 4.07 pF.cm^{-1}(ε_r ~ 46); whereas the low frequency plateau ($f < 10^3$ Hz) is frequency- and temperature-dependent with fluctuated capacitance values ranging from 0.1 nF.cm^{-1} at 548 K to 7 pF.cm^{-1} at 823 K, corresponding to the broad relaxation ε_r peaks in the *rf* fixed frequency measurements, Figure 6.6 (a). In the combined –Z"/M" spectroscopic plot, Figure 6.9 (d), the high frequency peak is attributed to the bulk conductivity of the sample and the low frequency peak in –Z" spectra is attributed to the bulk relaxation response of the sample.

The same equivalent circuit consisting of a parallel connection of R, C and Cole-Cole branch (CPE in series with a C), Figure 6.9 (e), was successfully modelled the high temperature IS data from 573 to 673 K over the frequency range of 10^2-10^6 Hz. The fitted results of the circuit parameters R_1, C_1, C_x and CPE (A and *n*) for $Bi_{0.03}P_{0.89}$ are listed in Table 6.8.

Table 6.8 Fitted high temperature IS values of $Bi_{12}(Bi_{0.03}P_{0.89})O_{20.27}$ from 573 to 673 K. Errors associated with the fitted circuit parameters R_1, C_1, C_x, A and *n* are < ±0.2 %, < ±0.7 %,< ±6.2 %,< ±7.8 % and < ±1.6 %, respectively.

Temperature (K)	R_1 (Ω cm)	C_1 (pF cm^{-1})	C_x (F cm^{-1})	A (Ω^{-1} cm^{-1} rad^{-1})	*n*
573	225180	3.77	1.06×10^{-10}	3.24×10^{-8}	0.31
598	101090	3.77	7.93×10^{-11}	4.42×10^{-8}	0.32
623	50142	3.79	4.51×10^{-11}	5.17×10^{-8}	0.33
648	34097	3.82	2.89×10^{-11}	5.10×10^{-8}	0.34
673	19774	3.79	2.23×10^{-11}	5.40×10^{-8}	0.36
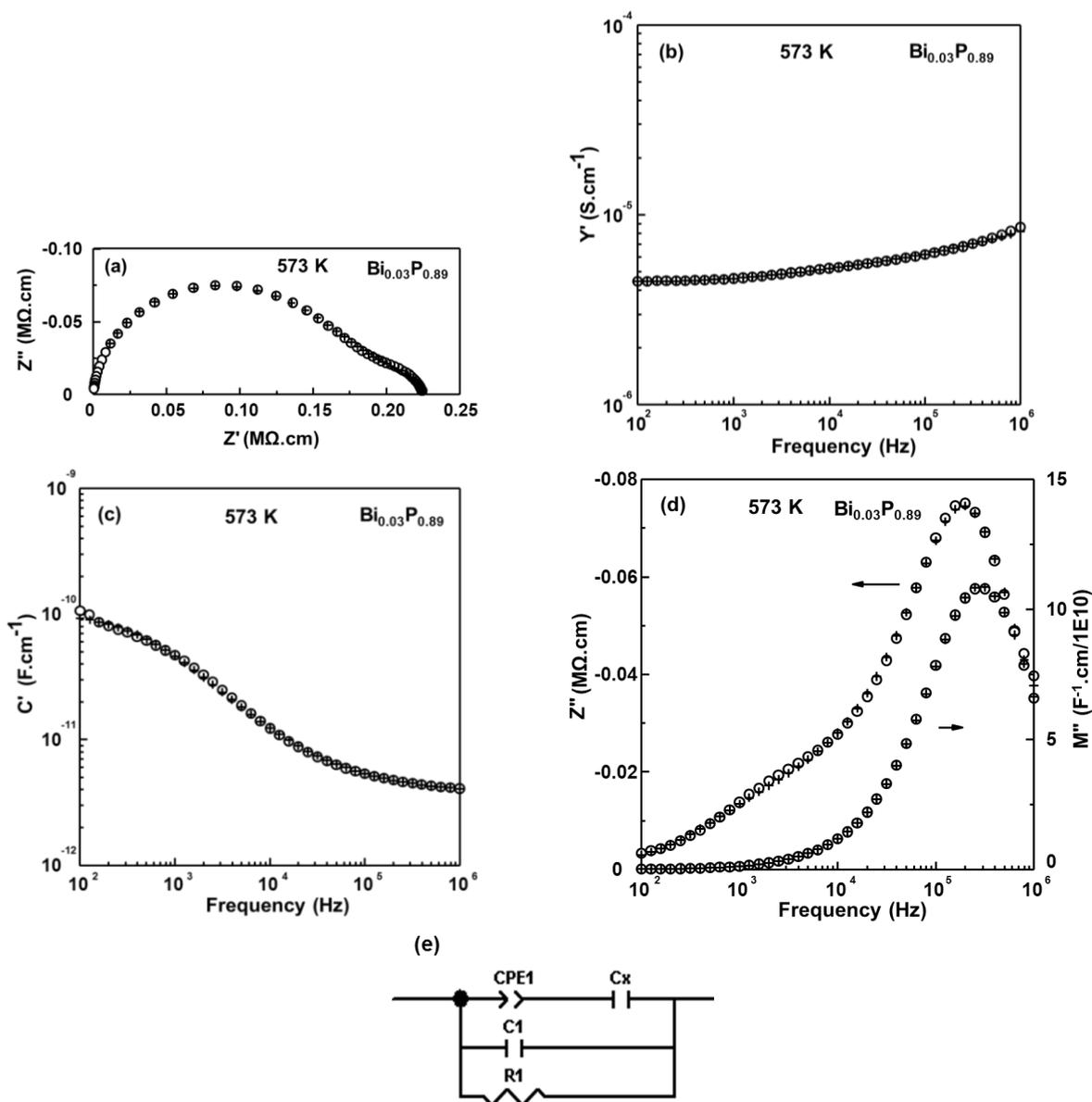
Figure 6.9 High temperature IS experimental data points (○) and the fitting results (+) to equivalent circuit shown in (e) with (a) Z* plot; (b) Y', (c) C', and (d) −Z"/M" spectroscopic plots at 573 K for $Bi_{12}(Bi_{0.03}P_{0.89})O_{20.27}$.

Direct evidence for the existence of LT and HT relaxation behaviour can be observed from C' spectroscopic plots with fluctuating C' plateaux at various temperatures, e.g. $Bi_{0.03}P_{0.89}$ in Figure 6.10 (a) and (b). LT relaxation behaviour existed between ~ 290 and 450 K; whereas HT relaxation behaviour existed between ~ 450 and 673 K. The coexistence of both low/high temperature relaxation behaviours for $Bi_{0.03}P_{0.86}$ occurred between 423 and 473 K, which can be observed more prominently in M" and tan δ spectroscopic plots, Figure 6.11 (a) and (b). The magnitudes of LT relaxation peaks is one fifth of those of HT

relaxation peaks in M" and tan δ spectroscopic plots.
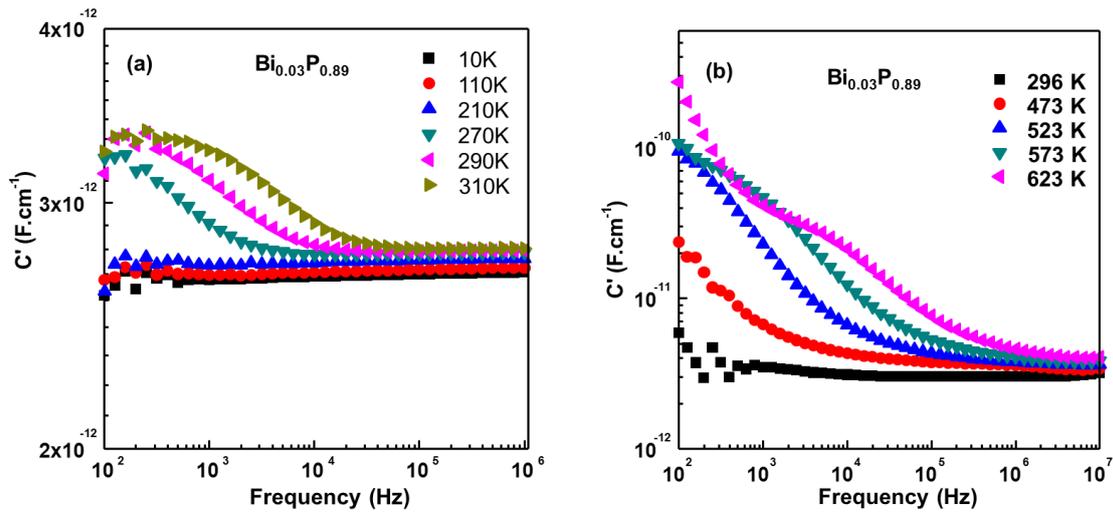
Figure 6.10 C' spectroscopic plot at various temperatures for $Bi_{12}(Bi_{0.03}P_{0.89})O_{20.27}$ to show (a) low and (b) high temperature relaxation behaviour.
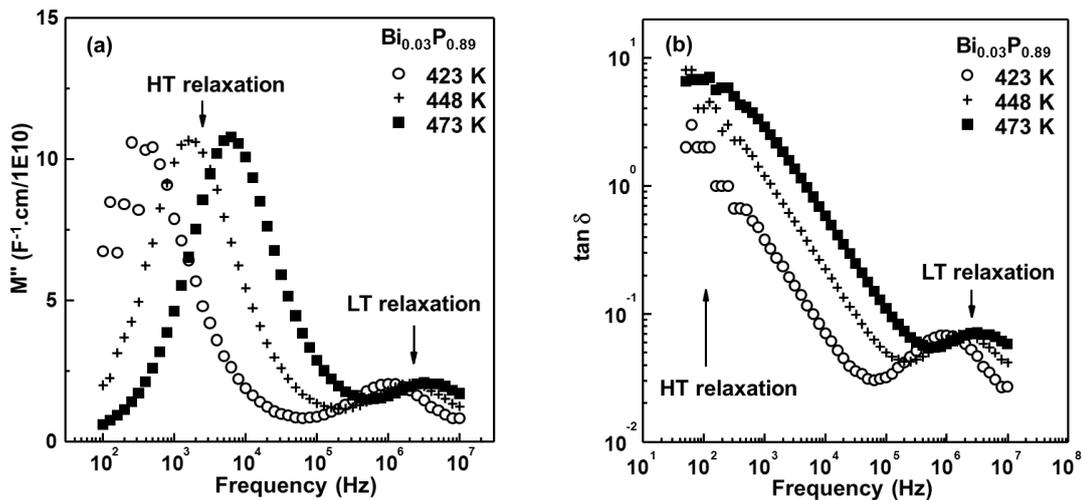
Figure 6.11 (a) M" and (b) tan δ spectroscopic plots for $Bi_{12}(Bi_{0.03}P_{0.89})O_{20.27}$ to show the coexistence of low/high temperature (LT/HT) relaxation phenomenon.

- ### Ionic Conductivity of Superstoichiometric Sillenites (T > 773 K)

In P^{5+} containing sillenites, superstoichiometric compounds $Bi_{12}(Bi^{3+}_{0.03}P^{5+}_{0.89}\square_{0.08})O_{20.27}$ and $Bi_{12}(P^{5+}_{0.86}\square_{0.14})O_{20.15}$ exhibit ionic conductivity at T > 773 K. A low frequency spike inclined at ~ 50 ° to the x-axis was shown in Z* plot with the associated capacitance of ~ 10^{-7} F.cm^{-1}, indicating ionic polarisation associated with a blocking electrode[16], Figure 6.12. The bulk conductivity is found to be sensitive to the contents of oxygen sublattice for

superstoichiometric sillenites as $Bi_{12}(Bi^{3+}_{0.03}P^{5+}_{0.89}\square_{0.08})O_{20.27}$ was more conducting than $Bi_{12}(P^{5+}_{0.86}\square_{0.14})O_{20.15}$.
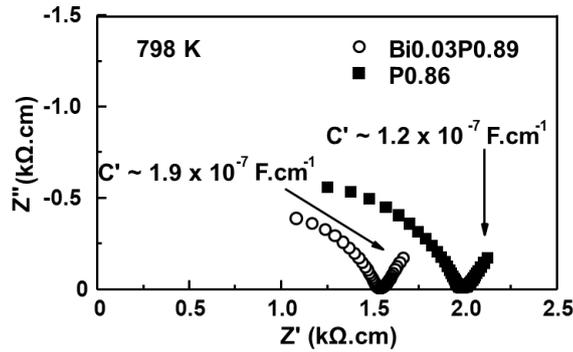
Figure 6.12 Z* plot of superstoichiometric sillenites $Bi_{0.03}P_{0.89}$ (empty circles) and $P_{0.86}$ (filled squares) at 798 K showing ionic conductivity.
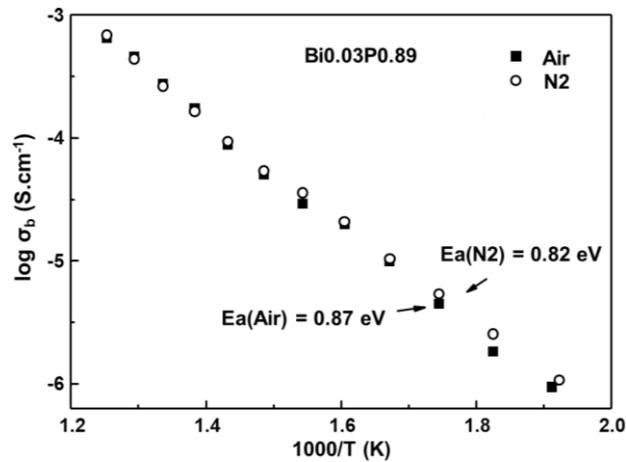
Figure 6.13 Conductivity of $Bi_{0.03}P_{0.89}$ measured in air (filled square) and nitrogen (empty circle).

To further investigate the conduction species, IS conductivity measurements carried out in oxygen free nitrogen atmosphere were compared with that in air, Figure 6.13. The conductivity was slightly higher (i.e. lower activation energy) for $Bi_{0.03}P_{0.89}$ in nitrogen atmosphere, indicating there is a small electronic contribution to the conduction. However, the conducting species should predominantly be oxide ions, where excess oxygen ions can hop through the void of the framework at high temperatures.[4, 17]

6.2.7.3 Arrhenius plot of bulk conductivity

Bulk conductivity data for all prepared P^{5+} containing sillenites were calculated from the M" Debye peak and plotted in Arrhenius format, as shown in Figure 6.14. The bulk conductivity for P^{5+} containing sillenites is dependent on the oxygen content. The activation energy for superstoichiometric sillenites $Bi_{12}(Bi^{3+}_{0.03}P^{5+}_{0.89}\square_{0.08})O_{20.27}$ and $Bi_{12}(P^{5+}_{0.86}\square_{0.14})O_{20.15}$ were similar with values of ~ 0.82 and ~ 0.86 eV, respectively. $Bi_{12}(Fe_{0.5}P_{0.5})O_{20}$ was the most conductive compound with the lowest activation energy value of 0.64 eV, indicating a possible formation of sub-stoichiometric compound by mixed valence state of Fe^{2+}/Fe^{3+} atoms. The most resistive compound was 'stoichiometric' sillenite $Bi_{12}(Mg_{0.33}P_{0.67})O_{20}$ with an activation energy value of 1.04 eV.
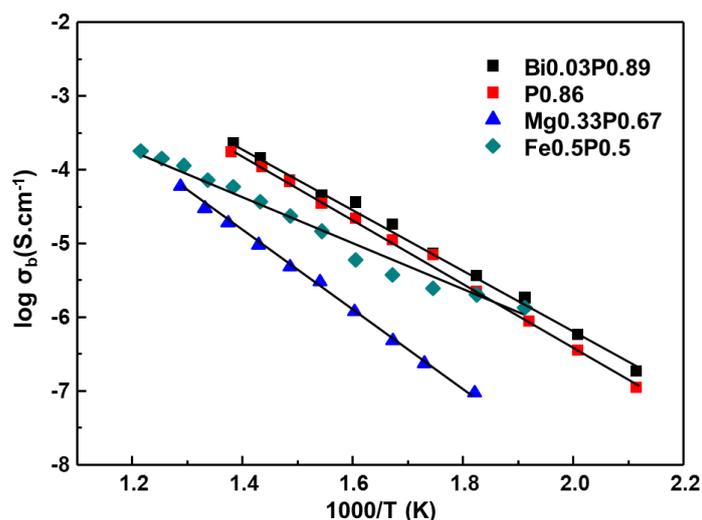
Figure 6.14 Arrhenius plot of bulk conductivity versus reciprocal temperature for P^{5+} containing sillenites.

6.3 Discussion

All single-phase phosphorus containing sillenites with their lattice parameters are listed in Table 6.9. Single-phase $Bi_{12}(Bi_{0.03}P_{0.89})O_{20.27}$ obeyed the same structural formula for V^{5+} sillenite proposed by Radaev and Simonov.[2] $Bi_{12}(P_{0.86})O_{20.15}$ was synthesised within the solid solution limits established by Lee and Sinclair.[4] The latter two compounds $Bi_{12}(Fe^{3+}_{0.5}P^{5+}_{0.5})O_{20}$ and $Bi_{12}(Mg^{2+}_{0.33}P^{5+}_{0.67})O_{20}$ have been reported previously by Radaev

et al. [18] and Avdeev *et al.* [19], respectively. Both of them obeyed the VS general formula and formed 'stoichiometric' sillenites with the average M-site cations equals to 4+. However, the exact stoichiometry for $Fe_{0.5}P_{0.5}$ is still worthy to investigate, as its unusual small activation energy suggested that mixed oxidation states of Fe^{2+}/Fe^{3+} may be exist in the sample to form a sub-stoichiometric sillenite.

Table 6.9 Summary of single-phase P^{5+} containing sillenites.

Single-phase Composition	Reaction Temperature / °C	Lattice Parameter, a / Å	Unit Cell Volume / Å^3
$Bi_{12}(Bi_{0.03}P_{0.89}\square_{0.08})O_{20.27}$	730	10.16580(9)	1050.571(17)
$Bi_{12}(P_{0.86}\square_{0.14})O_{20.15}$	780	10.1691(4)	1051.59(7)
$Bi_{12}(Fe^{3+}_{0.5}P^{5+}_{0.5})O_{20}$	790	10.10689(10)	1032.410(18)
$Bi_{12}(Mg^{2+}_{0.33}P^{5+}_{0.67})O_{20}$	780	10.15055(17)	1045.85(3)

The relationship between the size of the M-site ion(s) and the lattice parameters of P^{5+} containing sillenites is shown Figure 6.15. Data for the parent γ-Bi_2O_3 [20] and other studied sillenites from Chapters 3-5 are included in the figure for comparison. It seems that the four P^{5+} containing sillenites have large variations of lattice parameters and are scattered in the plot with no particular trend.
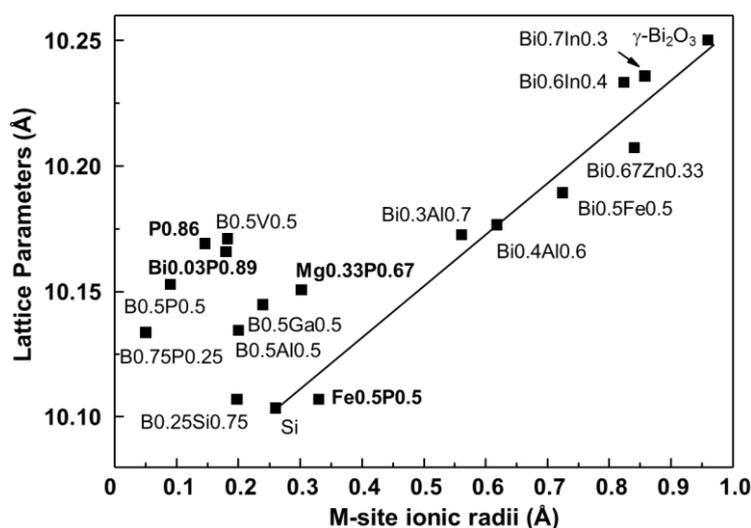
Figure 6.15 The relationship between the unit cell parameters and the M-site ionic radii of P^{5+} containing sillenites (shown as bold letters);data for $Bi_{12}SiO_{20}$ (Chapter 3), M^{2+}/M^{3+} sillenites (Chapter 4), B^{3+} containing sillenites (Chapter 5) and γ-Bi_2O_3 form literature[20] are included for comparison. Note: ionic radius for Bi^{3+} ($Bi^{3+}_{(V)}$ = 0.96 Å) was from Shannon[21].

The relaxation behaviour of P^{5+} containing sillenites was firstly investigated by using the dielectric properties as a function of temperature and frequency. Surprisingly two sillenites: $P_{0.86}$ and $Bi_{0.03}P_{0.89}$ exhibit similar low temperature relaxation as boron containing sillenites. This indicates that low temperature relaxation phenomenon is not unique in boron containing sillenites, but it can also exist in other sillenites, such as P^{5+} containing sillenites. However, not all P^{5+} containing sillenites exhibit the low temperature relaxation behaviour, e.g. $Mg_{0.33}P_{0.67}$ and $Fe_{0.5}P_{0.5}$. Unlike the universal high temperature relaxation behaviour which is present in all sillenites, the origin of the low temperature relaxation for P^{5+} containing sillenites is believed to be caused by redistribution of the small, disordered atoms on the tetrahedral site, which can be observed from the broadening of the NMR ^{31}P isotope peaks for $Bi_{0.03}P_{0.89}$. The associated activation energy for the LT relaxation of P^{5+} and B^{3+} containing sillenites are ~0.3 and ~ 0.5 eV, respectively, indicating there are probably two different mechanisms: the LT relaxation behaviour for B^{3+} containing sillenites was due to the rotational of BO_3/BO_4 units over the tetrahedral site, which was confirmed by low temperature Raman Spectroscopy; however, the LT relaxation behaviour for P^{5+} containing sillenites might be due to a disordered distribution of $P/Bi/\square$ over the tetrahedral sites according to NMR Spectroscopy. Nevertheless, additional Rietveld refinements on low temperature neutron powder diffraction data, especially by using differential Fourier maps, should be useful to investigate whether the origin of the LT relaxation for P^{5+} containing sillenites arises from disorder on the tetrahedral site.

6.4 Conclusions

Four synthesised single-phase phosphorus containing sillenites showed that $Bi_{12}(Fe^{3+}_{0.5}P^{5+}_{0.5})O_{20}$ and $Bi_{12}(Mg^{2+}_{0.33}P^{5+}_{0.67})O_{20}$ obeyed the VS formula; whereas $Bi_{12}(Bi^{3+}_{0.03}P^{5+}_{0.89}\square_{0.08})O_{20.27}$ and $Bi_{12}(P^{5+}_{0.86}\square_{0.14})O_{20.15}$ disobeyed the VS formula by forming superstoichiometric sillenites with excess oxygen sublattices (i.e. > 20) by oxygen atoms and/or unshared $6s^2$ Bi^{3+} lone electron pairs. Unlike $M^{2+}/M^{3+}/M^{4+}$ sillenites in Chapter 3 and 4, no linear relationship can be established between the size of the M-site

ion(s) and the lattice parameters for P^{5+} containing sillenites, Figure 6.15.

Sillenites can be considered as two parts: a 'soft' Bi-O skeleton and 'hard' MO$_4$ tetrahedra. The influence of the size of M-ions (r) on the lattice parameters is only valid when $r > 0.31$ Å. When $r < 0.31$ Å, the highly 'flexible' Bi-O framework starts to determine the lattice parameters of the sillenites.

A low temperature relaxation phenomenon was unexpectedly found in two phosphorus containing sillenites: Bi$_{0.03}$P$_{0.89}$ and P$_{0.86}$, which shows LT relaxation effects can exist in other doped sillenites apart from the boron containing sillenites in Chapter 5. Evidence of the LT relaxation phenomenon was scrutinized by Raman Spectroscopy via the variation of the magnitude of Raman peak ~ 825 cm^{-1} (line 18) assigned as asymmetric stretching of MO$_4$ tetrahedra was observed from 100 to 400 K. An associated downshifting of the Raman peak ~ 530 cm^{-1} (line 15) assigned as the vibrations of the framework units from 537 cm^{-1} at 100 K to 531 cm^{-1} at 400 K was also observed. NMR spectra showed a broadening of the isotope ^{31}P peak for Bi$_{0.03}$P$_{0.89}$, which indicates a disordered distribution of P/Bi/□ over the tetrahedral sites, which may be the origin of the LT relaxation phenomenon. The difference in magnitude of the associated activation energies for LT/HT relaxations indicate that (at least) two different mechanisms occur. In boron containing sillenites, the LT relaxation behaviour was due to the rotation of BO$_3$/BO$_4$ units over the tetrahedral site, which was confirmed by Raman spectroscopy. It is noteworthy that the origin of the LT relaxation in B^{3+} and P^{5+} containing sillenites should be different as NMR peak broadening was only observed for Bi$_{0.03}$P$_{0.89}$ rather than B$_{0.5}$P$_{0.5}$ and also their activation energies are different with B^{3+} and P^{5+} groups, i.e. ~ 0.3 and 0.5 eV, respectively. Nevertheless, the LT relaxation in B^{3+} and P^{5+} containing sillenites seems to arise from the local Bi^{3+} polarization effect of the BiO$_5$LP framework polyhedra, which is induced by the tetrahedra unit either with a switchover of BO$_3$/BO$_4$ units or with a random distribution of P/Bi/□ over the same M-site. It would be interesting to understand the LT relaxation behaviour in P^{5+}/□ containing sillenites from a structural point of view. Additional Rietveld refinement work on variable temperature neutron powder diffraction data, especially by using difference Fourier maps might be useful.

6.5 References

[1]   M. Valant and D. Suvorov, A stoichiometric model for sillenites, Chemistry of Materials, 2002. **14**: p. 3471-3476.

[2]   S. F. Radaev and V. I. Simonov, Structure of sillenites and atomic mechanisms of isomorphous substitutions, Kristallografiya, 1992. **37**: p. 914-941.

[3]   H. S. Horowitz, A. J. Jacobson, J. M. Newsam, J. T. Lewandowski and M. E. Leonowicz, Solution synthesis and characterization of sillenite phases, $Bi_{24}M_2O_{40}$ (M = Si, Ge, V, As, P), Solid State Ionics, 1989. **32-3**: p. 678-690.

[4]   S. L. Lee, C. K. Lee and D. C. Sinclair, Synthesis and characterisation of bismuth phosphate-based sillenites, Solid State Ionics, 2005. **176**: p. 393-400.

[5]   A. N. Yudin, E. A. Pobedimskaya, L. E. Terenteva, I. V. Petrova, L. N. Kaplunnik and G. V. Malakhova, Crystal-chemical characteristics of gallium and vanadium sillenites, Inorganic Materials, 1989. **25**: p. 1451-1454.

[6]   J. L. Soubeyroux, M. Devalette, N. Khachani and P. Hagenmuller, Neutron-diffraction study on a phase with sillenite structure, Journal of Solid State Chemistry, 1990. **86**: p. 59-63.

[7]   M. Devalette, G. Meunier, J. P. Manaud and P. Hagenmuller, New cationic deficient phases $Bi_{12}(B_{4/5-x}{}^{5+}Bi_x{}^{5+}P_{1/5})O_{20}$ with sillenite structure, Comptes Rendus De L Academie Des Sciences Serie Ii, 1983. **296**: p. 189-191.

[8]   A. Watanabe, H. Kodama and S. Takenouchi, Nonstoichiometric phase with sillenite-type structure in the system Bi_2O_3-P_2O_5, Journal of Solid State Chemistry, 1990. **85**: p. 76-82.

[9]   A. Watanabe, S. Takenouchi, P. Conflant, J. P. Wignacourt, M. Drache and J. C. Boivin, Preparation of a nonstoichiometric sillenite-type phase in the system Bi_2O_3-As_2O_5, Journal of Solid State Chemistry, 1993. **103**: p. 57-62.

[10]   S. F. Radaev, L. A. Muradyan and V. I. Simonov, Atomic structure and crystal chemistry of sillenites $Bi_{12}(Bi^{3+}{}_{0.50}Fe^{3+}{}_{0.50})O_{19.50}$ and $Bi_{12}(Bi^{3+}{}_{0.67}Zn^{2+}{}_{0.33})O_{19.33}$, Acta Crystallographica Section B-Structural Science, 1991. **47**: p. 1-6.

[11]   N. Khachani, M. Devalette and P. Hagenmuller, On the stoichiometry of the allotropic variation γ-Bi_2O_3, Zeitschrift Fur Anorganische Und Allgemeine Chemie, 1986. **533**: p. 93-98.

[12]   F. D. Hardcastle, I. E. Wachs, H. Eckert and D. A. Jefferson, Vanadium(V)

environments in bismuth vanadates - a structural investigation using Raman spectroscopy and solid state V^{51} NMR, Journal of Solid State Chemistry, 1991. **90**: p. 194-210.

[13] M. Valant and D. Suvorov, Synthesis and characterization of a new sillenite compound $Bi_{12}(B_{0.5}P_{0.5})O_{20}$, Journal of the American Ceramic Society, 2002. **85**: p. 355-358.

[14] A. V. Egorysheva, V. I. Burkov, Y. F. Kargin, V. G. Plotnichenko, V. V. Koltashev, E. D. Obraztsova and S. V. Terekhov, Atomic structure features of sillenite crystals as probed by Raman spectroscopy, Russian Journal of Inorganic Chemistry, 2005. **50**: p. 238-245.

[15] B. Mihailova, M. Gospodinov and L. Konstantinov, Raman spectroscopy study of sillenites. I. Comparison between $Bi_{12}(Si,Mn)O_{20}$ single crystals, Journal of Physics and Chemistry of Solids, 1999. **60**: p. 1821-1827.

[16] J. T. S. Irvine, D. C. Sinclair and A. R. West, Electroceramics: Characterization by impedance spectroscopy, Advanced Materials, 1990. **2**: p. 132-138.

[17] J. P. Wignacourt, M. Drache, P. Conflant and J. C. Boivin, New phases in the Bi_2O_3-$BiPO_4$ system. 2. Structure and electrical properties of a sillenite solution, Journal De Chimie Physique Et De Physico-Chimie Biologique, 1991. **88**: p. 1939-1949.

[18] S. F. Radaev, L. A. Muradian, I. F. Kargin, V. A. Sarin, E. E. Rider and V. I. Simonov, Single crystal atomic structure of the $Bi_{12}(Fe,P)O_{20}$ solid solution, Doklady Akademii Nauk Sssr, 1989. **307**: p. 1381-1384.

[19] G. V. Avdeev, T. I. Milenov, A. V. Egorysheva, K. P. Petrov, V. M. Skorikov, R. K. Titorenkova and P. M. Rafailov, Crystal structure of $Bi_{36}MgP_2O_{60-d}$, Russian Journal of Inorganic Chemistry, 2011. **56**: p. 913-918.

[20] H. A. Harwig and A. G. Gerards, Polymorphism of bismuth sesquioxide, Thermochimica Acta, 1979. **28**: p. 121-131.

[21] R. D. Shannon, Revised effective ionic radii and systematic studies of interatomic distances in halides and chalcogenides, Acta Crystallographica Section A, 1976. **32**: p. 751-767.

7   Discussion

In this chapter, sillenites from the previous chapters are reviewed together to establish an overview of their structure-composition-property relationships. The microwave dielectric properties of all the studied sillenites are discussed to establish possible compositions for LTCC technology.

7.1 Formation of Sillenite Phases

The Valant and Suvorov (VS) general formula: $Bi_{12}(Bi^{3+}_{4/5-nx}M^{n+}_{5x})O_{19.2+nx}$[1] was established for the isomorphous substitution of sillenites based on a stoichiometric model: the incorporation of a cation must be associated with a corresponding decrease in the Bi concentration on the M-site, which depends on the charge of the substituent. However, not all of the prepared sillenites in this study obeyed the VS general formula. It is found that the formation of sillenites should consider both the charge and size effects of the dopant.

In general, sillenite phases can be considered to have a composite structure consisting of two parts: 'rigid' MO_4 tetrahedral units and a 'flexible' Bi-O framework. For $r > 0.31$ Å (the ideal ionic radius of an interstitial ion for a regular MO_4 tetrahedron is 0.31 Å[2, 3]), the size of the M-site ion has a significant influence on the lattice parameter of sillenites; for $r < 0.31$ Å, the highly 'flexible' Bi-O framework determines the unit cell parameter of sillenites, Figure 7.1. Similar justifications were reported by Valant and Suvorov[3]: the O3-O3 distance in the MO_4 tetrahedra increases with $r > 0.31$ Å whereas it retains a value of 2.68 Å for $r < 0.31$ Å.

Poleti *et al.*[4] established a relationship between the M-cation ionic radius and the unit cell parameter of sillenites. They summarized data into two groups each with a linear trend and the same slope, where the lower group contained all the M^{n+}-ions with $n = 2$-4 and the upper group with $n = 5$. However, the accuracy of the plot was questioned in this thesis (for details refer to Section 5.1).

According to our work and preliminary results from Hutton[5], a linear region between

the overall M-cation ionic radius and the unit cell parameter of sillenites was found, Figure 7.1 (as indicated between dashed lines) and Table 7.1. This linear region includes all M^{n+} sillenites with n = 2-5 and with overall M-site ionic radius from 0.01 to 0.98 Å. Within this general linear region, various linear trends with different slopes exist, which indicate different doping mechanisms depending on whether or not they are incorporated with a structural change in the Bi-O framework. Examples of these small groups each with a linear trend but different slopes are: B/P0.5-B/P0.25 solid solutions (s.s); B/Si-Si (s.s); B/Si-B/Al-B/Ga-B/V (s.s); Bi/P-Bi/V (s.s); Na/V (s.s) etc. The linear trends in this region are as many as possible solid solution ranges; however, each trend can only be decided individually by experiments. Therefore, the trends mentioned by Poleti *et al.* [4] were only partially correct as they cannot explain all the experimental observations.
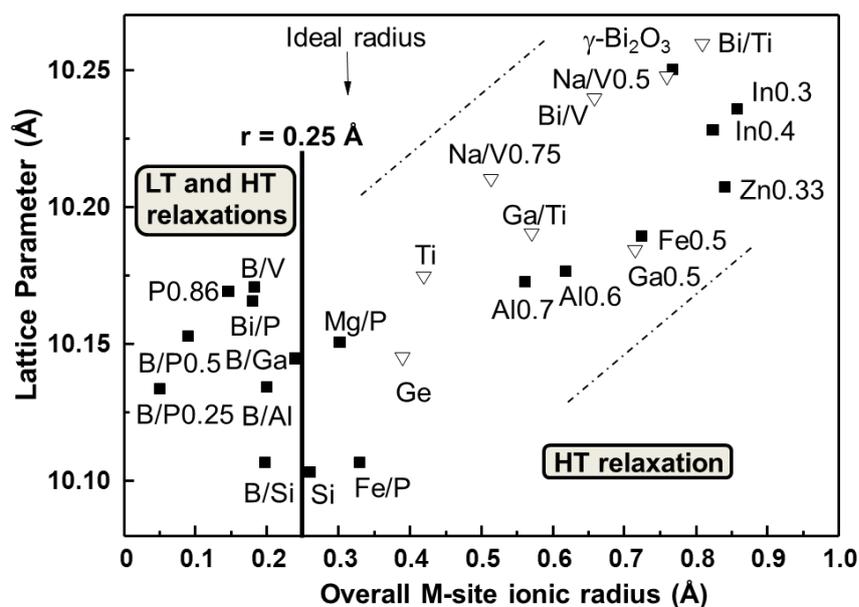
Figure 7.1 The relationship between lattice parameter and the overall M-site ionic radius of single-phase sillenites from this work (shown as filled squares). Data for γ-Bi$_2$O$_3$ [6] and from preliminary work by Hutton[5] (shown as open triangles) are also included for comparison. Dashed lines indicate a linear region between the overall M-cation ionic radius and the unit cell parameter of sillenites.

Table 7.1 Reaction conditions, overall M-site ionic radius and lattice parameter values for sillenites shown in Figure 7.1. Note: M-site ionic radii were based on Shannon[7]: $B^{3+}_{(III)}$ = 0.01 Å; $Bi^{3+}_{(V)}$ = 0.96 Å; $V^{4+}_{(V)}$ = 0.53 Å.

Abbreviation in Figure 7.1	Composition	Reaction Temperature/ °C	M-site Ionic Radii /Å	Lattice Parameter, a/Å
Si	$Bi_{12}SiO_{20}$	840	0.26	10.10345(7)
Zn0.33	$Bi_{12} (Bi_{0.67}Zn_{0.33}) O_{19.33}$	735	0.8412	10.2072(3)
Fe0.5	$Bi_{12} (Bi_{0.5}Fe_{0.5}) O_{19.5}$	745	0.725	10.18927(15)
Al0.7	$Bi_{12} (Bi_{0.3}Al_{0.7}) O_{19.5}$	730	0.561	10.17255(13)
Al0.6	$Bi_{12} (Bi_{0.4}Al_{0.6}) O_{19.5}$	730	0.618	10.1765(3)
In0.4	$Bi_{12}(Bi_{0.6}In_{0.4})O_{19.5}$	750	0.824	10.2293(2)
In0.3	$Bi_{12}(Bi_{0.7}In_{0.3})O_{19.5}$	750	0.858	10.23583(18)
B/P0.5	$Bi_{12} (B_{0.5}P_{0.5}) O_{20}$	730	0.09	10.1527(6)
B/P0.25	$Bi_{12} (B_{0.75}P_{0.25}) O_{19.75}$	730	0.05	10.13364(12)
B/Si	$Bi_{12} (B_{0.25}Si_{0.75}) O_{19.875}$	730	0.1975	10.10689(10)
B/Al	$Bi_{12}(B_{0.5}Al_{0.5})O_{19.5}$	680	0.2	10.1344(3)
B/Ga	$Bi_{12}(B_{0.5}Ga_{0.5})O_{19.5}$	700	0.24	10.1447(4)
B/V	$Bi_{12} (B_{0.5}V_{0.5}) O_{20}$	740	0.1825	10.1709(4)
Bi/P	$Bi_{12}(Bi_{0.03}P_{0.89}\square_{0.08})O_{20.27}$	730	0.1801	10.16580(9)
P0.86	$Bi_{12}(P_{0.86}\square_{0.14})O_{20.15}$	780	0.1462	10.1691(4)
Fe/P	$Bi_{12}(Fe^{3+}_{0.5}P^{5+}_{0.5})O_{20}$	790	0.33	10.10689(10)
Mg/P	$Bi_{12}(Mg^{2+}_{0.33}P^{5+}_{0.67})O_{20}$	780	0.302	10.15055(17)
γ-Bi_2O_3	$Bi_{12}(Bi_{0.8}\square_{0.2})O_{19.2}$	400/Air Quenched	0.768	10.2501(5)[8]
Ge	$Bi_{12}GeO_{20}$	835/Air Quenched	0.39	10.14516(10) [5]
Ti	$Bi_{12}TiO_{20}$	820/Air Quenched	0.42(Ti^{4+})	10.17482(18) [5]
Ga/Ti	$Bi_{12}(Ga^{3+}_{0.5}Ti^{4+}_{0.5})_{19.75}$	805/Air Quenched	0.445(Ti^{4+})	10.19051(20) [5]
Na/V0.75	$Bi_{12}(Na^{+}_{0.25}V^{5+}_{0.75})O_{20}$	830/Air Quenched	0.51375(V^{5+})	10.21025(13) [5]
Na/V0.5	$Bi_{12}(Na^{+}_{0.5}V^{4+}_{0.5})O_{19.5}$	750/Air Quenched	0.76(V^{4+})	10.2475(4) [5]
Bi/V	$Bi_{12}(Bi^{3+}_{0.5}V^{5+}_{0.5})O_{20}$	820/Air Quenched	0.6575(V^{5+})	10.23976(18) [5]
Ga0.5	$Bi_{12}(Bi^{3+}_{0.5}Ga^{3+}_{0.5})O_{19.5}$	800	0.715	10.18448(25) [5]
Bi/Ti	$Bi_{12}(Bi^{3+}_{0.48}Ti^{4+}_{0.52})O_{19.76}$	835/Air Quenched	0.6792(Ti^{4+})	10.25949(22) [5]

7.2 Low Temperature (LT) and High Temperature (HT) Relaxation Phenomena

Valant and Suvorov[9] were the first to report a sillenite, $Bi_{12}(B^{3+}_{1/2}P^{5+}_{1/2})O_{20}$, to exhibit a broad, frequency dispersive, "relaxor-like" ε_r anomaly at low temperature (~ -80-100 °C). They attributed the electrical behaviour to a random distribution of the small B^{3+} and P^{5+} ions over the tetrahedral sites.

The dielectric properties of various sillenite analogues were thoroughly investigated in this thesis using *rf* fixed frequency and Impedance Spectroscopy (IS) measurements. Two main frequency-dispersive relaxation regions were observed with one present at high temperatures (HT), i.e. > 400 K and one present at low temperatures (LT), i.e. < 400 K. The frequency response of complex equivalent circuits on IS data confirmed these HT and LT relaxation phenomena to be bulk responses and clearly different from other electrical responses containing bulk, grain boundary, and electrode-sample interface issues associated with heterogeneous ceramics.[10, 11]

The appearance of the LT and HT relaxation phenomena for sillenites from this work can be concluded into an empirical correlation with the overall M-site ionic radii (*r*): LT relaxation behaviour is only present for *r* < 0.25 Å; whereas HT relaxation behaviour is universal and exists in all sillenites, Figure 7.1.

Table 7.2 Onset temperature of tan δ peak maximum (at 10 kHz) and activation energy (Ea) (obtained from log f_{max} versus 1000/T of the tan δ peak maxima) of LT and HT relaxation process(es) for the prepared sillenites.

Composition	LT Relaxation(s)		HT Relaxation(s)	
	Onset Temperature (K)	LT Activation Energy (eV)	Onset Temperature (K)	HT Activation Energy (eV)
$Bi_{12}SiO_{20}$	- / -	- / -	628	0.79
$Bi_{12}(Bi_{0.67}Zn_{0.33})O_{19.33}$	- / -	- / -	> 800	-
$Bi_{12}(Bi_{0.5}Fe_{0.5})O_{19.5}$	- / -	- / -	500 / > 800	0.60 / -
$Bi_{12}(Bi_{0.7}In_{0.3})O_{19.5}$	- / -	- / -	> 800	-
$Bi_{12}(Bi_{0.6}In_{0.4})O_{19.5}$	- / -	- / -	> 800	-
$Bi_{12}(B_{0.5}P_{0.5})O_{20}$	- / 216	- / 0.29	627	0.92
$Bi_{12}(B_{0.75}P_{0.25})O_{19.75}$	112 / 218	0.12 / 0.32	> 800	-
$Bi_{12}(B_{0.25}Si_{0.75})O_{19.875}$	84 / 206	0.08 / 0.26	633	1.10
$Bi_{12}(B_{0.5}Al_{0.5})O_{19.5}$	124 / 208	0.13 / 0.31	> 800	-
$Bi_{12}(B_{0.5}Ga_{0.5})O_{19.5}$	138 / 216	0.19 / 0.32	> 800	-
$Bi_{12}(B_{0.5}V_{0.5})O_{20}$	- / 222	- / 0.30	652	0.82
$Bi_{12}(Bi_{0.03}P_{0.89}\square_{0.08})O_{20.27}$	- / 320	- / 0.48	754	1.21
$Bi_{12}(P_{0.86}\square_{0.14})O_{20.15}$	- / 320	- / 0.51	775	0.98
$Bi_{12}(Fe_{0.5}P_{0.5})O_{20}$	**- / -**	**- / -**	598	0.83
$Bi_{12}(Mg_{0.33}P_{0.67})O_{20}$	**- / -**	**- / -**	670	1.24

Activation energy values of both LT and HT relaxation processes were obtained (log f_{max} versus 1000/T of the tan δ peak maxima) from *rf* fixed frequency measurements and

are summarized in Table 7.2. The difference in activation energy values indicates different mechanisms are responsible for the LT and HT relaxation effects. The temperature range over which this relaxor-type behaviour can be observed by *rf* measurements depends on the stoichiometry and size of the M-site cation(s) of the sillenites.

7.2.1 Origin of High Temperature (HT) Relaxation Phenomenon

HT relaxation is a universal phenomenon which exists in all the studied sillenites, even in the ideal sillenite $Bi_{12}SiO_{20}$. As a consequence, the sillenite framework must play a vital role in the HT relaxation behaviour.

Sillenite is well-known for its highly disordered framework structure caused by the irregular Bi-O octahedra, which have one vertex missing and is occupied by its stererochemically active $6s^2$ lone pair of electrons. The Bi-O framework unit is 'flexible' as Bi^{3+} ions can easily be accommodated into many irregular geometries with coordination numbers (CN) ranging from 3 to 8.[12, 13] The Bi-[LP] distance in the sillenite octahedral environment is the shortest leading to many random oriented electric dipole moments.

The Raman Spectroscopy (RS) data of all studied sillenites show significant temperature dependence associated with Bi-O1 vibrations (~ 538 cm^{-1}) whereas there is negligible change in Bi-O2/O3 vibrations (~ 85 cm^{-1}). The downshifting and broadening of the ~ 538 cm^{-1} peak with increasing temperature indicates increasing distortion of the framework and increasing interatomic distances between Bi and O1 atoms. The peak at ~ 85 cm^{-1} remains unchanged, indicating little change in the Bi-O3 and Bi-O2 bond lengths with increasing temperature. The bridging O3 atoms between M and Bi atoms constrain the movement of the Bi atoms; however, the connectivity of adjacent Bi atoms via O1 atoms (site 1b and 1c) and the presence of the $6s^2$ electron lone pair on the Bi atoms permits considerable structural flexibility associated with the BiO_5LP bipyramids. Hence, the universal HT relaxation behaviour observed in sillenites is associated with local polarization effects due to the flexibility of the framework structure and, in particular, with small but non-correlated movement of the Bi atoms in the framework to create local dipole

moments.

The IS data showing the same HT relaxation behaviour were successfully modelled by an equivalent circuit consisting of a parallel connection of an R, C and a Cole-Cole branch (CPE in series with a C). This branch indicates the relaxation process associated with short-range orientation of the dipoles from the BiO_5LP units in the framework. The resistive component of the CPE becomes smaller due to increased thermal energy and ease of movement of the Bi atoms with increasing temperature. In this case, the CPE seems to be linked inherently to the co-operative nature of the vibrations and distortions associated with the framework structure that ultimately influence the polarisation behaviour of sillenites.

7.2.2 Origin of Low Temperature (LT) Relaxation Phenomenon

LT relaxation behaviour was only found in boron containing and phosphorous/vacancy containing sillenites with overall M-site ionic radius $r < 0.25$ Å. This critical threshold value, $r = 0.25$ Å, is a general idea and it might vary with different sillenite systems. Other sillenite analogues should be used to testify this empirical threshold value.

Except for $B_{0.5}P_{0.5}$ and $B_{0.5}V_{0.5}$, the rest of the boron containing sillenites showed two LT relaxation processes, with one present at ~ 100 K and one at ~ 220 K, Table 7.2. The origin for this behaviour is still not well understood. However, the second LT relaxation behaviour was found in both boron containing and phosphorous/vacancy containing sillenites with onset temperatures of ~ 220 and 320 K, respectively.

In boron-containing sillenites, the coexistence of BO_3 and BO_4 units was confirmed by [11]B Nuclear Magnetic Resonance (NMR) measurements, where there are 91.8 % BO_3 and 8.2 % BO_4 units contained in $Bi_{12}(B_{0.5}P_{0.5})O_{20}$ at room temperature. Similar results from variable temperature RS results revealed that the existence of dominant BO_3 unit vibrations at higher temperatures with a switchover to BO_4 unit vibrations at lower temperatures. This switching from BO_4 to BO_3 units on the M-site with increasing temperature cause Bi^{3+} ions from adjacent $Bi(1)O_5LP$ octahedra to move toward the BO_3 groups to ensure

redistribution of charge balance. With increasing temperature, significant temperature dependence associated with Bi-O1 vibrations was observed as the downshifting and broadening of ~ 538 cm^{-1} peak and negligible change in Bi-O2/O3 vibrations as the unchanged peak position of ~ 85 cm^{-1} peak. Hence, the origin of the LT relaxation behaviour for boron containing sillenites is believed to arise from the BiO_5LP framework units induced by the rotational of BO_4/BO_3 units on the M-site.

In phosphorus-containing sillenites, *rf* fixed frequency and IS measurements revealed that only samples containing vacancies over the M-sites showed the LT relaxation behaviour, e.g. $Bi_{12}(P_{0.86}\square_{0.14})O_{20.15}$ and $Bi_{12}(Bi_{0.03}P_{0.89}\square_{0.08})O_{20.27}$; whereas samples with fully filled M-sites did not, e.g. $Bi_{12}(Fe_{0.5}P_{0.5})O_{20}$ and $Bi_{12}(Mg_{0.33}P_{0.67})O_{20}$. NMR results for $Bi_{12}(Bi_{0.03}P_{0.89}\square_{0.08})O_{20.27}$ revealed a broadening of the ^{31}P resonance indicating a disordered tetrahedral site. RS results for $Bi_{12}(Bi_{0.03}P_{0.89}\square_{0.08})O_{20.27}$ again revealed a variation of the vibration associated with the MO_4 tetrahedra from 100 to 400 K and a significant downshifting and broadening of the ~ 538 cm^{-1} peak assigned to temperature dependent Bi-O1 vibrations. Hence, the local Bi^{3+} polarization effect from the BiO_5LP polyhedra due to the random distribution of neighbouring tetrahedral units seems to be the origin of the LT relaxations for phosphorus/vacancy containing sillenites. Further neutron powder diffraction work by using difference Fourier maps may be helpful to probe the structural distortions over the BiO_5LP polyhedra, particularly the movement of Bi^{3+} ions towards the M-sites at elevated temperatures.

Nevertheless, the presence of the LT relaxation behaviour(s) in sillenites seems to be competing vibrations associated with BiO_5LP polyhedra connected via the MO_4 tetrahedral units. Small and disordered MO_4 tetrahedra in a relatively large framework cell are thermodynamically favoured, where the created local strain effects are vital for the LT relaxations.

7.3 Microwave Dielectric Properties

Due to their low sintering temperature ($\sim 850\ °C$), chemical compatibility with silver, low dielectric losses and temperature-stable permittivity, sillenites have been reported as suitable candidates for applications in low-temperature co-fired ceramic (LTCC) technology, e.g. $Bi_{12}MO_{20-\delta}$ (M = Si, Ge, Ti, Pb, Mn, $B_{0.5}P_{0.5}$) [3, 14]. The microwave dielectric properties for single-phase sillenites from this work are an attempt to expand on the microwave dielectric properties from the literature and to establish possible structure-composition-MW property relationships of all sillenites, Table 7.3.

Table 7.3 MW dielectric properties for single-phase sillenites by the resonant cavity method.

Composition	Sintering Temperature ($°C$)	Pellet Density (%)	ε_r^M	Q	f_0 (GHz)	Q.f (GHz)	τ_f (ppm/K)
$Bi_{12}SiO_{20}$	880	90	36	1030	6.83	7037	-30
$Bi_{12}(Bi_{2/3}Zn_{1/3})O_{19.33}$	740	86	32.5	293	6.503	1905	-31
$Bi_{12}(Bi_{0.5}Fe_{0.5})O_{19.5}$	770	87	36.6	407	6.124	2493	-15
$Bi_{12}(Bi_{0.3}Al_{0.7})O_{19.5}$	735	56	26.4	205	7.199	1475	-71
$Bi_{12}(Bi_{0.4}Al_{0.6})O_{19.5}$	735	57	28.2	220	7.523	1654	-67
$Bi_{12}(Bi_{0.6}In_{0.4})O_{19.5}$	780	87	31.8	231	7.031	1624	-202
$Bi_{12}(Bi_{0.7}In_{0.3})O_{19.5}$	780	88	34.2	298	6.067	1807	-192
$Bi_{12}(B_{0.5}P_{0.5})O_{20}$	790	92	35	54	7.561	408	0
$Bi_{12}(B_{0.75}P_{0.25})O_{19.75}$	787	90	33	51	7.060	360	0
$Bi_{12}(B_{0.25}Si_{0.75})O_{19.875}$	730	92	38	56	7.182	402	0
$Bi_{12}(B_{0.5}Al_{0.5})O_{19.5}$	715	91	37	35	6.468	226	0
$Bi_{12}(B_{0.5}Ga_{0.5})O_{19.5}$	775	86	31	39	7.058	275	0
$Bi_{12}(B_{0.5}V_{0.5})O_{20}$	780	86	30	44	7.732	340	0
$Bi_{12}(Bi_{0.03}P_{0.89}\square_{0.08})O_{20.27}$	850	90	Too lossy to be measured				
$Bi_{12}(P_{0.86}\square_{0.14})O_{20.15}$	855	93	Too lossy to be measured				
$Bi_{12}(Fe^{3+}_{0.5}P^{5+}_{0.5})O_{20}$	850	83	31	150	7.058	1059	-15
$Bi_{12}(Mg^{2+}_{0.33}P^{5+}_{0.67})O_{20}$	864	83	32	179	7.215	1291	43

7.3.1 Clausius-Mossotti (CM) Equation and Relative Permittivity (ε_r)

With the exceptions of the metastable aluminium sillenites and the two 'lossy' phosphorus-containing sillenites, all the others (sintered at < 900 °C with relative density ~ 85-91 (± 2) %) showed similar permittivity (ε_r) of ~ 30-40 regardless of the M-dopant(s), Table 7.4. The similarity of ε_r with different M-dopants in sillenites can be explained as the total polarizability of the sillenite unit cell (α_D^T) was not influenced dramatically by the small concentration of M-cations in these materials.

Table 7.4 Summary of the relative permittivity for sillenites. Calculated relative permittivity, ε_r^C, are obtained from the Clausius-Mossotti equation [15], where α_D^T is total dielectric polarisability and calculated by summation of individual ion polarizability from Shannon [16].

Composition	Molar Volume, V_m (Å^3)	α_D^T (Å^3)	α_D^T/V_m	ε_r^M	ε_r^C	$\sigma = \varepsilon_r^M - \varepsilon_r^C$
$Bi_{12}SiO_{20}$	515.68	114.51	0.222	36	40.9	-4.9
$Bi_{12}(Bi_{2/3}Zn_{1/3})O_{19.33}$	531.57	117.07	0.220	32.5	36.7	-4.2
$Bi_{12}(Bi_{0.5}Fe_{0.5})O_{19.5}$	528.89	116.84	0.221	36.6	38.2	-1.6
$Bi_{12}(Bi_{0.3}Al_{0.7})O_{19.5}$	526.33	115.02	0.219	26.4	33.5	-7.1
$Bi_{12}(Bi_{0.4}Al_{0.6})O_{19.5}$	526.95	115.56	0.219	28.2	34.9	-6.7
$Bi_{12}(Bi_{0.6}In_{0.4})O_{19.5}$	535.8	117.36	0.219	31.8	34.4	-2.6
$Bi_{12}(Bi_{0.7}In_{0.3})O_{19.5}$	536.2	117.71	0.220	34.2	35.3	-1.1
$Bi_{12}(B_{0.5}P_{0.5})O_{20}$	522.07	114.28	0.219	35	34.1	0.9
$Bi_{12}(B_{0.75}P_{0.25})O_{19.75}$	520.32	113.48	0.218	33	32.7	0.3
$Bi_{12}(B_{0.25}Si_{0.75})O_{19.875}$	516.21	114.05	0.221	38	38.3	-0.3
$Bi_{12}(B_{0.5}Al_{0.5})O_{19.5}$	520.43	113.06	0.217	37	31.3	5.7
$Bi_{12}(B_{0.5}Ga_{0.5})O_{19.5}$	522.02	113.40	0.217	31	31.3	-0.3
$Bi_{12}(B_{0.5}V_{0.5})O_{20}$	527.37	115.13	0.218	30	33.1	-3.1
$Bi_{12}(Bi_{0.03}P_{0.89}\square_{0.08})O_{20.27}$	525.285	115.45	0.220	-	35.8	-
$Bi_{12}(P_{0.86}\square_{0.14})O_{20.15}$	525.8	114.99	0.219	-	33.8	-
$Bi_{12}(Fe^{3+}_{0.5}P^{5+}_{0.5})O_{20}$	522.925	115.40	0.221	31	37.7	-6.7
$Bi_{12}(Mg^{2+}_{0.33}P^{5+}_{0.67})O_{20}$	524.53	114.89	0.219	32	34.3	-2.3

The CM equation was used to predict the relative permittivity for sillenites. It measures the weighted number of polarisable ions per unit volume and has been used to estimate the mean static permittivity for well-behaved oxides and fluorides with known structures [16, 17]. In the CM equation, relative permittivity can be enhanced by substituting

a higher polarisable cation in a relatively smaller unit cell. A linear relationship was derived between the calculated permittivity, ε_r^C and the weighted average of the polarizabilities of all ions per unit molar volume, α_D^T/V_m for all the studied sillenites, Figure 7.2.
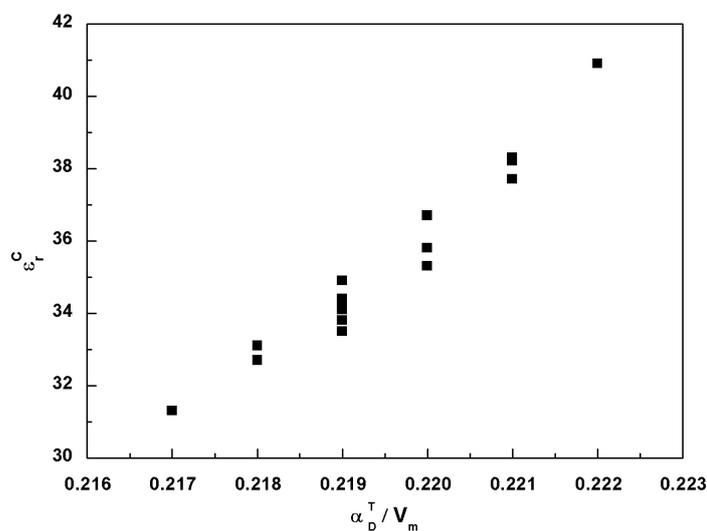
Figure 7.2 Linear relationship between ε_r^C and α_D^T/V_m for all the studied sillenites listed in Table 7.4.

A comparison between the measured permittivity, ε_r^M and the calculated permittivity, ε_r^C from the CM equation is shown in Figure 7.3. Deviations between ε_r^M and ε_r^C can be explained by one or a combination of the following reasons: inaccurate ion polarizability values such as for the highly polarisable Bi^{3+} ion in tetrahedral coordination; incorrect molar volumes or porosity in the ceramics. Other plausible causes could be ionic or electronic conductivity and/or the presence of relaxation behaviour in some samples over the measured temperature range.
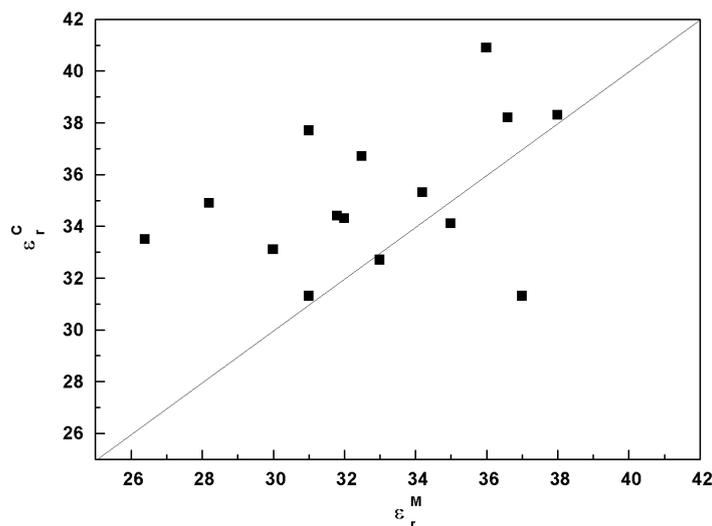
Figure 7.3 The measured permittivity, ε_r^M versus the calculated permittivity, ε_r^C for sillenites listed in Table 7.4.

7.3.2 Temperature Coefficient of Resonant Frequency (τ_f)

In contrast to ε_r, the temperature coefficient of resonant frequency (τ_f) changes significantly with composition and is particularly sensitive to the M-dopant(s). Valant and Suvorov reported an empirical correlation between the ionic radius of the M-site ions and τ_f. For large M-dopants with ionic radii greater than ideal, τ_f increases with a decrease in ionic size; while for small M-dopants with ionic radii less than ideal, τ_f is insensitive to the ionic size with a value of -20 ppm/K.[3] However, our results show deviations from those reported by Valant and Suvorov[3], Figure 7.4. For instance, Fe0.5 and Zn0.33 sillenites with large M-site ions do not follow the linear correlation of having an increase in τ_f with ion size. In addition, sillenites with small M-site ions show a range of τ_f with a clear perturbation, e.g. in Mg/P sillenite. This indicates the trends for τ_f to be more complicated in 'composite' sillenites, where more than one cation occupies the tetrahedral site.

Valant and Suvorov[3] also reported that τ_f is strongly influenced by the O(3)-O(3) distance in the tetrahedra, i.e. the size(s) of M-dopant(s). However, for 'composite' sillenites, the strong dependency of τ_f on the perturbation of the oxygen sublattice on the tetrahedra is now weakened and the O(3)-O(3) distance is averaged from dopants with different ion sizes. The variation of τ_f in sillenites should be a competition between the 'rattling' or 'compression' of the tetrahedra and the tilting of the BiO$_5$LP octahedra in the

framework.
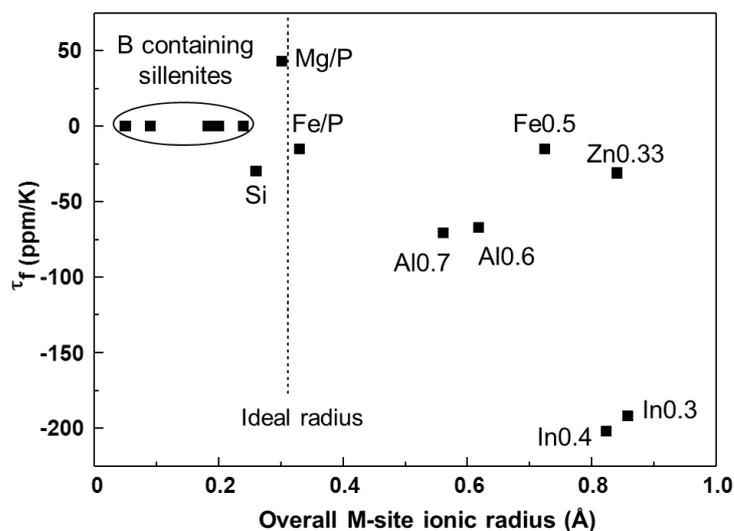
Figure 7.4 τ_f versus overall M-ion ionic radius of the studied sillenites.

7.3.3 Dielectric Losses (tan δ)

The dielectric losses are a combination of intrinsic losses arising from the anharmonic vibrations of the material itself [18, 19] and extrinsic losses from materials processing such as porosity, secondary phases, grain size, grain boundaries and point defects etc.[20, 21] It is well-known that oxides with highly ordered cation arrangements have lower dielectric losses and larger Q.f's, therefore, sillenites with an ideal close-packed configuration for the tetrahedral sites (i.e. M-site ionic radius is 0.31 Å [7]) should have the highest Q.f values [3], e.g. ~ 7000 GHz for $Bi_{12}SiO_{20}$, Figure 7.5. However, Q.f values for 'composite' sillenites with overall M-site ionic radius close to the ideal decreased, presumably due to the local lattice distortions in the tetrahedral arrangements caused by size mismatch of the dopants. Among all the studied sillenites, Boron containing sillenites exhibited the lowest Q.f values and the highest dielectric losses (tan δ) due to the disruptions of the LT relaxation behaviour in the measured temperature range.
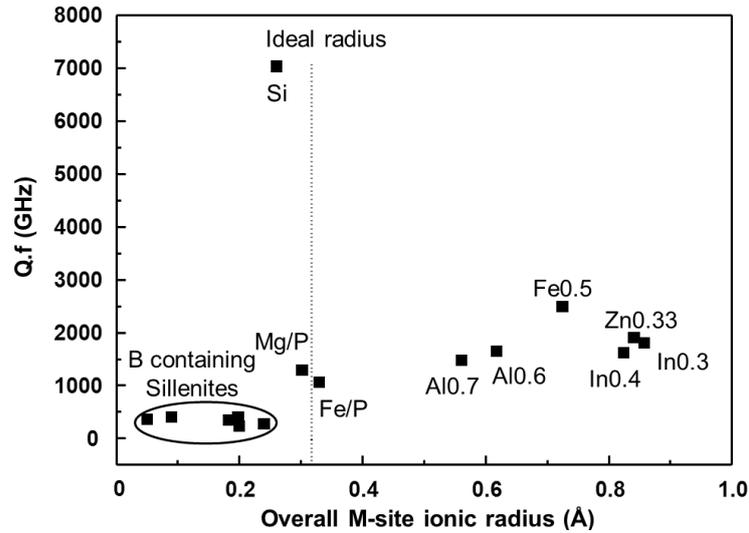
Figure 7.5 Q.f versus the overall M-site ionic radius of sillenites.

7.3.4 Low Temperature Co-fired Ceramic (LTCC)

The basic requirements of materials suitable for LTCC technology are: $\varepsilon_r > 20$; Q.f > 1000 GHz measured at 6-7 GHz; $\tau_f \sim 0$ ppm/K; chemical compatibility with Au/Ag metal electrodes and optimizing thermo-mechanical properties.[14] The primary advantage of investigating sillenites for use in LTCC microwave technology is their low sintering temperature of ≤ 850 °C, which would then allow co-firing with electrode materials such as silver metal (melting point of 961 ℃), in sandwich-like 3D stripline circuitry. In order to be cost-effective, commercial LTCC microwave materials heavily focus on mix-and-match glass-ceramics to obtain low sintering temperatures. Glass-forming oxides such as B_2O_3, SiO_2, ZnO etc. are commonly mixed with an excellent microwave dielectric material to tailor the properties. However, there is always a trade-off between low sintering temperatures and excellent microwave properties. Current commercial LTCC materials have sintering temperature of ~ 900 ℃. Therefore, sillenites with a low sintering temperature ~ 750 ℃ become strong candidates as LTCC materials. Comparison between some selected commercial LTCC materials and suitable candidates from our results is shown in Table 7.5.

Table 7.5 Dielectric properties of LTCC materials. Suitable candidates from this work are shown in bold letters and compared with existing LTCC materials.

Composition	Sintering Temperature (°C)	ε_r	Q.f / 6-7 (GHz)	τ_f (ppm/K)
$(Mg_{0.95}Ca_{0.05})TiO_3$+5 mol.% V_2O_5 [22]	1000	16.6	13700	50
$Ca[(Li_{1/3}Nb_{2/3})_{0.95}Ti_{0.05}]O_{3-\delta}$+5 wt.% Bi_2O_3 [23]	900	20	6500	-4
$BiNbO_4$+0.5wt.% V_2O_5 [24]	895	44	15800	18
$Ba(Zn_{1/3}Ta_{2/3})O_5$+5 mol.% B_2O_3+CuO [25]	875	36	19000	21
$BaTi_4O_9$+5 wt. % ZnO-B_2O_3 glass [26]	900	33	27000	7
$Bi_{12}SiO_{20}$	**880**	**36**	**7037**	**-30**
$Bi_{12}(Bi_{2/3}Zn_{1/3})O_{19.33}$	**740**	**32.5**	**1905**	**-31**
$Bi_{12}(Bi_{0.5}Fe_{0.5})O_{19.5}$	**770**	**36.6**	**2493**	**-15**
$Bi_{12}(Fe_{0.5}P_{0.5})O_{20}$	**850**	**31**	**1059**	**-15**
$Bi_{12}(Mg_{0.33}P_{0.67})O_{20}$	**864**	**32**	**1291**	**43**

7.4 Bulk Conductivity, Quality Factor (Q.f) and the Polymorphic Phase Transition Temperature

Table 7.6 Summary of bulk conductivity at 500 °C from IS data (σ_b), bulk activation energy (Ea), Q.f and polymorphic phase transition temperature for sillenites from this work.

Composition	σ_b at 500 °C (S.cm^{-1})	Ea(bulk) (eV)	Q.f (GHz)	Temperature of γ to δ phase from DSC (°C)
$Bi_{12}SiO_{20}$	2.00×10^{-5}	0.84	7037	913 ($\gamma \rightarrow \beta$)
				1106 ($\beta \rightarrow \delta$)
$Bi_{12}(Bi_{2/3}Zn_{1/3})O_{19.33}$	1.30×10^{-5}	1.20	1905	750
$Bi_{12}(Bi_{0.5}Fe_{0.5})O_{19.5}$	1.09×10^{-4}	0.57	2493	806
$Bi_{12}(Bi_{0.3}Al_{0.7})O_{19.5}$	3.27×10^{-6}	0.80	1475	742
$Bi_{12}(Bi_{0.4}Al_{0.6})O_{19.5}$	3.72×10^{-6}	0.84	1654	740
$Bi_{12}(Bi_{0.6}In_{0.4})O_{19.5}$	7.25×10^{-5}	0.73	1624	712
$Bi_{12}(Bi_{0.7}In_{0.3})O_{19.5}$	7.32×10^{-5}	0.74	1807	711
$Bi_{12}(B_{0.5}P_{0.5})O_{20}$	7.14×10^{-5}	0.94	408	> 750
$Bi_{12}(B_{0.75}P_{0.25})O_{19.75}$	1.17×10^{-5}	1.26	360	> 750
$Bi_{12}(B_{0.25}Si_{0.75})O_{19.875}$	2.05×10^{-5}	0.85	402	686
$Bi_{12}(B_{0.5}Al_{0.5})O_{19.5}$	4.06×10^{-6}	1.22	226	626
$Bi_{12}(B_{0.5}Ga_{0.5})O_{19.5}$	2.67×10^{-5}	1.20	275	604
$Bi_{12}(B_{0.5}V_{0.5})O_{20}$	2.08×10^{-5}	0.71	340	693
$Bi_{12}(Bi_{0.03}P_{0.89}\square_{0.08})O_{20.27}$	4.55×10^{-4}	0.82	-	> 750
$Bi_{12}(P_{0.86}\square_{0.14})O_{20.15}$	3.15×10^{-4}	0.86	-	> 750
$Bi_{12}(Fe^{3+}_{0.5}P^{5+}_{0.5})O_{20}$	1.14×10^{-4}	0.64	1059	> 800
$Bi_{12}(Mg^{2+}_{0.33}P^{5+}_{0.67})O_{20}$	5.96×10^{-5}	1.04	1291	> 820

Table 7.6 lists the bulk conductivity (at ~ 500 °C frm IS data), the bulk activation energy,

quality factor (Q.f) and the onset temperature(s) for sillenite polymorphic phase transitions.

The bulk conductivity data were obtained from the M" Debye peak and the activation energy calculated from Arrhenius plots of the bulk conductivity data. It is shown that the bulk conductivity of sillenites is not only dependent on the oxygen content but it is also significantly affected by the M-site dopant.
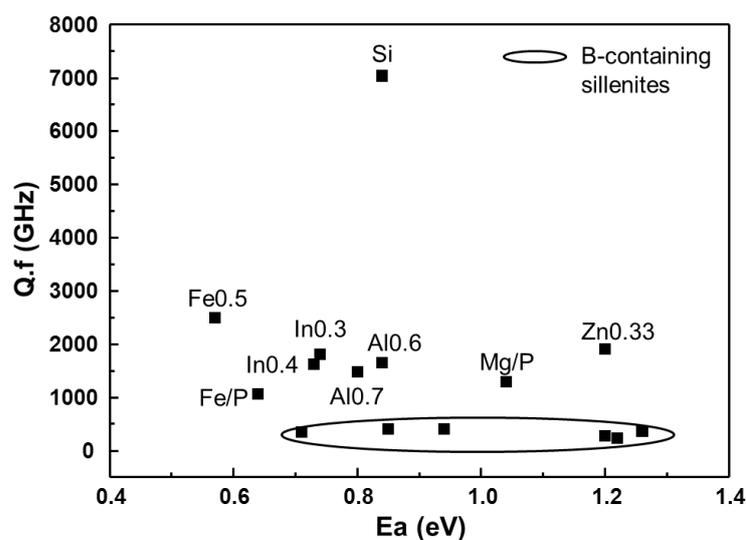
Figure 7.6 Bulk activation energy (Ea) versus quality factor (Q.f) for sillenites.

Assuming that all samples had similar levels of extrinsic losses and therefore a similar extrinsic influence on Q.f, a compound with a higher Q.f should indicate it has a more ordered or regular structure, e.g. $Bi_{12}SiO_{20}$, which is confirmed by Raman spectra. The correlation between the bulk conductivity and Q.f, Figure 7.6, did not show any linear trend of an increase in activation energy (or a decrease in conductivity) with increasing Q.f. It is found that the Q.f value and the onset temperature of γ-δ polymorphic phase transition for $Bi_{12}SiO_{20}$ were the highest, which indicates $Bi_{12}SiO_{20}$ was the most stable sillenite with the most regular lattice vibrations at microwave frequencies, Figure 7.7.
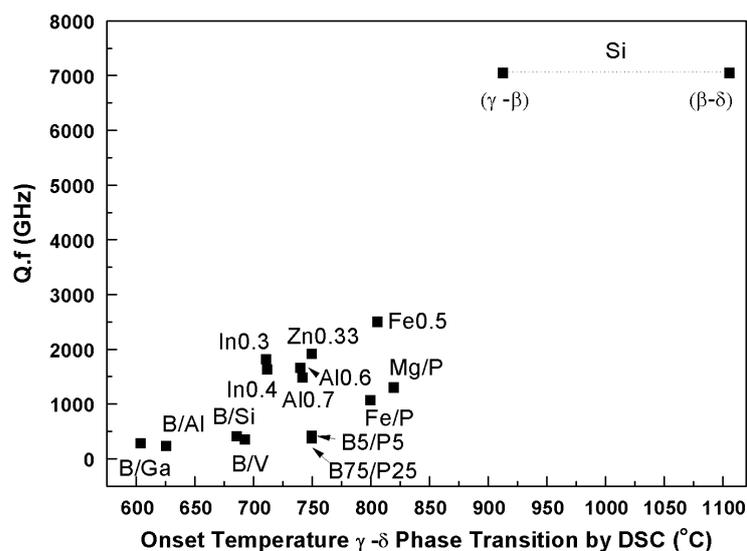
Figure 7.7 Q.f versus polymorphic γ-δ phase transition temperature from DSC (heating cycles) for sillenites.

7.5   References

[1]   M. Valant and D. Suvorov, A stoichiometric model for sillenites, Chemistry of Materials, 2002. **14**: p. 3471-3476.

[2]   R. D. Shannon, Revised effective ionic-radii and systematic studies of interatomic distances in halides and chalcogenides, Acta Crystallographica Section A, 1976. **32**: p. 751-767.

[3]   M. Valant and D. Suvorov, Processing and dielectric properties of sillenite compounds $Bi_{12}MO_{20-d}$ (M = Si, Ge, Ti, Pb, Mn, $B_{1/2}P_{1/2}$), Journal of the American Ceramic Society, 2001. **84**: p. 2900-2904.

[4]   D. Poleti, L. Karanovic and A. Hadzi-Tonic, Doped gamma-Bi_2O_3: synthesis of microcrystalline samples and crystal chemical analysis of structural data, Zeitschrift Fur Kristallographie, 2007. **222**: p. 59-72.

[5]   W. A. D. I. Hutton, "Investigations into the structure, thermal stability and electrical properties of various bismuth-based oxides, including sillenite materials," Ph.D. Thesis, University of Sheffield, 2004.

[6]   H. A. Harwig and A. G. Gerards, Polymorphism of bismuth sesquioxide, Thermochimica Acta, 1979. **28**: p. 121-131.

[7]   R. D. Shannon, Revised effective ionic radii and systematic studies of interatomic

distances in halides and chalcogenides, Acta Crystallographica Section A, 1976. **32**: p. 751-767.

[8]   S. F. Radaev, V. I. Simonov and Y. F. Kargin, Structural features of g-phase Bi_2O_3 and its place in the sillenite family, Acta Crystallographica Section B-Structural Science, 1992. **48**: p. 604-609.

[9]   M. Valant and D. Suvorov, Synthesis and characterization of a new sillenite compound $Bi_{12}(B_{0.5}P_{0.5})O_{20}$, Journal of the American Ceramic Society, 2002. **85**: p. 355-358.

[10]   M. Li, D. C. Sinclair and A. R. West, Extrinsic origins of the apparent relaxorlike behavior in $CaCu_3Ti_4O_{12}$ ceramics at high temperatures: A cautionary tale, Journal of Applied Physics, 2011. **109**: p. 084106.

[11]   C. C. Tan, A. Feteira and D. C. Sinclair, $Ba_2Bi_{1.4}Nb_{0.6}O_6$: A nonferroelectric, high permittivity oxide, Chemistry of Materials, 2012. **24**: p. 2247-2249.

[12]   E. Makovicky, Modular classification of sulfosalts - current status. Definition and application of homologous series, Neues Jahrbuch Fur Mineralogie-Abhandlungen, 1989. **160**: p. 269-297.

[13]   E. Makovicky, Crystal chemistry of complex sulfides and its chemical application, Modern Perspectives in Inorganic Crystal Chemistry, 1992. **382**: p. 131-161.

[14]   M. T. Sebastian and H. Jantunen, Low loss dielectric materials for LTCC applications: a review, International Materials Reviews, 2008. **53**: p. 57-90.

[15]   D. A. A. S. Narayana Rao, "Ionic polatisation in crystals: additivity in double salts," in *Proceedings of the Indian Academy of Sciences, Section A* vol. 30, ed, 1949, pp. 317-319.

[16]   R. D. Shannon, Dielectric polarizabilities of ions in oxides and fluorides, Journal of Applied Physics, 1993. **73**: p. 348-366.

[17]   S. Roberts, Dielectric constants and polarizabilities of ions in simple crystals and barium titanate, Physical Review, 1949. **76**: p. 1215-1220.

[18]   V. L. Gurevich and A. K. Tagantsev, Intrinsic dielectric loss in crystals, Advances in Physics, 1991. **40**: p. 719-767.

[19]   A. K. Tagantsev, J. Petzelt and N. Setter, Relation between intrinsic microwave and submillimeter losses and permittivity in dielectrics, Solid State Communications, 1993. **87**: p. 1117-1120.

[20] S. J. Penn, N. M. Alford, A. Templeton, X. R. Wang, M. S. Xu, M. Reece and K. Schrapel, Effect of porosity and grain size on the microwave dielectric properties of sintered alumina, Journal of the American Ceramic Society, 1997. **80**: p. 1885-1888.

[21] M. Valant and D. Suvorov, Microstructural phenomena in low-firing ceramics, Materials Chemistry and Physics, 2003. **79**: p. 104-110.

[22] N. Ichinose and H. Yamamoto, Effect of additives on microwave dielectric properties in low-temperature firing $(Mg,Ca)TiO_3$ based ceramics, Ferroelectrics, 1997. **201**: p. 255-262.

[23] J. Y. Ha, J. W. Choi, S. J. Yoon, D. J. Choi, K. H. Yoon and H. J. Kim, Microwave dielectric properties of Bi_2O_3-doped $Ca[(Li_{1/3}Nb_{2/3})_{(1-x)}Ti_x]O_{3-d}$ ceramics, Journal of the European Ceramic Society, 2003. **23**: p. 2413-2416.

[24] A. Y. Borisevich and P. K. Davies, Crystalline structure and dielectric properties of $Li_{(1+x-y)}Nb_{(1-x-3y)}Ti_{(x+4y)}O_3$ M-phase solid solutions, Journal of the American Ceramic Society, 2002. **85**: p. 573-578.

[25] M. H. Kim, Y. H. Jeong, S. Nahm, H. T. Kim and H. J. Lee, Effect of B_2O_3 and CuO additives on the sintering temperature and microwave dielectric properties of $Ba(Zn_{1/3}Nb_{2/3})O_3$ ceramics, Journal of the European Ceramic Society, 2006. **26**: p. 2139-2142.

[26] D. W. Kim, D. G. Lee and K. S. Hong, Low-temperature firing and microwave dielectric properties of $BaTi_4O_9$ with Zn-B-O glass system, Materials Research Bulletin, 2001. **36**: p. 585-595.

8 Conclusions and Further Work

8.1 Conclusions

An extensive range of sillenite family members with M^{n+} dopant ions (n = 2-5) and ionic radii ranging from 0.1 to ~ 0.9 Å were prepared by a traditional solid state reaction method and were successfully studied. The structure-composition-property relationships between different sillenite phases are established.

Structural analysis on the NPD data of sillenite phases: $Bi_{12}(Bi_{0.5}Zn_{0.5})O_{19.25}$, $Bi_{12}(Bi_{0.3}Al_{0.7})O_{19.5}$ and $Bi_{12}(Bi_{0.7}In_{0.3})O_{19.5}$ were performed by Rietveld refinement analysis. These three sillenites represent stoichiometric, sub-stoichiometric and super-stoichiometric type for Zn^{2+}, Al^{3+} and In^{3+} sillenites, respectively. The starting model was based on the R model of $Bi_{12}(Bi^{3+}_{0.67}Zn^{2+}_{0.33})O_{19.33}LP_{0.67}$ and $Bi_{12}(Bi^{3+}_{0.5}Fe^{3+}_{0.5})O_{19.5}LP_{0.5}$ for samples with M^{2+} and M^{3+} dopants, respectively.[1] NPD data revealed $Bi_{12}(Bi_{0.3}Al_{0.7})O_{19.5}$ and $Bi_{12}(Bi_{0.7}In_{0.3})O_{19.5}$ were phase pure whereas $Bi_{12}(Bi_{0.5}Zn_{0.5})O_{19.25}$ contained ~ 3.48 weight% ZnO secondary phase (phase 2) based on a fixed composition of $Bi_{12}(Bi_{0.67}Zn_{0.33})O_{19.33}$ as phase 1. This is consistent with the reported stoichiometry for Zn sillenite according to the VS general formula. The Rietveld analysis gave the best fit for stoichiometric Zn^{2+} sillenite; however, this technique seemed limited to explain the atomic arrangements on the tetrahedral sites for non-stoichiometric Al^{3+} and In^{3+} sillenites. Nevertheless, the final refinement results, including refined fitting parameters, refinement profile plots, bond length/angles and BVS showed the R model is the most appropriate structural model for all the experimental characteristics observed in these three sillenites. This results also confirmed the sillenites belong to space group $I23$ and eliminated the possibility of changing into a subgroup e.g. $P23$.

The Valant and Suvorov's (VS) general formula: $Bi_{12}(Bi^{3+}_{4/5-nx}M^{n+}_{5x})O_{19.2+nx}$[2] was established for many stoichiometric-type sillenites. The substitution mechanism is associated with a corresponding decrease in the Bi concentration on the tetrahedral site (M-site), which depends on the charge of the dopant. The validity of the VS general

formula was testified by studied sillenites. Not all sillenites obeyed this formula and the formation of sillenites is complex with consideration of both charge and size effects of the dopant(s) being required.

Poleti *et al*. [3] established a plot showing linear relationships between M-dopant size and the formed unit cell parameter of a sillenite. Indeed, the overall M-site ionic radius, r, shows significant influence on the unit cell of sillenites when $r > 0.31$ Å, which is the ideal ionic radius of an interstitial ion for a regular MO4 tetrahedron. [4, 5] However, when $r <$ 0.31 Å the highly 'flexible' Bi-O framework determines the size of the sillenite unit cell and the M-dopant size effect becomes insignificant. Valant and Suvorov[5] reported a similar statement: the O3-O3 distance in the MO_4 tetrahedra increases with $r > 0.31$ Å whereas it retains a value of 2.68 Å for $r < 0.31$ Å. Therefore, Poleti's plot seems only partially correct. In this work, instead of a particular linear trend between the overall M-ion size and the unit cell of the sillenite, a linear region was proposed, Figure 7.1. Within this linear region, various linear trends with different slopes exist, which indicate different doping mechanisms depending on the degree of incorporation with a structural influence of the Bi-O framework.

Two non-ferroelectric relaxation regions with one at high temperature (> 400 K) and one at low temperature (< 400 K) were observed by the *rf* fixed frequency and Impedance Spectroscopy (IS) measurements. An empirical correlation was found between the relaxation phenomenon and the overall M-site ion size, r: LT relaxation behaviour is only present for $r < 0.25$ Å; whereas HT relaxation behaviour is universal and exists in all sillenites, Figure 7.1. Under each relaxation phenomenon, the capacitance (C') spectroscopic plot in IS data display two capacitance plateaux: a frequency-independent high frequency plateau and a frequency-dependent low frequency plateau. Both of the capacitance plateaux have C'~ pF.cm^{-1} and are assigned as the bulk response of the sample. This capacitance fluctuation is correlated to the broad relaxor-like peaks in the *rf* fixed frequency measurement. Equivalent circuit analysis of the IS data further confirmed these relaxations are a bulk response and clearly different from other electrical responses such as grain boundary, electrode-sample interface effects. [6, 7] IS data are successfully modelled by a typical equivalent circuit for dielectric relaxation behaviour with a parallel connection

of an R, C and a Cole-Cole branch (CPE in series with a C).

For HT relaxation behaviour, Raman spectroscopy (RS) results show significant temperature dependence associated with Bi-O1 vibrations ($\sim$ 538 cm^{-1}) whereas there is negligible change in Bi-O2/O3 vibrations ($\sim$ 85 cm^{-1}). The downshifting and broadening of the $\sim$ 538 cm^{-1} peak with increasing temperature indicates increasing distortion of the framework and increasing interatomic distances between Bi and O1 atoms. The connectivity of adjacent Bi atoms via O1 atoms (site 1b and 1c) and the presence of the $6s^2$ electron lone pair on the Bi atoms permits considerable structural flexibility associated with the BiO$_5$LP bipyramids. Combined RS and IS results suggest this HT relaxation behaviour originates from non-correlated local dipole moments associated with the movement of Bi^{3+} in BiO$_5$LP framework units.

LT relaxation behaviour was only found in boron containing and phosphorous/vacancy containing sillenites with an empirical M-site ionic radius $r < 0.25$ Å. For boron containing sillenites, the origin of the LT relaxation was confirmed to arise from Bi-O framework units induced by the rotational of Bi$_4$/BO$_3$ units on the M-site. RS and NMR data show the existence of BO$_3$ and BO$_4$ units in boron containing samples. Accompanied with downshifting and broadening of $\sim$ 538 cm^{-1} peak (assigned as Bi-O framework vibration), the switching from BO$_4$ to BO$_3$ units with increasing temperature were observed from RS data. This indicates the adjacent Bi^{3+} ions of BiO$_5$LP octahedra move toward the BO$_3$ groups to ensure redistribution of charge balance, which is the origin of the LT relaxation behaviour in boron containing sillenites. For phosphorous/vacancy containing sillenites, RS results again reveal a significant downshifting and broadening of the $\sim$ 538 cm^{-1} peak and NMR results show a broadening of the isotope ^{31}P peak indicating a disordered tetrahedral site. This indirect evidence seems to reveal the origin of the LT relaxation for phosphorous/vacancy containing sillenites is triggered by a small, random distribution of the tetrahedral site.

The bulk conductivity, quality factors and the onset temperature of γ-δ phase transitions of sillenites were compared. It is found that generally the increase in activation energy (i.e. decrease of conductivity) near room temperature would cause an increase of Q.f. A compound with higher Q.f indicates that it has a more robust structure. The higher

the onset temperature of the γ-δ phase transition indicates higher stability in the sillenite.

Sillenites have been reported as potential useful dielectric materials in LTCC applications.[5] Microwave dielectric results here show ε_r, Q.f and τ_f can be significantly influenced by the relaxation behaviour within the measured temperature and microwave frequency ranges, particularly, the LT relaxation behaviour that is present near ambient temperature. Under the relaxation effect, e.g. boron containing sillenites, ε_r can be significantly boosted, $\tau_f \sim 0$ ppm/K; whereas Q.f drops dramatically with values ~ 220-400 GHz at a resonant frequency of ~ 6-7.7 GHz due to the high dielectric loss, tan δ, occurs in the sample. The later drawback therefore impedes the sample for LTCC applications. For other sillenites with no relaxation behaviour near ambient temperatures and microwave frequencies, excellent microwave dielectric properties can be gained, e.g. $Bi_{12}SiO_{20}$, $\varepsilon_r \sim 36$; $\tau_f \sim -30$ ppm/K; Q.f ~ 7037 GHz at a resonant frequency of 6.83 GHz. Its low sintering temperature (< 900 ℃) and chemical compatibility with Ag electrodes confirms $Bi_{12}SiO_{20}$ to be a potential useful material in LTCC applications. It is also found that the M-site ion size and close-packing environment significantly reflected in the dielectric losses, for instance, a near ideal M-site ionic radius for $Bi_{12}SiO_{20}$ ($Si^{4+}_{(VI)} = 0.26$ Å) gave the highest Q.f of ~ 7000 GHz.

Superstoichiometric sillenites with excess oxygen sublattice such as $Bi_{12}(Bi^{3+}_{0.03}P^{5+}_{0.89}\square_{0.08})O_{20.27}$, $Bi_{12}(P^{5+}_{0.86}\square_{0.14})O_{20.15}$ and even $Bi_{12}(Bi_{0.7}In_{0.3})O_{19.5}LP_{0.7}$ and $Bi_{12}(Bi_{0.6}In_{0.4})O_{19.5}LP_{0.6}$ exhibit ionic conductivity at T > 773 K. A low frequency spike inclined at ~ 50° to the x-axis was shown in Z* plot with the associated capacitance of ~ 10^{-7} F.cm^{-1}, indicating ionic polarisation associated with a blocking electrode[8]. The sample conductivity species should be oxide ions, where excess oxygen ions can hop through the void of the framework (i.e. O4 site). [9, 10] However, electronic contribution to the conduction was found by comparing IS results under oxygen free nitrogen (OFN) atmosphere and Air atmosphere. This confirms the conductivity for superstoichiometric sillenites is mixed, which could be developed and used as electrode materials for electrochemical devices such as solid oxide fuel cells, electrolysers *etc*.

8.2 Further Work

- Further expansion of sillenite phases with incorporation of 2 or 3 M-site dopants could be carried out. The possibility of the existence of $P23$ in a more distorted sillenite can be further investigated.

- Difference Fourier maps of neutron powder diffraction (NPD) data at high temperatures would be useful to observe the HT framework relaxation effect, particularly the movement of Bi^{3+} ions towards the M-sites at elevated temperatures. Applying the same technique of NPD data at low temperature (i.e. P^{5+} containing sillenites) may be useful to observe the co-operation between the disordered tetrahedral site and the movement of framework Bi ion of adjacent BiO_5LP polyhedra with temperature.

- DSC measurements for boron and phosphate containing sillenites should be carried out at higher temperatures to establish the exact γ-δ polymorphic phase transition temperatures.

- Thermal stability tests could be completed to investigate the phase stability of the other formed sillenites.

- Lower frequency and/or high temperature IS analysis should be useful to investigate the physical origin of the electrical behaviour (space charge polarization effect) of sillenites at $f < 10^3$ Hz.

- LT relaxation behaviour was only found when overall M-site ionic radius, $r < 0.25$ Å. Other sillenites with small M-site dopants should be used to testify this empirical r value.

- Double LT relaxation behaviour was observed in most of the boron containing sillenites, except for $B_{0.5}P_{0.5}$ and $B_{0.5}V_{0.5}$, Table 7.2. The origin of this behaviour is still

not well understood. Processing factors e.g. sample fabrication; firing time and temperature *etc.* that affect the appearance of these relaxation phenomena in sillenites are interesting and worthy to investigate. It might be possible to tailor the microwave dielectric properties of these sillenites by shifting the relaxation behaviour away from ambient temperatures.

- The equivalent circuit fitting parameter C_x (indicating the lattice relaxation) is still not fully understood. Further study of the correlation among the three parameters C_x, R_{CPE} and C_{CPE} is useful to probe the local structure distortions in sillenites.

- True stoichiometries of $Bi_{12}(B_{0.25}Si_{0.75})O_{19.875}$ and $Bi_{12}(Fe_{0.5}P_{0.5})O_{20}$ need to be studied. $Bi_{12}(Fe_{0.5}P_{0.5})O_{20}$ with an unusual small activation energy indicates a possible mixed Fe^{2+}/Fe^{3+} ions in the sample, which results in a sub-stoichiometric sillenite.

- Sillenites with excellent microwave dielectric properties that are suitable for LTCC technology are listed in Table 7.5. Chemical compatibility test with silver should be performed.

8.3 References

[1]   S. F. Radaev, L. A. Muradyan and V. I. Simonov, Atomic structure and crystal chemistry of sillenites $Bi_{12}(Bi^{3+}_{0.50}Fe^{3+}_{0.50})O_{19.50}$ and $Bi_{12}(Bi^{3+}_{0.67}Zn^{2+}_{0.33})O_{19.33}$, Acta Crystallographica Section B-Structural Science, 1991. **47**: p. 1-6.

[2]   M. Valant and D. Suvorov, A stoichiometric model for sillenites, Chemistry of Materials, 2002. **14**: p. 3471-3476.

[3]   D. Poleti, L. Karanovic and A. Hadzi-Tonic, Doped gamma-Bi_2O_3: synthesis of microcrystalline samples and crystal chemical analysis of structural data, Zeitschrift Fur Kristallographie, 2007. **222**: p. 59-72.

[4]   R. D. Shannon, Revised effective ionic-radii and systematic studies of interatomic distances in halides and chalcogenides, Acta Crystallographica Section A, 1976. **32**:

p. 751-767.

[5]   M. Valant and D. Suvorov, Processing and dielectric properties of sillenite compounds $Bi_{12}MO_{20-d}$ (M = Si, Ge, Ti, Pb, Mn, $B_{1/2}P_{1/2}$), Journal of the American Ceramic Society, 2001. **84**: p. 2900-2904.

[6]   M. Li, D. C. Sinclair and A. R. West, Extrinsic origins of the apparent relaxorlike behavior in $CaCu_3Ti_4O_{12}$ ceramics at high temperatures: A cautionary tale, Journal of Applied Physics, 2011. **109**: p. 084106.

[7]   C. C. Tan, A. Feteira and D. C. Sinclair, $Ba_2Bi_{1.4}Nb_{0.6}O_6$: A nonferroelectric, high permittivity oxide, Chemistry of Materials, 2012. **24**: p. 2247-2249.

[8]   J. T. S. Irvine, D. C. Sinclair and A. R. West, Electroceramics: Characterization by impedance spectroscopy, Advanced Materials, 1990. **2**: p. 132-138.

[9]   J. P. Wignacourt, M. Drache, P. Conflant and J. C. Boivin, New phases in the Bi_2O_3-$BiPO_4$ system. 2. Structure and electrical properties of a sillenite solution, Journal De Chimie Physique Et De Physico-Chimie Biologique, 1991. **88**: p. 1939-1949.

[10]   S. L. Lee, C. K. Lee and D. C. Sinclair, Synthesis and characterisation of bismuth phosphate-based sillenites, Solid State Ionics, 2005. **176**: p. 393-400.

9   Appendix

Appendix I: XRPD Results

XRPD results for attempted M-dopants, i.e. Li^+, Mg^{2+}, Sc^{3+}, Ti^{4+}, Ge^{4+}, B^{3+}, P^{5+}, that did not successfully form single-phase sillenites by solid state reaction method are shown in Figures 9.1 – 9.7. The drying temperatures and purity of reagents are listed in Table 9.1. Samples with reagents that have low melting temperatures were heated initially to 400 ℃ for 2 hours with a heating rate of 1 ℃/min to evaporate any H_2O, CO_2 and NH_3 *etc.* and then heated to the reaction temperature with a heating and cooling rate of 10 ℃/min.

Table 9.1 Drying temperature and purity of selected reagents.

Reagent	Drying Temperature (℃)	Manufacturer and Purity
Bi_2O_3	180	Sigma-Aldrich, 99.9 %
Li_2CO_3	180	Sigma-Aldrich, 99.99 %
$Mg(CO_3)_4\ Mg(OH)_2\ 5H_2O$	Not Applicable	Aldrich, 99 %
Sc_2O_3	900	Sigma-Aldrich, 99.9 %
TiO_2	900	Sigma-Aldrich, 99.9%
GeO_2	900	Sigma-Aldrich, 99.9 %
$B(OH)_3$	Not Applicable	Sigma-Aldrich, 99.5 %
$(NH_4)H_2PO_4$	Not Applicable	Sigma-Aldrich, 99.5%

● Li^+
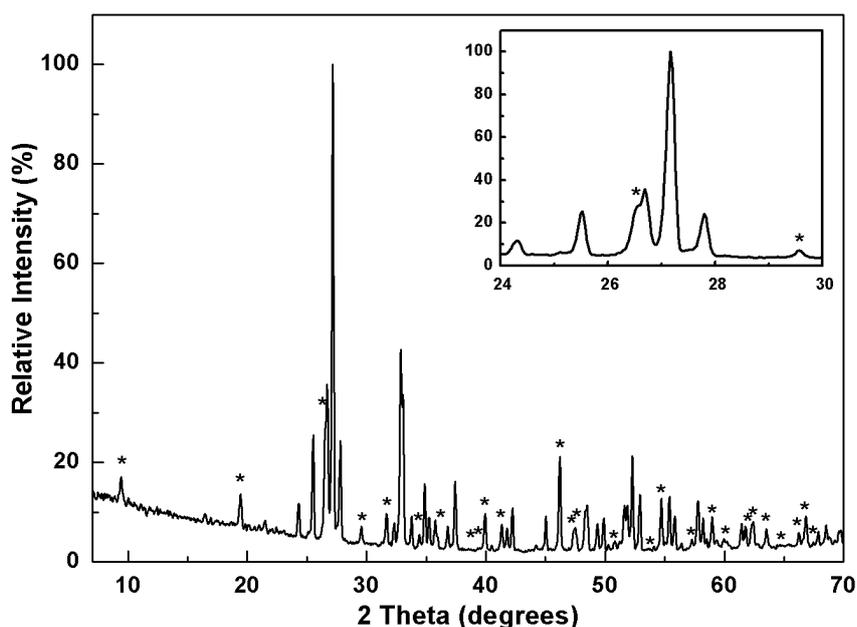
Figure 9.1 XRPD results of $Bi_{12}LiO_{18.5}$ heated at 725 ℃ for 72 hours. Impurity phases are

BiLiO$_2$ (ICCD card [77-1192]) labelled as * and α-Bi$_2$O$_3$ (ICCD card [41-1449]). Inset shows the enlarged XRPD pattern for 2θ angles from 24 to 30 °.

● Mg^{2+}

Bi$_{12}$(Bi$_{0.7}$Mg$_{0.3}$)O$_{19.35}$, Bi$_{12}$(Bi$_{0.67}$Mg$_{0.33}$)O$_{19.33}$, Bi$_{12}$(Bi$_{0.5}$Mg$_{0.5}$)O$_{19.25}$ and Bi$_{12}$MgO$_{19}$ were prepared and heated at 780-800 ℃ for 72 hours. XRPD results of some selected compositions, Figure 9.2, show no sillenite phase was formed. The co-existence of α-Bi$_2$O$_3$ and MgO is observed in Bi$_{12}$MgO$_{19}$ by XRPD, whereas light element MgO with small concentration in Bi$_{12}$(Bi$_{0.7}$Mg$_{0.3}$)O$_{19.35}$ is not detectable by XRPD.
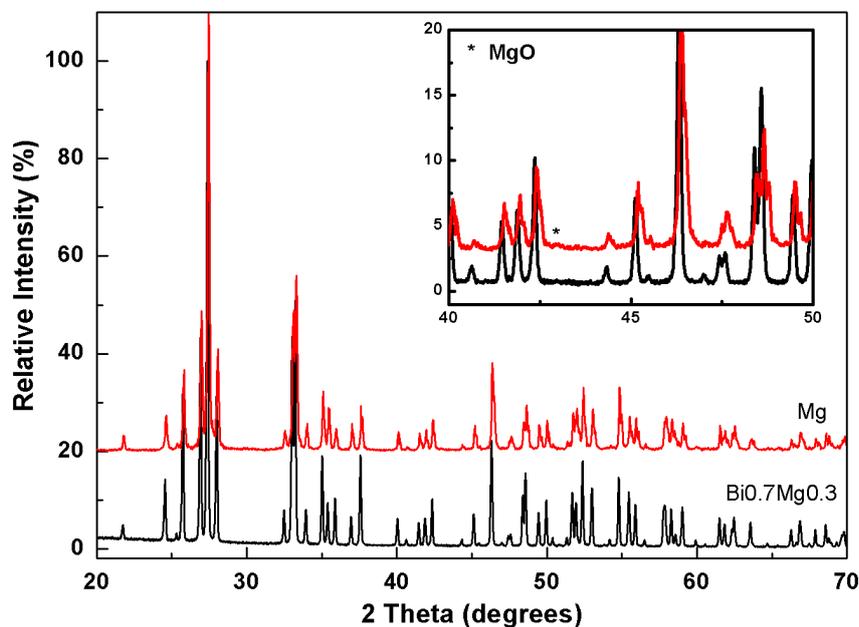
Figure 9.2 XRPD results of Bi$_{12}$(Bi$_{0.7}$Mg$_{0.3}$)O$_{19.35}$ and Bi$_{12}$MgO$_{19}$ heated at 800 ℃ for 72 hours. Notion * in the inset indicates the strongest peak of MgO (ICCD card [78-430]) in Bi$_{12}$MgO$_{19}$.

- Sc^{3+}
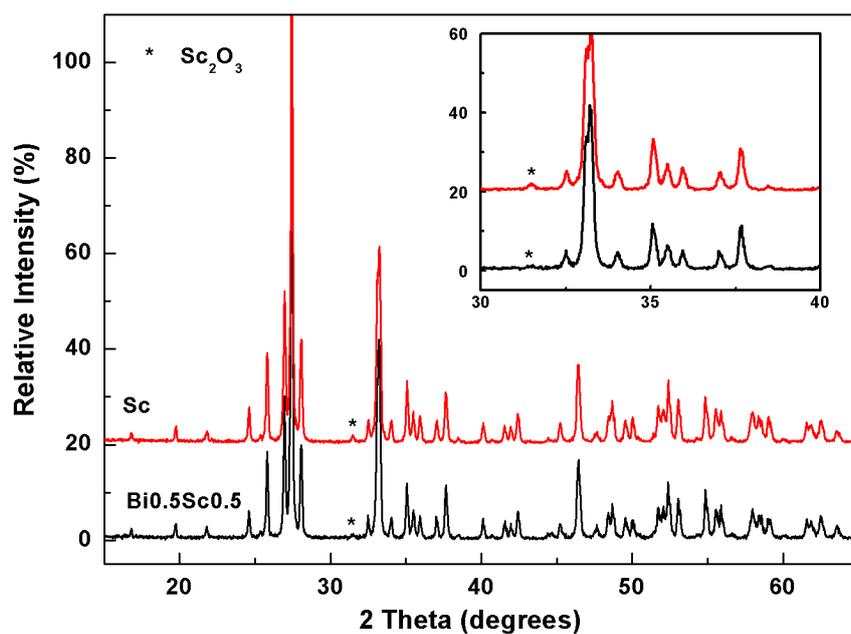
Figure 9.3 XRPD results of $Bi_{12}(Bi_{0.5}Sc_{0.5})O_{19.35}$ and $Bi_{12}ScO_{19.5}$ heated at 820 ℃ for 72 hours. Impurity phases are Sc_2O_3 (ICCD card [5-629]) labelled as * and α-Bi_2O_3 (ICCD card [41-1449]).

- Ti^{4+}
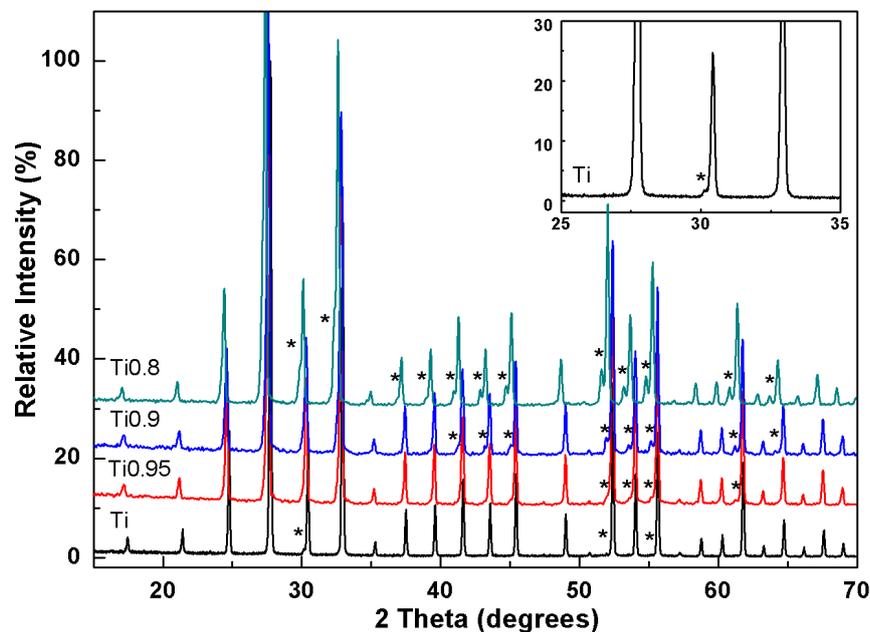
Figure 9.4 XRPD results of titanium sillenites $Bi_{12}TiO_{20}$, $Bi_{12}Ti_{0.95}O_{19.9}$, $Bi_{12}Ti_{0.9}O_{19.8}$ and $Bi_{12}Ti_{0.8}O_{19.6}$ heated at 750 ℃ for 72 hours. None of them are phase-pure sillenites with impurity phase of γ-Bi_2O_3 (ICCD card [45-1344], notation *).

- Ge^{4+}
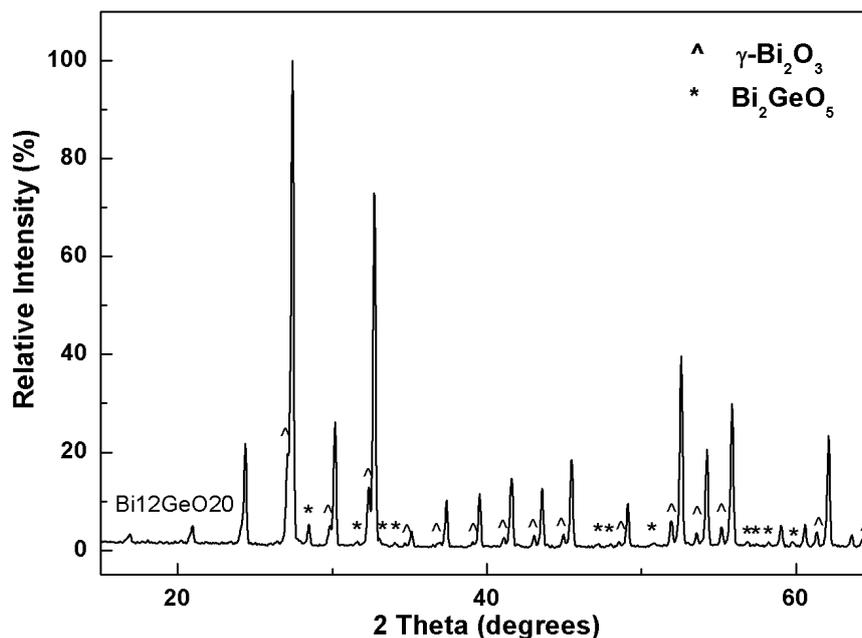
Figure 9.5 XRPD results of $Bi_{12}GeO_{20}$ heated at 800 ℃ for 48 hours. Notations ^ and * indicate impurity phases of γ-Bi_2O_3 (ICCD card [45-1344]) and Bi_2GeO_5 (ICCD card [36-289]), respectively.

- B^{3+}
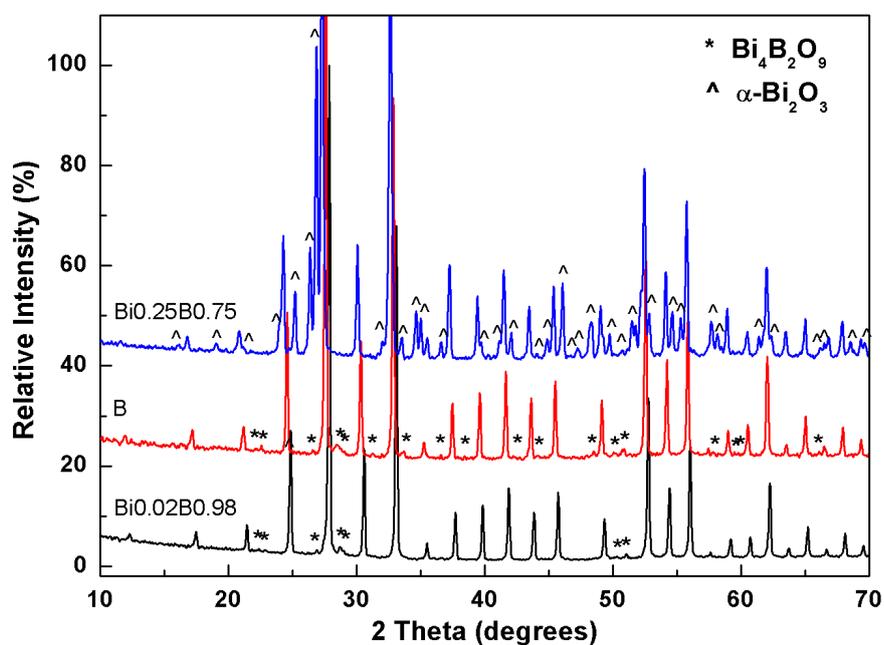
Figure 9.6 XRPD results of $Bi_{12}BO_{19.5}$, $Bi_{12}(Bi_{0.02}B_{0.98})O_{19.5}$ and $Bi_{12}(Bi_{0.25}B_{0.5})O_{19.125}$ heated at 625 ℃ for 72 hours. Phase-pure sillenite is not formed with impurity phase of α-Bi_2O_3 (ICCD card [41-1449], notation ^) in $Bi_{12}(Bi_{0.25}B_{0.5})O_{19.125}$ and impurity phase of $Bi_4B_2O_9$ (ICCD card [41-1449], notation *) in $Bi_{12}BO_{19.5}$ and $Bi_{12}(Bi_{0.02}B_{0.98})O_{19.5}$.

- P^{5+}
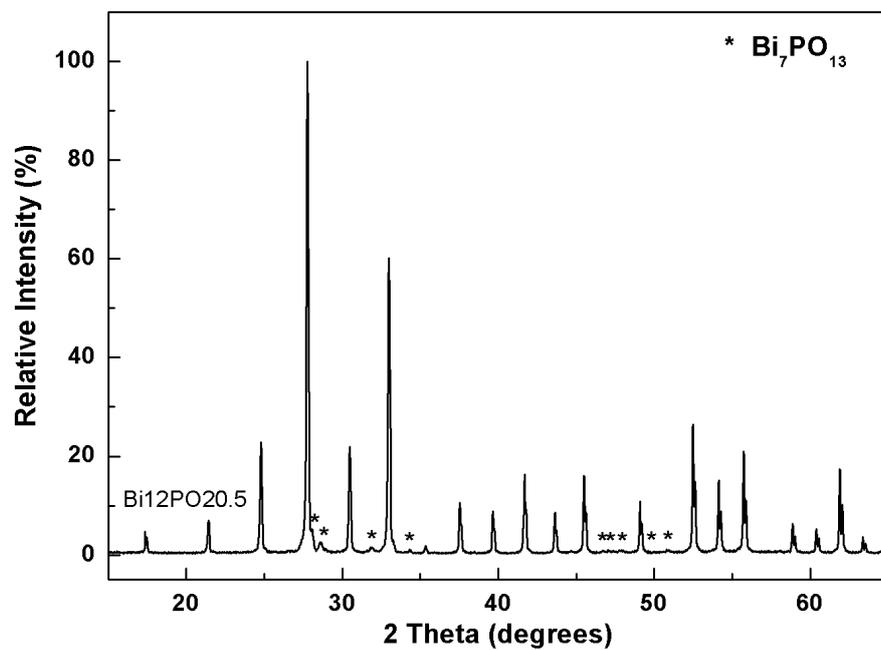
Figure 9.7 XRPD result of $Bi_{12}PO_{20.5}$ heated at 800 °C for 72 hours shows a phase mixture of sillenite and impurity phase of Bi_7PO_{13} (ICCD card [49-38], notation *).

Appendix II: Impedance Derivative Equations

Two Parallel RC Elements in Series
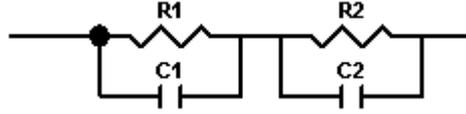
$$Z^* = \frac{1}{Y^*}$$

$$= \frac{1}{1/R_1 + j\omega C_1} + \frac{1}{1/R_2 + j\omega C_2}$$

$$= \frac{R_1}{1 + j\omega R_1 C_1} + \frac{R_2}{1 + j\omega R_2 C_2}$$

$$= \frac{R_1}{1 + j\omega R_1 C_1} \cdot \left[\frac{1 - j\omega R_1 C_1}{1 - j\omega R_1 C_1}\right] + \frac{R_2}{1 + j\omega R_2 C_2} \cdot \left[\frac{1 - j\omega R_2 C_2}{1 - j\omega R_2 C_2}\right]$$

$$= \frac{R_1 - j\omega (R_1)^2 C_1}{1 + (\omega R_1 C_1)^2} + \frac{R_2 - j\omega (R_2)^2 C_2}{1 + (\omega R_2 C_2)^2}$$

$$= \frac{R_1}{1 + (\omega R_1 C_1)^2} + \frac{R_2}{1 + (\omega R_2 C_2)^2} - j\left\{R_1\left[\frac{\omega R_1 C_1}{1 + (\omega R_1 C_1)^2}\right] + R_2\left[\frac{\omega R_2 C_2}{1 + (\omega R_2 C_2)^2}\right]\right\}$$

$$\omega \to 0, \quad Z_1' = R_1$$

$$\omega \to 0, \quad Z_2' = R_2$$

$$\omega R_1 C_1 = 1, \qquad Z_1'' = \frac{R_1}{2}$$

$$\omega R_2 C_2 = 1, \qquad Z_2'' = \frac{R_2}{2}$$

$$Y^* = \frac{1}{Z^*}$$

$$= \frac{1}{Z_1{}^* + Z_2{}^*}$$

$$= 1 \Big/ \left[\frac{R_1 - j\omega(R_1)^2 C_1}{1+(\omega R_1 C_1)^2} + \frac{R_2 - j\omega(R_2)^2 C_2}{1+(\omega R_2 C_2)^2}\right]$$

$$= 1 \Big/ \left\{\frac{\left[R_1 - j\omega(R_1)^2 C_1\right]\cdot\left[1+(\omega R_2 C_2)^2\right] + \left[R_2 - j\omega(R_2)^2 C_2\right]\cdot\left[1+(\omega R_1 C_1)^2\right]}{\left[1+(\omega R_1 C_1)^2\right]\cdot\left[1+(\omega R_2 C_2)^2\right]}\right\}$$

$$= \frac{\left[1+(\omega R_1 C_1)^2\right]\cdot\left[1+(\omega R_2 C_2)^2\right]}{R_1[1+(\omega R_2 C_2)^2] + R_2[1+(\omega R_1 C_1)^2] - j\left\{\left[\omega(R_1)^2 C_1[1+(\omega R_2 C_2)^2]\right] + \left[\omega(R_2)^2 C_2[1+(\omega R_1 C_1)^2]\right]\right\}}$$

$$Y' = \frac{\left\{[1+(\omega R_1 C_1)^2]\cdot[1+(\omega R_2 C_2)^2]\right\}\cdot\left\{R_1[1+(\omega R_2 C_2)^2] + R_2[1+(\omega R_1 C_1)^2]\right\}}{\left\{R_1[1+(\omega R_2 C_2)^2] + R_2[1+(\omega R_1 C_1)^2]\right\}^2 + \left\{\left[\omega(R_1)^2 C_1[1+(\omega R_2 C_2)^2]\right] + \left[\omega(R_2)^2 C_2[1+(\omega R_1 C_1)^2]\right]\right\}^2}$$

$$Y'' = \frac{\left\{[1+(\omega R_1 C_1)^2]\cdot[1+(\omega R_2 C_2)^2]\right\}\cdot\left\{\left[\omega(R_1)^2 C_1[1+(\omega R_2 C_2)^2]\right] + \left[\omega(R_2)^2 C_2[1+(\omega R_1 C_1)^2]\right]\right\}}{\left\{R_1[1+(\omega R_2 C_2)^2] + R_2[1+(\omega R_1 C_1)^2]\right\}^2 + \left\{\left[\omega(R_1)^2 C_1[1+(\omega R_2 C_2)^2]\right] + \left[\omega(R_2)^2 C_2[1+(\omega R_1 C_1)^2]\right]\right\}^2}$$

$$\omega \to 0, \qquad Y' = \frac{1}{R_1 + R_2}$$

$$\omega \to \infty, \qquad Y' = \frac{1}{R_1}$$
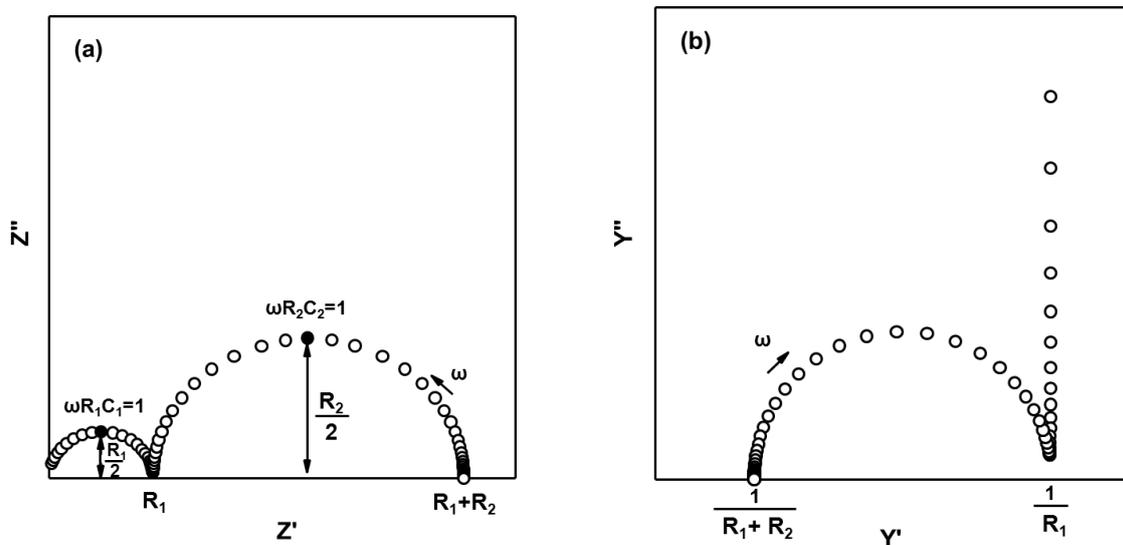
Figure 9.8 Simulated (a) complex impedance Z* plot and (b) complex admittance Y* plot for two parallel RC elements in series.

Cole-Cole branch in Parallel with R and C Elements
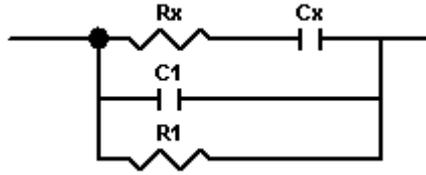
$$Y^* = \frac{1}{Z_1{}^*} + Y_2{}^* + Y_3{}^*$$

$$= \frac{1}{R_x - \frac{j}{\omega C_x}} + j\omega C_1 + \frac{1}{R_1}$$

$$= \frac{\omega C_x}{\omega R_x C_x - j} \cdot \frac{\omega R_x C_x + j}{\omega R_x C_x + j} + j\omega C_1 + \frac{1}{R_1}$$

$$= \frac{\omega C_x(\omega R_x C_x + j)}{1 + (\omega R_x C_x)^2} + j\omega C_1 + \frac{1}{R_1}$$

$$= \frac{1}{R_x}\left[\frac{(\omega R_x C_x)^2}{1 + (\omega R_x C_x)^2}\right] + \frac{j}{R_x}\left[\frac{(\omega R_x C_x)}{1 + (\omega R_x C_x)^2}\right] + j\omega C_1 + \frac{1}{R_1}$$

$$= \frac{1}{R_x}\left[\frac{(\omega R_x C_x)^2}{1 + (\omega R_x C_x)^2}\right] + \frac{1}{R_1} + j \cdot \left\{\frac{1}{R_x}\left[\frac{(\omega R_x C_x)}{1 + (\omega R_x C_x)^2}\right] + \omega C_1\right\}$$

$$Y' = \frac{1}{R_x}\left[\frac{(\omega R_x C_x)^2}{1 + (\omega R_x C_x)^2}\right] + \frac{1}{R_1}$$

$$Y'' = \frac{1}{R_x}\left[\frac{(\omega R_x C_x)}{1 + (\omega R_x C_x)^2}\right] + \omega C_1$$

$$\omega \to 0, \quad Y' = \frac{1}{R_1}$$

$$\omega \to \infty, \quad Y' = \frac{1}{R_1} + \frac{1}{R_x}$$

$$Z^* = \frac{1}{Y^*}$$

$$= 1 \Big/ \left\{ \left[\frac{1}{R_x} \left[\frac{(\omega R_x C_x)^2}{1+(\omega R_x C_x)^2} \right] + \frac{1}{R_1} \right] + j \cdot \left\{ \frac{1}{R_x} \left[\frac{(\omega R_x C_x)}{1+(\omega R_x C_x)^2} \right] + \omega C_1 \right\} \right\}$$

$$= \frac{1}{\left\{ \left[\frac{1}{R_x} \left[\frac{(\omega R_x C_x)^2}{1+(\omega R_x C_x)^2} \right] + \frac{1}{R_1} \right] + j \cdot \left\{ \frac{1}{R_x} \left[\frac{(\omega R_x C_x)}{1+(\omega R_x C_x)^2} \right] + \omega C_1 \right\} \right\}} \cdot \frac{\left\{ \left[\frac{1}{R_x} \left[\frac{(\omega R_x C_x)^2}{1+(\omega R_x C_x)^2} \right] + \frac{1}{R_1} \right] - j \cdot \left\{ \frac{1}{R_x} \left[\frac{(\omega R_x C_x)}{1+(\omega R_x C_x)^2} \right] + \omega C_1 \right\} \right\}}{\left\{ \left[\frac{1}{R_x} \left[\frac{(\omega R_x C_x)^2}{1+(\omega R_x C_x)^2} \right] + \frac{1}{R_1} \right] - j \cdot \left\{ \frac{1}{R_x} \left[\frac{(\omega R_x C_x)}{1+(\omega R_x C_x)^2} \right] + \omega C_1 \right\} \right\}}$$

$$= \frac{\left[\frac{1}{R_x} \left[\frac{(\omega R_x C_x)^2}{1+(\omega R_x C_x)^2} \right] + \frac{1}{R_1} \right] - j \cdot \left\{ \frac{1}{R_x} \left[\frac{(\omega R_x C_x)}{1+(\omega R_x C_x)^2} \right] + \omega C_1 \right\}}{\left[\frac{1}{R_x} \left[\frac{(\omega R_x C_x)^2}{1+(\omega R_x C_x)^2} \right] + \frac{1}{R_1} \right]^2 + \left[\frac{1}{R_x} \left[\frac{(\omega R_x C_x)}{1+(\omega R_x C_x)^2} \right] + \omega C_1 \right]^2}$$

$$\omega \to 0, \qquad Z' = R_1$$

$$\omega \to \infty, \qquad Z' = \frac{R_1 R_x}{R_1 + R_x}$$
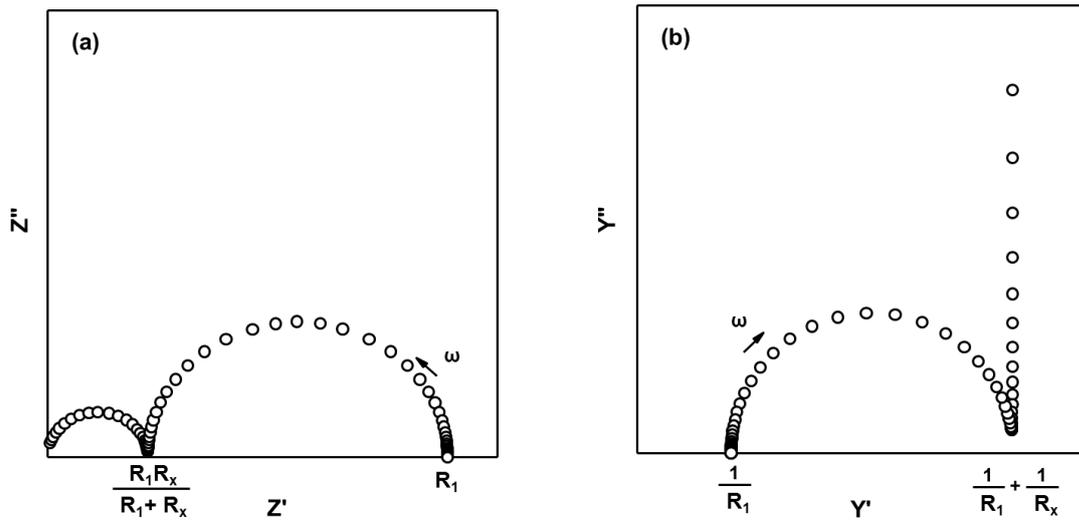
Figure 9.9 Simulated (a) complex impedance Z* plot and (b) complex admittance Y* plot for the Cole-Cole branch in parallel with R and C elements.

Appendix III: Equivalent Circuit Fitted Impedance Spectroscopy Data

The IS data for compounds not shown in the previous chapters with the associated equivalent circuit fitting results are shown in this section. For the universal high temperature (HT) relaxation behaviour, equivalent circuit in Figure 9.10 (a) is used; and for the low temperature (LT) relaxation behaviour, equivalent circuit in Figure 9.10 (b) is used.
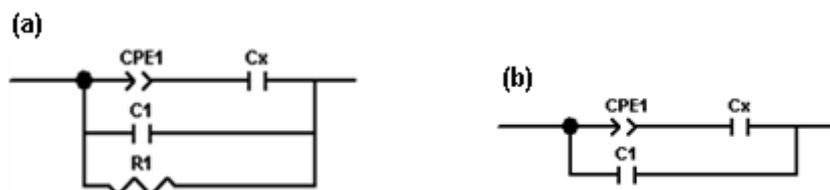
Figure 9.10 (a) and **(b)** Equation circuit for dielectric relaxation.

- ## Chapter 4: M^{2+}/M^{3+} doping sillenites

$Bi_{12}(Bi_{0.67}Zn_{0.33})O_{19.33}$
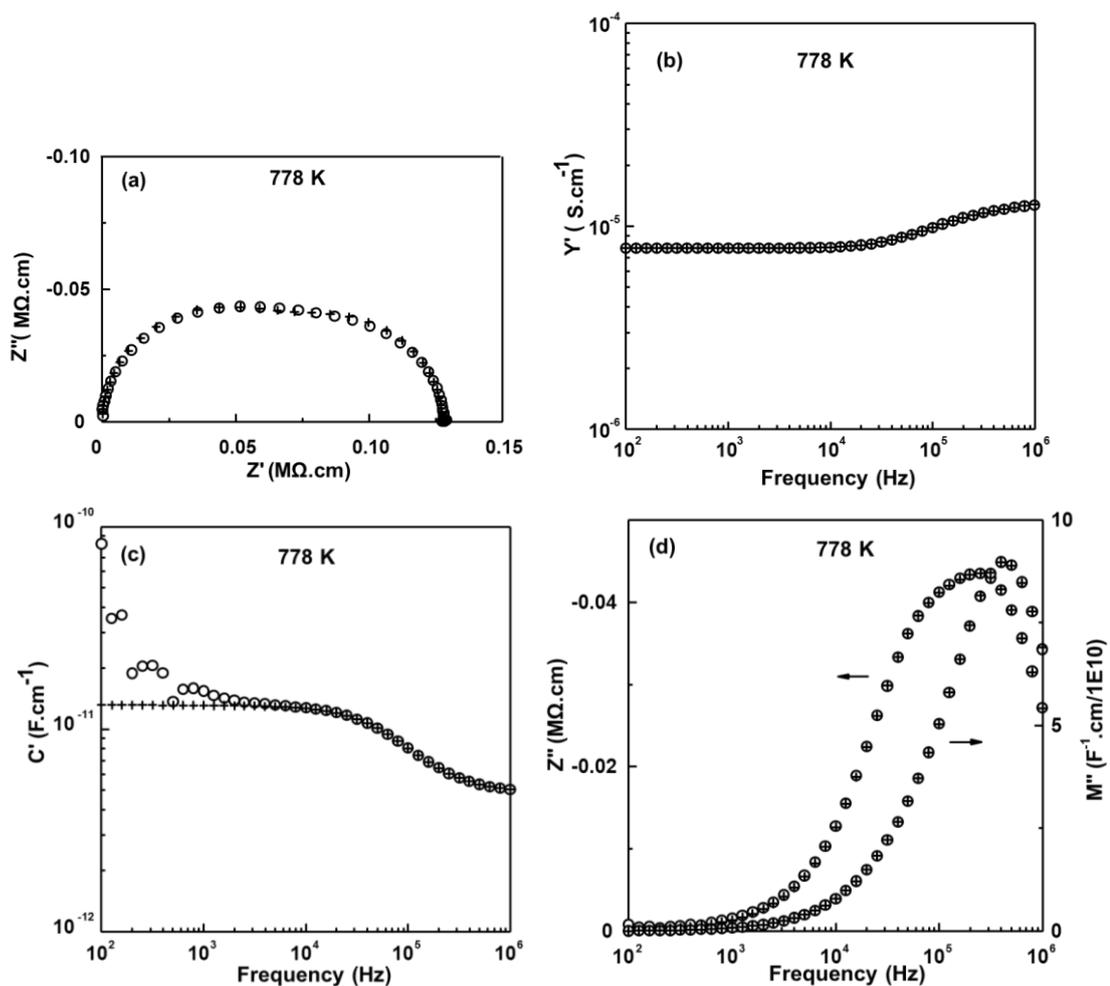
Figure 9.11 High temperature IS experimental data points (○) and the fitting results (+) to equivalent circuit in Figure 9.10 (a) with (a) Z^* plot; (b) Y', (c) C', and (d) $-Z''/M''$ spectroscopic plots at 778 K for $Bi_{12}(Bi_{0.67}Zn_{0.33})O_{19.33}$.

Table 9.2 Fitted high temperature IS values of $Bi_{12}(Bi_{0.67}Zn_{0.33})O_{19.33}$ from 698 to 818 K. Errors associated with the fitted circuit parameters R_1, C_1, C_x, A and n are $< \pm 0.1$ %, $< \pm 0.2$ %, $< \pm 1.6$ %, $< \pm 6.3$ % and $< \pm 3.9$ %, respectively.

Temperature (K)	R_1 (Ω cm)	C_1 (pF cm^{-1})	C_x (pF cm^{-1})	A (Ω^{-1} cm^{-1} rad^{-1})	n
698	1182900	4.78	8.36	9.23×10^{-8}	0.13
718	610910	4.79	8.30	1.79×10^{-7}	0.13
738	345660	4.79	8.45	2.89×10^{-7}	0.13
753	212010	4.79	8.46	4.47×10^{-7}	0.13
778	128220	4.79	8.36	7.11×10^{-7}	0.13
793	80311	4.78	8.34	1.04×10^{-6}	0.13
818	51091	4.75	8.23	1.50×10^{-6}	0.14

$Bi_{12}(Bi_{0.5}Fe_{0.5})O_{19.5}$
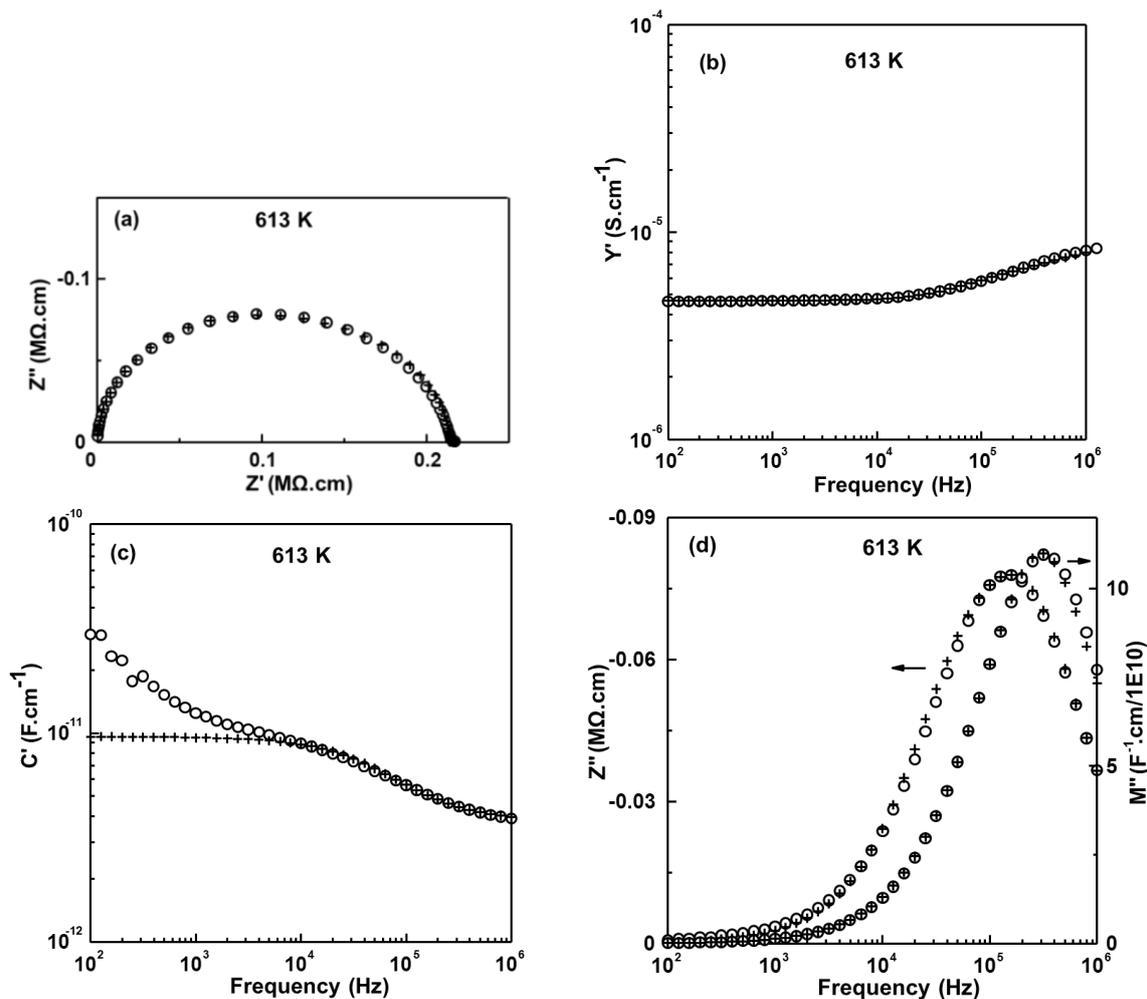
Figure 9.12 High temperature IS experimental data points (○) and the fitting results (+) to

equivalent circuit in Figure 9.10 (a) with (a) Z* plot; (b) Y', (c) C', and (d) −Z"/M" spectroscopic plots at 613 K for $Bi_{12}(Bi_{0.5}Fe_{0.5})O_{19.5}$.

Table 9.3 Fitted high temperature IS values of $Bi_{12}(Bi_{0.5}Fe_{0.5})O_{19.5}$ from 573 to 653 K. Errors associated with the fitted circuit parameters R_1, C_1, C_x, A and n are < ±0.2 %, < ±0.5 %,< ±4.3 %,< ±20.7 % and < ±5.7 %, respectively.

Temperature (K)	R_1 (Ω cm)	C_1 (pF cm^{-1})	C_x (pF cm^{-1})	A (Ω^{-1} cm^{-1} rad^{-1})	n
573	329350	3.72	5.03	1.11×10^{-7}	0.20
593	294900	3.71	5.72	1.01×10^{-7}	0.21
613	211590	3.71	5.80	1.16×10^{-7}	0.22
633	149040	3.71	5.80	1.31×10^{-7}	0.23
653	98074	3.71	5.64	1.45×10^{-7}	0.24

$Bi_{12}(Bi_{0.3}Al_{0.7})O_{19.5}$
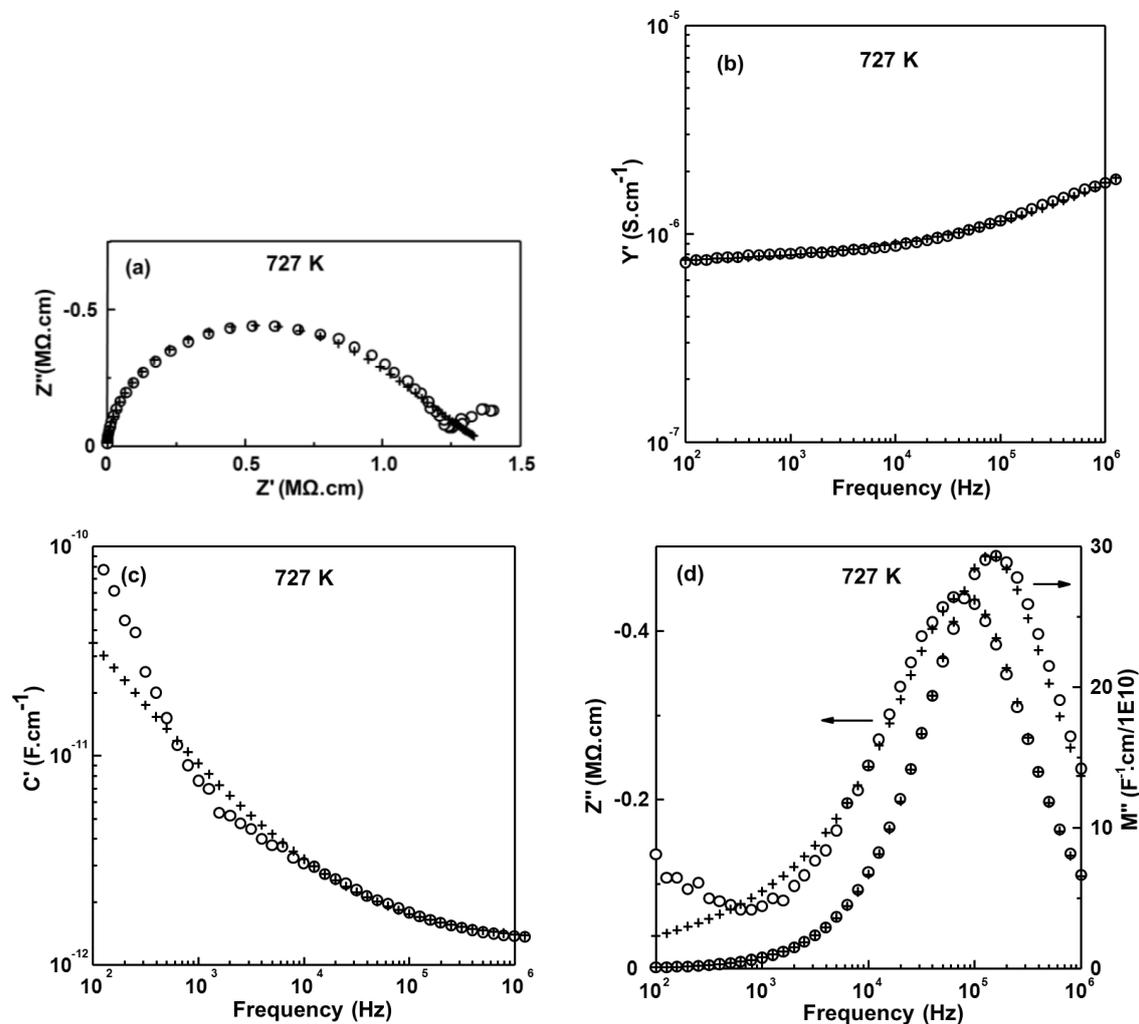
Figure 9.13 High temperature IS experimental data points (○) and the fitting results (+) to equivalent circuit in Figure 9.10 (a) with (a) Z* plot; (b) Y', (c) C', and (d) −Z"/M" spectroscopic plots at 727 K for $Bi_{12}(Bi_{0.3}Al_{0.7})O_{19.5}$.

Table 9.4 Fitted high temperature IS values of $Bi_{12}(Bi_{0.3}Al_{0.7})O_{19.5}$ from 645 to 746 K. Errors associated with the fitted circuit parameters R_1, C_1, C_x, A and n are $< \pm 6.7$ %, $< \pm 1.1$ %,$< \pm 129.3$ %,$< \pm 58.6$ % and $< \pm 9.9$ %, respectively.

Temperature (K)	R_1 (Ω cm)	C_1 (pF cm^{-1})	C_x (F cm^{-1})	A (Ω^{-1} cm^{-1} rad^{-1})	n
645	7105800	1.30	1.49×10^{-11}	7.63×10^{-10}	0.42
673	4356900	1.30	1.29×10^{-9}	1.28×10^{-9}	0.40
703	2082400	1.29	1.19×10^{-9}	1.51×10^{-9}	0.42
727	1376300	1.29	3.62×10^{-10}	2.80×10^{-9}	0.39
746	1017000	1.28	3.49×10^{-10}	3.27×10^{-9}	0.39
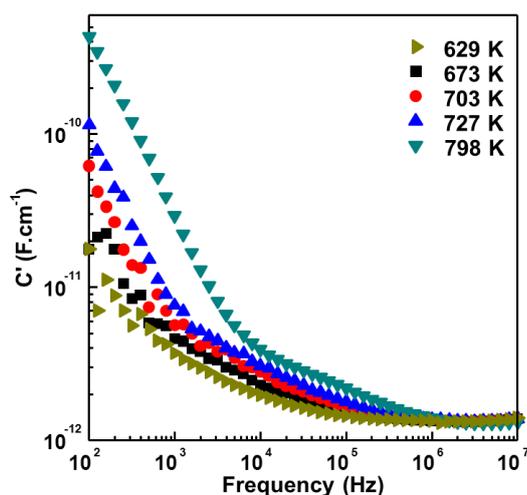
Figure 9.14 C' spectroscopic plot showing the capacitance fluctuation at various temperatures for $Bi_{12}(Bi_{0.3}Al_{0.7})O_{19.5}$.
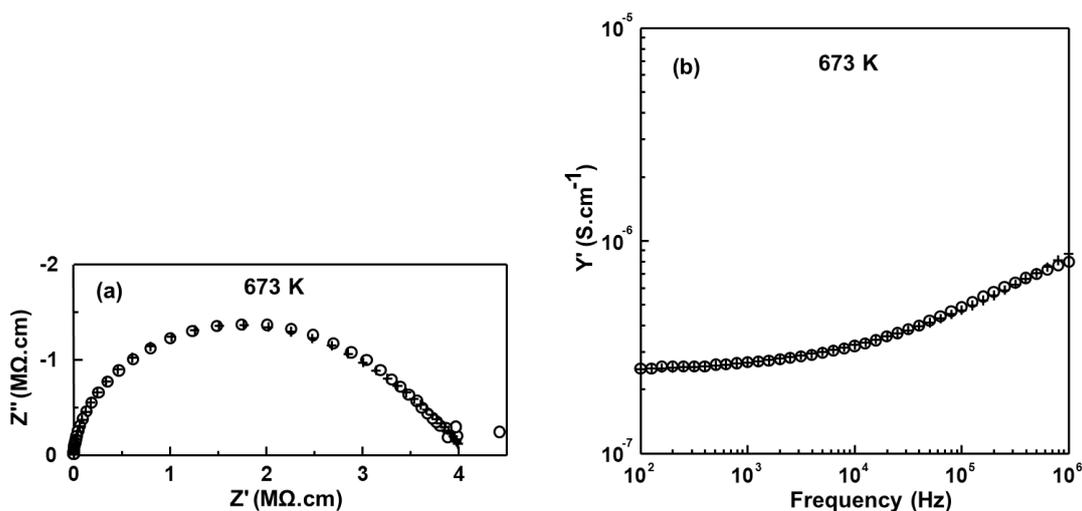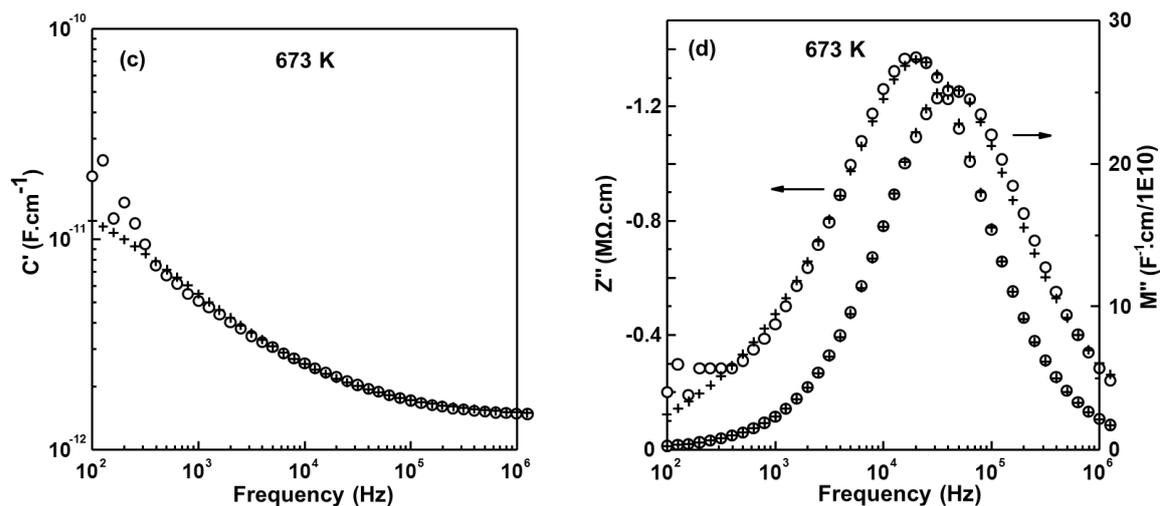
$Bi_{12}(Bi_{0.4}Al_{0.6})O_{19.5}$

Figure 9.15 High temperature IS experimental data points (○) and the fitting results (+) to equivalent circuit in Figure 9.10 (a) with (a) Z* plot; (b) Y', (c) C', and (d) −Z"/M" spectroscopic plots at 673 K for $Bi_{12}(Bi_{0.4}Al_{0.6})O_{19.5}$.

Table 9.5 Fitted high temperature IS values of $Bi_{12}(Bi_{0.4}Al_{0.6})O_{19.5}$ from 673 to 753 K. Errors associated with the fitted circuit parameters R_1, C_1, C_x, A and n are < ±8.7 %, < ±1.4 %,< ±130.8 %,< ±67.5 % and < ±10.9 %, respectively.

Temperature (K)	R_1 (Ω cm)	C_1 (pF cm^{-1})	C_x (F cm^{-1})	A (Ω^{-1} cm^{-1} rad^{-1})	n
673	4040600	1.43	1.86×10^{-11}	9.52×10^{-10}	0.43
703	2198800	1.42	1.39×10^{-9}	1.24×10^{-9}	0.43
723	1533400	1.42	5.59×10^{-10}	1.53×10^{-9}	0.43
753	886980	1.43	3.77×10^{-10}	2.97×10^{-9}	0.41
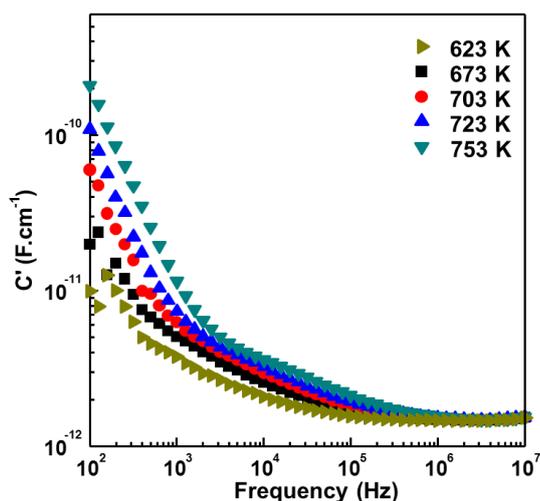
Figure 9.16 C' spectroscopic plot showing the capacitance fluctuation at various temperatures for $Bi_{12}(Bi_{0.4}Al_{0.6})O_{19.5}$.

$Bi_{12}(Bi_{0.6}In_{0.4})O_{19.5}$
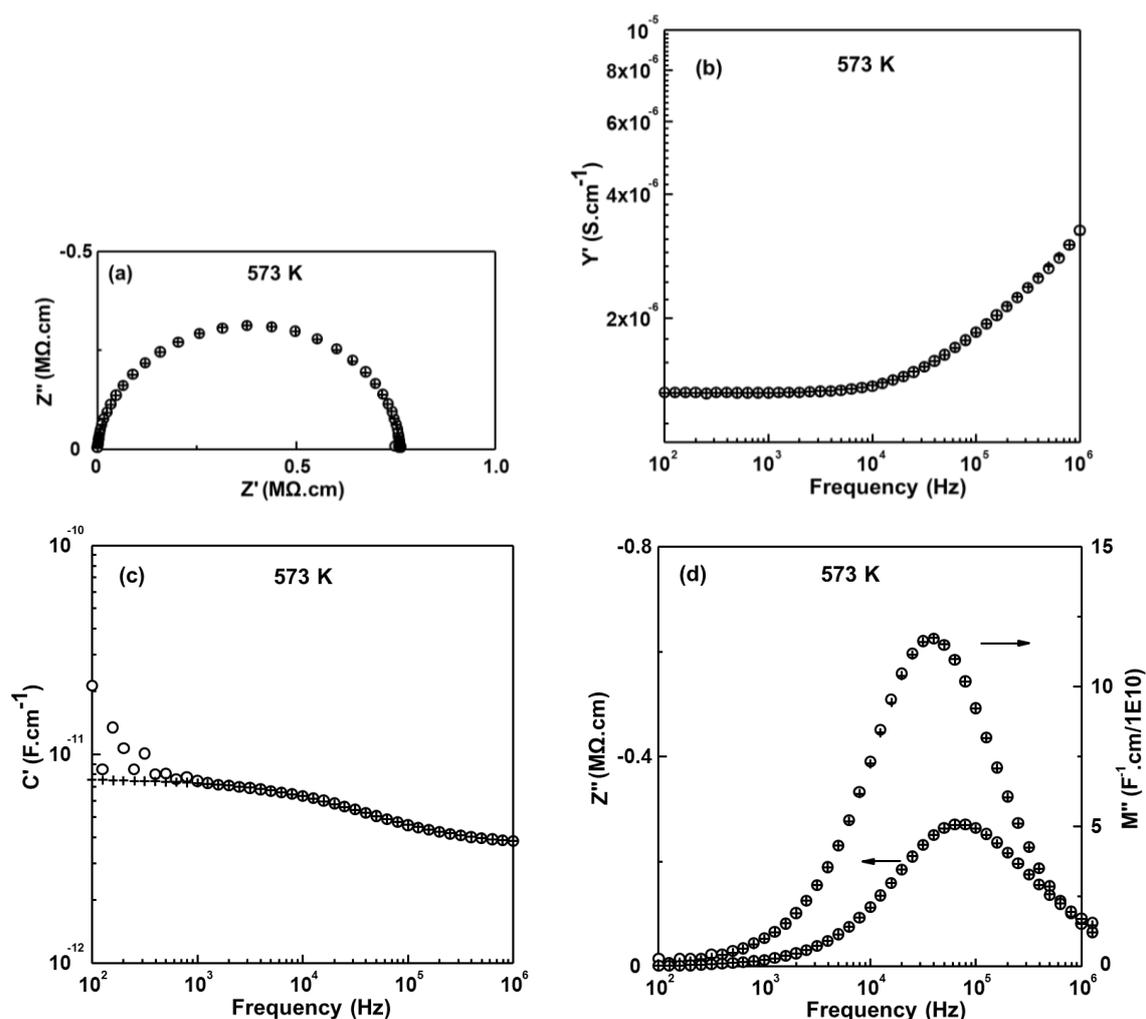
Figure 9.17 High temperature IS experimental data points (○) and the fitting results (+) to equivalent circuit in Figure 9.10 (a) with (a) Z* plot; (b) Y', (c) C', and (d) −Z"/M" spectroscopic plots at 573 K for $Bi_{12}(Bi_{0.6}In_{0.4})O_{19.5}$.

Table 9.6 Fitted high temperature IS values of $Bi_{12}(Bi_{0.6}In_{0.4})O_{19.5}$ from 498 to 673 K. Errors associated with the fitted circuit parameters R_1, C_1, C_x, A and n are < ±0.2 %, < ±1.1 %,< ±3.9 %,< ±16.0 % and < ±3.1 %, respectively.

Temperature (K)	R_1 (Ω cm)	C_1 (pF cm^{-1})	C_x (pF cm^{-1})	A (Ω^{-1} cm^{-1} rad^{-1})	n
498	7938200	3.57	4.89	1.67×10^{-9}	0.38
528	2378900	3.58	4.52	3.29×10^{-9}	0.38
548	1364200	3.59	4.33	4.55×10^{-9}	0.38
573	761210	3.60	4.01	6.56×10^{-9}	0.38
601	335760	3.60	3.76	1.02×10^{-8}	0.38
623	17650	3.59	3.85	1.13×10^{-8}	0.39
650	115970	3.59	3.73	1.54×10^{-8}	0.39
673	74099	3.65	2.84	4.95×10^{-8}	0.33

- ## Chapter 5: Boron containing sillenites

$Bi_{12}(B_{0.5}Ga_{0.5})O_{19.5}$

HT relaxation:
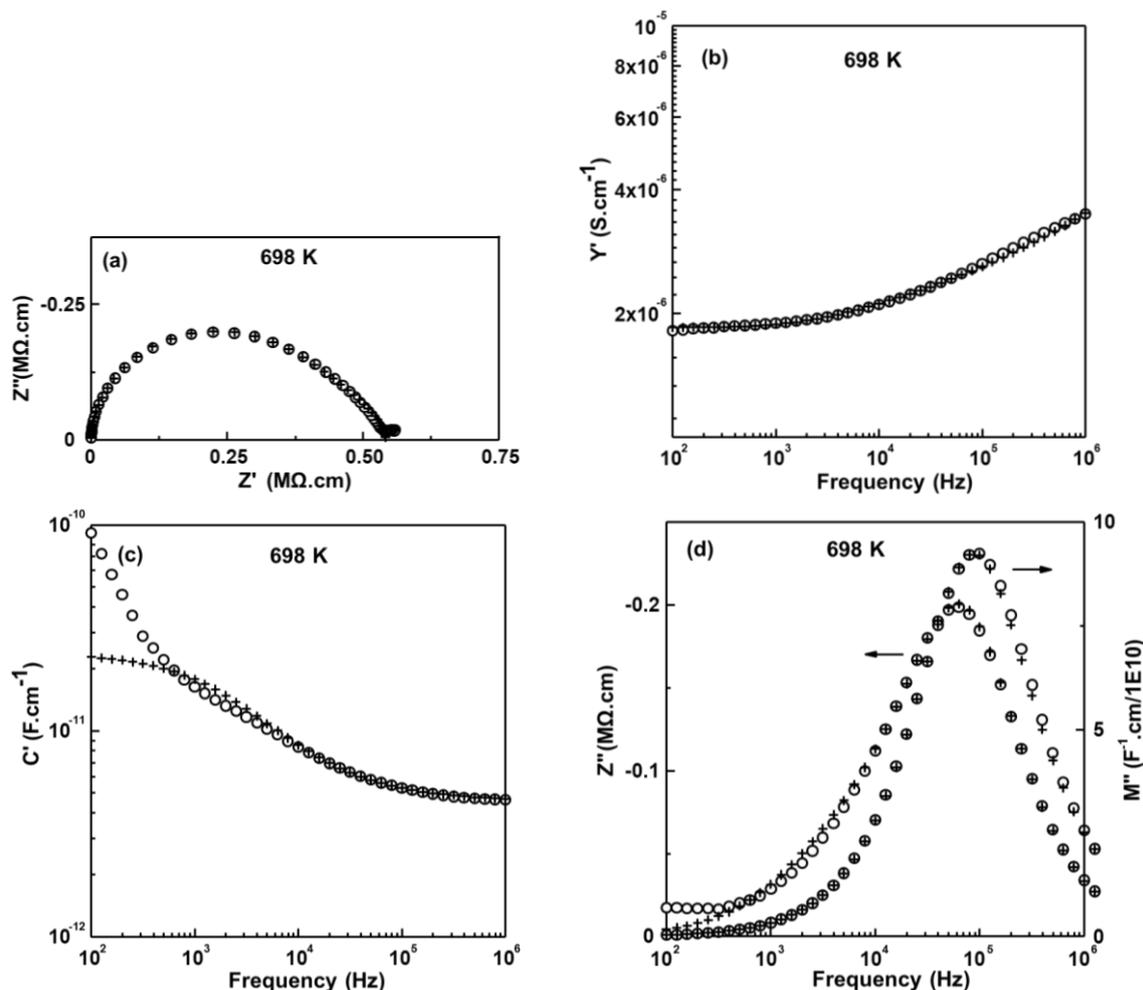
Figure 9.18 High temperature IS experimental data points (○) and the fitting results (+) to equivalent circuit in Figure 9.10 (a) with (a) Z* plot; (b) Y', (c) C', and (d) −Z"/M" spectroscopic plots at 698 K for $Bi_{12}(B_{0.5}Ga_{0.5})O_{19.5}$.

Table 9.7 Fitted high temperature IS values of $Bi_{12}(Bi_{0.5}Ga_{0.5})O_{19.5}$ from 623 to 698 K. Errors associated with the fitted circuit parameters R_1, C_1, C_x, A and n are $< \pm1.5$ %, $< \pm0.5$ %,$< \pm1.1$ %,$< \pm24.4$ % and $< \pm6.7$ %, respectively.

Temperature (K)	R_1 (Ω cm)	C_1 (pF cm⁻¹)	C_x (pF cm⁻¹)	A (Ω⁻¹ cm⁻¹ rad⁻¹)	n
623	6073000	4.59	6.30	6.73×10^{-9}	0.22
645	3185900	4.56	8.49	8.61×10^{-9}	0.24
673	1322290	4.55	11.73	1.11×10^{-8}	0.28
698	541590	4.52	19.51	1.34×10^{-8}	0.32

LT relaxation:
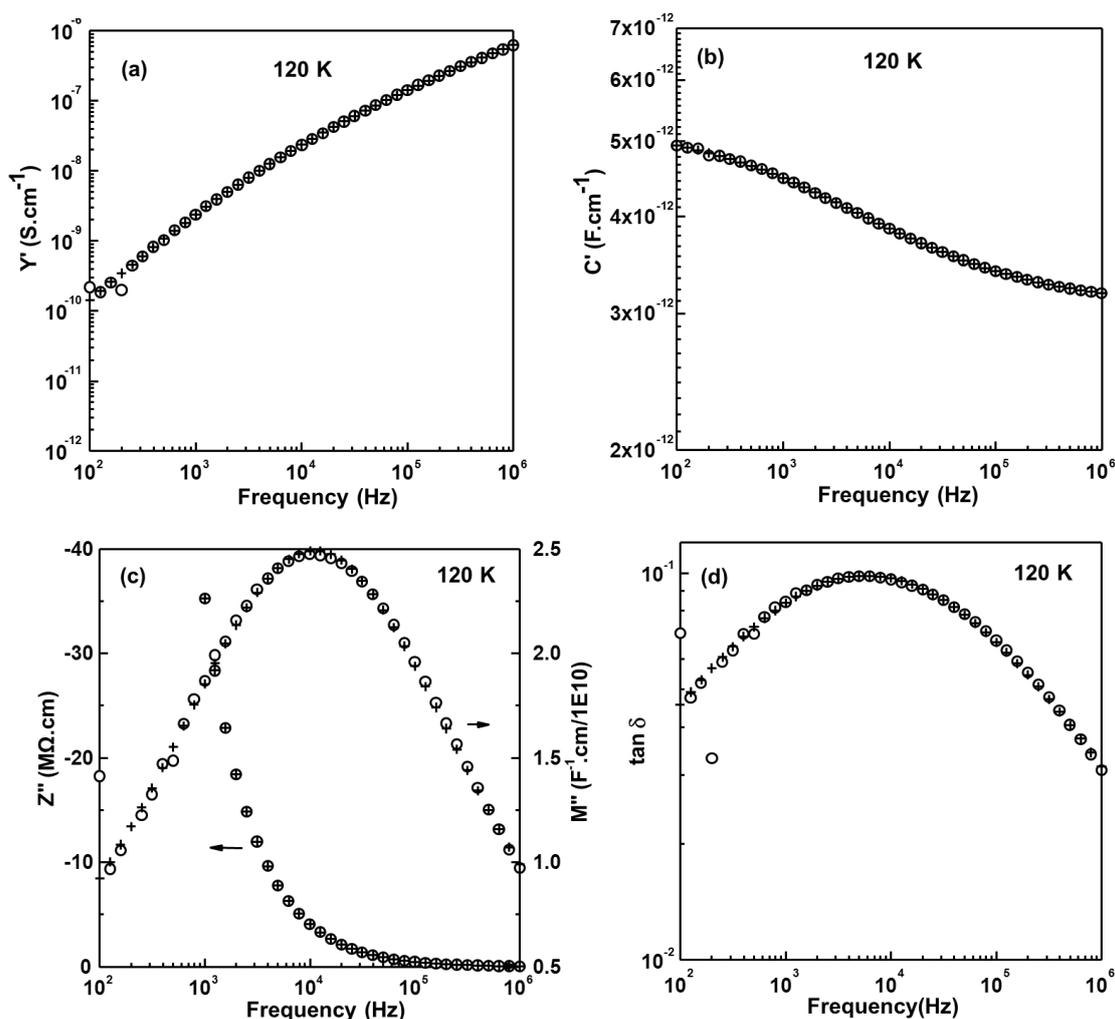
Figure 9.19 Low temperature IS experimental data points (○) and the fitting results (+) to equivalent circuit shown in Figure 9.10 (b) with (a) Y'; (b) C', (c) −Z''/M'', and (d) tan δ spectroscopic plots at 120 K for $Bi_{12}(B_{0.5}Ga_{0.5})O_{19.5}$.

Table 9.8 Ftted subambient IS values of $Bi_{12}(B_{0.5}Ga_{0.5})O_{19.5}$ from 120 to 170 K (for the 1st low temperature relaxation). Errors associated with the fitted circuit parameters C_1, C_x, A and n are $< \pm1.7$ %,$< \pm2.0$ %,$< \pm8.8$ % and $< \pm1.6$ %, respectively.

Temperature (K)	C_1 (pF cm^{-1})	C_x (pF cm^{-1})	A (Ω^{-1} cm^{-1} rad^{-1})	n
120	3.05	2.24	1.72×10^{-10}	0.56
130	3.06	2.32	3.40×10^{-10}	0.54
140	3.04	2.43	5.48×10^{-10}	0.54
150	3.02	2.50	9.34×10^{-10}	0.53
160	2.93	2.70	1.16×10^{-9}	0.55
170	2.81	2.87	1.61×10^{-9}	0.56

$Bi_{12}(B_{0.5}Al_{0.5})O_{19.5}$

HT relaxation:
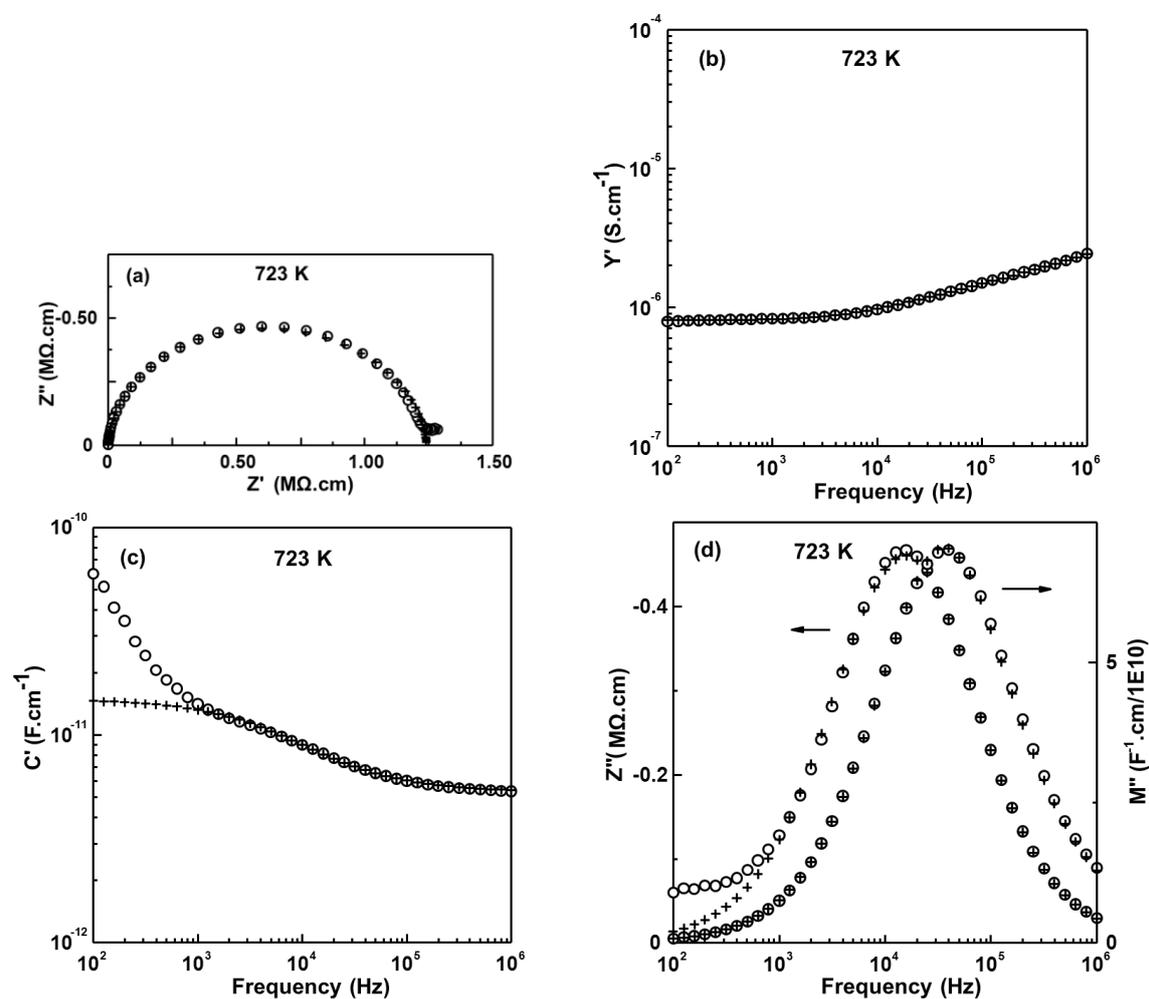
Figure 9.20 High temperature IS experimental data points (○) and the fitting results (+) to equivalent circuit shown in Figure 9.10 (a) with (a) Z* plot; (b) Y', (c) C', and (d) −Z''/M'' spectroscopic plots at 723 K for $Bi_{12}(B_{0.5}Al_{0.5})O_{19.5}$.

Table 9.9 Fitted high temperature IS values of $Bi_{12}(Bi_{0.5}Al_{0.5})O_{19.5}$ from 673 to 798 K. Errors associated with the fitted circuit parameters R_1, C_1, C_x, A and n are < ±0.4 %, < ±0.6 %, < ±7.8 %, < ±38.5 % and < ±11.7 %, respectively.

Temperature (K)	R_1 (Ω cm)	C_1 (pF cm^{-1})	C_x (pF cm^{-1})	A (Ω^{-1} cm^{-1} rad^{-1})	n
673	6717000	5.31	6.71	8.90×10^{-9}	0.24
698	3196900	5.28	7.42	1.17×10^{-8}	0.27
723	1241000	5.26	9.62	1.16×10^{-8}	0.33
748	762370	5.20	5.49	4.66×10^{-8}	0.22
773	429020	5.16	5.34	7.10×10^{-8}	0.22
798	248800	5.12	5.56	8.68×10^{-8}	0.24

LT relaxation:
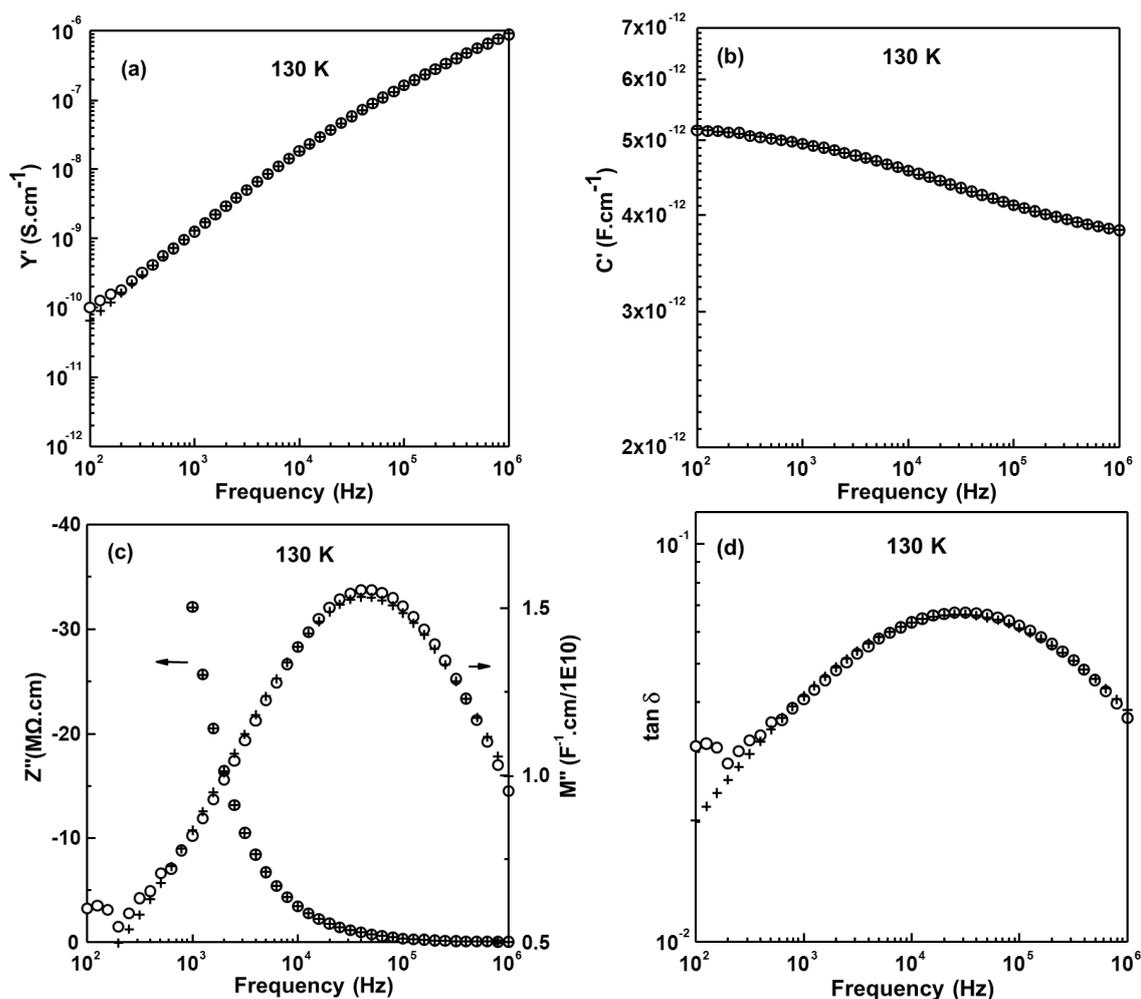
Figure 9.21 Low temperature IS experimental data points (○) and the fitting results (+) to equivalent circuit shown in Figure 9.10 (b) with (a) Y'; (b) C', (c) −Z"/M", and (d) tan δ spectroscopic plots at 130 K for $Bi_{12}(B_{0.5}Al_{0.5})O_{19.5}$.

Table 9.10 Fitted subambient IS values of $Bi_{12}(B_{0.5}Al_{0.5})O_{19.5}$ from 100 to 130 K (for the 1st low temperature relaxation). Errors associated with the fitted circuit parameters C_1, C_x, A and n are < ±0.2 %,< ±0.9 %,< ±4.9 % and < ±0.8 %, respectively.

Temperature (K)	C_1 (pF cm^{-1})	C_x (pF cm^{-1})	A (Ω^{-1} cm^{-1} rad^{-1})	n
100	3.64	1.41	6.18×10^{-11}	0.58
110	3.63	1.51	9.95×10^{-11}	0.57
120	3.63	1.59	1.64×10^{-10}	0.57
130	3.59	1.74	2.11×10^{-10}	0.59

Bi$_{12}$(B$_{0.25}$Si$_{0.75}$)O$_{19.875}$

HT relaxation:
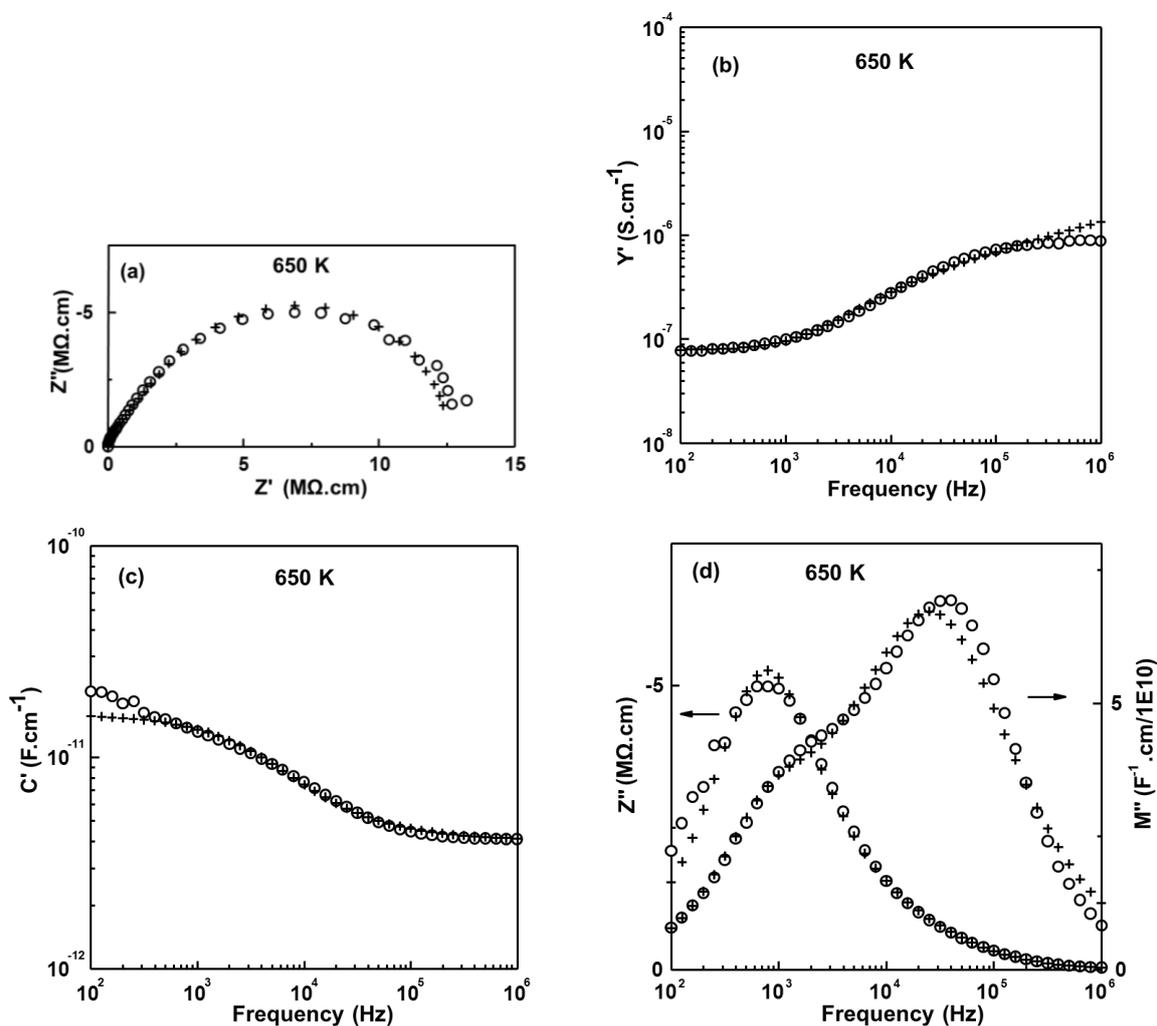
Figure 9.22 High temperature IS experimental data points (○) and the fitting results (+) to equivalent circuit shown in Figure 9.10 (a) with (a) Z* plot; (b) Y', (c) C', and (d) −Z"/M" spectroscopic plots at 650 K for Bi$_{12}$(B$_{0.25}$Si$_{0.75}$)O$_{19.875}$.

Table 9.11 Fitted high temperature IS values of Bi$_{12}$(Bi$_{0.25}$Si$_{0.75}$)O$_{19.875}$ from 596 to 650 K. Errors associated with the fitted circuit parameters R$_1$, C$_1$, C$_x$, A and n are < ±1.3 %, < ±2.4 %,< ±2.9 %,< ±14.4 % and < ±5.2 %, respectively.

Temperature (K)	R$_1$ (Ω cm)	C$_1$ (pF cm^{-1})	C$_x$ (pF cm^{-1})	A (Ω^{-1} cm^{-1} rad^{-1})	n
596	6852200	4.10	11.4	1.01×10^{-8}	0.25
603	5484900	4.08	12.5	9.92×10^{-9}	0.26
623	2938400	4.05	13.3	1.11×10^{-8}	0.28
637	1696800	4.04	13.3	1.35×10^{-8}	0.29
650	1263800	4.04	12.1	1.68×10^{-8}	0.28

LT relaxation:
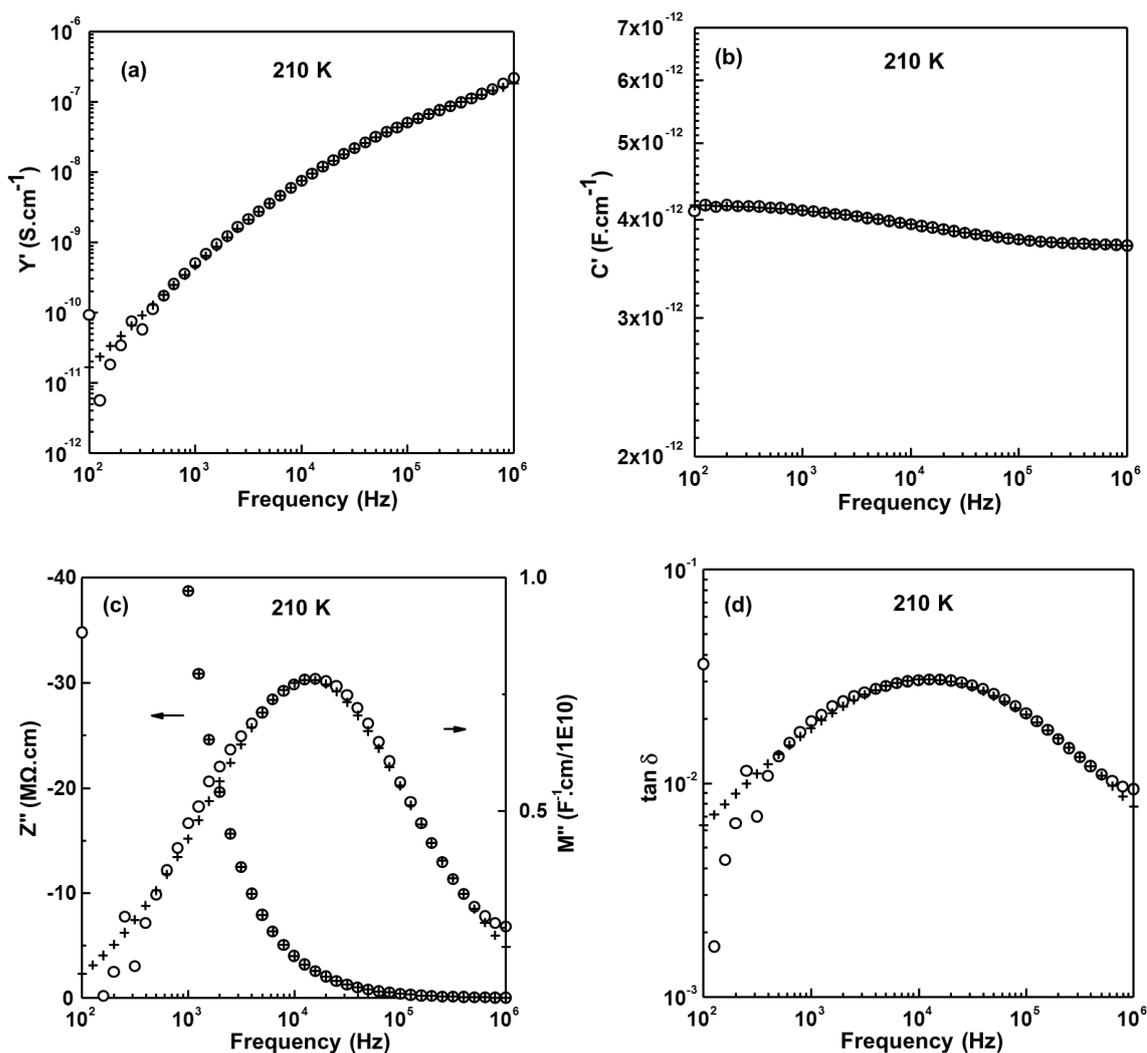
Figure 9.23 Low temperature IS experimental data points ($\circ$) and the fitting results ($+$) to equivalent circuit shown in Figure 9.10 (b) with (a) Y'; (b) C', (c) $-Z''/M''$, and (d) tan δ spectroscopic plots at 210 K for $Bi_{12}(B_{0.25}Si_{0.75})O_{19.875}$.

Table 9.12 Fitted subambient IS values of $Bi_{12}(B_{0.25}Si_{0.75})O_{19.875}$ from 200 to 270 K (for the 2nd low temperature relaxation). Errors associated with the fitted circuit parameters C_1, C_x, A and n are $< \pm0.5$ %, $< \pm5.0$ %, $< \pm40.7$ % and $< \pm11.1$ %, respectively.

Temperature (K)	C_1 (pF cm^{-1})	C_x (pF cm^{-1})	A (Ω^{-1} cm^{-1} rad^{-1})	n
200	3.68	0.51	1.98×10^{-10}	0.43
210	3.68	0.52	2.54×10^{-10}	0.44
220	3.69	0.49	6.42×10^{-10}	0.39
230	3.69	0.52	6.74×10^{-10}	0.42
240	3.70	0.50	1.46×10^{-9}	0.39
250	3.72	0.46	4.21×10^{-9}	0.33
260	3.73	0.57	6.28×10^{-9}	0.33
270	3.74	0.44	1.18×10^{-8}	0.30

$Bi_{12}(B_{0.5}P_{0.5})O_{19.5}$

HT relaxation:
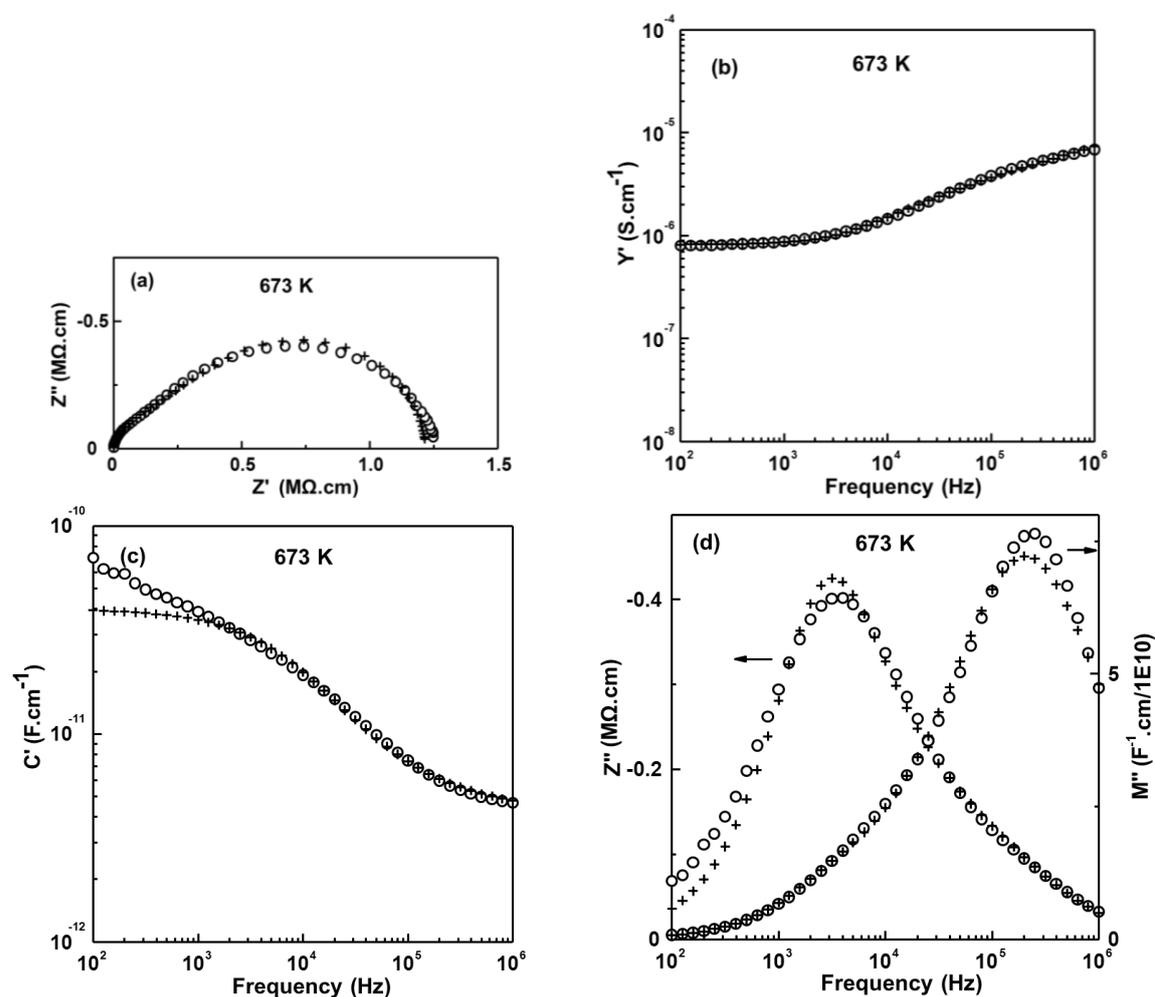
Figure 9.24 High temperature IS data points (○) and the fitting results (+) to equivalent circuit shown in Figure 9.10 (a) with (a) Z^* plot; (b) Y', (c) C', and (d) $-Z''/M''$ spectroscopic plots at 673 K for $Bi_{12}(B_{0.5}P_{0.5})O_{19.5}$.

Table 9.13 Fitted high temperature IS values of $Bi_{12}(Bi_{0.5}P_{0.5})O_{19.5}$ from 623 to 798 K. Errors associated with the fitted circuit parameters R_1, C_1, C_x, A and n are $< \pm1.3$ %, $< \pm0.9$ %,$< \pm3.0$ %,$< \pm11.4$ % and $< \pm2.9$ %, respectively.

Temperature (K)	R_1 (Ω cm)	C_1 (pF cm^{-1})	C_x (pF cm^{-1})	A (Ω^{-1} cm^{-1} rad^{-1})	n
623	7406500	4.27	40.1	2.93×10^{-8}	0.30
648	3164200	4.25	39.5	4.13×10^{-8}	0.31
673	1215800	4.21	35.9	6.54×10^{-8}	0.30
698	554230	4.10	33.2	8.68×10^{-8}	0.31
723	266780	4.01	29.2	1.22×10^{-7}	0.30
748	132060	3.98	26.4	1.62×10^{-7}	0.31
773	61841	3.97	22.6	2.19×10^{-7}	0.31
798	34039	3.83	21.4	2.11×10^{-7}	0.32

LT relaxation:
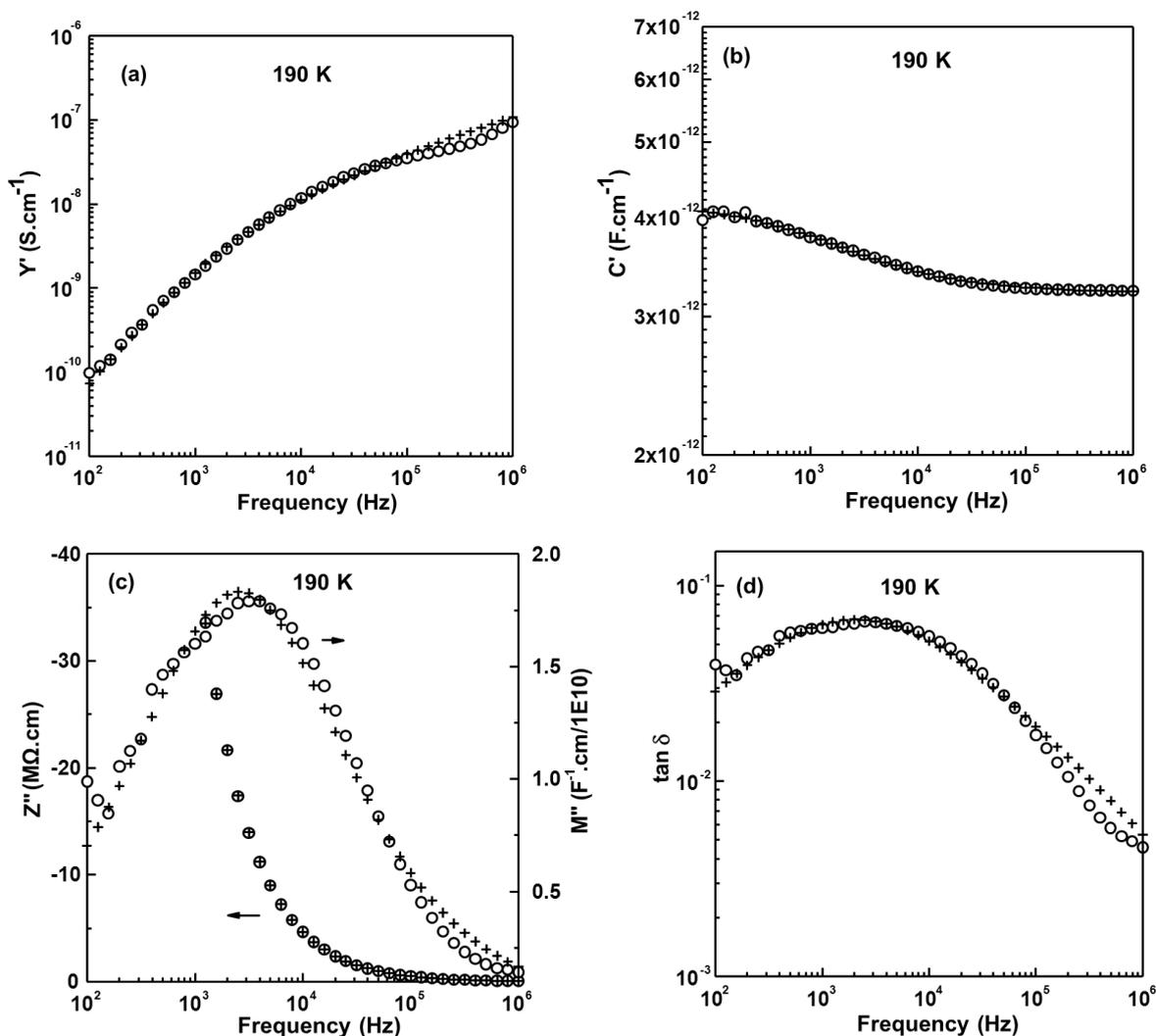
Figure 9.25 Low temperature IS experimental data points (○) and the fitting results (+) to equivalent circuit shown in Figure 9.10 (b) with (a) Y'; (b) C', (c) −Z"/M", and (d) tan δ spectroscopic plots at 190 K for $Bi_{12}(B_{0.5}P_{0.5})O_{19.5}$.

Table 9.14 Fitted subambient IS values of $Bi_{12}(B_{0.5}P_{0.5})O_{19.5}$ from 190 to 310 K (for the low temperature relaxation). Errors associated with the fitted circuit parameters C_1, C_x, A and n are $< \pm1.0$ %,$< \pm3.4$ %,$< \pm16.1$ % and $< \pm4.3$ %, respectively.

Temperature (K)	C_1 (pF cm^{-1})	C_x (pF cm^{-1})	A (Ω^{-1} cm^{-1} rad^{-1})	n
190	3.21	0.98	2.41×10^{-10}	0.41
210	3.22	1.01	5.34×10^{-10}	0.41
230	3.22	1.02	1.24×10^{-9}	0.40
250	3.21	1.04	2.71×10^{-9}	0.40
270	3.22	1.03	6.67×10^{-9}	0.38
290	3.23	1.01	1.66×10^{-8}	0.35
310	3.25	0.99	3.48×10^{-8}	0.34

$Bi_{12}(B_{0.5}V_{0.5})O_{19.5}$

HT relaxation:
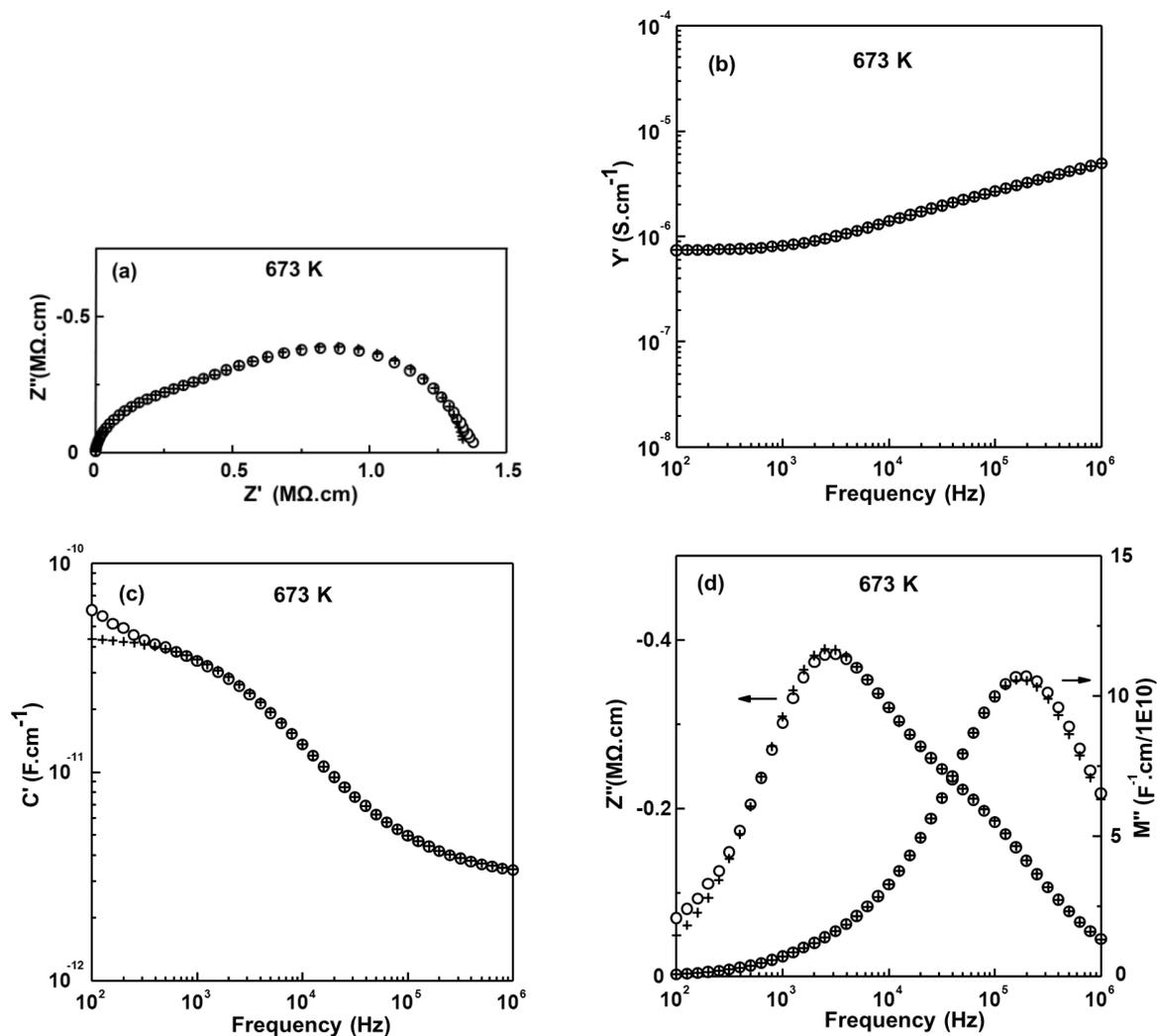
Figure 9.26 High temperature IS experimental data points (○) and the fitting results (+) to equivalent circuit shown in Figure 9.10 (a) with (a) Z* plot; (b) Y', (c) C', and (d) −Z"/M" spectroscopic plots at 673 K for $Bi_{12}(B_{0.5}V_{0.5})O_{19.5}$.

Table 9.15 Fitted high temperature IS values of $Bi_{12}(Bi_{0.5}V_{0.5})O_{19.5}$ from 623 to 798 K. Errors associated with the fitted circuit parameters R_1, C_1, C_x, A and n are < ±0.6 %, < ±1.7 %,< ±12.6 %,< ±26.2 % and < ±4.0 %, respectively.

Temperature (K)	R_1 (Ω cm)	C_1 (pF cm^{-1})	C_x (pF cm^{-1})	A (Ω^{-1} cm^{-1} rad^{-1})	n
623	3761700	3.50	61.5	3.08×10^{-8}	0.29
653	2122700	3.39	51.8	3.84×10^{-8}	0.30
673	1344200	3.07	42.5	4.08×10^{-8}	0.30
698	553440	2.92	30.7	5.03×10^{-8}	0.31
723	333610	2.73	20.7	4.83×10^{-8}	0.32
748	188980	2.50	15.6	3.49×10^{-8}	0.36

| 773 | 123440 | 2.35 | 11.2 | 3.89×10^{-8} | 0.35 |
| 798 | 62223 | 2.22 | 16.2 | 1.54×10^{-8} | 0.43 |

LT relaxation:
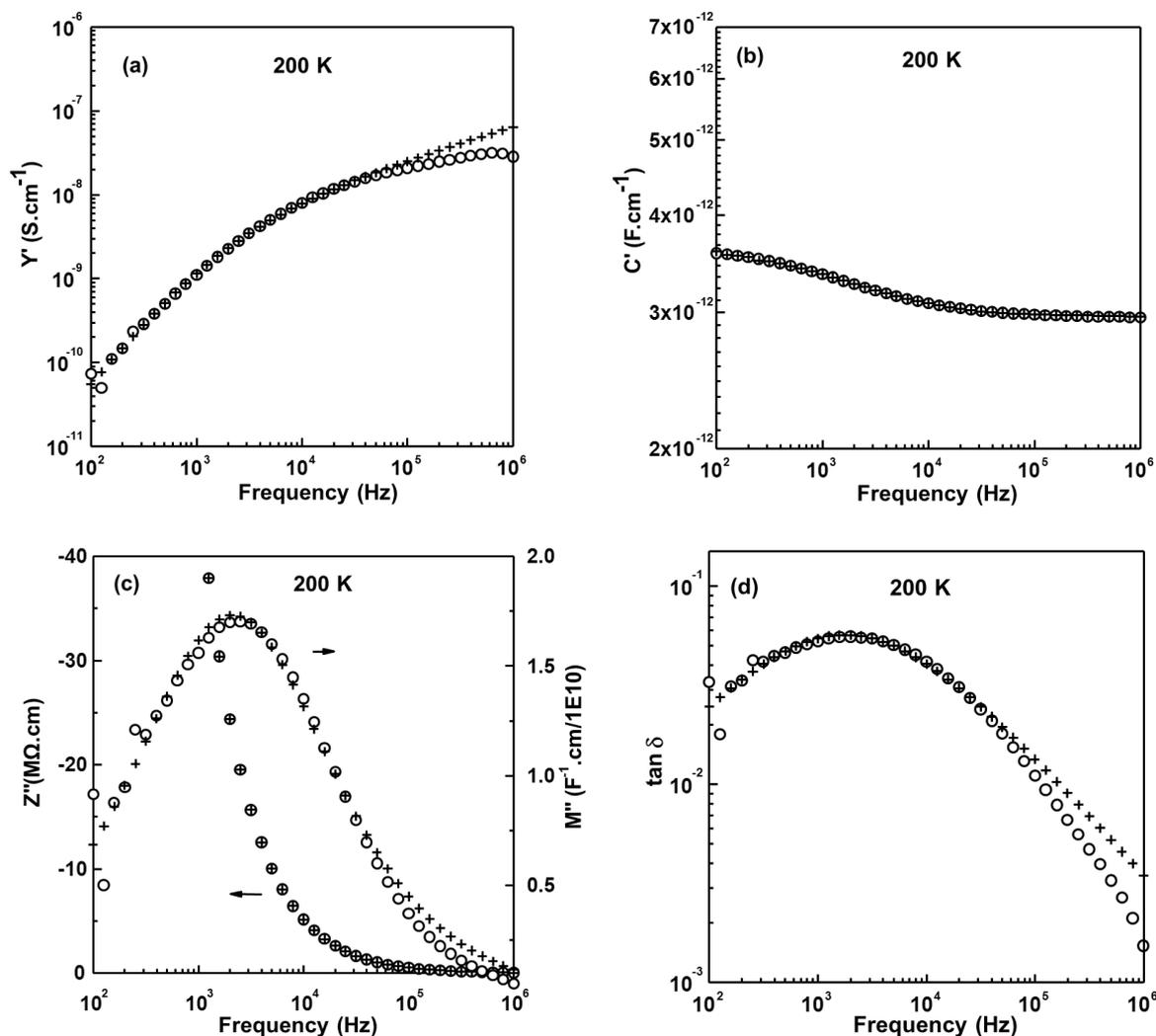
Figure 9.27 Low temperature IS experimental data points (○) and the fitting results (+) to equivalent circuit shown in Figure 9.10 (b) with (a) Y'; (b) C', (c) –Z"/M", and (d) tan δ spectroscopic plots at 200 K for $Bi_{12}(B_{0.5}V_{0.5})O_{19.5}$.

Table 9.16 Fitted subambient IS values of $Bi_{12}(B_{0.5}V_{0.5})O_{19.5}$ from 190 to 310 K (for the low temperature relaxation). Errors associated with the fitted circuit parameters C_1, C_x, A and n are < ±0.7 %,< ±2.9 %,< ±16.8 % and < ±4.6 %, respectively.

Temperature (K)	C_1 (pF cm^{-1})	C_x (pF cm^{-1})	A (Ω^{-1} cm^{-1} rad^{-1})	n
190	2.95	0.66	1.21×10^{-10}	0.38
200	2.95	0.71	2.02×10^{-10}	0.38
210	2.95	0.71	4.22×10^{-10}	0.36
220	2.95	0.74	5.81×10^{-10}	0.37

230	2.95	0.76	8.73×10^{-10}	0.38
240	2.95	0.76	1.60×10^{-9}	0.36
250	2.94	0.77	2.38×10^{-9}	0.36
260	2.95	0.76	4.48×10^{-9}	0.34
270	2.94	0.77	6.40×10^{-9}	0.34
280	2.95	0.77	9.77×10^{-9}	0.33
290	2.95	0.76	1.50×10^{-8}	0.33
300	2.96	0.76	1.99×10^{-8}	0.33
310	2.97	0.74	2.91×10^{-8}	0.32

- ## Chapter 6: Phosphate containing sillenites

$Bi_{12}P_{0.86}O_{20.15}$

HT relaxation:
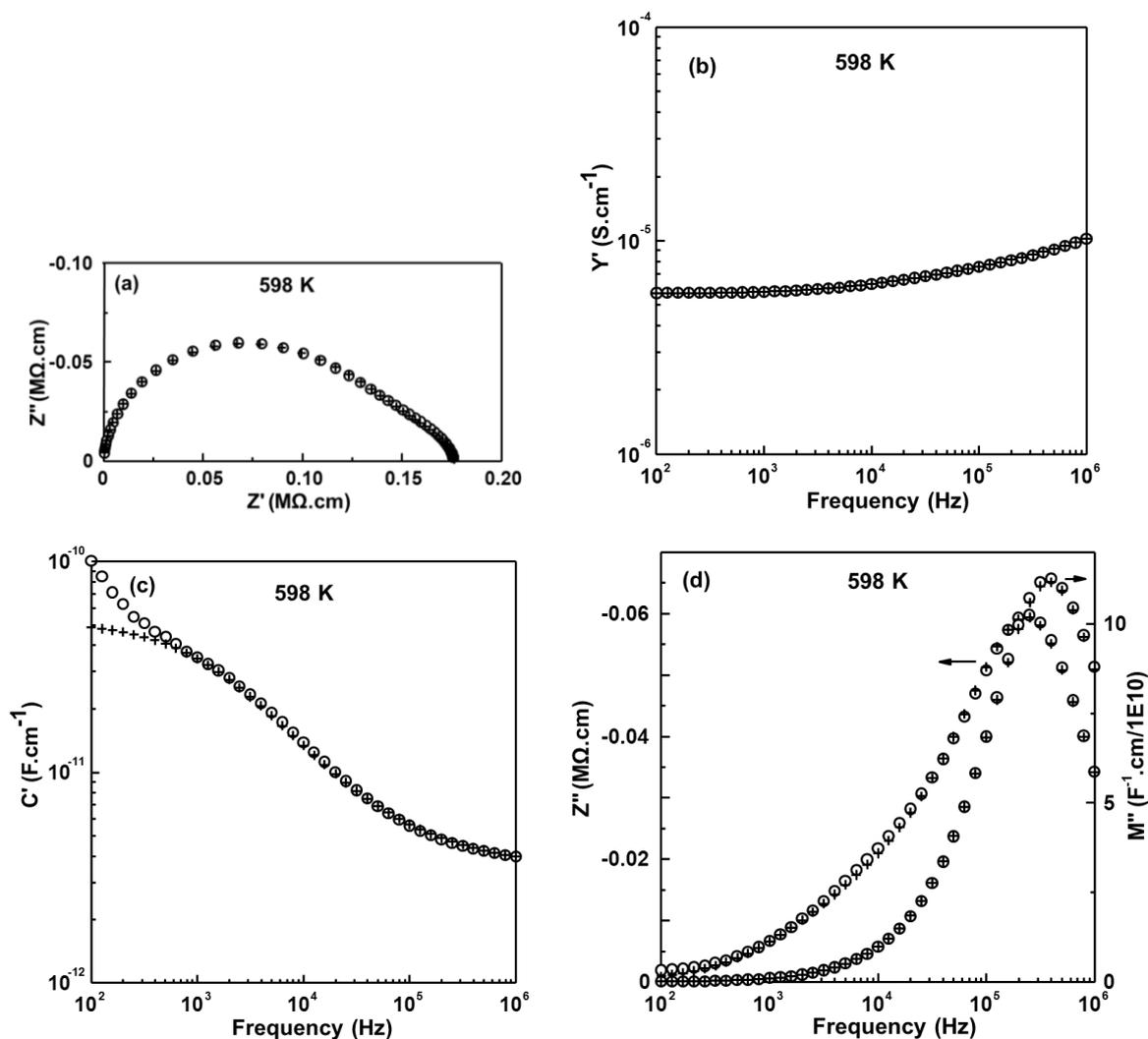
Figure 9.28 High temperature IS experimental data points (○) and the fitting results (+) to equivalent circuit shown in Figure 9.10 (a) with (a) Z* plot; (b) Y', (c) C', and (d) −Z"/M"

spectroscopic plots at 598 K for $Bi_{12}P_{0.86}O_{20.15}$.

Table 9.17 Fitted high temperature IS values of $Bi_{12}(Bi_{0.5}V_{0.5})O_{19.5}$ from 548 to 698 K. Errors associated with the fitted circuit parameters R_1, C_1, C_x, A and n are $< \pm0.4$ %, $< \pm1.6$ %, $< \pm23.2$ %, $< \pm29.7$ % and $< \pm4.2$ %, respectively.

Temperature (K)	R_1 (Ω cm)	C_1 (pF cm^{-1})	C_x (pF cm^{-1})	A (Ω^{-1} cm^{-1} rad^{-1})	n
548	899850	3.48	100.5	1.11×10^{-8}	0.34
573	290640	3.51	75.1	1.75×10^{-8}	0.35
598	176350	3.53	49.7	2.03×10^{-8}	0.36
623	89512	3.54	47.5	2.87×10^{-8}	0.36
648	48668	3.57	24.3	3.04×10^{-8}	0.37
673	26350	3.54	22.8	2.99×10^{-8}	0.40
698	15020	3.41	30.9	1.96×10^{-8}	0.44

LT relaxation:
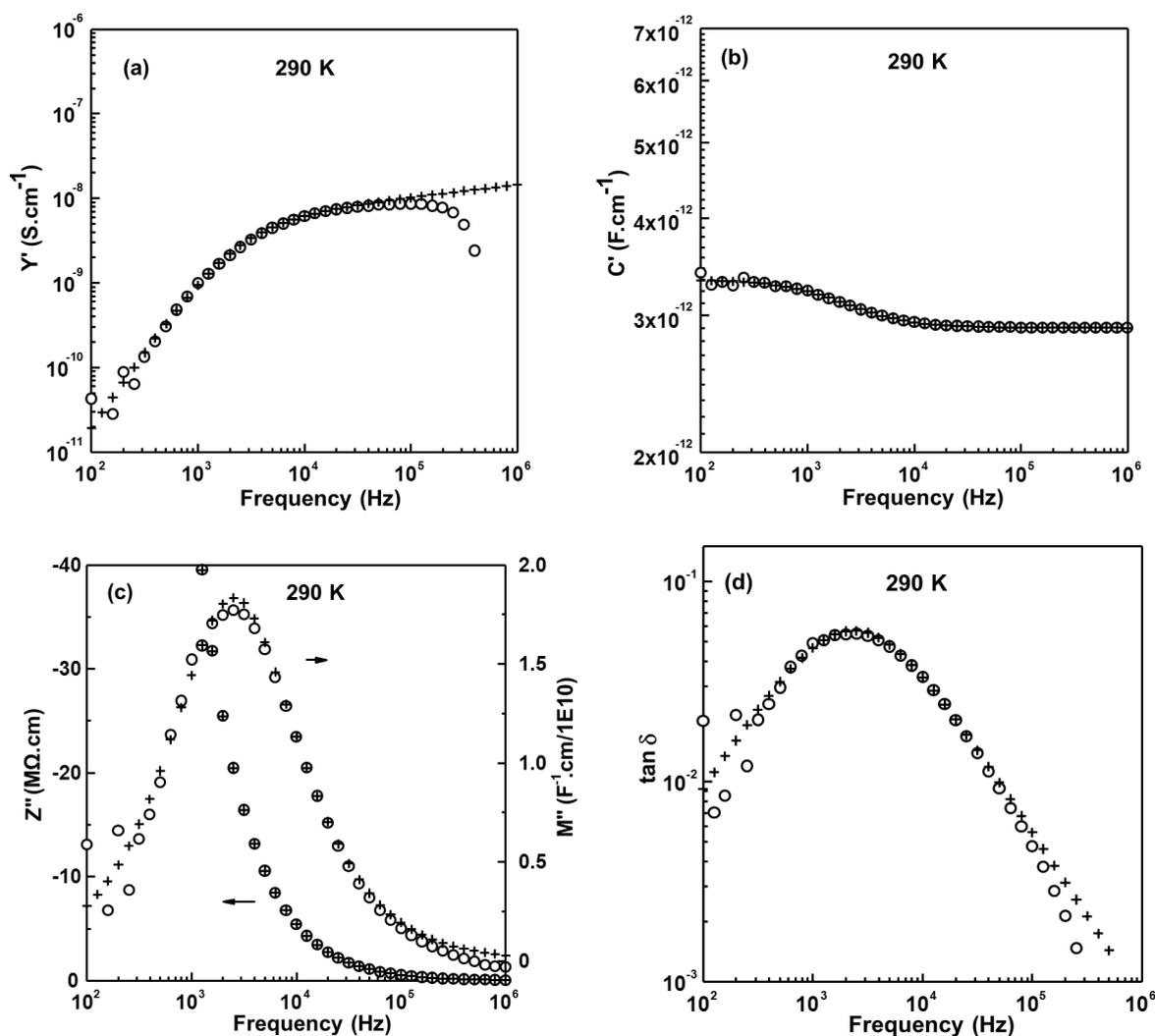
Figure 9.29 Low temperature IS experimental data points ($\circ$) and the fitting results ($+$) to equivalent circuit shown in Figure 9.10 (b) with (a) Y'; (b) C', (c) –Z''/M'', and (d) tan δ

spectroscopic plots at 290 K for $Bi_{12}P_{.86}O_{20.15}$.

Table 9.18 Fitted subambient IS values of $Bi_{12}P_{.86}O_{20.15}$ from 280 to 310 K (for the low temperature relaxation). Errors associated with the fitted circuit parameters C_1, C_x, A and n are $< \pm 0.1\ \%$, $< \pm 1.5\ \%$, $< \pm 17.4\ \%$ and $< \pm 12.8\ \%$, respectively.

Temperature (K)	C_1 (pF cm^{-1})	C_x (pF cm^{-1})	A (Ω^{-1} cm^{-1} rad^{-1})	n
280	2.88	0.46	7.45×10^{-10}	0.17
290	2.89	0.45	1.47×10^{-9}	0.15
300	2.89	0.44	2.45×10^{-9}	0.14
310	2.90	0.45	4.27×10^{-9}	0.13

$Bi_{12}(Fe_{0.5}P_{0.5})O_{20}$

HT relaxation:
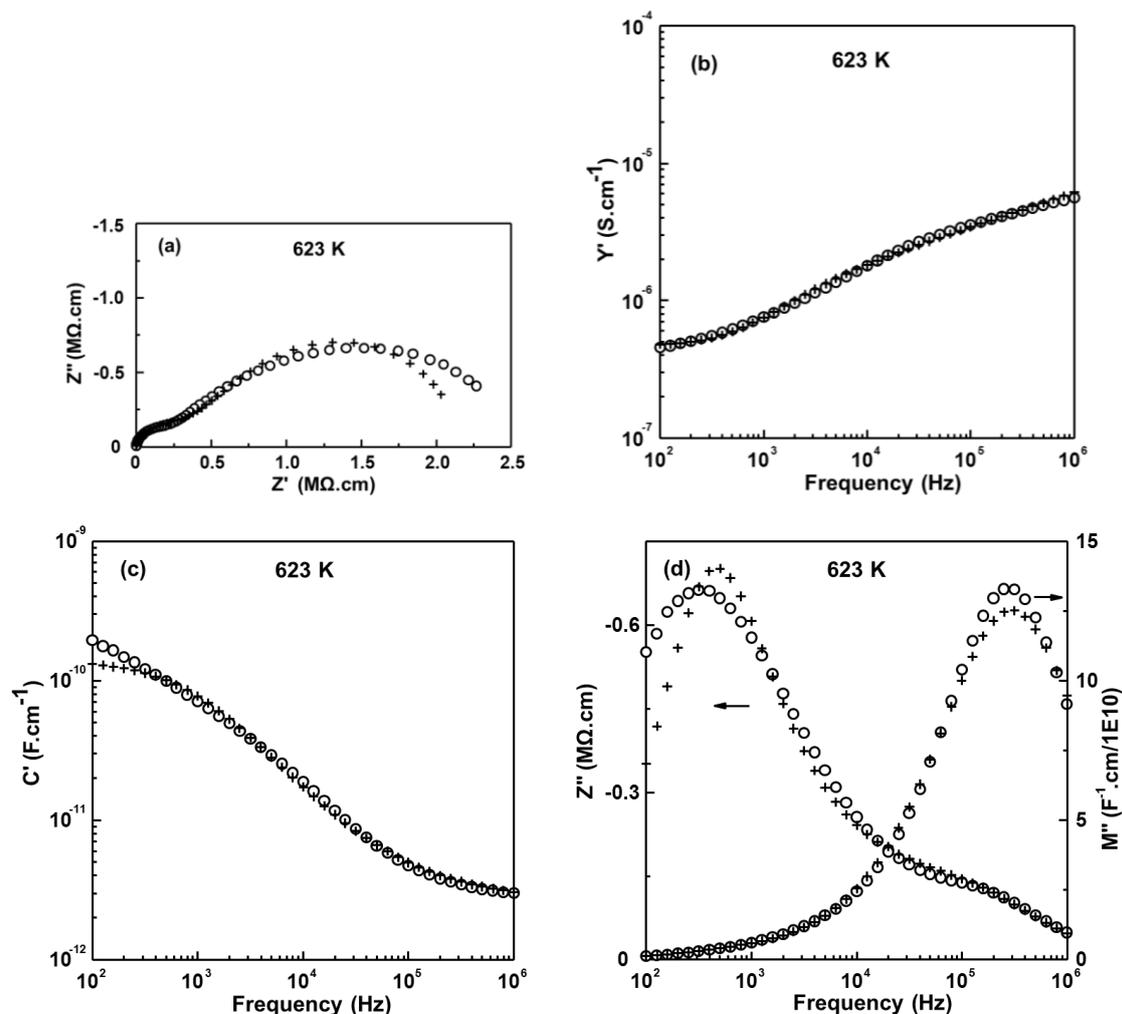
Figure 9.30 High temperature IS experimental data points (○) and the fitting results (+) to equivalent circuit shown in Figure 9.10 (a) with (a) Z* plot; (b) Y', (c) C', and (d) −Z"/M" spectroscopic plots at 623 K for $Bi_{12}(Fe_{0.5}P_{0.5})O_{20}$.

Table 9.19 Fitted high temperature IS values of $Bi_{12}(Fe_{0.5}P_{0.5})O_{20}$ from 623 to 798 K. Errors associated with the fitted circuit parameters R_1, C_1, C_x, A and n are $< \pm1.6$ %, $< \pm1.2$ %, $< \pm5.4$ %, $< \pm10.1$ % and $< \pm2.4$ %, respectively.

Temperature (K)	R_1 (Ω cm)	C_1 (pF cm^{-1})	C_x (F cm^{-1})	A (Ω^{-1} cm^{-1} rad^{-1})	n
623	2144800	2.64	1.41×10^{-10}	9.06×10^{-8}	0.27
648	1026000	2.60	1.70×10^{-10}	1.49×10^{-7}	0.27
673	639150	2.55	1.99×10^{-10}	1.98×10^{-7}	0.28
698	354550	2.51	2.19×10^{-10}	2.87×10^{-7}	0.29
723	221650	2.47	2.33×10^{-10}	3.84×10^{-7}	0.28
748	137730	2.42	2.39×10^{-10}	5.15×10^{-7}	0.28
773	85740	2.35	2.45×10^{-10}	6.52×10^{-7}	0.28
798	51765	2.20	2.62×10^{-10}	7.47×10^{-7}	0.29

$Bi_{12}(Mg_{0.33}P_{0.67})O_{20}$

HT relaxation:
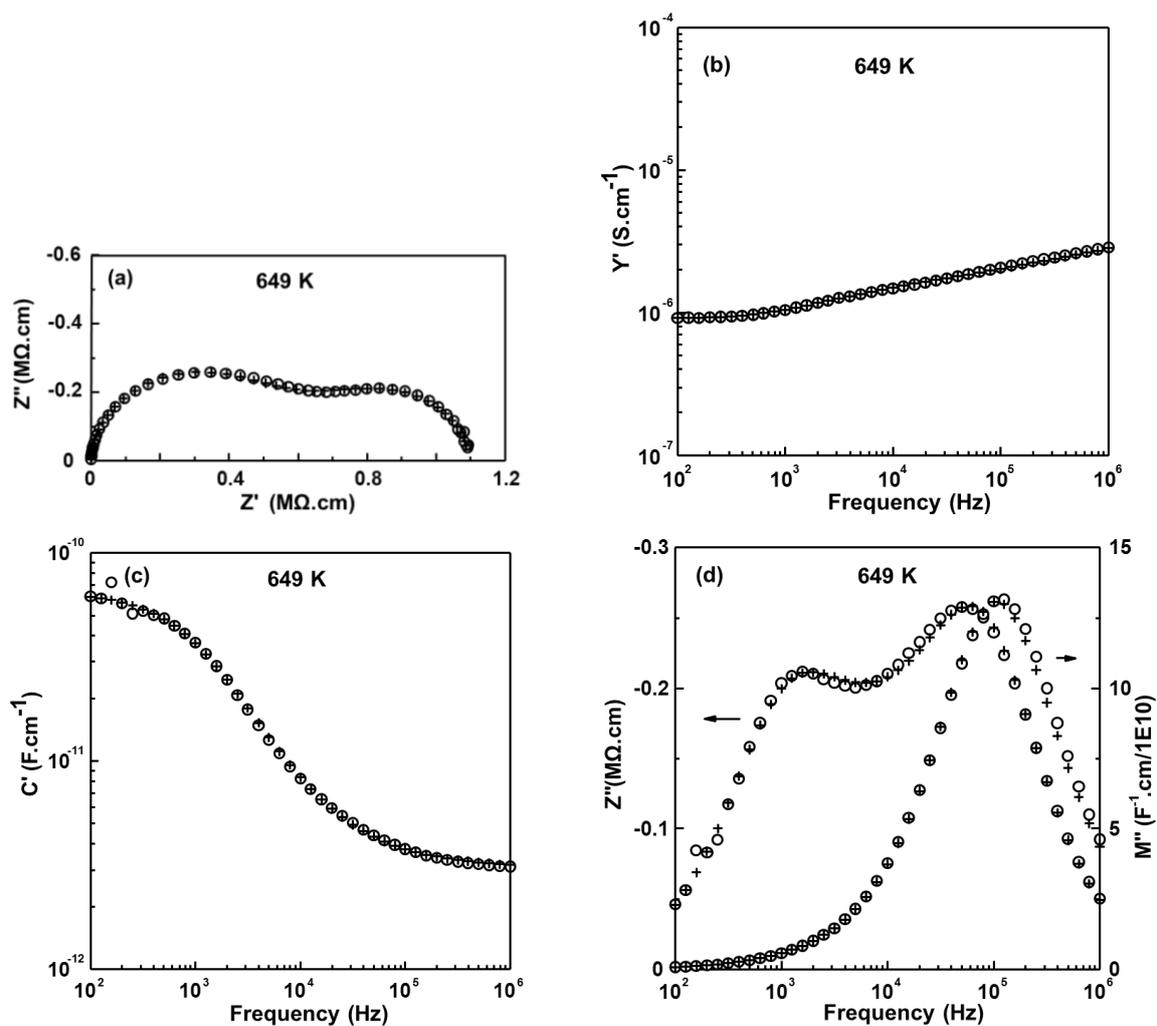
Figure 9.31 High temperature IS experimental data points ($\circ$) and the fitting results (+) to

equivalent circuit shown in Figure 9.10 (a) with (a) Z* plot; (b) Y', (c) C', and (d) −Z"/M" spectroscopic plots at 649 K for $Bi_{12}(Mg_{0.33}P_{0.67})O_{20}$.

Table 9.20 Fitted high temperature IS values of $Bi_{12}(Mg_{0.33}P_{0.67})O_{20}$ from 623 to 778 K. Errors associated with the fitted circuit parameters R_1, C_1, C_x, A and n are $< \pm1.9$ %, $< \pm0.8$ %,$< \pm12.5$ %,$< \pm31.3$ % and $< \pm8.9$ %, respectively.

Temperature (K)	R_1 (Ω cm)	C_1 (pF cm^{-1})	C_x (pF cm^{-1})	A (Ω^{-1} cm^{-1} rad^{-1})	n
623	2703300	3.04	81.1	3.45×10^{-8}	0.22
649	1096100	3.07	62.5	6.08×10^{-8}	0.22
673	544880	5.04	50.4	9.54×10^{-8}	0.22
698	264730	3.12	41.2	1.47×10^{-7}	0.23
728	128150	3.17	31.2	2.35×10^{-7}	0.23
750	73865	3.22	26.1	3.27×10^{-7}	0.23
778	43003	3.28	23.4	4.05×10^{-7}	0.23